Investigation of Nanostructured Heterogeneous Catalysts for Automotive Applications Using Advanced Electron Microscopy

by

Obiefune K. Ezekoye

A dissertation submitted in partial fulfillment
of the requirements for the degree of
Doctor of Philosophy
(Materials Science and Engineering)
in the University of Michigan
2010

Doctoral Committee:

       Professor Xiaoqing Pan, Chair
       Professor Levi T. Thompson Jr.
       Assistant Professor Anton Van der Ven
       Adjunct Professor George W. Graham

"Gloria Dei vivens homo"
                    -Sancti Irenaei

DEDICATION

I would like to dedicate this thesis to my family and friends for debts that I will never be able to repay.

ACKNOWLEDGEMENTS

First, I would like to thank the members of my thesis committee individually. I would like to extend my thanks to Professor Anton Van Der Ven for his support of this work. I would like to acknowledge Professor Levi Thompson for his advice and mentorship and for giving me the opportunity to collaborate with his group on many interesting projects. I would extend a special thanks to Professor George Graham for his day-to-day guidance on these projects, but more importantly, for his mentorship and support throughout my Ph.D. studies. Finally, I would like to acknowledge my advisor, Professor Xiaoqing Pan, for his patience and giving me many opportunities to grow both as an engineer and personally.

This work would not have been possible without the work of collaborators at the Ford Motor Company. The advice and contributions of Dr. Bob McCabe, Dr. Chi Paik, Dr. Hung-Wen Jen, Dr. Karen Adams, Mr. Bob Kudla and Dr. Andy Drews were invaluable in framing and conducting these studies.

I would like to give a special acknowledgment to my collaborators and colleagues at Oak Ridge National Laboratory. Specifically, I would like to thank Dr. Larry Allard, Dr. Jane Howe, Dr. Karren Moore, Dr. Chad Parish, and Dr. Edgar Lara-Curzio for microscopy access, assistance, and useful advice.

I would like to thank Bai Hai Li and Liang Chen of the Institute of Material Technology and Engineering of the Chinese Academy of Sciences in Ningbo, China for

their dedicated collaboration to further understand the experimentally observed results in the study of CeO_2-supported Pd and Rh- model catalysts.

Ceria-zirconia film growth was performed at Environmental Molecular Sciences Laboratory (EMSL) at Pacific Northwest National Laboratory (PNNL). I and would like to thank my dedicated collaborators specifically, Manjula Nandasiri, Dr. Suntharampillai Thevuthasan, Dr. Satyanarayana Kuchibhatla, Dr. Tamas Varga, and Dr. Charles Peden for access and their dedicated collaboration.

I must mention the staff members that made this research possible. Keith McIntyre, Justin Scanlon, Harold Eberhart all were helpful in completing this work. I must make a special acknowledgment to Renee Hilgendorf who has been both a navigator and confidant for me through my graduate education. I would also like to mention the faculty and other graduate students in the Materials Science and Engineering department. I always found both the faculty and fellow students very open and accessible for questions and friendly conversation. I am deeply indebted to the department's graduate committee for their support and nominations for various university awards. I would like to thank members of the EMAL staff, especially Dr. Haiping Sun and Dr. Kai Sun for their many late nights and early mornings spent guiding me though difficult characterization techniques. Furthermore I would like thank to Dr. John Mansfield, Ying Qi and Bev Clampit forgiving me my many trespasses. I would also like to thank Debbie Mitchell, Debbie Harris, and many others in the Michigan AGEP alliance.

I must thank my comrades in the research group, especially Mike Katz for keeping the lab well supplied and for being an overall good sport. I would like to thank Chris Nelson for teaching me that "friends carry no debts." I would like to the thank Dr.

Yanbin Chen for taking so much time to teach me microscopy and the importance of lunchtime. Dr. Wei Guo and Dr. Arnold Allenic came to lab every day with a cheerful attitude and taught me everything I know about pulsed laser deposition. I also would like thank Hong Liu for assisting me in ceria film growth. Last, but certainly not least, thank you Sung Joo Kim and Yi Zhang for providing an atmosphere of general bonhomie.

Before finishing, I would like to thank many friends and family who supported me during my educational journey. There are too many to name here, but I must thank my parents Dr. Levi Ike Ezekoye and Adaeze Otue Ezekoye for their extraordinary help and support in completing this dissertation. I would also like to thank the community and staff of Saint Mary's Student Parish in Ann Arbor, MI.

TABLE OF CONTENTS

LIST OF TABLES

LIST OF FIGURES

Chapter 1

Introduction and Motivation

1.1 Introduction

On May 19, 2009, the United States President, Barack Obama, proposed changes to current federal law concerning both fuel economy and emissions from automobiles and trucks.[1] The aim of this proposed national policy is twofold. The first goal is to provide a more uniform standard for automakers to follow when meeting emission and corporate average fuel economy (CAFÉ) standards rather than disparate regulations from the Environmental Protection Agency (EPA), the Department of Transportation (DOT) and the state regulators. A second and more far-reaching goal of the proposed legislation is that it would be the first federal law that requires the reduction of carbon dioxide (CO_2) and other greenhouse gas emissions for all new cars and trucks sold in the US from 2012 to 2016. The EPA's basis for regulating tailpipe emissions is its authority under the Clean Air Act (CAA). In the proposal, the DOT National Highway Transportation Safety Administration (NHTSA), will pass parallel regulations under the Energy Policy and Conservation Act (EPCA).[2] According to EPA estimates, the agreement, which covers the 2012-2016 model years, would require an average fuel economy of 35.5 miles per gallon and reduce greenhouse gas emission by 900 million metric tons of CO_2.[2] The

proposed rules are ambitious and it is clear that treating greenhouse gasses as a pollutant, regardless of the magnitude, will present unique challenges for the global automotive industry.

Whatever path (or paths) the industry uses to meet these challenges, heterogeneous catalysis is almost certain to play a critical role. Several emerging vehicle fuel technologies, such as biofuel production, Fischer-Tropsch synthetic fuels, and several types of fuel cells are reliant on heterogeneous catalysts.[3] Catalysts are also essential to more established exhaust after treatment for gasoline and diesel engines. Therefore, this thesis will present investigations of three heterogeneous catalyst systems for automotive applications, all of which are relevant to current energy, environmental, and regulatory challenges. Three catalyst systems covered in this thesis are 1) Pt-Co alloy catalysts for fuel cell applications, 2) alumina supported Pt-Pd for NO oxidation, and 3) both Rhodium (Rh) and Palladium (Pd) on ceria-based supports for gasoline exhaust aftertreatment.

1.2 Background

In recent years, there has been a heightened public awareness of the impact of vehicle emissions on the health of the planet. Additionally, since the 1973 OPEC oil embargo, the public has been sensitized to the vulnerability that comes with increased dependence on foreign oil. Historically, the term "energy security" can be defined as "simply the availability of sufficient supplies of affordable energy."[4] Given this background, it might be helpful to discuss the size and scope of US oil consumption, and specifically address where the US automotive industry fits into the energy picture.

Current demand for oil in the US is approximately 19.5 million barrels per day of which 71% (or 14 million barrels per day) is used in the transportation sector. Within the transportation sector, reports estimate that 8-9 million barrels per day are used to power light duty vehicles such as passenger cars and light trucks.[5] Trends in US oil consumption are summarized in Figure 1.1, and it is evident that the light duty vehicle segment is the single largest driver for US crude oil consumption.

A major concern for the energy security issue is that US production peaked in the 1970's, however domestic consumption has continued to grow. To make up for this difference between consumption and production, the US has become increasingly dependent on importing foreign oil to meet energy demands. Currently, the US imports over 11 million barrels of petroleum per day, a number which represents 57% of total US consumption (Figure 1.2).[6] Current projections predict that the US will become progressively more dependent on foreign sources of oil in upcoming years.

In addition to reducing energy supply vulnerability, environmental protection is a complementary goal of this policy change. Just as the light duty vehicles make up the single largest component of US oil consumption, light duty vehicles are also a major contributor to the release of several environmental pollutants. Traditionally, the three main emissions from gasoline vehicles have been carbon monoxide (CO), unburned hydrocarbons (HC), and various compounds of nitrogen and oxygen (NO_x).[7] All of these compounds have been known to present environmental and human health risks. CO is a result of non-stoichiometric combustion and is toxic to humans. Although CO emissions have been decreasing since 1970, on-road vehicles accounted for an estimated 50 percent of U.S. emissions in 2008 and up to 95 percent in urban areas.[8-10] Unburned HC result

from unburned or partially burned fuel and are a major contributor to smog and ground level ozone. Nitrogen oxides (NO_x) contribute to several environmental problems including acid rain, water quality deterioration, production of toxic chemicals, and plant (vegetation) damage.[7]

In order to address the harmful effects of these compounds, automobile emissions control legislation (both on the state and national level) began in the mid 1960's. Early compliance with these new emissions standards was achieved by adjustments in ignition systems, but eventually catalytic after treatment devices were introduced in the US in 1975.[11-13] Early in this development, platinum, palladium, and rhodium were identified as candidate materials for automotive catalysis because of their intrinsic reactivity, thermal stability, durability, poison resistance, and low tendency to react with the supporting materials.[11] These metals later became the basis of modern automotive three way catalysts (TWCs). The term "three way catalyst" refers to the three functions of an automotive catalyst: 1) oxidation of carbon monoxide, 2) reduction of NO_x and 3) oxidation of unburned hydrocarbons.[12]

Over the past four decades, three way catalysts have been very successful in reducing emissions of HC, NO_x, and CO from gasoline vehicles. However, the catalytic after-treatment of diesel exhaust gasses, notably NO_x and particulate matter (PM), presents unique challenges. PM consists of a mixture of carbon, heavy hydrocarbons, and inorganic compounds, and presents a public health risk of particular concern. These particles, which can be less than 10μm, have been associated with premature deaths as well as both cancerous and non-cancerous lung damage.[13-14] PM is also associated with several environmental problems including contributing to smog and urban haze[15].

Unlike automotive TWCs, diesel exhaust after treatment does not rely on a single dominant technology, and the problem of controlling both PM and NO_x is ongoing.[16-17] and will be discussed further in Chapter 4.

Historically, greenhouse gasses, particularly CO_2 have not been considered "pollutants" in the same sense as CO, NO_x, HC, and PM. However, as scientific consensus of anthropogenic global warming has increased in recent years[18], greenhouse gas emissions (GHG) have received much greater attention. This change is reflected in the May 2009 policy shift, and the addition of GHG to the list of pollutants presents new challenges for the industry.

Carbon dioxide is widely considered the most important GHG, and the major anthropogenic source of CO_2 is the burning of fossil fuels. According to a 2009 EIA report[5], an estimated 7,385.41 million metric tons of CO_2 were released by the US in 2008. Although high fuel prices and slow economic growth led to a decrease in emissions across all end use sectors, transportation led all end use sectors with emissions of 1,930.1 MMT of CO_2, approximately 27% of the US total. Similar to the picture for petroleum consumption, emissions from combustion of light duty gasoline and distillate fuels comprise the majority of CO_2 emissions in the transportation sector.

Clearly, light duty vehicles represent a critical lever in reducing US dependence on foreign oil and reducing environmentally harmful emissions. Accordingly, heterogeneous catalysis is expected to play an essential part in the automotive industry's solution to meet current and future demands from regulatory, environmental, and energy perspectives. Given this, it is useful to briefly explore some of the dynamics of catalyst industry in areas that relate to energy and automotive applications.

1.3 The global heterogeneous catalyst industry

In 2006, the global catalyst industry was estimated to be a $14-14.6 billion market.[19] Moreover, goods and services which use catalysts in their production contribute over $1 trillion to the gross domestic product in the US alone, and trillions more globally.[20] Catalysts producers and markets are highly dependent on the needs of their client sectors (e.g., petrochemicals, refining, polymers, and environmental), and thus are often categorized as such (Figure 1.3). Environmental and energy catalysts represent about one third of the total catalysis market. As a sector, environmental and energy catalysts (which include automotive emissions catalysts) also have the strongest growth rate (7-9% per year) in the catalysts market and these trends are expected to continue into the future.[19] The driver for growth in this sector is largely environmental regulations both in Western Europe, North America, and Japan. However in recent years, developing economies such as India and China are increasingly applying tighter environmental controls [16, 21] which will likely increase the worldwide demand for autocatalysts.

Compared to traditional automotive catalysts, the market for fuel cell catalyst is quite small (only $51.1 million in 2006), but it is projected to grow significantly as more mobile and stationary fuel systems are installed.[22] As will be discussed later (Chapter 3), proton exchange membrane (PEM) fuel cells are primarily reliant on platinum electrocatalysts for the oxygen reduction reaction (ORR). Despite the small size of the market, this reliance on Pt exposes fuel cells to many of the same market forces as more traditional automotive and diesel after treatment catalysts.

1.4 Platinum and precious metal supply considerations.

A prominent challenge in the implementation of many heterogeneous catalyst systems, for both established and emerging applications, is the fact that these systems are dependent on platinum and other platinum group metals, such as rhodium (Rh) and palladium (Pd). Use of the platinum group metals (PGMs) can be costly, and Pt and Pd have experienced an increase in price in recent years (Fig 1.4). On the whole, autocatalysts are the largest user of PGMs, although significant demand also arises from investment, jewelry, and other industrial applications (Fig 1.4).[23-24]

Platinum is a scarce resource that occupies approximately 5 parts per billion of the earth's crust.[25] Further complicating matters from a strategic point of view, platinum is also highly concentrated geographically, with almost 90% of production coming from, South Africa and Russia (Fig 1.5). Proven reserves of platinum are well characterized and most geologists do not expect significant new reserves to be discovered.[26] Because of this high concentration, the threat of geopolitical or labor instability is a major concern for catalyst producers. While the price and supply situation for palladium is somewhat more favorable, the situation for rhodium is more tightly constrained, with over 86% of the world supply in southern Africa. Due to extreme rarity, supply concentration, and lack of suitable substitutes in the autocatalysts sector (87% of production goes into automotive catalysts[21]) , rhodium has undergone substantial price fluctuations in recent years, and cost forecasting is difficult.[27] These cost and supply issues are critical drivers for all three of the research areas to be discussed in this thesis.

1.4.1 Proton exchange membrane fuel cell catalysts

Global PGM supply considerations figure prominently in all of the catalyst systems discussed in this thesis. At the present levels of technology, there are hurdles to the widespread implementation of proton exchange membrane fuel cells (PEMFCs) for diverse applications such as replacing internal combustion (IC) engines in automotive power trains. The three most commonly cited of these challenges are 1) lack of hydrogen infrastructure, 2) challenges in hydrogen storage, and 3) cost of the fuel cell systems themselves.[28] Perhaps unsurprisingly, current economic modeling indicates that catalyst related costs are the largest cost elements in the production PEM fuel cell systems.[29] Recent estimates that take into account the worldwide availability of platinum indicate that proton exchange membrane fuel cells (PEMFCs) will have to achieve a precious metal loading of less than 0.4 g_{Pt}/kW for large-scale implementation in the automotive sector.[23] If this level of platinum loading is achieved, replacing the engine of typical passenger car (180 hp) in the US with an equivalent PEMFC would require almost 53 g of platinum, a number which exceeds current levels in a catalytic converter by more than an order of magnitude.[30] Geologist R.B. Gordon and coworkers[26] performed a study that assumed a less powerful fuel cell stack (75 kW) and platinum catalyst recycling. They estimated that a fleet of 500 million fuel cells at this metal loading would deplete known platinum reserves in the earth's lithosphere in approximately 15 years. Therefore, reducing the precious metal requirements is a critical challenge for the realistic large scale implementation of PEMFCs for automotive applications.

1.4.2 NO$_x$ abatement diesel catalysts

Owing to the increase in popularity of diesel vehicles in Europe (Fig 1.6a), that region has become the world's largest market for platinum autocatalyst, accounting for over 50% of the worldwide demand.[31] For some time, platinum has been the principal metal in the catalytic control of CO and HC emissions resulting from diesel combustion.[32] A typical diesel vehicle utilizes significantly more platinum than an average gasoline engine. Currently, 90% of European platinum for autocatalysts is used in diesel vehicles.[31] In recent years, regulations for particulate matter (PM) and NO$_x$ have become more stringent, thus requiring innovation in vehicle emissions abatement technology. Some of these techniques such as lean NO$_x$ traps, and SCR catalysts will be briefly outlined in Chapter 4. Regardless of which technical solution is ultimately successful in addressing these more stringent PM and NO$_x$ standards, platinum and other PGM's are likely to continue to play a prominent role in diesel exhaust after treatment. Primarily due to these increases in both regulation and diesel vehicle sales, European platinum demand has increased at a compound annual growth rate of 12.86% during the period between 1999 and 2007 (Fig. 1.6 b).

1.4.3 Automotive three way catalysts

As noted earlier, platinum, palladium, and rhodium are the basis of modern automotive three way catalysts. Platinum and palladium catalyze the oxidation of HC and CO into CO_2 and water vapor, while rhodium catalyzes the reduction of NO$_x$ to N_2 and O_2.[21] Despite some complications, platinum and palladium can be used

interchangeably in gasoline applications.[30] However, there is virtually no known

substitute for rhodium.[33] As Rh is critical for NO_x abatement, new regulations (such as

EURO I-V) for NO_x emissions are likely to drive an increase in demand in the future.[34]

1.5 Objective and Outline of This Thesis

Achievement of the three-fold goal of regulatory compliance, energy security and

environmental protection while dependent on such tightly constrained materials as

platinum, palladium, and rhodium, presents both unique challenges and opportunities for

the automotive and catalysis community. Although global macroeconomic forces may

control the supply and demand of these materials, characterizing these systems on an

atomic scale is also essential in developing business and policy solutions to these

challenges. Structural and chemical characterization of these materials is needed in order

to develop catalysts with improved activity, selectivity, and stability.

In this work, the structure and morphology of nanostructured heterogeneous

catalysts was investigated using a variety of materials characterization techniques,

including x-ray diffractometry, high resolution transmission electron microscopy,

aberration corrected electron microscopy, and z-contrast scanning transmission electron

microscopy. This thesis will present investigations of three heterogenous catalyst

systems, Pt-Co alloy catalysts for fuel cell applications, alumina supported Pt-Pd for NO

oxidation, and both Rh and Pd on ceria-based supports for gasoline exhaust

aftertreatment. A unifying objective of all of these studies is the use of materials

characterization techniques to investigate how catalyst stability and performance are

affected by morphology and composition. A secondary objective of this study is to

discuss the mechanism of structure property relationships in these three heterogeneous catalysis systems.

1.5.1 Carbon Supported Pt and PtCo PEMFC catalysts

The first catalyst system presented in this thesis is nanoscale carbon supported Pt-alloy catalysts for proton-exchange membrane fuel cells. Carbon supported PtCo is a promising catalyst material that has the potential to mitigate some of the cost, performance and durability issues associated with pure Pt PEMFC catalysts. However, the mechanisms of this improvement are not entirely clear.   Advanced materials characterization techniques, most notably aberration corrected high angle annular dark field (HAADF) imaging, in a scanning transmission electron microscope (STEM), are powerful tools for atomic scale characterization that yield a more complete understanding of deactivation mechanisms in these catalysts.

In this project, commercial carbon supported Pt and PtCo were treated with varying amounts of aggressive electrochemical cycling designed to simulate automotive start-stop conditions. During and after treatment, catalyst samples were structurally and chemically characterized using a variety of materials characterization techniques including high resolution transmission electron microscopy (HRTEM), high angle annular dark field (HAADF) scanning transmission electron microscopy (STEM), and x-ray diffraction XRD in order to relate observed structural and chemical differences between Pt and PtCo to changes in catalytic activity.

1.5.2 Pt-Pd alloy catalyst for NO oxidation

The second project presented in this thesis is the investigation of alumina supported platinum and platinum-palladium (Pt-Pd) bimetallic catalysts for nitric oxide (NO) oxidation. Oxidation of NO is a critical step in the catalytic after treatment of lean-burn diesel vehicles. Alumina-supported Pt is one of the best NO oxidation catalysts, but it quickly tends to lose surface area through particle coarsening at high temperatures. This study expands previous studies[35] on the thermal stability of Pt-Pd bimetallic catalysts that indicated that alloying Pt with Pd improved sintering resistance. Because multimetallic alloy catalysts may have different catalytic properties than their constituents[36], it is important to investigate both structure and catalytic performance simultaneously.

In this work, various compositions of nano-particulate Pt-Pd catalysts on Al_2O_3 were prepared from acetlyacetonate precursors. These samples were subsequently aged and characterized using HRTEM along with energy dispersive spectroscopy (EDS) to determine the size, distribution, and chemical composition of the precious metal nanoparticles in each of the catalyst samples. Microscopy data collected was then combined with NO oxidation and CO chemisorption data in order to better understand the effect of Pd alloying on the catalytic properties of Pt. In addition, this work was extended in order to utilize more advanced microscopy techniques, such as aberration corrected HAADF-STEM . Furthermore, as a part of this extension, results from acetlyacetonate precursors were compared to catalysts fabricated from more commercially significant nitrate precursors.

1.5.3 Pd and Rh model catalysts on CeO$_2$ and Ce$_{0.7}$Zr$_{0.3}$O$_2$ supports

The third topic in this thesis involves investigating the fundamental interactions of Pd and Rh on ceria (CeO$_2$) and ceria-based (Ce$_{0.7}$Zr$_{0.3}$O$_2$) oxide supports. Ceria and ceria-based oxides have been widely investigated as electronic promoters of activity, selectivity, and thermal stability in a variety of catalysts. Ceria supported Pd is an important catalyst for a variety of applications, including the catalytic combustion of methane, diesel oxidation, and modern automotive TWCs. The overall objective of this work is to develop a better understanding of fundamental interactions between Pd and ceria-based supports. In a primary study, cross sectional HRTEM was combined with theoretical calculations and simulations to determine the fundamental interactions between precious metals (Pd and Rh) and the CeO$_2$ support surface.

In an additional study, the role of stress, relative to chemical bonding between Ce$_{0.7}$Zr$_{0.3}$O$_2$ and Pd, in driving the oxide-wetting process, was investigated. This work expands on previous work[37] and reveals additional subtleties involved in ceria-based catalyst support migration and particle wetting. Aside from any impact on these specific energy applications, this work seeks to better understand key mechanisms of thermal degradation in these important catalysts. Such fundamental knowledge is needed for a more complete scientific understanding of aging phenomena in this important class of environmental catalysts.

All of these projects are part of larger collaborative efforts to relate catalyst morphology to cost, performance, and reliability. To make progress toward this goal, data from structural characterization of catalyst materials are combined with chemical and electrochemical measurements of these materials.

1.6 Figures

(a)

(b)
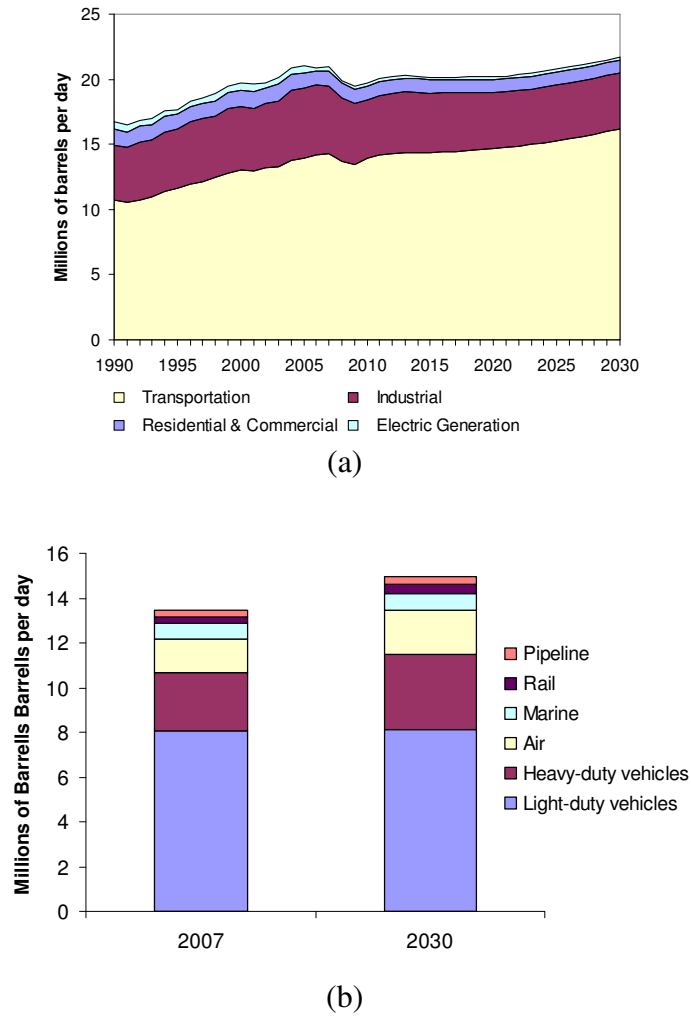
Figure 1.1: (a) Current and projected U.S. daily oil consumption by application (b) 2007 and projected transportation energy consumption by mode (data from Energy Information Administration[5]).
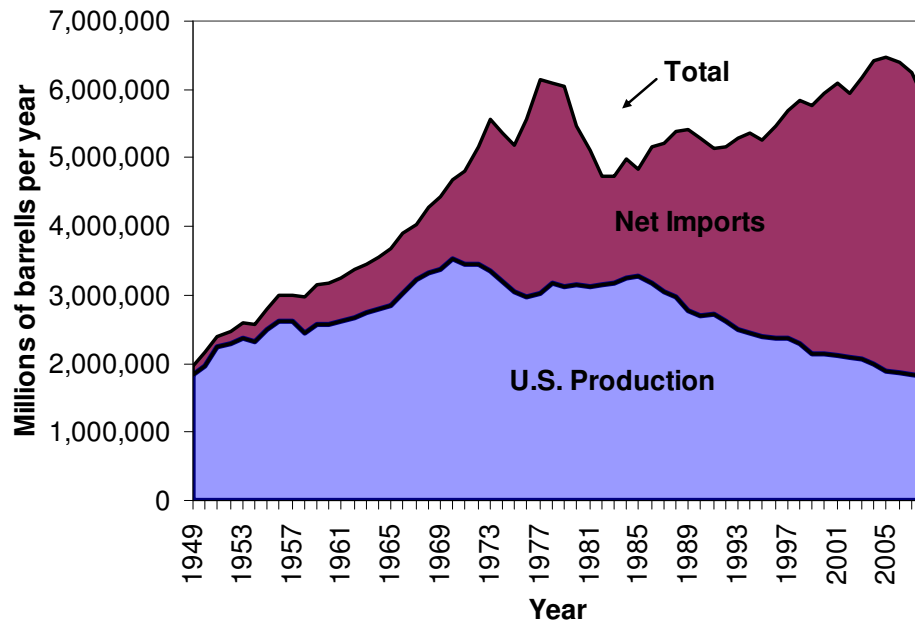
Figure 1.2: U.S. oil sources, showing the increased dependence on imported petroleum (data from Energy Information Administration[6])
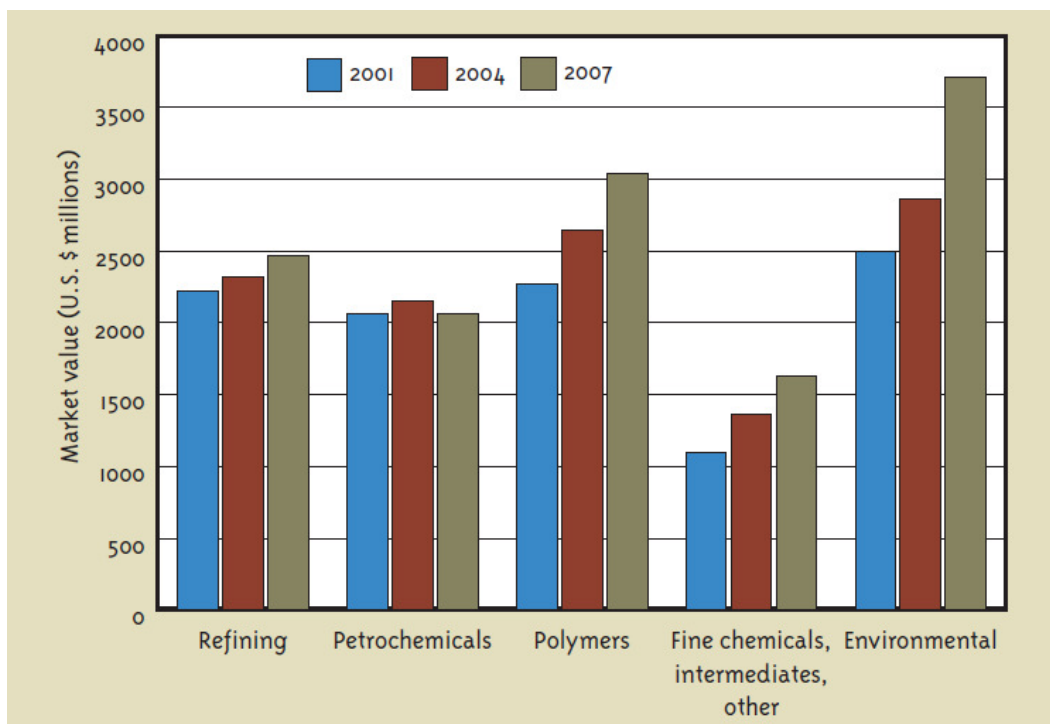
Figure 1.3: Projected global catalyst market values, by customer industries, 2001–2007 (From Filmore[38]).
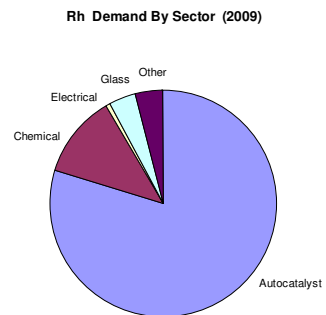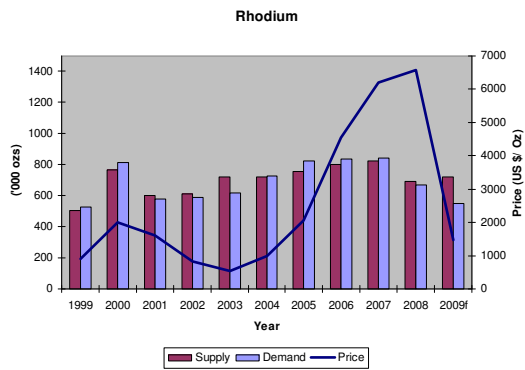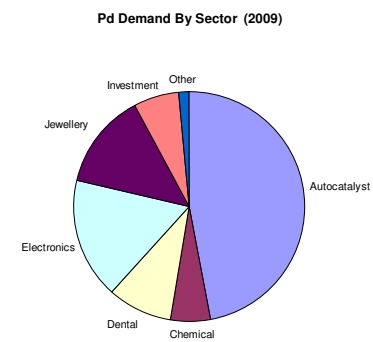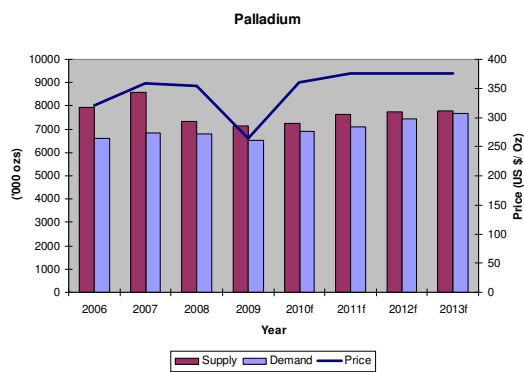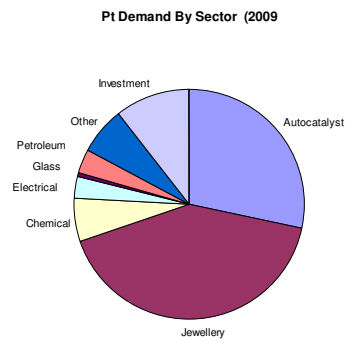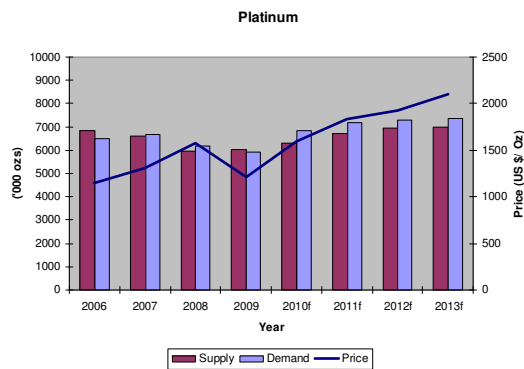
Figure 1.4: Recent trends and projections, along with demand by end use sector, for platinum group metals. Note: Due to price volatility, accurate projections for Rh were not available. (Data from Southwood *et. al* [27])

Pt

Pd

Rh
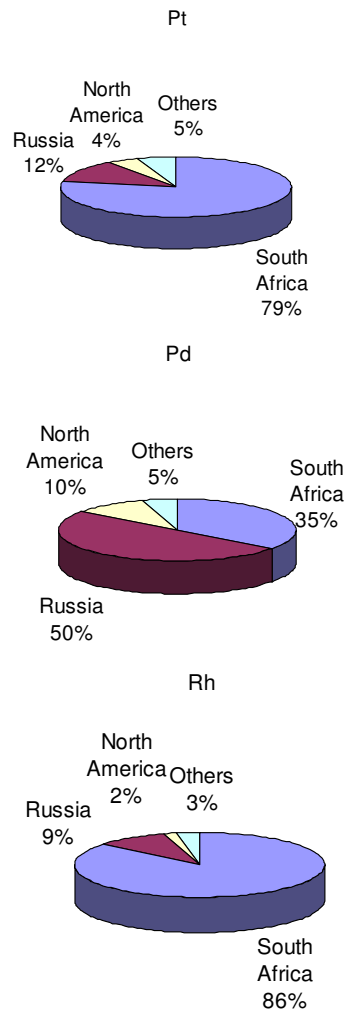
Figure 1.5: 2009 geographic distribution of production of PGM's (Data from Southwood *et. al.*[27])
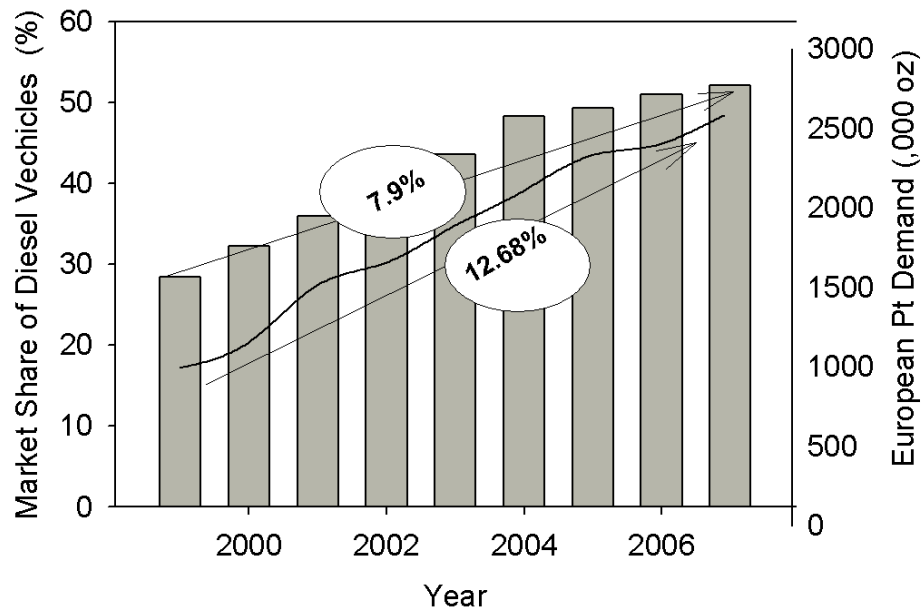
Figure 1.6: Market share of diesel vehicles and European platinum demand 1999 -2007 with growth rates (Data from Johnson Matthey[39] and Energy Information Administration[40])

1.7 References

1.   The White House Office of the Press Secretary, "Remarks by the President on National Fuel Efficiency Standards E", (2009).

2.   E.P.A. Office of Transportation and Air Quality, "EPA Will Propose Historic Greenhouse Gas Emissions Standards for Light-Duty Vehicles", (2009).

3.   D.G. Vlachos and S. Caratzoulas, "The roles of catalysis and reaction engineering in overcoming the energy and the environment crisis." *Chem. Eng. Sci.* **65**(1): p. 18-29 (2010).

4.   D. Yergin, "Ensuring energy security." *Foreign Affairs*. **85**(2): p. 69 (2006).

5.   Energy Information Administration, "Annual Energy Outlook 2009 with Projections to 2030", (2010).

6.   Energy Information Administration, "Annual Energy Review 2008", (2009).

7.   Enviromental Protection Agency Office of Mobile Sources, "Automobile Emissions: An Overview", (1994).

8.   Enviromental Protection Agency, "National Emissions Inventory (NEI) Air Pollutant Emissions Trends Data", (2009).

9.   P.G. Flachsbart, "Human exposure to carbon monoxide from mobile sources." *Chemosphere - Global Change Science*. **1**(1-3): p. 301-329 (1999).

10.   K. Smith, *Powering Our Future: An Energy Sourcebook for Sustainable Living*. Iuniverse Inc. (2005).

11.   H.S. Gandhi, G.W. Graham, and R.W. McCabe, "Automotive exhaust catalysis." *J. Catal.* **216**(1-2): p. 433-442.

12.   J. Kaspar, P. Fornasiero, and N. Hickey, "Automotive catalytic converters: current status and some perspectives." *Catal. Today*. **77**(4): p. 419-449 (2003).

13.   B. Brunekreef and S.T. Holgate, "Air pollution and health." *The Lancet*. **360**(9341): p. 1233-1242 (2002).

14.   P. Kinney, M. Aggarwal, M. Northridge, N. Janssen, and P. Shepard, "Airborne concentrations of PM (2.5) and diesel exhaust particles on Harlem sidewalks: a community-based pilot study." *Environ. Health Perspect.* **108**(3): p. 213 (2000).

15. J. Trijonis, "Effect of diesel vehicles on visibility in California." *Sci. Total Environ.* **36**: p. 131-140 (1984).

16. P. Eastwood, *Critical topics in exhaust gas aftertreatment*. Engineering design series. Baldock, Hertfordshire: Research Studies Press ; Research Studies Press. (2000).

17. I. Silver, *The future of the diesel engine*. Rail Safety and Standards Board Ltd. (2007).

18. R.A. Pielke, "A broader view of the role of humans in the climate system." *Physics Today*. **61**(11): p. 54-55 (2008).

19. M. Bryner, "Catalysts: possible changes on the horizon.(Catalyst industry)." *Chem. Week*. **168**(13): p. 22(2) (2006).

20. R.J. Davis, V.V. Guliants, G. Huber, R.F. Lobo, J. Miller, M. Neurock, R. Sharma, and L. Thompson, "An International Assessment of Research in Catalysis by Nanostructured Materials". World Technology Evaluation Center, Inc. : Baltimore, MD(2009).

21. J. Tollefson, "Worth its weight in platinum." *Nature*. **450**(7168): p. 334-335 (2007).

22. Wintergreen Research, "Fuel Cell Catalysts Market Opportunities, Strategies, and Forecasts 2007 to 2013", (2007).

23. C. Jaffray and G. Hards, "Precious metal supply requirements." in *Handbook of Fuel Cells: Fundamentals, Technology, and Applications*, W. Vielstich, A. Lamm, and H.A. Gasteiger, Editors., Wiley. p. 509 (2003).

24. M. Southwood, I. Preston, and P. Gray, "Platinum Group Metals: Further Upgrade On Strong Demand Outlook". 2009 Goldman Sachs JBWere Pty Ltd,. p. 2009 Goldman Sachs JBWere Pty Ltd,(2009).

25. B. Das Sarma, B.N. Sen, and A.N. Chowdhury, "Studies on geochemistry of platinum." *Economic Geology*. **61**(3): p. 592-597 (1966).

26. R.B. Gordon, M. Bertram, and T.E. Graedel, "Metal stocks and sustainability." *Proceedings of the National Academy of Sciences of the United States of America*. **103**(5): p. 1209-1214 (2006).

27. Malcolm Southwood, Ian Preston, and P. Gray., "Platinum Group Metals: Further Upgrade On Strong Demand Outlook". 2009 Goldman Sachs JBWere Pty Ltd,. p. 2009 Goldman Sachs JBWere Pty Ltd,(2009).

28. F.M. Vanek, L.D. Albright, and Knovel, *Energy systems engineering: evaluation and implementation*. New York: McGraw-Hill. (2008).

29. B.D. James and J.A. Jalionoski, "V.A.2 Mass Production Cost Estimation for Direct H2 PEM Fuel Cell System for Atomotive Applications." in *2009 Progress Report for the DOE Hydrogen Program*, J. Milliken, Editor.: Washington, D.C. (2009).

30. C.-J. Yang, "An impending platinum crisis and its implications for the future of the automobile." *Energy Policy*. **37**(5): p. 1805-1808 (2009).

31. J.W. van Gelder and K. Kammeraat, "Platium from AngloPlatinum in catalyst of European car manufacurers", in *A reseach paper prepared for Netherlands Institute for Southern Africa (NiZA)*. Profundo Economic Reseach(2008).

32. P. Hawker, "Diesel emission control technology." *Platinum Metals Rev*. **39**(1): p. 2-8 (1995).

33. C. National Research and I. ebrary, *Minerals, critical minerals, and the U.S. economy*. Washington, D.C.: National Academies Press. (2008).

34. C. Hageluken, "Markets for the catalyst metals platinum, palladium and rhodium." *METALL-BERLIN-*. **60**(1): p. 31 (2006).

35. M. Chen and L.D. Schmidt, "Morphology and composition of Pt---Pd alloy crystallites on SiO2 in reactive atmospheres." *J. Catal.* **56**(2): p. 198-218 (1979).

36. G.W. Graham, H. Sun, H.W. Jen, X.Q. Pan, and R.W. McCabe, "Aging-Induced Metal Redistribution in Bimetallic Catalysts." *Catal. Lett.* **81**(1): p. 1-7 (2002).

37. H.P. Sun, X.P. Pan, G.W. Graham, H.W. Jen, R.W. McCabe, S. Thevuthasan, and C.H.F. Peden, "Partial encapsulation of Pd particles by reduced ceria-zirconia." *Appl. Phys. Lett.* **87**(20)(2005).

38. D. Filmore, "Catalysts Rising." *Today's Chemist at Work.*,(November): p. 33 (2002).

39. D. Jollie, "Johnson Matthey: Platinum 2009", (2009).

40. Energy Information Administration, "Light Duty Diesel Vehicles: Market Issues and Potenital Energy and Emissions Impacts": Washignton, DC(2009).

Chapter 2

Experimental Methods

2.1 Introduction

The objective of this thesis is to use atomic scale characterization techniques to investigate structure property relationships in three heterogeneous catalysts systems. This chapter will briefly introduce some of the materials characterization techniques used to accomplish this objective.   Details of any of these techniques can be found in the archival literature. However, this chapter will present both the fundamental principles of the major techniques as well as details on the specific instruments used in this thesis.   An additional goal of this chapter is to present some of the film growth and deposition methods used to prepare the model catalyst discussed in Chapter 5.

2.2 Characterization Techniques

2.2.1 Transmission Electron Microscopy

The principle instrument for materials characterization for all of the projects presented in this thesis is the transmission electron microscope (TEM). The TEM, analogous to a transmitted light microscope, is a microscopy technique whereby an

incident energy beam consisting of electrons (instead of light) is transmitted though an ultra thin specimen. The electron beam interacts with the sample as it passes through, and the image formed from this interaction is magnified and recorded. In any microscope, the resolution is limited by the wavelength of the incident beam as described by the Rayleigh criterion (Equation: 2.1).

$$\Delta l = 1.220 \frac{\lambda}{N.A.}$$
Equation 2.1

Where Δl =   spatial resolution
    λ =   wavelength of the incident beam
    N.A.   =   numerical aperture of the microscope

Due to their higher energy, the incident electrons have a much smaller wavelength than visible light (0.0022nm for 200kV electrons versus 450nm for blue light). Therefore, in TEM this shorter wavelength allows much greater spatial resolution. This principle, first demonstrated by researchers at the Technological University of Berlin in 1931[1], has made TEM one of the preeminent tools for microstructural characterization since commercial instruments were first introduced in 1937.[1-2]

Accordingly, TEM techniques have been widely utilized in the study of catalysts systems for direct visualization of catalyst structure at the atomic scale.[3] Conventional catalyst characterization techniques are typically based on averaging chemical or spectroscopic signals over a relatively large volume or area and require interpretation for site specific results.[4] Because the active phases of commercial catalysts are increasingly composed of nanoscale materials[5], electron microscopy has become an invaluable tool for the investigation of heterogeneous catalysts. Today, many commercial catalyst systems

24

can be directly imaged by TEM with minimal sample preparation. TEM can be used to investigate the size, shape, and chemical composition of both metal particles and support materials.[6] As the role of interfacial phenomena in catalytic reactions has gained more attention, TEM has been a valuable technique for investigating interactions between catalyst particles and support materials.[3, 7]

Although there are several useful texts on the subject of transmission electron microscopy[8-9], it would be useful to present some basic principles here. As the name implies, in TEM, incident electrons are *transmitted* through the sample. Details about material structure can be obtained by interpreting either the transmitted image or the image on the diffraction plane. A schematic of a TEM and a ray diagram are shown in Figure 2.1. The source of the electron beam is referred to as the gun, which can be thermionic or field emission. Before the beam interacts with the sample, it passes through a series of condenser apertures and lenses. Likewise, after the sample, the beam passes through objective and projector apertures and lenses before being viewed and recorded by the user on the imaging plane. Aside from basic imaging, TEM can be used in combination with a variety of structural and spectroscopic characterization tools which will be discussed in subsequent paragraphs.

2.2.1.1 HRTEM

High resolution transmission electron microscopy (HRTEM) is a form of TEM that allows for imaging of crystallographic lattices and discrete atomic columns. In HRTEM, image contrast arises from differences in phase. After the electron beam passes through a material, the diffracted waveform is the Fourier transform of the scattering

factor distribution in the material, ρ(r). Therefore, the Fourier transform of ρ(r) can be expressed with the following Equation 2.2:

$$F(\rho(r)) = \frac{1}{\sqrt{2\pi}} \int_{-\infty}^{+\infty} \rho(r) e^{-i\Delta k \cdot r} d^3 r \qquad \text{[Equation 2.2]}$$

In this equation, Δk is a "diffraction vector," which accounts for periodicities in the specimen. The resulting HRTEM image is an interference pattern between defracted and forward scattering electron waves.[2]

Extending the discussion of HRTEM and the wave nature of electrons, we should present the weak phase object approximation (WPOA) for transmission electron microscopy. Although more exhaustive descriptions of the fundamental physics in HRETM are found in several textbooks and reviews[2, 10-14], it might be helpful to very briefly discuss some of the critical concepts here in a method summarized by Wang.[10] If Ψ(r) is the electron waveform at the exit face of the specimen, and ψ(u) is its Fourier transform, then the diffraction amplitude ψ'(u) function at the back focal plane is given in Equation 2.3:

$$\psi'(u) = \psi(u) e^{i\chi(u)} \qquad \text{[Equation 2.3]}$$

Where: u = reciprocal space vector

χ(u) = phase function (shown in Equation 2.4)

$$\chi(u) = \frac{\pi}{2} C_s \lambda^3 u^4 - \pi \Delta f \lambda u^2 \qquad \text{[Equation 2.4]}$$

Where C_s = spherical aberration coefficient

Δf = lens defocus

λ = electron wavelength

Therefore, the phase function (χ) arising from the objective lens is a function of C_s and the lens defocus. The defocus value with the maximum directly interpretable resolution is termed the *Scherzer* defocus. The Scherzer resolution (r_{sch}) can simply be summarized in terms of the Scherzer defocus in Equation 2.5:[8, 11]

$$r_{sch} = 0.66 C_s^{\frac{1}{4}} \lambda^{\frac{3}{4}} \qquad \text{[Equation 2.5]}$$

The actual resolution limit of the microscope depends on the design of a particular instrument and might be somewhat larger than the Scherzer resolution, due to energy spreads, higher order aberrations, and fluctuations in high voltage.[15]

The HRTEM data presented in this thesis was performed on a JEOL 3011 located in the Electron Microbeam Analysis Laboratory (EMAL) at the University of Michigan. The JEOL 3011 is a 300 kV microscope with a lanthanum hexaboride (LaB_6) thermionic emission filament and has a point-to-point resolution of 0.17 nm. This instrument is equipped with an integrated EDAX ® energy dispersive spectroscopy (EDS) system for compositional analysis (further discussed in 2.2.1.4).

2.2.1.2 Scanning Transmission Electron Microscopy

Scanning transmission electron microscopy (STEM) differs from conventional TEM and HRTEM. In STEM, the incident electron beam is focused into a probe, which is rastered (or scanned) across a specimen. A major advantage of STEM is that the user can focus the probe on specific regions of the sample to obtain highly localized imaging or spectroscopic information. Therefore, high resolution compositional analysis is possible in a STEM. A schematic of a typical STEM instrument is shown in Figure 2.2.

Furthermore, in STEM, spatial resolutions for both imaging and chemical analysis are strong functions of the diameter of the incident probe. The Scherzer resolution (r_{sch}) in a STEM is given by Equation 2.6.[15]

$$r_{sch} = 0.43\lambda^{\frac{3}{4}}C_s^{\frac{1}{4}}$$
[Equation 2.6]

STEM instruments can be equipped with a high angle annular dark field (HAADF) detector. HAADF works by collecting incoherent elastically scattered electrons at high angles (75-150 mRad)[15]. At these angles, intensity of the scattered beam is proportional to a power of the atomic number ($Z^{1.7-2.0}$).[16-18] In HAADF imaging, otherwise known as "z-contrast" imaging, contrast arises primarily from the differences in the atomic number and not primarily from the phase present. Although differences in atomic number are the primary source of contrast, other factors, most notably mass thickness contrast, must be considered when interpreting HAADF images.[19]

In this thesis, four microscopes were used for HAADF-STEM analysis. The first of these is a JEOL 2010F located in EMAL at the University of Michigan. The JEOL 2010F is operated at 200KV with a field emission gun and a point to point resolution (in STEM mode) of less than 2Å. However, typical analytical use specifies a probe size of 0.5 nm and a camera length of 12 cm. This limits actual resolution to be significantly less than the ultimate STEM resolution; however, this condition was preferable for compositional analysis. The JEOL 2010F was also equipped with a Gatan Image Filter (GIF) for electron energy loss spectroscopy (EELS) and an integrated EDAX® EDS system.

HAADF imaging was also performed on a Hitachi HF3300 located at the High Temperatures Materials Laboratory at Oak Ridge National Laboratory. The HF3300

(shown in Figure 2.3). is operated at 300 kV with STEM resolution 0.2 nm This microscope is equipped with a cold field emission electron source that provides higher brightness and greater coherency[20-21] and also has an integrated Thermo-Noran EDS analyzer for compositional analysis.

The HF 3330 was used extensively for the PtPd bimetallic catalysts discussed in Chapter 4. A notable feature of this microscope and of many STEM instruments is that it is equipped with a secondary electron (SE) detector.[22] This enabled the HF3300 to be used in ultra high resolution scanning electron microscopy (SEM) imaging, HRTEM imaging, and HAADF imaging. Typical SE and HAADF STEM images of alumina supported PtPd bimetallic catalysts are presented in Figure 2.4. The other STEM instruments both used aberration correction and will be discussed in the following section.

2.2.1.3 Aberration Corrected Electron Microscopy

All forms of microscopy are constrained by the fact that the realistic resolution of a particular instrument is always less than the theoretical limit. These deviations from the ideal resolution are caused by aberrations, or imperfections, in the image forming optical system.[23] Spherical aberration (C_s) is one of the most important types of aberrations, but it is only one of many imperfections that can affect resolution. Recalling Equation 2.5, one can see that the information limit of a microscope is a function of the (C_s).

Scherzer first proposed using multiple lenses to cancel out aberrations in 1947.[24] One of the critical hurdles encountered was controlling various electronic and magnetic

elements simultaneously in a systematic fashion. This problem has largely been

overcome with automatic image acquisition and computer controlled alignment.[25] The

last decade has seen the development and commercial introduction of computer

controlled aberration correctors. Aberration correction software calculates the probe

forming lens aberrations by performing a tilt series of HAADF images on a standard

carbon supported gold (Au/C) standard sample.[26-27] Figure 2.5 (a) is a screenshot of the

CEOS probe correction software after completion of the aberration correction. From this

image, we can see that the electron probe remains flat over a 40mRad area. This allows

the user to use a significantly larger collection angle over an uncorrected TEM.[27] This

effect can also be seen by investigation of the "shadow image" or Ronchigram. After

aberration-correction, the corrected flat phase field is much larger in the corresponding

Ronchigram, than that of an uncorrected probe (illustrated in Figure 2.5 b and c).

Two corrected TEM's were used for both HAADF STEM and bright field

(STEM) imaging in this thesis. The first of these, a JEOL 2200FS fitted with a hexapole

aberration corrector (CEOS GmbH) for the probe-forming optics, is capable of sub-100

pm spatial resolution in STEM mode. This microscope was equipped with a Bruker SDD

EDS detector for high sensitivity chemical analysis with high spatial resolution.[28] Further

details of the instrument, which is located in the Advanced Microscopy Laboratory

(AML) at Oak Ridge National Laboratory, can be found in several earlier reports.[29-31]

Additional aberration corrected imaging was performed on a similar instrument, a JEOL

2100F. This 200kV STEM/TEM (located in EMAL at the University of Michigan and

shown in Figure 2.6) is also equipped with a CEOS hexapole probe corrector and an

EDAX EDS detector.

2.2.1.4 Energy Dispersive Spectroscopy

Energy dispersive spectroscopy (EDS), sometimes referred to as X-ray energy dispersive spectroscopy (XEDS), is a chemical spectroscopy technique that can be used in connection with TEM. This type of spectroscopy arises from an interaction between the electron beam and the sample in question. EDS works by detecting X-rays that are emitted by the specimen upon electron beam relaxation. The X-ray photons are generated by a relaxation of an outer shell electron to an inner shell hole. This is shown schematically in Figure 2.7. These X-rays pass through a protective window and are absorbed by a detector. Typically, silicon-lithium detectors have been used with TEM, but newer silicon drift detectors (SDD) have been introduced in recent years. The X-ray energy is transferred to the Si-Li and processed into a digital signal that is typically displayed as a histogram of the number of photons plotted against energy. A critical variable in X-ray microanalysis is the rate at which photons interact with the detector. This variable is usually reported as the counts per second (CPS). A key parameter that affects the CPS is the X-ray scattering and absorption cross section of the sample. Other parameters that affect the CPS include the condenser aperture size, the probe size, beam current, and sample thickness. The optimal count rate value for Si-Li detectors is 1000-15,000CPS. If the CPS is too low, then it is difficult to collect adequate counting statistics; if it is too high, and the detector can be damaged. This demonstrates one of the main advantages of SDD technology, which can achieve a much higher count rate for high sensitivity analysis.[28]

The spatial resolution of EDS is approximately 1nm in most conventional systems, but a modern aberration corrected STEM with an SDD detector (such as the

JEOL 2200FS discussed in section 2.2.1.2) can achieve sub-nanometer resolution. EDS

adds some opportunities for quantification. Several methods have been used to quantify

EDS spectra, but one of the simplest and most enduring methods is the method described

by Cliff and Lormier in 1975 [1, 32-33] (described in Equation 2.7).

$$\frac{C_A}{C_B} = k_{AB} \frac{I_A}{I_B} \text{ and } C_A + C_B = 1$$

[Equation 2.7]

$C_A =$ concentration of element A

$I_A =$ X-ray intensity from element A

$k_{AB} =$ Cliff-Lorimer sensitivity factor (experimentally

determined for specific A-B combinations[14])

2.2.1.5 Electron Energy Loss Spectroscopy

Electron energy loss spectroscopy (EELS) is another type of chemical

spectroscopy that can be used in connection with both TEM and STEM. EELS was first

demonstrated in a TEM in 1949 by Möllensradt[34], and the basic design of a EELS

spectrometer is shown in Figure 2.8. Recall that in section 2.2.1.2 that in HAADF

imaging, some electrons are elastically scattered at high angles which form the Z-contrast

image. However, EELS utilizes inelastically scattered electrons at significantly smaller

angles than HAADF imaging.

The fundamental principle of EELS is the Coulombic interaction of an electron

beam with atoms in the sample solid. When the electron beam interacts (with initial

energy E_0) with atoms in the sample (Figure 2.8a), the beam is scattered inelastically by

the outer electron shells.[35] Because this scattering event is inelastic, it involves a small loss of energy (ΔE). This lost energy corresponds to a core level vacancy created by the electron beam. The energy needed to create a particular vacancy is characteristic to each element, and there have been several well-documented "atlases" of EELS spectra.[36]

Quantification of EELS spectra is possible, and can be quite accurate when standards are used.[35] Precise quantification of EELS spectra is dependent not only on the energy of these scattered electrons, but also on the angle at which they are collected.[37] Similar to EDS, spatial resolution in EELS is limited by the probe size, and several recent reports have been able to discriminate between single atoms on modern aberration corrected STEM instruments.[38-40] EELS can also be used to investigate valence state and local bonding structure. EELS was performed to determine the composition in the PtCo/C fuel cell catalysts discussed in Chapter 4, and to determine the degree of valence state of cerium oxide in the model catalyst study of Chapter 5.

2.2.1.6 TEM Sample Preparation

In general, all TEM specimens must be thin enough to be transparent to the incident electron beam[2, 14], and several methods have been reported as techniques for TEM specimen preparation of powder materials. For the alumina supported Pt-Pd powder materials discussed in Chapters 4, the particle size for the samples in this study was very small, thus no additional thinning was required to make the specimens suitable for HRTEM imaging. Each powder sample was dispersed onto a 300 mesh Holey Carbon coated copper grid (Structure Probe, Inc.). This is a common method for

preparing powder samples if primary particle size is sufficiently small.[41] For the carbon

supported PtCo fuel cell catalysts discussed in Chapter 3, the metal loading was much

higher, and the samples were dispersed in liquid to facilitate HRTEM of individual

particles. Therefore, in the case of the fuel cell catalysts, each catalyst powder was

immersed in a solution of 50% ethanol and 50% de-ionized water and ultrasonicated for

several minutes before being dispersed onto 300 mesh carbon-coated copper TEM grids

(Structure Probe, Inc.).

Sample preparation for model catalysts was considerably more involved. The first

step involves cleaning a piece of sacrificial silicon and coating it with a scientific

adhesive. In this study, M-Bond 610 was used for gluing the film side of the sample to

the cleaned and polished surface of the sacrificial silicon. M-bond 610 is a two

component, solvent-thinned, epoxy-phenolic thermosetting adhesive. It is typically cured

at elevated temperatures (approximately 130ºC) for 8 to 12 hours. However, in the model

catalyst studies reported in Chapter 5 of this thesis, the M-bond was cured without heat so

as to not disturb the metal particles on the oxide surface. Next, cross sections were

created by cutting the film and silicon with a diamond saw and mechanically polishing

the sample's newly cut edge with SiC sand paper diamond lapping film (South Bay

Technologies). This newly polished cross section was then glued using M-Bond to a

3mm molybdenum ring (SPI Inc.).   Again, these samples were allowed to cure without

heat for at least 12 hours. After curing, the cross sections on rings were thinned using

mechanical polishing (using SiC paper and diamond films) so that the ring and cross

section together had a total thickness of between 100 -110 μm, followed by further

mechanical thinning with a Gatan Model 696 dimple grinder.

The final step in cross sectional TEM sample preparation was argon ion milling

using a Gatan Model 691 PIPS (precision ion polishing system). Before ion milling, the

samples were cleaned with acetone and placed on a Gatan clamp-type DuoPost®

followed by argon ion milling using an accelerating voltage of 3.7-4.2kV with an incident

angle between 3-5º. The sacrificial silicon usually milled faster than the substrate.

Samples are considered thin enough to image (20-200 nm thick) when the hole in the

silicon reaches the interface as illustrated in Figure 2.9.

2.2.2 X-ray Scattering Techniques

2.2.2.1 Phase and Particle Size Analysis of Powder Samples

X-ray scattering was used for several analyses in this thesis. For the fuel cell

catalyst discussed in Chapter 4, $\theta/2\theta$ X-ray diffraction (XRD) measurements were

performed on the electrode catalyst samples. These measurements were taken on a

Rigaku rotating anode diffractometer using Cu Kα radiation (λ=1.54Å). These electrodes

were attached to a silicon coupon and packed into a steel sample holder to be in-line with

the incident beam. Patterns were obtained over the range 10 – 90° (2θ).

Diffraction data was analyzed with Jade Software (MDI, Inc.) using the ICDD

(International Center for Diffraction Data) PDF4 database. Jade software was used to

identify and fit peaks, and the Debye-Scherrer relation (Equation 2.8) was used to

estimate an average diffracting-particle size.[42-43]

$$B = \frac{K\lambda}{L \cdot \cos(\theta/2)} \hspace{3cm} \text{[Equation 2.8]}$$

where: B   =   full width (in radians) at half maximum intensity of the powder pattern peak

                 K   =   crystallite shape factor (0.9 is generally used [3])

                 λ =   the wave length of the incident X-rays

                 $\theta/2$ =   a the Bragg angle

                 L   =   characteristic length scale of the diffracting crystals

For the Pt-Pd bimetallic catalysts study presented in Chapter 4, X-ray diffraction (XRD) data were collected in a Scintag X2 diffractometer located at the Research and Innovation Center (RIC) at Ford Motor Company (Dearborn, MI). This instrument was quipped with a Si(Li) solid state detector and also used Cu Kα radiation. It was configured in Bragg-Bretano focusing geometry. Catalyst powders were prepared by packing in a shallow cavity etched into a glass plate. Because of the severe overlap between the Pt or Pd peaks and the Al_2O_3 substrate, net intensity diffraction data were prepared by subtracting a scan of untreated alumina powder from intensities obtained from the catalyst samples. The resulting net intensity scan was profile-fit to characterize the breadth and position of the Pt and Pt-Pd peaks. Peak profiles were fit using the Pearson 7 function[44] and the breadth and position of the peaks were corrected with factors obtained by analyzing the NIST Standard Reference Material SRM 660 (LaB_6).[45] Diffraction data were obtained over the range 10 – 90° (2θ) in steps of 0.03°. Scherrer analysis of the Pt (311) peak of the fcc lattice (located near 81.2° for Pt) was used to determine to the crystallite size. The lattice parameter for the fcc phase of each catalyst was estimated from the positions of the (111), (200) and (311) peaks.

36

Lattice parameter for the precious metal particles was determined by

measurement of the plane spacing using the Bragg law (Equation 2.9):

$$n\lambda = 2d \sin(\theta)$$

[Equation 2.9]

where: λ =   the wave length of the incident X-rays

d   =   spacing of a particular set of lattice planes

θ =   a the Bragg angle

Plane spacing was used to calculate lattice parameter using the plane spacing equation for

cubic systems (Equation 2.10).

$$a = d\sqrt{h^2 + k^2 + l^2}$$

[Equation 2.10]

where: a   =   lattice parameter of particular crystal

h,h,l   =   miller indices of a cubic crystal

2.2.2.2 X-Ray Analysis of Thin Films

X-ray scattering was also used to evaluate the thickness and quality of thin films

grown as supports for the model catalyst study presented in Chapter 5. In addition to the

Rigaku rotating anode described in section 2.2.2.1 above, these studies also used a Bede

DI diffractometer located at The University of Michigan.

High-resolution X-ray diffraction (HRXRD) measurements were performed on

the films grown at Pacific Northwest National Laboratory (PNL), using four-circle

Philips X'pert materials research diffractometer operating at 45 kV and 40 mA with a

fixed Cu anode. A hybrid monochromator, consisting of four bounce Ge(220) crystals

and a Cu X-ray mirror, was employed in the incident beam path to provide

monochromatic X-rays from Cu Kα_1 (λ=0.154056 nm and $\Delta\lambda/\lambda$=23 ppm) with a beam divergence of 12 arc-sec.

In X-ray reflecxometry (XRR), the diffractometer is operating in a similar $\theta/2\theta$ configuration; however the 2θ angles are much smaller. Using the grazing incidence technique allows for higher resolution investigation of surface layers and thin films Grazing incidence X-ray diffraction (GIXRD) is often used over conventional X-ray diffractometry (XRD) for crystallographic and structural analysis of thin films and other nanoscale surface features.[46-47] This is due to the fact that a small incident angle increases the path length of the incident beam through the film, which simultaneously yields a stronger signal from the film and reduces the signal from the substrate. GIXRD and XRR measurements were performed using Philips X'pert multi-purpose diffractometer operating at 45 kV and 40 mA with a fixed Cu anode and a Cu X-ray mirror.

Film thickness can be determined from analysis of the interference fringes close to the main scattering peaks. Assuming that the scattering planes are parallel to the surface, a characteristic length scale can be determined from the Bragg (Equation 2.9). Determining the film thickness from XRR and from the spacing of the interference or Kiessig fringes is given in Equation 2.11. An example is presented in Figure 2.10.

$$t = \frac{(n_1 - n_2)\lambda}{2(\sin \omega_1 - \omega_2)}$$
[Equation 2.11]

where: λ = the wave length of the incident X-rays

ω_x = angular position (in radians) of local maxima peaks

n_x = local maxima of interference fringes

t = the film thickness

For the films grown at both UM and PNNL , the analysis of diffraction data was performed using JADE 8.5 and JPOWD 51 from Materials Data Inc. and PDF4+ data from Inorganic Crystal Structure Database (ICSD).

2.2.3 Other Materials Characterization Techniques

2.2.3.1 Atomic Force Microscopy

Both the pulsed laser deposition (PLD) films and molecular beam epitaxy (MBE) films grown at PNNL were examined ex-situ using atomic force microscopic (AFM).   These studies were carried out using the Digital Instrument (DI) Nanoscope IIIa multimode scanning probe microscope under tapping mode.

2.2.3.2 X-Ray Photoelectron Spectroscopy

As a means to check film composition, X-ray Photoelectron Spectroscopy (XPS) was performed on four CZO films grown at PNNL. This chemical analysis was

39

performed using a Physical Electronics Instruments (PHI) Quantum 2000. The X-ray source was monochromatic aluminum K radiation (1486.6 eV). The X-ray beam could be focused to a spot size as low as 10μm. The approximate sampling depth under these conditions is 25 Å. The samples were sputtered with 4 keV Ar^+ ion beam in order to obtain a depth profile and to correct for surface contamination. The approximate sputter rate was 50nm Å/min.

XPS was also performed at UM to monitor precious metal deposition. On these films XPS was performed using a Perkin Elmer XPS spectrometer that was integrated in the UHV chamber described in Section 2.3.3 below. The X-ray source was Mg K, although this source was not monochomated, which limits the fundamental energy resolution.[48]

2.2.3.3 Rutherford Backscattering Spectrometry

Rutherford backscattering spectrometry (RBS) is a powerful analytical tool for non-destructive quantitative analysis of surfaces, thin films, and interfaces.[49] For single crystalline materials, RBS channeling can be used to investigate crystal structure and quality. In RBS channeling, a low index zone axis is aligned with an incident beam of high energy (2 MeV) He atoms. The backscattered signal from the aligned film is then compared to the intensity of that of a randomly aligned film, and the ratio of these two signals is used to provide a quantitative measure of crystalline quality.[50] For the studies of model catalysts discussed in Section 5.2.4, RBS channeling experiments were carried out in the Environmental Molecular Sciences Laboratory (EMSL) accelerator facility at the Pacific Northwest National Laboratory (PNNL). The backscattering spectra were

collected using a silicon surface barrier detector at a scattering angle of 150°. The details

of the accelerator facility and the end stations were described elsewhere.[51]

2.3 Model Catalysts Preparation

2.3.1 Pulsed Laser Deposition

Some of the planar supports for the model catalyst studies discussed in Chapter 5

were grown using pulsed laser deposition PLD. PLD, first described in 1965 by Smith

and Turner[52], has proven to be a versatile film deposition technique for a variety of

applications.[53] The technique had gained considerable attention in the deposition of high

temperature superconductor[54] and transparent conducting oxides.[55]

In the PLD technique, a high power laser is used to vaporize a source (target)

material, and the resultant flux is geometrically directed towards the growing film.

Although conceptually PLD is straight forward, the underlying physical principles of

laser ablation can be quite complex.   One of the advantages of PLD is the ability to

stoichiometrically deposit complex multi-element materials.[56] PLD has been used in

catalysis research for some time. Several recent studies have reported using PLD to

produce highly ordered 3D nanostructures (nanoparticles and nanorods) that would be

useful in heterogeneous catalysis.[57-58] Since PLD has been used in model catalyst studies

including Pt/YSZ[59], PLD deposition in this thesis, however, will focus on producing

supports for model catalysts studies.

Targets were made from a sintered pellet of commercially available ceria powders. The CeO$_2$ target was sintered in air at 1400ºC for 8 hours and the CZO target was sintered in air at 1550º C for 8 hours following methods generally described by Duh[60]. The sintered targets were approximately 3mm think and 21 mm in diameter, and target quality was confirmed by XRD and by confirming the theoretical density of the sintered pellet before deposition. The CeO$_2$ target had a final density of 6.44 g/cm3 (88.25% theoretical density), while the CZO target had a final density of 6.31g/cm3 (92.59% theoretical density). XRD patterns for both of these targets (showing the desired fluorite structure) are provided in Figure 2.11.

The PLD system utilized in this study is shown schematically in Figure 2.12. The system used a pulsed eximer KrF laser (Compex 205, Lambda-Physik) as the photon source. The laser has an operating wavelength of 248nm and a nominal pulse width of 22 ns. The PLD chamber had on-axis geometry, such that the substrate was directly in front of the surface of the target. In this chamber, the target to substrate distance was approximately 6.5 cm, and the substrate was mounted, using colloidal Ag- paste (Ted Pella, Inc.), onto a radiative heating stage (Neocera Inc.) that could heat the substrate to 900ºC. The laser beam was focused onto the target with an angle of incidence of approximately 40º. The targets were mounted on a six target carousel (Neocera) that could rotate and raster the targets at the same time to prevent excessive target damage.

In the study discussed in Chapter 5, this chamber was used to grow thin CeO$_2$ films on the 111 surface of commercial YSZ substrates. Deposition parameters were varied to optimize both crystalline quality (measured by ω-rocking curves in XRD) and

smoothness (measured by AFM).   Details of growth conditions will be presented in

further detail in section 5.2**.**

2.3.2 Oxide Film Growth Using Molecular Beam Epitaxy

In the last decade, molecular beam epitaxy (MBE) has been used to provide single

crystalline supports for the study of the catalytic properties of cerium-zirconium mixed

oxides. In the investigation of Pd supported on ceria based oxides, $Ce_{0.7}Zr_{0.3}O_2$ thin films

on YSZ(111) by oxygen plasma-assisted molecular beam epitaxy (OPA-MBE) in a

dedicated dual chamber ultrahigh vacuum (UHV) system configured specifically for

oxide epitaxy. In-situ characterization was carried out in a dual chamber ultrahigh

vacuum (UHV) system, shown schematically in Figure 2.13. In-situ characterization was

carried out in a dual chamber ultrahigh vacuum (UHV) system. The chamber consists of

metal evaporation sources, a UHV compatible electron cyclotron resonance (ECR)

oxygen plasma source, and reflection high-energy electron diffraction (RHEED) for real

time characterization of thin film growth. Growth rate of thin films was measured in-situ

by a quartz crystal oscillator (QCO) which was calibrated by analyzing the as-grown

films using ex-situ techniques, such as X-ray reflectivity, Rutherford backscattering

spectrometry, and X-ray photoelectron spectroscopy.

2.3.3 Precious Metal Deposition in UHV Conditions

In the model catalysts studies presented in this thesis, precious metals were deposited using a UHV deposition system. UHV deposition techniques have been used in fundamental catalysis research for some time, and are particularly useful in the area of model catalysts preparation.[61] Operating at UHV conditions (generally defined as $< 10^{-8}$ Torr) can be used to prepare atomically-clean and well ordered surfaces and monolayers to be used in model catalysts studies.[62]

The UHV system used in this study was equipped with a variety of tools for in-situ characterization including electron spectrometry (Physical Electronics Industries), Auger electron spectroscopy (AES), X-ray photoelectron spectroscopy (XPS), ultraviolet photoelectron spectroscopy (UPS), and low energy ion scattering spectroscopy (LEISS). More details of this system can be found in earlier reports.[63-64] Following deposition of the CeO_2 and CZO support films using MBE or PLD a monolayer equivalent of Pd or Rh was deposited in this UHV chamber. This system was equipped with thermal Pd and Rh sources for highly controlled in situ evaporation and deposition of metals. The base pressure of the UHV system was in the low 10^{-10} Torr range, and the working pressure was typically in the low 10^{-9} Torr range. Film coverage was monitored using XPS. A photograph of the UHV chamber is shown in Figure 2.14.

2.4 Figures

(a)   (b)
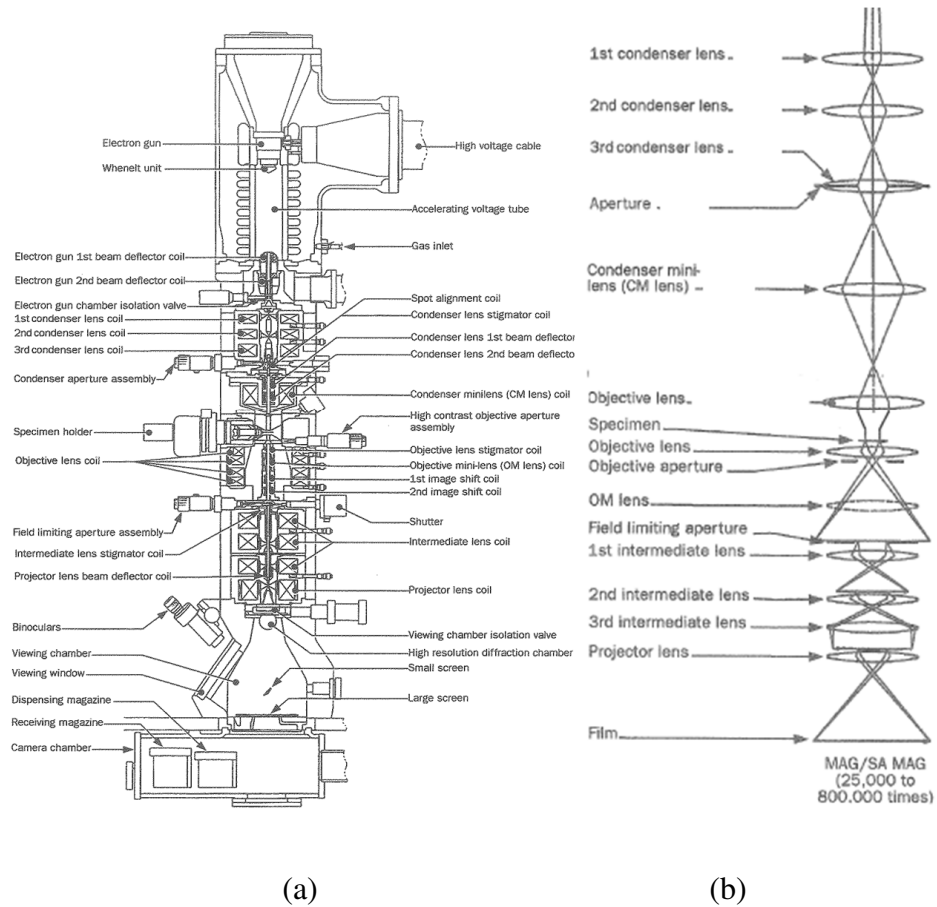
Figure 2.1: (a) cross section of a JEOL 3000 series TEM (b) TEM ray diagram for imaging (figure from JEOL USA)[65].

Incident Probe

to EDS detector

Sample

High angle annular
detector

BF Detector
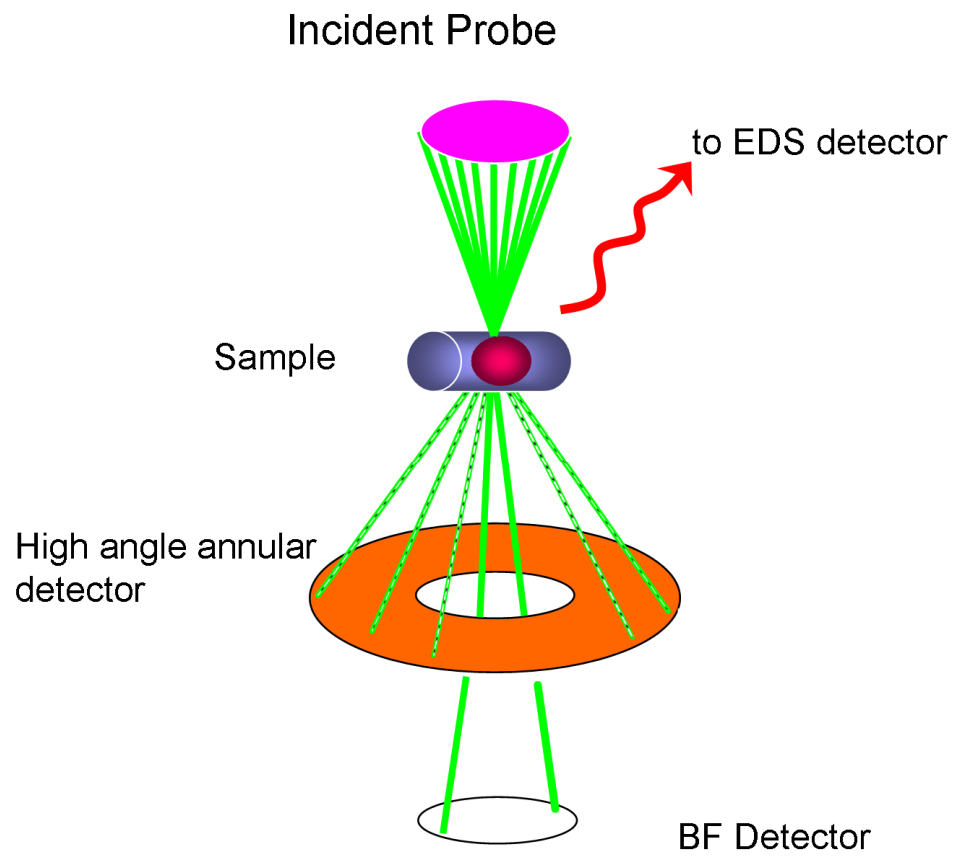
Figure 2.2: Schematic of a typical STEM (figure courtesy of K. Sun)

Figure 2.3: Hitachi HF-3300 located in the High Temperature Materials Laboratory in Oak Ridge National Laboratory.
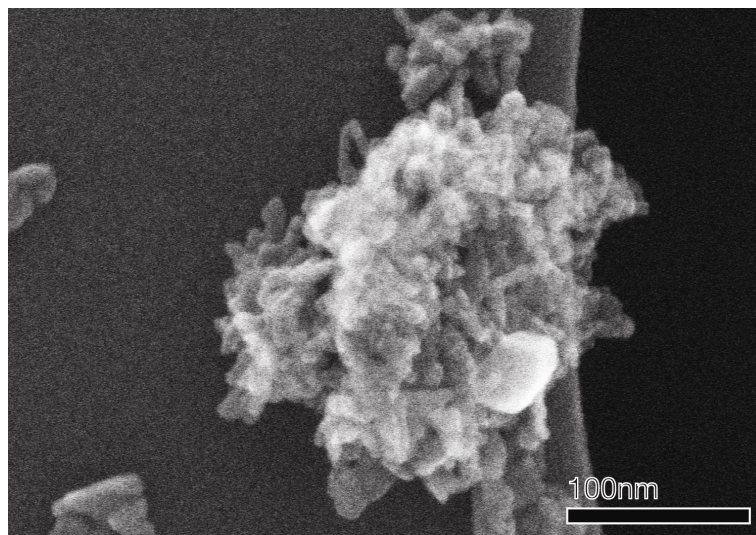
(a)
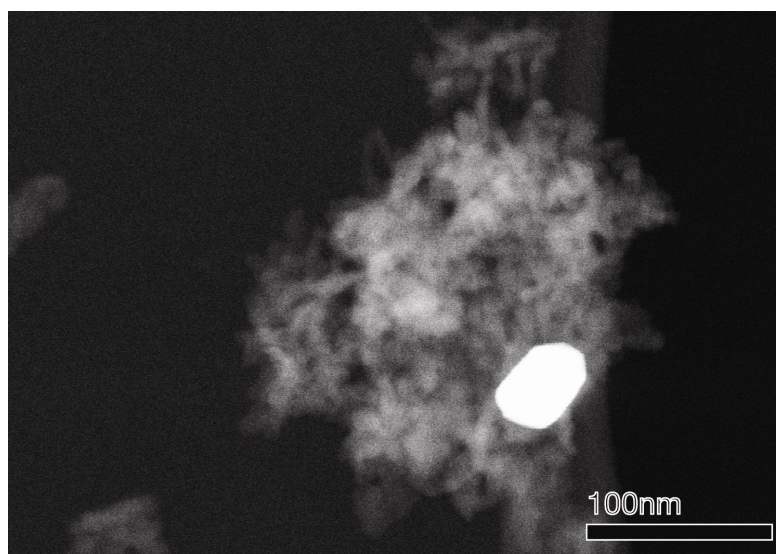
(b)

Figure 2.4: Typical (a) SE and (b) HAADF STEM images of alumina supported PtPd bimetallic catalysts collected from the HF-3300. Contrast in the HAADF STEM image arises primarily from atomic number, therefore the precious metal nanoparticle is distinctly brighter then the surrounding alumina support.
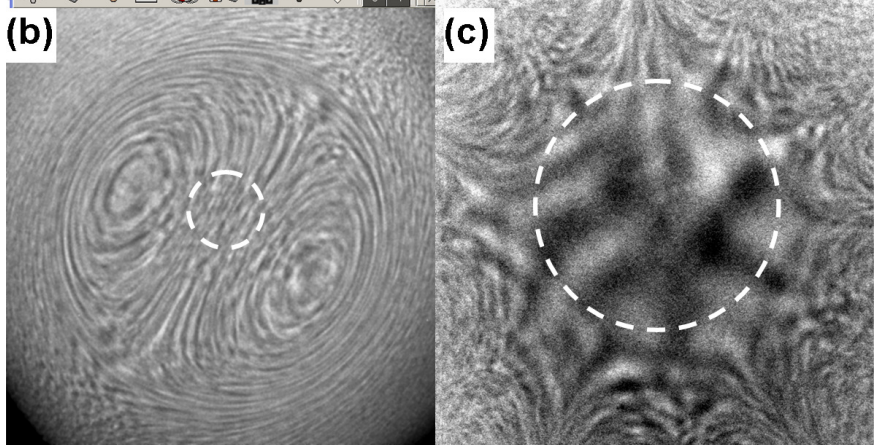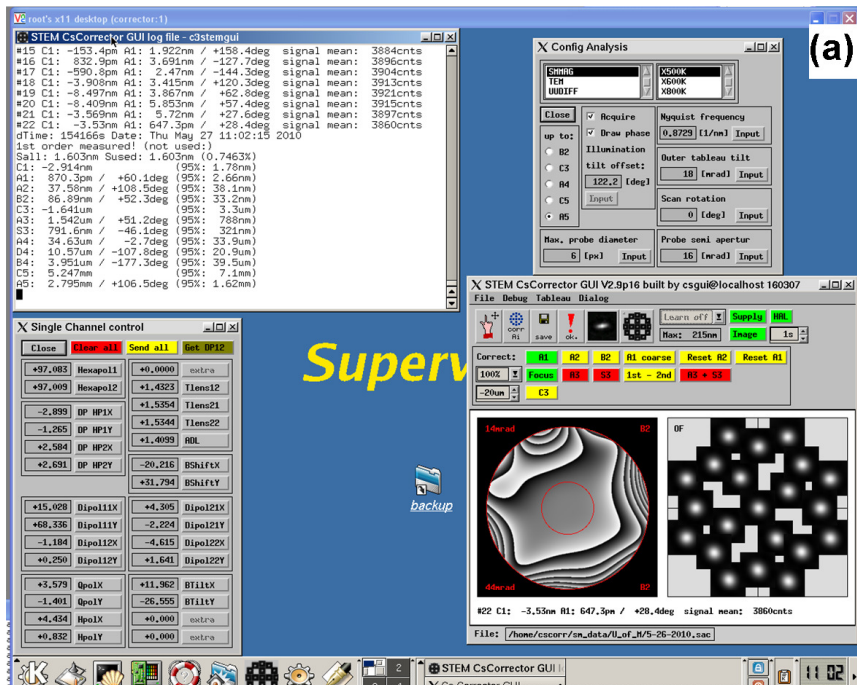
Figure 2.5: (a) screenshot of CEOS probe correction software on JEOL 2100F (b) uncorrected Ronchigram (c) corrected Ronchigram showing much larger "flat" area and reasonable six fold symmetry

CEOS in-
column
aberration
corrector

aberration
corrector computer
controller
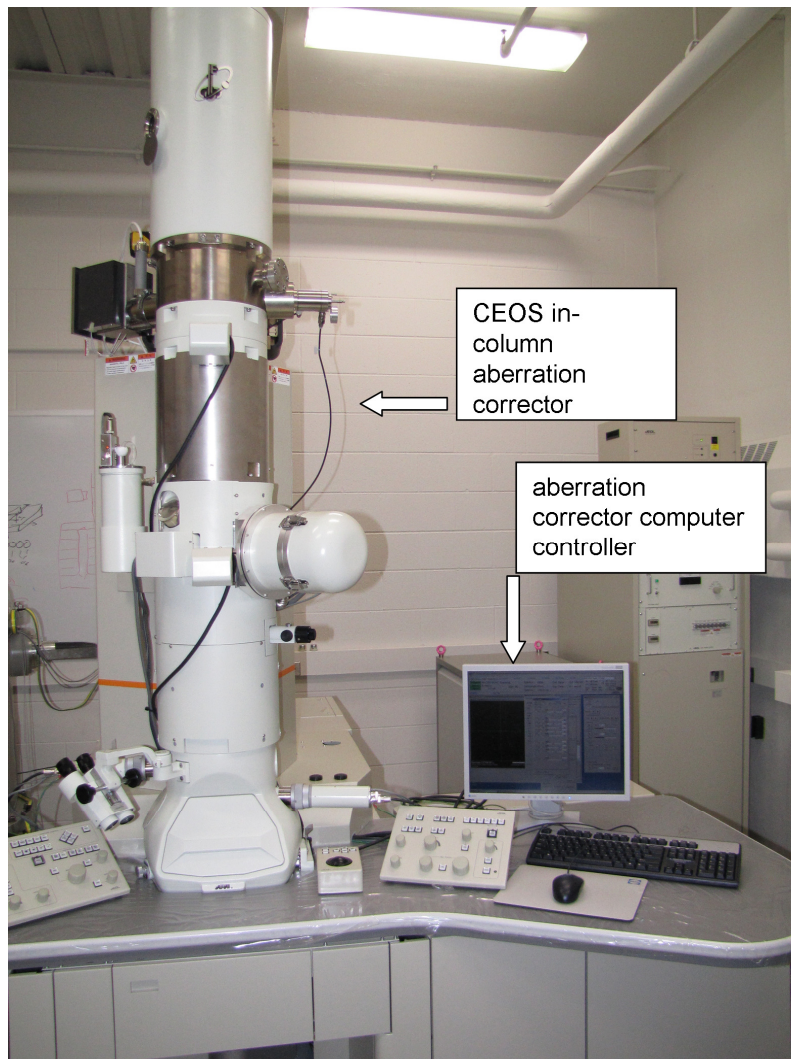
Figure 2.6: JEOL 2100F located in EMAL at the University of Michigan
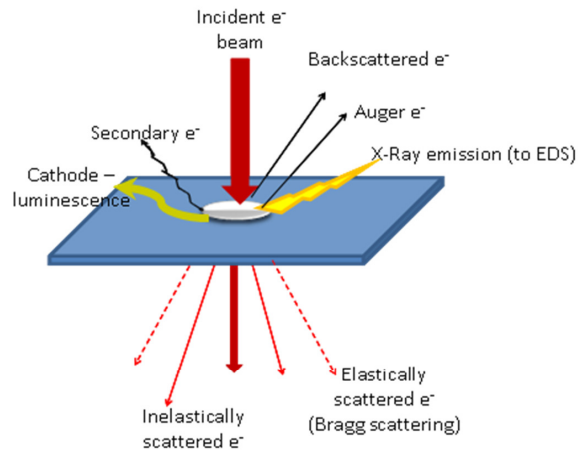
(a)
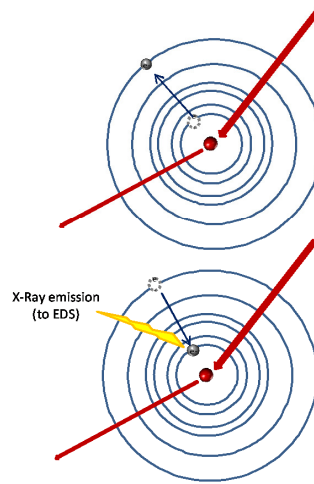
(b)

Figure 2.7: (a)Schematic of some of the signal created from the interaction of a high energy electron beam with a thin sample (adapted from Brydson[34]) and (b) schematic of atomic processes occurring with X-ray emission.
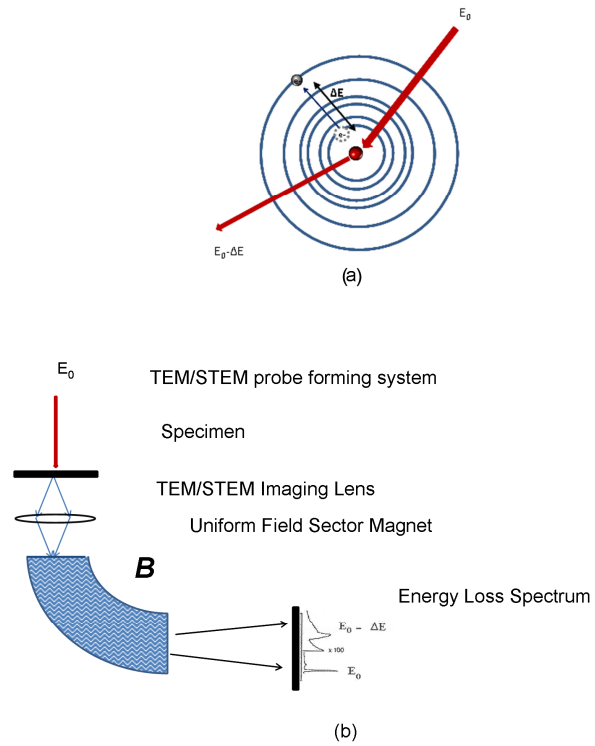
Figure 2.8: (a) schematic of the fundamental properties EELS (adapted from Fultz and Howe[2]and Brydson[34]) (b) schematic of an EELS collection system. (adapted from Zaluzec[35])
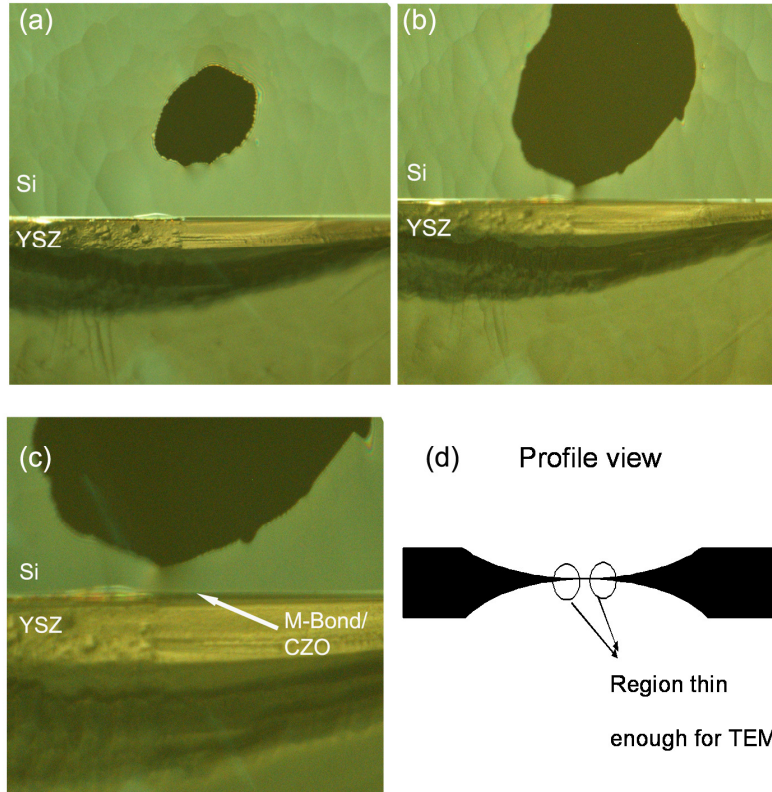
Figure 2.9: (a-c) Optical micrographs of silicon – CZO/YSZ cross sections at successive levels of ion milling (d) profile view schematic indicating thin regions suitable for TEM study.
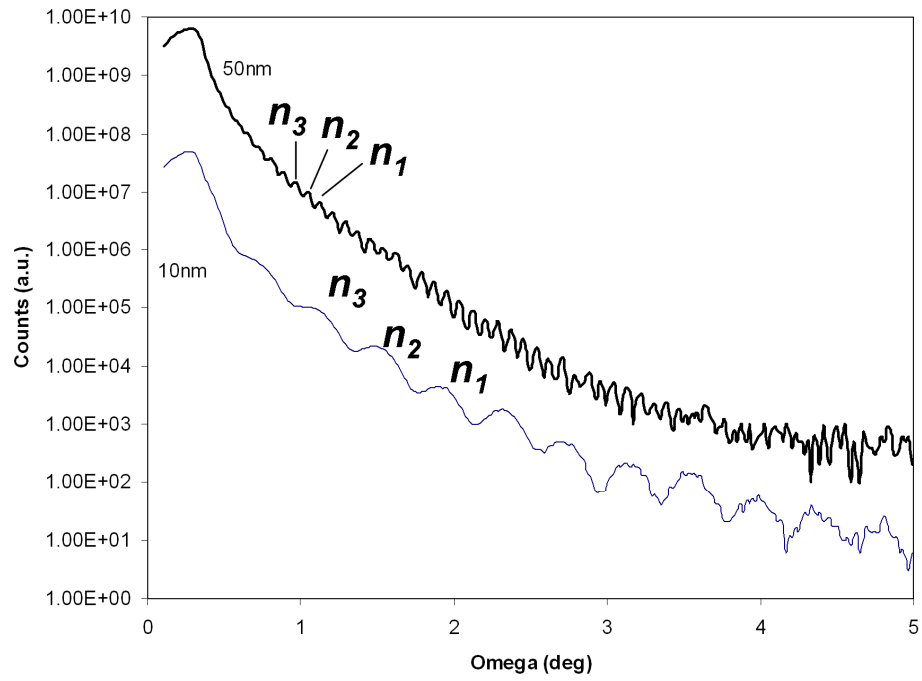
Figure 2.10: Example of film thickness determination from the Kiessing fringes on the XRR scan of two thin $Ce_{0.7}Zr_{0.3}O_2$ films (10nm and 50nm) on a 111-cut YSZ substrate.
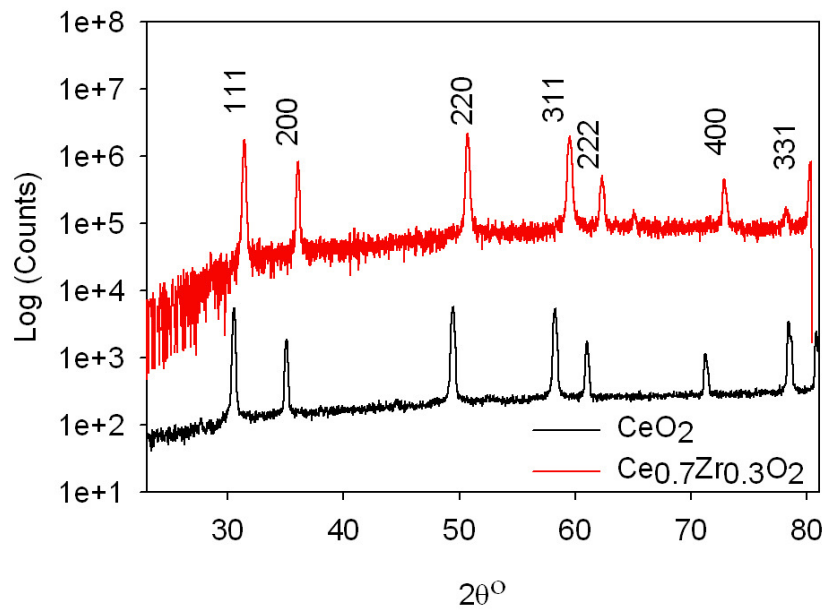
Figure 2.11: θ/2θ XRD patterns of the CeO_2 and $Ce_{0.7}Zr_{0.3}O_2$ targets. Both patterns indicate the desired fluorite structure.
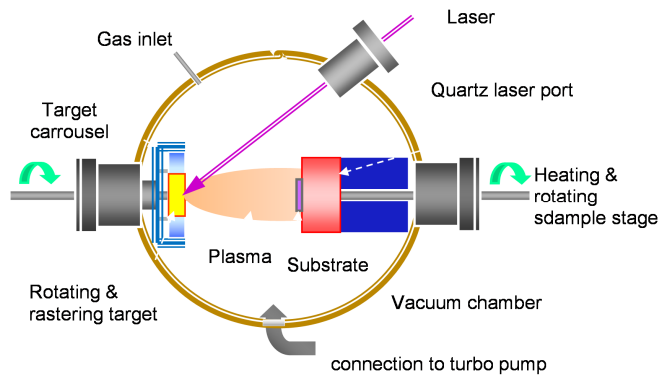
Figure 2.12: Schematic diagram of an PLD system at The University of Michigan (adapted from Guo[66])
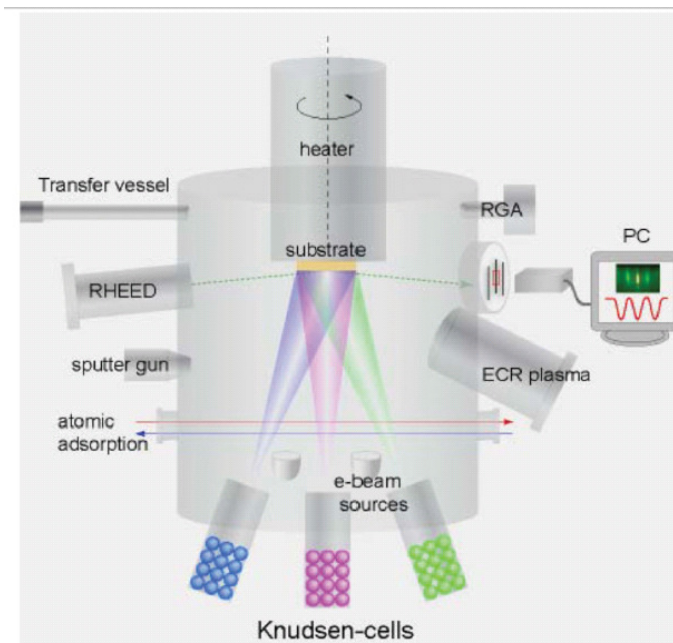
Figure 2.13: Schematic diagram of a flexible OPA-MBE system developed in the Environmental Molecular Science Laboratory at PNNL specifically for the growth of a variety of oxide materials (From Chambers[67])
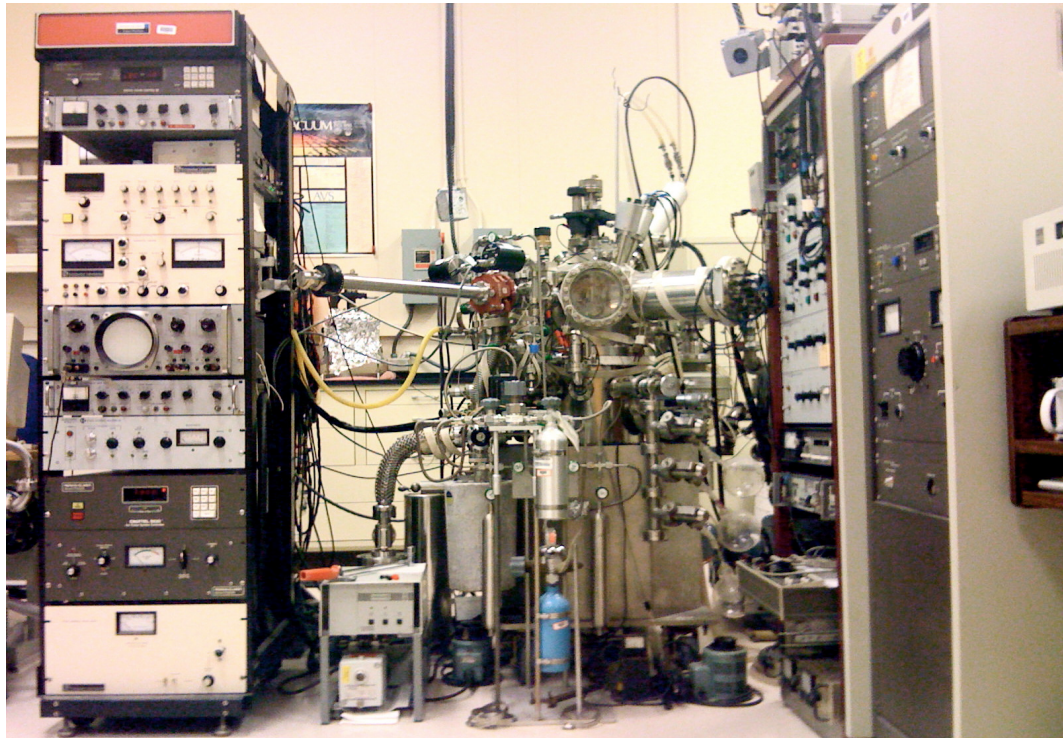
Figure 2.14: UHV Spectrometer at The University of Michigan with Pd and Rh metal deposition sources, and equipped for XPS, AES , and LEIS spectroscopy.

2.5 References

1. F. Haguenau, P.W. Hawkes, J.L. Hutchison, B. Satiat-Jeunemaicirctre, G.T. Simon, and D.B. Williams, "Key Events in the History of Electron Microscopy." *Microsc. Microanal.* **9**(02): p. 96-138 (2003).

2. B. Fultz and J.M. Howe, *Transmission Electron Microscopy and Diffractometry of Materials*. 2 ed., New York, NY: Springer. (2002).

3. J. Liu, "Advanced Electron Microscopy Characterization of Nanostructured Heterogeneous Catalysts." *Microsc. Microanal.* **10**(1): p. 55-76 (2003).

4. P.L. Gai and E.D. Boyes, *Electron microscopy in heterogeneous catalysis*. Series in microscopy in materials science. Bristol: Institute of Physics Pub. (2003).

5. J.P. Brunelle, "Preparation of Catalysts by Metallic Complex Adsorption on Mineral Oxides." *Pure Appl. Chem.* **50**(9-10): p. 1211-1229 (1978).

6. J. Hagen, *Industrial catalysis: a practical approach*. Weinheim: Wiley-VCH. (1999).

7. A.T. Bell, "The impact of nanoscience on heterogeneous catalysis." *Science*. **299**(5613): p. 1688-1691 (2003).

8. D.B. Williams and C.B. Carter, *Transmission electron microscopy: a textbook for materials science*. New York: Plenum Press. (1996).

9. B. Fultz and J.M. Howe, *Transmission electron microscopy and diffractometry of materials*. Berlin: Springer. (2001).

10. Z.L. Wang, "Transmission Electron Microscopy of Shape-Controlled Nanocrystals and Their Assemblies." *The Journal of Physical Chemistry B*. **104**(6): p. 1153-1175 (2000).

11. M. De Graef, *Introduction to conventional transmission electron microscopy*. (2003).

12. L. Reimer and H. Kohl, *Transmission electron microscopy : physics of image formation*. New York, NY: Springer. (2008).

13. J.C.H. Spence, *High-resolution electron microscopy*. (2003).

14. D.B. Williams and C.B. Carter, *Transmission Electron Microscopy: A Textbook for Materials Science*. 1 ed., New York, N.Y.: Kluwer Academic / Plenum Publishers. (1996).

15.   B. Fultz and J.M. Howe, *Transmission electron microscopy and diffractometry of materials*. Physics and astronomy online library. Berlin: Springer. (2001).

16.   S.J. Pennycook, "Z-contrast stem for materials science." *Ultramicroscopy*. **30**(1-2): p. 58-69 (1989).

17.   N.D. Browning, E.M. James, K. Kishida, I. Arslan, J.P.Z. Buban, J. A , S.J. Pennycook, Y. Xin, and G. Duscher, "Scanning transmission electron microscopy An experimental tool for atomic scale interface science." *Reviews on Advanced Materials Science* **1**(1): p. 1-26 (2000).

18.   O.L. Krivanek, M.F. Chisholm, V. Nicolosi, T.J. Pennycook, G.J. Corbin, N. Dellby, M.F. Murfitt, C.S. Own, Z.S. Szilagyi, M.P. Oxley, S.T. Pantelides, and S.J. Pennycook, "Atom-by-atom structural and chemical analysis by annular dark-field electron microscopy." *Nature*. **464**(7288): p. 571-574 (2010).

19.   E. Carlino, "Quantitative Z-contrast atomic resolution studies of semiconductor nanostructured materials." *Journal of Physics: Conference Series*. **209**(1): p. 012005 (2010).

20.   M.T. Otten and W.M.J. Coene, "High-resolution imaging on a field emission TEM." *Ultramicroscopy*. **48**(1-2): p. 77-91 (1993).

21.   T. Sato, M. Konno, Y. Taniguchi, and S. Mamishin, "Hitachi's High-end Analytical Electron Microscope: HF-3300." *Hitachi Review*. **57**(2): p. 132-135 (2008).

22.   A. Bogner, P.-H. Jouneau, G. Thollet, D. Basset, and C. Gauthier, "A history of scanning electron microscopy developments: Towards "wet-STEM" imaging." *Micron*. **38**(4): p. 390-401 (2007).

23.   R. Winston, W.T. Welford, J.C. Miñano, and P. Benítez, *Nonimaging optics*. Amsterdam: Elsevier Academic Press. (2005).

24.   H. Rose, "In Remembrance of Otto Scherzer, the Eminent Pioneer of Electron Optics." *Microsc. Microanal.* **15**(SupplementS2): p. 1452-1453 (2009).

25.   J.C.H. Spence, *High-resolution electron microscopy*. Monographs on the physics and chemistry of materials, 60. Oxford: Oxford University Press. (2009).

26.   A.I. Kirkland and et al., "Aberration corrected TEM: current status and future prospects." *Journal of Physics: Conference Series*. **126**(1): p. 012034 (2008).

27.   R.F. Klie, C. Johnson, and Y. Zhu, "Atomic-Resolution STEM in the Aberration-Corrected JEOL JEM2200FS." *Microsc. Microanal.* **14**(01): p. 104-112 (2008).

28.   L. Allard and S. Rozeveld, "Performance of a Silicon-Drift Detector in 200kV TEM Environments." *Microsc. Microanal.* **15**(SupplementS2): p. 228-229 (2009).

29.   D.A. Blom, L.F. Allard, S. Mishina, and M.A. O'Keefe, "Early results from an aberration-corrected JEOL 2200FS STEM/TEM at Oak Ridge National Laboratory." *Microsc. Microanal.* **12**(6): p. 483-491 (2006).

30.   L.F. Allard, D.A. Blom, M.A. O'Keefe, and S. Mishina, "Design and Performance Characteristics of the ORNL Advanced Microscopy Laboratory and JEOL 2200FS-AC Aberration-Corrected STEM/TEM." *Microsc. Microanal.* **11**(SupplementS02): p. 2136-2137 (2005).

31.   L.F. Allard, D.A. Blom , M.A. O'Keefe, C.J. Kiely, D. Ackland, M. Watanabe, M. Kawasaki, T. Kaneyama, and H. Sawada, "First Results from the Aberration-Corrected JEOL 2200FS-AC STEM/TEM." *Microsc. Microanal.* **10**(SupplementS02): p. 110-111 (2004).

32.   G. Cliff and G.W. Lorimer, "Quantitative-Analysis of Thin Specimens." *J. Microsc.-Oxf.* **103**(MAR): p. 203-207 (1975).

33.   H. Hoeft and P. Schwaab, "Investigations Towards Optimizing EDS Analysis by the Cliff-Lorimer Method in Scanning Transmission Electron Microscopy." *X-Ray Spectrom.* **17**(5): p. 201-208 (1988).

34.   R. Brydson, *Electron energy loss spectroscopy*. Microscopy handbooks. Oxford: Bios in association with the Royal Microscopical Society. (2001).

35.   N. Zaluzec, "EELS: Electron Energy Loss Spectroscopy in the Transmission Elecrron Micorscope." in *Encyclopedia of materials characterization: surfaces, interfaces, thin films*, C.R. Brundle, C.A. Evans, and S. Wilson, Editors., Butterworth-Heinemann ; Manning: Boston. p. 135-148 (1992).

36.   C.C. Ahn and O.L. Krivanek, *EELS Atlas*. Warrendale: Gata. (1983).

37.   A.J. Bourdillon and W.M. Stobbs, "Elastic scattering in EELS-fundamental corrections to quantification." *Ultramicroscopy*. **17**(2): p. 147-150 (1985).

38.   P.E. Batson, "Near-atomic-resolution EELS in silicon-germanium alloys." *J. Microsc.-Oxf.* **180**: p. 204-210 (1995).

39.   P. Batson, "Advanced spatially resolved EELS in the STEM." *Ultramicroscopy*. **78**(1-4): p. 33-42 (1999).

40.   P.E. Batson, N. Dellby, and O.L. Krivanek, "Sub-angstrom resolution using aberration corrected electron optics." *Nature*. **418**(6898): p. 617-620 (2002).

41.   L. Wei and T. Li, "Ultramicrotomy of powder material for TEM/STEM study." *Microsc Res Tech.* **36**(5): p. 380-381 (1997).

42.   P. Scherrer, *Göttinger Nachrichten; Math. Phys.*: p. 98 (1918).

43. A.L. Patterson, "The Scherrer formula for x-ray particle size determination." *Physical Review*. **56**(10): p. 978-982 (1939).

44. M.M. Hall, Jnr, V.G. Veeraraghavan, H. Rubin, and P.G. Winchell, "The approximation of symmetric X-ray peaks by Pearson type VII distributions." *J. Appl. Crystallogr.* **10**(1): p. 66-68 (1977).

45. National Institute of Standards, "Certificate of Analysis: Standard Reference Material 660". National Institute of Standards, Office of Standard Materials: Gaithersburg, Md (1989).

46. M. Rauscher, R. Paniago, H. Metzger, Z. Kovats, J. Domke, J. Peisl, H.D. Pfannes, J. Schulze, and I. Eisele, "Grazing incidence small angle x-ray scattering from free-standing nanostructures." *J. Appl. Phys.* **86**(12): p. 6763-6769 (1999).

47. M. Schmidbauer, D. Grigoriev, M. Hanke, P. Schäfer, T. Wiebach, and R. Köhler, "Effects of grazing incidence conditions on the x-ray diffuse scattering from self-assembled nanoscale islands." *Physical Review B*. **71**(11): p. 115324 (2005).

48. C.J. Blomfield, "Spatially resolved X-ray photoelectron spectroscopy." *J. Electron. Spectrosc. Relat. Phenom.* **143**(2-3): p. 241-249 (2005).

49. W. Chu, "Rutherford backscattering spectrometry." *ASM Handbook.* **10**: p. 628-636 (1986).

50. S.M. Baumann, "Rutherford Backscattering Spectrometry." in *Encyclopedia of materials characterization: surfaces, interfaces, thin films*, C.R. Brundle, C.A. Evans, and S. Wilson, Editors., Butterworth-Heinemann ; Manning: Boston. p. 135-148 (1992).

51. Y. Gao, G.S. Herman, S. Thevuthasan, C.H.F. Peden, and S.A. Chambers, "Epitaxial growth and characterization of $Ce_{1-x}Zr_xO_2$ thin films." *Journal of Vacuum Science & Technology A: Vacuum, Surfaces, and Films*. **17**(3): p. 961-969 (1999).

52. H.M. Smith and A.F. Turner, "Vacuum Deposited Thin Films Using a Ruby Laser." *Appl. Opt.* **4**(1): p. 147-& (1965).

53. H.-U. Krebs, M. Weisheit, J. Faupel, E. Suske, T. Scharf, C. Fuhse, M. Stormer, K. Sturm, M. Seibt, H. Kijewski, D. Nelke, E. Panchenko, and M. Buback, "Pulsed Laser Deposition (PLD) -- A Versatile Thin Film Technique", in *Advances in Solid State Physics*. p. 101-107 (2003).

54. G. Hubler, "Pulsed Laser Deposition." *MRS Bull.* **17**(2): p. 26-27 (1992).

55. Y.R. Ryu, S. Zhu, S.W. Han, H.W. White, P.F. Miceli, and H.R. Chandrasekhar, "ZnSe and ZnO film growth by pulsed-laser deposition." *Appl. Surf. Sci.* **127**: p. 496-499 (1998).

56. D.L. Smith, *Thin Film Deposition: Principles and Practices*. 1 ed., Boston, MA: McGraw-Hill, Inc. (1995).

57. W. Marine, L. Patrone, B. Luk'Yanchuk, and M. Sentis, "Strategy of nanocluster and nanostructure synthesis by conventional pulsed laser ablation." *Appl. Surf. Sci.* **154**: p. 345-352 (2000).

58. A.S. Eppler, G. Rupprechter, L. Guczi, and G.A. Somorjai, "Model Catalysts Fabricated Using Electron Beam Lithography and Pulsed Laser Deposition." *The Journal of Physical Chemistry B*. **101**(48): p. 9973-9977 (1997).

59. B. Luerßen, E. Mutoro, H. Fischer, S. Günther, R. Imbihl, and J. Janek, "In Situ Imaging of Electrochemically Induced Oxygen Spillover on Pt/YSZ Catalysts13." *Angew. Chem. Int. Ed.* **45**(9): p. 1473-1476 (2006).

60. J.G. Duh, H.T. Dai, and W.Y. Hsu, "Synthesis and Sintering Behavior in CeO_2-ZrO_2 Ceramics." *Journal of Materials Science*. **23**(8): p. 2786-2791 (1988).

61. G. Rupprechter, "Sum Frequency Generation and Polarization-Modulation Infrared Reflection Absorption Spectroscopy of Functioning Model Catalysts from Ultrahigh Vacuum to Ambient Pressure." in *Advances in Catalysis*, B.C.G.a.H. Knözinger, Editor., Academic Press. p. 133-263 (2007).

62. C.F. McFadden and A.J. Gellman, "Effect of surface contamination on the UHV tribological behavior of the Cu(111)/Cu(111) interface." *Tribology Letters*. **1**(2): p. 201-210 (1995).

63. G.W. Graham, "NO chemisorption on supported Pd." *Surf. Sci.* **268**(1-3): p. 25-35 (1992).

64. G.W. Graham, "Carbon monoxide chemisorption on $Cu_3Au(100)$ and related surfaces." *Surf. Sci.* **187**(2-3): p. 490-498 (1987).

65. Jeol Ltd., "Operating Manual/Intrsuctions for Use JEOL JEM-3010", (2002).

66. W. Guo, "Epitaxial Growth and Properties of ZnO Thin Films on Si Substrates.". Michigan,Ph.D. Thesis (2010).

67. S.A. Chambers, "Epitaxial Growth and Properties of Doped Transition Metal and Complex Oxide Films." *Adv. Mater.* **22**(2): p. 219-248 (2010).

Chapter 3

Comparative Study of the Evolution of Carbon-Supported Pt and PtCo Fuel Cell Catalysts Aged Under Aggressive Potentiodynamic Cycling

3.1 Introduction

One of the major costs of proton-exchange membrane fuel cells (PEMFCs) is the carbon-supported platinum that is used as an electrocatalyst material.[1-2] As discussed previously in section 2.2.1, alloying platinum with transition metals has been identified as a possible method to mitigate some of the cost (and performance) issues associated with Pt electrocatalysts.[3-10] Although PtNi [5], PtRu [11], PtW, PtCr [12], PtPd, PtFe [5] and a host of ternary alloys[6] have all been investigated as potential PEMFC catalyst materials, PtCo is one of the most thoroughly investigated bimetallic catalysts for this application [4, 8, 13-15] because of its low cost, high activity, and durability. However, the nature of the enhancement mechanisms remains unclear.

In their review[16], Ralph and Hogarth discussed several theories that have been put forward for the improvement in performance of Pt-alloy electrocatalysts. One theory is that alloying with a base metal (such as Co) affects the Pt-Pt interatomic distance in a way that contributes to beneficial electronic effects. There is also some evidence that PtM/C alloys are more resistant to poisoning than pure Pt (see Appleby *et.al.*[17]). Additionally, several studies have suggested that the improved performance of PtCo catalysts can be partially attributed to increased surface roughening due to preferential

leaching of Co under the acidic conditions in which fuel cells operate. This leaching would increase Pt surface area by creating nanoporous platinum [16-17]. Because it is likely that several of these factors are at play simultaneously, it is difficult to conclusively state which ones are most critical to the performance of Pt-alloy catalysts.

Many studies have also identified materials degradation issues that affect the lifetime and long-term performance of fuel cells.[18] The performance loss has been partially attributed to the reduction of electrochemically active surface area (ECA) in the Pt electrocatalyst.[14-15] Possible approaches to improve catalytic durability include tailoring both the support materials and the catalyst metals as well as understanding the interaction between these two components.[19] Several mechanisms have been identified for the loss of electrochemically active surface area, including dissolution of the electrocatalyst materials[20-21], oxidation of the carbon support [22], and precious metal particle growth.[11, 23-24] Particle growth under voltage cycling conditions is especially important because it results in both a decrease in mass activity and an increase in costs associated with PEMFCs.[25]

In this study, aberration-corrected scatting transmission electron microscopy (STEM) and high resolution transmission electron microscopy (HRTEM) were used to characterize changes in carbon-supported Pt and PtCo alloy catalysts after both high-temperature aging and aggressive voltage electrochemical cycling. Structural and compositional changes throughout cycling were also characterized using X-ray diffraction (XRD). This study addresses the affects of various treatment conditions on size, shape, and dispersion in carbon-supported Pt-alloy catalysts. The XRD and aberration-corrected STEM provided direct evidence of Co dealloying with cycling,

while a statistical particle size analysis of HRTEM was used to propose a mechanism for catalyst deactivation under our testing protocol.

3.2 Experimental

3.2.1 Catalyst Selection and Composition

Carbon-supported Pt and PtCo ($Pt_{75}Co_{25}$) powder catalysts with a metal loading of 40 wt% were obtained from Tanaka Kikinzoku Kogyo (TKK). The PtCo alloy powder catalyst used in this study was prepared by high-temperature (800°C -1000°C) carbothermal reduction of Pt and a Co precursor in an inert atmosphere.[26]

3.2.1.1 Acid Treatment and Thermal Aging

Both Pt/C and PtCo/C catalysts were aged at 900°C in N_2 for 1 hour in order to create more comparable catalysts. The thermal treatment was also performed to further characterize sintering properties. Additionally, free powder samples were leached in 1M H_2SO_4 for 24 hours at room temperature.

3.2.1.2 Electrochemical Cycling and Characterization

For electrochemical characterization, the fresh Pt/C and PtCo/C catalysts were fashioned into electrodes by dispersing them onto pieces of conductive fabric. The target catalyst loading for these electrodes was approximately 0.4 mg Pt/cm^2. Electrochemical studies were performed using a standard three electrode cell coupled with a Solartron SI

1287 potentiostat/galvanostat. Pt foil was used as the counter electrode, and an Ag/AgCl electrode was used as the reference electrode. The catalyst samples were immersed in a 1M H_2SO_4 electrolyte, and all testing was performed at room temperature.   Pryor to cycling, the catalyst electrodes were conditioned by holding for 2 hours at a constant voltage of 1.3V $_{RHE}$. A square wave consisting of 15s at 1.3V followed by 15s at 0.5V was then applied. This test condition was designed to aggressively simulate automotive start-stop operation and was identified in our previous study as a test protocol that resulted in significant particle growth.[18] Cyclic voltammograms at a 10 mV/s sweep rate were periodically collected to monitor changes in the catalysts. ECA was calculated by integrating the charge passed during hydrogen adsorption after accounting for double-layer capacity.[27]

3.2.2 Transmission Electron Microscopy

For TEM sample preparation, the catalyst was removed from the electrode by scraping the catalyst powder from the conductive fabric. Catalyst powders were immersed in a solution of 50% ethanol and 50% de-ionized water and ultrasonicated for several minutes before being dispersed onto a 300-mesh carbon-coated copper TEM grid.

TEM was performed with a JEOL 3011 microscope operated at 300 kV with a point-to-point resolution of 0.17 nm. Particle diameters were measured directly on HRTEM images using an integrated software package. Particle-size distributions were constructed from diameter measurements of at least 100 particles taken for each sample. Means comparison tests were performed using SPSS (SPSS Inc., Chicago IL). Descriptive statistics and profile fitting of measured distributions was performed using

Minitab. For profile fitting, the largest and the smallest values were trimmed from each distribution. In addition to the particle size distribution data that went into the profile fitting used to test possible particle growth mechanisms, atomic resolution HRTEM images of each sample were taken in order to qualitatively observe any morphological differences (in particle size, shape, or lattice features) that might exist among the catalysts in this study.

Aberration corrected scanning transmission electron microscopy (STEM) is a powerful and effective tool for the study of heterogeneous supported catalysts due to the fact that it is capable of providing structural and compositional information with sub-Å spatial resolution.[28-29] In this study, fresh and aged catalyst samples were further characterized using high angle annular dark field (HAADF) with an aberration corrected JEOL 2100F. This 200 kV STEM/TEM (located in EMAL at the University of Michigan) is equipped with a CEOS hexapole probe corrector.

Additional analysis was performed on a JEOL 220FS, an aberration corrected STEM/TEM instrument, located in the High Temperature Materials Laboratory (HTML) at Oak Ridge National Laboratory, which is capable of sub-100 pm spatial resolution.[29-30] The JEOL 2200FS is equipped with a Bruker 4030 AXS silicon drift detector (SDD) EDS system. SDD detectors are becoming increasingly popular for nanoscale compositional analysis because of their high count rate and sensitivity[31], and have been developed in recent years for high resolution elemental X-ray mapping.[32] Both HAADF imaging and EDS mapping were was used to investigate the fresh and cycled PtCo/C catalysts.

3.2.3 XRD Measurements

X-ray diffraction (XRD) measurements were also performed on the electrode catalyst samples in the "as received" (fresh) condition and at various points of electrochemical cycling. $\theta/2\theta$ measurements were taken using a Rigaku rotating anode diffractometer with Cu Kα radiation (λ=1.54Å). The electrodes were attached to a silicon coupon and placed in the sample holder. Patterns were obtained over a range of 10º – 90º (2θ) with a scan speed of 5º/min and a sampling interval of 0.03º. The region of the fcc 111 peak (at 39.76º for Pt [33] and 40.53º for CoPt$_3$ [34]) was selected for profile fitting analysis using the Jade software package (MDI Inc.) using the ICDD (International Center for Diffraction Data) PDF4 database. Lattice parameters for the metal particles were calculated by combining the Bragg law with the plane spacing equation.

3.3 Results

3.3.1 Characterization of Fresh Catalysts

TEM images were obtained for both the fresh Pt/C and PtCo/C catalysts. Typical images for the Pt/C and PtCo/C samples are shown in Figure 3.2 and Figure 3.3 respectively. Aside from differences in particle size, the Pt and PtCo particles closely resemble each other before cycling. Smaller Pt particles tend to exhibit more faceting than larger PtCo particles. The fresh Pt/C and PtCo/C catalyst were also characterized using an aberration-corrected electron microscope. The aberration-corrected HAADF images, shown in Figure 3.4, provide no evidence of Co segregation in the fresh PtCo/C sample.

Platinum crystal structure and particle size were further characterized for both Pt/C and PtCo using XRD. Full scale diffraction patterns are shown in Figure 3.1. The diffraction pattern for Pt/C appears to be similar to PtCo/C, however the platinum peaks of the Pt/C catalyst are wider than those of PtCo/C. This indicates that the 'as- received' Pt/C catalyst has a lower crystallite size than the PtCo catalysts. This result supports previously reported results by Yu and others.[4]

3.3.2 Microstructure of Acid Leached and Thermally Aged Catalysts

HRTEM images were collected for acid leached and high temperature aged catalysts. Typical images for the acid leached and thermally aged Pt/C and PtCo/C samples are given in Figure 3.5 and Figure 3.6 respectively. Atomic resolution features and twin planes are visible these HRTEM images.

3.3.3 TEM Dispersions Measurements of Fresh, Acid Leached, and Thermally Aged Catalysts

During TEM observation, size measurements of at least 100 particles were taken for each sample before and after thermal aging, and these results are summarized in Figure 3.7 and Table 3.1. The TEM measurements indicate that fresh PtCo/C particles have a larger mean particle size than the fresh Pt/C particles. High-temperature aging promoted significant particle growth in the Pt/C catalysts, yet this thermal treatment did not significantly affect the particle size of the PtCo/C catalyst.

3.3.4 Electrochemical Analysis

Following standard procedure, the electrochemical area was calculated from the integrated charge from hydrogen adsorption measured from cyclic voltammograms. Plots showing typical cyclic voltammograms of the Pt/C catalyst after 0, 800, and 2280 cycles of square of wave potential cycling (0, 200, and 450 minutes at 1.3 V_{RHE}) are shown in Figure 3.8. The shaded region in Figure 3.8(a) represents the integrated charge used to calculate the ECA.

Change in the ECAs for both catalysts as a function of cycle number under our square wave potential cycling protocol is shown in Figure 3.9 . In each case, the ECA has been normalized by the value attained after the initial 2-hour conditioning treatment, denoted as ECA_o. A notable difference between the two catalysts is that the electrochemical area for the PtCo alloy catalyst stays relatively constant for the first 480 cycles (two cumulative hours at 1.3 V_{RHE}). The electrochemical area of the pure Pt/C, however, decreases immediately. After the initial 480 cycles, the decline in ECA of both catalysts occurs at roughly the same rate. Due to the delayed onset of the PtCo/C ECA decline, it retained over 40% of its original electrochemical area whereas the pure Pt catalyst retained only approximately 25% of its ECA.

3.3.5 Effect of Voltage Cycling Tests on Catalyst Morphology and Composition

TEM and HRTEM images of the PtCo/C catalysts after 480 cycles are shown in Figure 3.11. Aside from particle growth, we were not able to discern any specific structural changes in the catalyst nanoparticles in the HRTEM images. In particular, the image shown in Figure 3.11 (b) provides no evidence of dealloying or other compositional inhomogenities attributed to cycling.

Aberration-corrected HAADF images of both the Pt/C and PtCo/C catalysts after 480 cycles are shown in Figure 3.12 . In the Pt/C image, there is no clearly observable difference in intensity across the particle other than that which would be expected for particle shape and thickness. In the case of the PtCo/C catalyst (fig. 6(b)), typical particles show a clear difference in intensity, indicating the possibility of either compositional or structural inhomogeneity.

TEM images of the Pt and PtCo catalysts after 2400 cycles are shown in Figure 3.13. By comparing these micrographs of the two catalysts with those from before (Figures 3.2, 3.3), one can see that noticeable metallic particle growth has occurred. From the TEM observations summarized in Figure 3.10 (along with the data from fresh, acid leached, and thermally aged) and Table 3.2, we can conclude that the PtCo/C catalyst underwent much less particle growth during cycling than the Pt/C catalyst did. Although the two catalyst samples had substantially different particle sizes initially, after 2400 cycles (10 cumulative hours at 1.3 V_{RHE}) no statistically significant (p>0.05) difference in mean particle size was found between the Pt/C and PtCo/C catalysts. Data collected with aberration-corrected HAADF images agree with results from the HRTEM after this point of aging.

HRTEM images of the catalysts revealed the presence of grain boundaries, generally in the form of twin boundaries. Examples of these grain boundaries can be found in Figure 3.18. Boundaries and twinning were more apparent in particles larger than 2 nm. Before cycling, HRTEM images revealed clearly observable boundaries in approximately 5.3% (3 of the 57 observed particles) of Pt/Co particles and 2.5% (2 out of 77) of the Pt nanoparticles. However, after completion of the cycling test (Figure 3.18(c)

and (d)), boundaries were observed in 29% (16 of 55) and 17% (11 of 64) of observed PtCo and Pt particles, respectively. Additionally, in the case of aged Pt catalysts (Figure 3.18(c)), single twinning was more commonly observed in larger (d>15 nm) catalyst particles.

XRD analysis provides some clues regarding the possible affect of Co on particle growth. Figure 3.19 shows details of the $\theta/2\theta$ XRD pattern of the PtCo/C catalyst at various stages of aging. These scans illustrate that compositional changes in the catalyst particles are also taking place during cycling. The location of the 111 reflection shifts from 40.84º before cycling to 39.84º after 2400 cycles. While the lattice parameter of the pure Pt catalyst did not change appreciably with cycling (Figure 3.19), the lattice parameter of the PtCo catalyst increased from 3.82 Å for the fresh catalyst to 3.93Å (the value for bulk Pt) after 2400 cycles.

EELS analysis was performed using the Gatan Image Filter (GIF) on the JEOL 2100F. Characteristic EELS spectra for typical particles (with diameters near the median in our measured particle size distributions) are presented in Figure 3.14. The intensity of the Co (L2,3) was largest for the fresh catalyst and decreased with cycling. It should be noted that characteristic Co peaks were not detected with EELS on typical particles after the 2400 cycles, however Co signal was found in some larger (d>~20nm)particles

The above mentioned EELS analysis was performed as point analysis on individual particles. In order to determine the spatial distribution of Pt and Co, EDS analysis with spectrum imaging was performed on the integrated bucker SDD detector on the JEOL 2200FS at ORNL. Spectrum images for both the fresh and the 480 cycled PtCo/C catalysts are presented in Figure 3.15. These images show that while the fresh

73

catalyst was a well mixed alloy, the aged catalyst tended to have a Pt shell with a PtCo core. Furthermore, sum-spectra from these images (Figure 3.16) showed that the fresh catalyst contained more Co than the aged catalyst, providing further evidence of a loss of Co with cycling.

3.4 Discussion

Aside from differences in particle size, both HRTEM and aberration-corrected HAADF stem imaging did not yield clear differences in the atomic structure of the fresh catalysts aside from the fact that fresh Pt/C were found to be more highly faceted than corresponding fresh PtCo/C catalysts. This can be attributed to the fact that PtCo particles are generally larger than Pt particles, and smaller particles have been shown to exhibit more faceting by adopting FCC equilibrium shapes even at quite small particles sizes.[35-36] Both HRTEM and HAADF imaging revealed well-mixed alloy particles with no significant Co segregation or ordered phases in the fresh PtCo/C catalyst.

The mean particle sizes for the fresh, acid leached and thermally aged catalysts are given in Figure 3.7. Several statistical data analysis techniques were used to determine the significance of the observed differences in the mean particle sizes. In the distribution data, the variances within groups were not homogenous. Because analysis of variance (ANOVA) techniques assume homogeneity of the variances, non-parametric techniques were used to compare the means.[37] SPSS was used to perform a Kruskal-Wallis analysis with Mann-Whitney post-tests. In all tests, values of $p < 0.05$ were judged to be significant. The relevant statistical analysis results are summarized in Table 3.3.

Statistical testing indicates that high-temperature aging did promote significant particle growth in the Pt/C catalyst; however, the thermal treatment did not have a statistically significant effect on the mean PtCo/C particle size, presumably because it had previously experienced high temperatures during carbothermal fabrication. Significant differences were also found between 'as received' PtCo/C and acid leached PtCo/C, however it should be noted that acid leaching did not have a statistically significant effect on the Pt/C particle size.

Cyclic aging, on the other hand, produced more pronounced changes in the PtCo/C catalyst, as revealed in the aberration-corrected HAADF images after 480 cycles. Although the HRTEM image (Figure 3.11) shows no atomic resolution differences after aging, the HAADF image (Figure 3.12b) clearly reveals that some structural change has occurred with aging. As intensity in HAADF scales proportionally to atomic number, it is reasonable to attribute these differences in intensity to areas with Co or with voids in the nanoparticles. EDS spectrum imaging indicates that these particles indeed have less Co in the outer layers. Other researchers[38] have reported similar results for H_2SO_4 leached structures of Pt_3Co. Earlier reports have suggested that selective Co dissolution might be localized to the outer few atomic layers.[39] Our current observation of Pt-Co core encapsulated by a Pt shell indicates that this mechanism is taking place to some degree. It has been suggested that the increase in oxygen reduction activity can be, at least partially attributed, to the increase in surface area, due to the selective dissolution (dealloying) of the less-noble metal from the PtM (M = Ni, Co, etc.) alloy catalysts.[16-17, 40] Both EELS and EDS analysis further support the idea of selective dissolution. This model is shown schematically in Figure 3.17.

The electrochemical aging protocol revealed some structural changes that were observable in XRD. As noted earlier, detailed analysis of the PtCo (111) peak (Figure 3.19) indicated a shift in peak location and lattice parameter with aging. Platinum-cobalt alloys retain FCC structure for Pt-rich compositions with a near-linear decrease in lattice spacing with increasing Co content and a slightly positive deviation from Vegard's Law.[7, 41] Therefore, this shift and the resulting change in the lattice parameter indicate that Co is being removed from the particles during cycling. This diffraction analysis provides further evidence that Co removal is a "bulk" process and not limited to the surface of the individual nanoparticles.

Additionally, XRD analysis reveals that the 111 peak narrows and the intensity increases with increasing cycling time, indicating that crystallite size increases with electrochemical cycling. Debye-Scherrer[42-43] analysis of the XRD peak breadth generally supports the trends found in the TEM observations, *i.e.*, that the Pt/C catalyst particles begin with a smaller mean particle size than those in the PtCo/C catalyst, however, the Pt/C catalyst particles undergo more growth (on average) than the PtCo catalysts.

In an effort to gain some further insight on the mechanisms of catalyst deactivation via particle growth, particle size distributions measured directly from TEM images were analyzed and fitted to the smallest extreme value (SEV) distribution function and the lognormal distribution function (LNDF). Classical studies have identified two primary mechanisms for particle growth under a wide variety of conditions.[44-45] The interparticle transport mechanism characterizes particle growth through redeposition of dissolved Pt species (a process similar to Ostwald ripening). The driving force of Ostwald ripening (O-R) is the minimization of cluster Gibbs free

energy.[46] The kinetics of this process have been described in detail in the Lifshitz-Slyozov-Wagner (LSW) theory, which shows a resultant particle-size distribution with the tail skewed toward smaller particles sizes. Mathematically, this distribution can be modeled very closely by Gumbel type I or the smallest extreme value (SEV) distribution function (Figure 3.20a).[44-45, 47] The probability density function of the SEV distribution function is given by Equation 3.1 :

$$f(d) = \frac{1}{\beta} e^{\frac{d-\mu}{\beta}} e^{-e^{\frac{d-\mu}{\beta}}}$$

Equation 3.1

Where: d   =   measured particle diameter

μ   =   location parameter (mode)

β   =   scale parameter

Another growth mechanism that has been proposed is particle migration and coalescence.[24, 47] This process can be described as growth by coalescence after direct impingement of particles randomly moving in a Brownian fashion on a support surface, and the rate-limiting step can be either the mobility of the catalyst on the support or the kinetics of the coalescence process [44]. In contrast to O-R, migration and coalescence leads to a distribution shape of a lognormal distribution function (LNDF) (Figure 3.20b). The probability density function is given by Equation 3.2 :

$$f(d) = \frac{e^{\frac{(-\ln(d-\theta))^2}{2\sigma^2}}}{(d-\theta)\sigma\sqrt{2\pi}}$$

Equation 3.2

Where: d   =   measured particle diameter

θ   =   location parameter

σ   =   shape parameter

77

Individual distribution identification was performed using the Minitab software package, and a probability plot was constructed for each distribution in question. A given population is a good fit if the data points roughly follow a straight line and the p-value is greater than the desired alpha value (0.05 in this study). If the data fits more than one distribution, then the highest p-value is selected. Probability plots used for distribution identification for the Pt/C (after 2400 cycles) are given along with histograms in Figure 3.20. As shown, the data best fits the LNDF indicated by the straight line on probability plot and its corresponding large p-value (p=0.414).

The LNDF was, in fact, the better fit of the two distributions for all samples tested, and histograms of measured particle size distributions fitted to the log-normal distribution for the cycled Pt and PtCo catalysts are shown in Figure 3.21. This result indicates that migration and coalescence was the dominant mechanism for catalyst particle growth under this type of testing. Migration and coalescence has also been found to be the primary growth mechanism in previous work involving single-cell accelerated life tests with Pt catalysts[11], and the present result is in agreement. It has been previously reported [48] that interparticle transport through dissolution/redeposition is the more prevalent sintering mechanism under load cycling protocols; however, we found no strong evidence of ripening in our study. The fact that none of the distributions fit the distribution typical of O-R does not mean the O-R is not taking place since more than one growth mechanism might be taking place at the same time.[47] XRD provides solid evidence that PtCo-particle dissolution and subsequent Pt redeposition with concomitant loss of Co is taking place, though the fate of the lost Co remains unknown.

The increase in the prevalence of grain boundaries and twinned particles with aging provides further evidence for migration and coalescence as the primary growth mechanism. McGinn and others[49] proposed a model for the growth of gold on amorphous SiO$_2$, based on an extension of Glieter's "growth accident" model, to include the coalescence of particles. This model proposed that perfect 111 twin boundaries can arise, through interparticle transport, from migration and coalescence of two particles in order to minimize the boundary energy between these grains. Additionally, Harris[50] has provided evidence that the increase in prevalence of these twin boundaries can be attributed to particle coalescence. The formation of singly twined particles is an indication of kinetic (rather than thermodynamic) growth.[51] Thus, the increase in density of the grain boundaries is consistent with simple coalescence of the original particles.

The delay of the onset of ECA decline for the PtCo/C catalyst relative to the Pt/C catalyst appears to be clearly associated with the loss of Co from the PtCo alloy particles in the catalyst sample. Aside from selective dealloying, it can also be surmised that more significant particle growth from migration and coalescence is also associated with the loss of Co from the PtCo particles. This may be explained by the "anchoring effect" of Co on Pt nanoparticles. Previous studies[12, 52] have suggested that the addition of base metals (such as Co and Ni) to Pt can lower particle mobility on a carbon support. The mechanism for this lowering in particle mobility is that base metals increase the interaction between the nanoparticles and the carbon support.[8] In this study, as the PtCo alloy catalysts lost Co to become more platinum-like they became more susceptible to migration and coalescence, resulting in the observed loss in ECA. This study provides further evidence for this mechanism in that the anchoring effect of Co decreases as Co is

lost from PtCo particles during dissolution/redeposition of the metal nanoparticles with cycling.

3.5 Conclusions

In this study, direct TEM observation of commercial Pt and PtCo alloy catalysts enabled both atomic-scale structural characterization and quantitative analysis of dispersion loss leading to deactivation. In comparing carbon-supported Pt and PtCo, PtCo particles were initially larger in size than Pt particles, due to their synthesis, but particle growth under aggressive electrochemical aging was initially delayed. Aberration-corrected HAADF imaging revealed inhomogeneities in the PtCo particles after 480 cycles, the formation of which we presume to be due to selective Co dissolution. XRD diffraction demonstrated that a gradual removal of Co metal occurs with electrochemical cycling. Furthermore, statistical analysis of TEM results indicates that significant differences exist between the PtCo/C and the Pt/C dispersions. In both catalysts, significant differences in the mean particle size could be attributed to cyclic aging; however, the PtCo catalyst retained twice as much of its original electrochemical area as the pure Pt catalysts. The shape of the resulting distribution supports the idea that migration and coalescence are the dominant particle growth mechanisms in these catalysts. Differences in the particle growth behavior may be attributed to the anchoring effect of Co, which diminishes as Co is lost during electrochemical cycling.

3.6 Tables

Table 3.1: Descriptive Statistics for particle sizes of fresh, acid leached and thermally aged catalysts

Sample	N	Mean	Std. Dev	95% Confidence Interval for Mean		Minimum	Maximum
				Lower Bound	Upper Bound		
Pt/C	108	2.58	0.85	2.42	2.74	1.12	4.90
Pt/C Acid Leached	106	2.45	0.64	2.32	2.57	0.93	4.38
Pt/C Aged 900C	103	4.11	1.15	3.88	4.33	1.57	8.17
PtCo/C	107	4.80	2.22	4.37	5.22	1.93	15.60
PtCo/C Acid Leached	101	4.19	1.91	3.81	4.57	1.14	15.60
PtCo/C 900°C	120	4.86	1.49	4.59	5.13	2.11	10.80
Total	645	3.85	1.77	3.71	3.98	0.93	15.60

Table 3.2: Descriptive Statistics for particle sizes of fresh, acid leached and thermally aged catalysts.

Catalyst	Treatment	No. of Measurements	Mean (nm)	Sts. Dev. (nm)	Min (nm)	Median (nm)	Max (nm)
Pt/C	0 cycles	113	2.42	1.09	0.74	2.20	8.18
Pt/C	480 cycles	102	4.22	2.02	0.79	4.25	12.50
Pt/C	2400 cycles	112	7.62	5.42	1.53	5.70	30.20
PtCo/C	0 cycles	110	4.45	3.56	1.99	3.72	32.20
PtCo/C	480 cycles	110	5.85	6.44	1.46	4.77	64.10
PtCo/C	2400 cycles	112	7.46	3.66	1.90	6.29	19.80

Table 3.3: Statistical (Mann Whitney) comparison of mean particle sizes. Mean particle sizes given with ± 1σ. Results with p<0.05 from Mann-Whitney test are underlined

	Sample 1	**Sample 2**	*p*-value
	Pt/C 'as received'	PtCo/C 'as received'	
mean size(nm)	2.58±0.85	4.8±2.22	<0.001
	Pt/C 'as received'	Pt/C 'acid leached'	
mean size(nm)	2.58±0.85	2.45±0.45	0.594
	Pt/C 'as received	Pt/C aged 900°C	
mean size(nm)	2.58±0.85	4.11±1.15	<0.001
	PtCo/C 'as received'	PCo/C 'acid leached'	
mean size(nm)	4.8±2.22	4.19±1.91	0.021
	PtCo/C 'as received	PtCo/C aged 900°C	
mean size(nm)	4.8±2.22	4.86±1.49	0.09

3.7 Figures

Figure 3.1: Full scale XRD pattern for the fresh PtCo and the Pt/C catalysts. The Pt peaks are higher and more will defined for the PtCo catalysts. The PtCo111 and PtCo311 are located at larger 2θ angles than corresponding Pt catalysts.
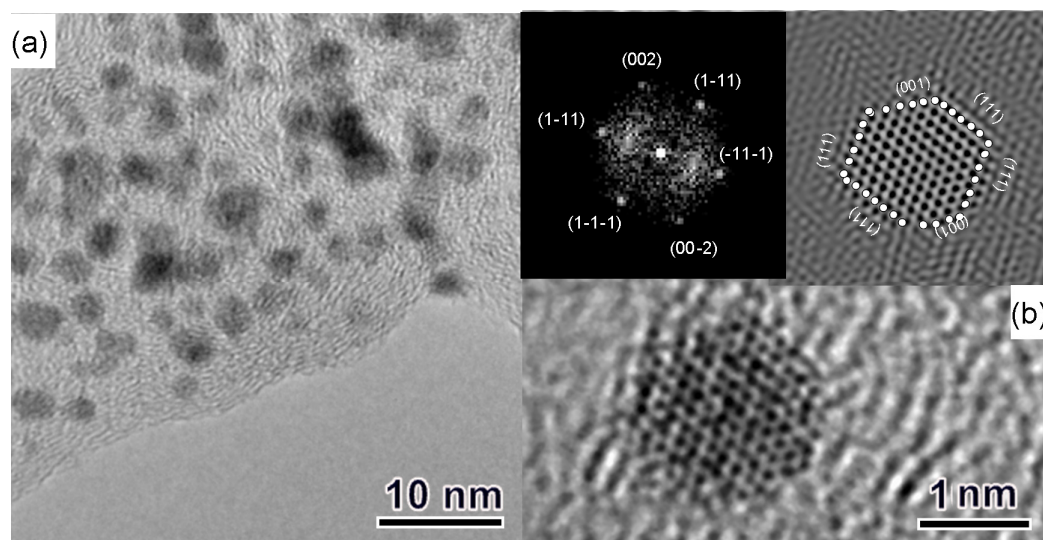
Figure 3.2: (a) TEM and (b) HRTEM images for fresh Pt/C catalyst. Insets in (b) show FFT (left) of the particle, indicating that the zone axis of the particle is along the [110] FCC zone axis. The plane spacings measured in image agree with that of the Pt FCC structure.
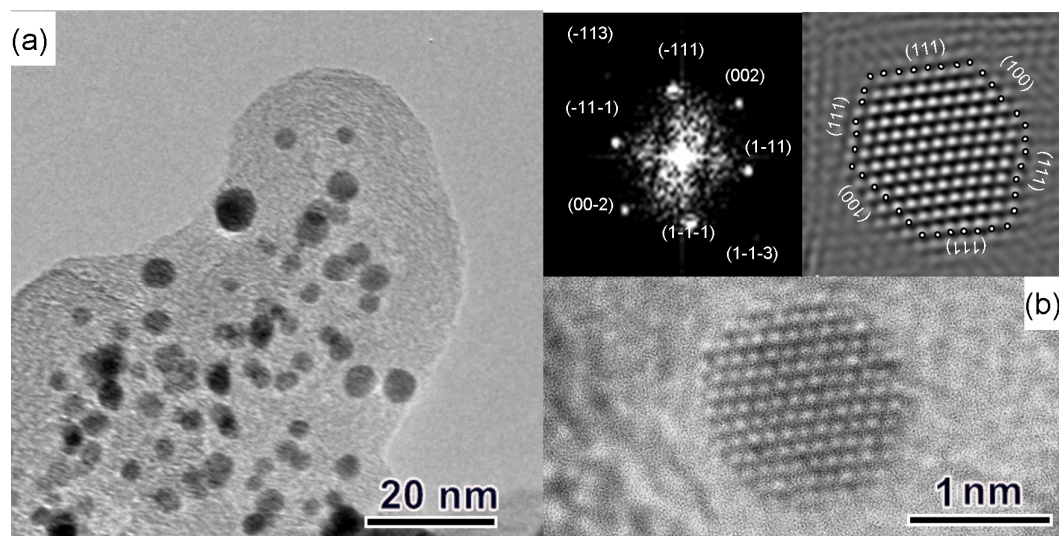
Figure 3.3: (a) TEM and (b) HRTEM images for fresh PtCo/C catalyst. Insets in (b) show FFT (left) of the particle, indicating that viewing is along the [110] FCC zone axis, and inverse FFT (right) of the Fourier filtered image, showing representative lattice planes.
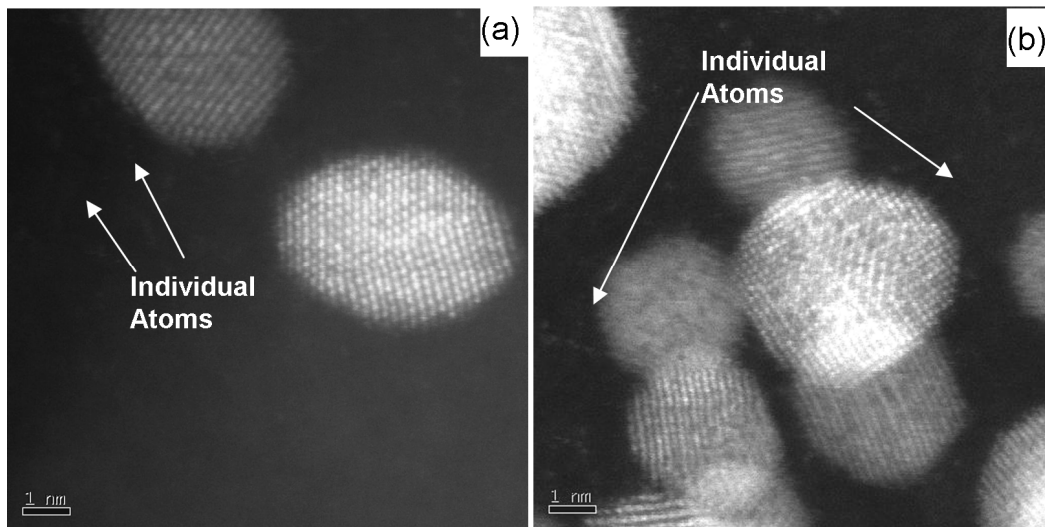
Figure 3.4: Aberration corrected HAADF STEM image of fresh (a) Pt/C and (b) PtCo/C catalyst particles. Atomically dispersed metal particles are evident in both samples.
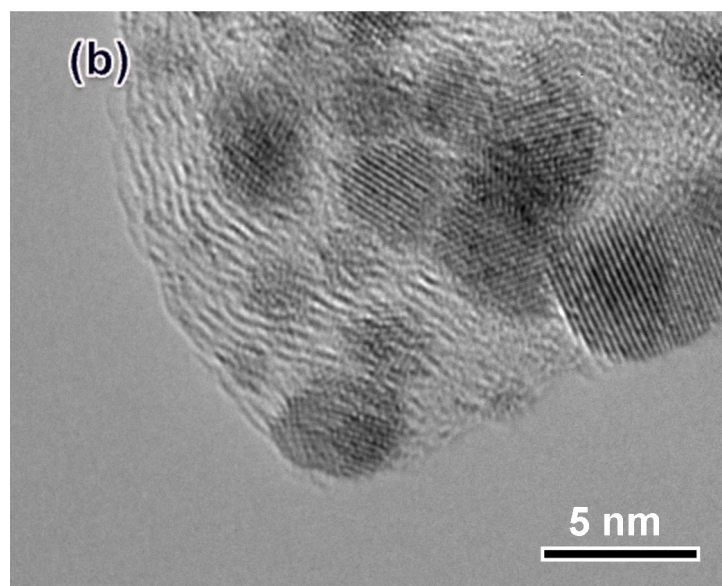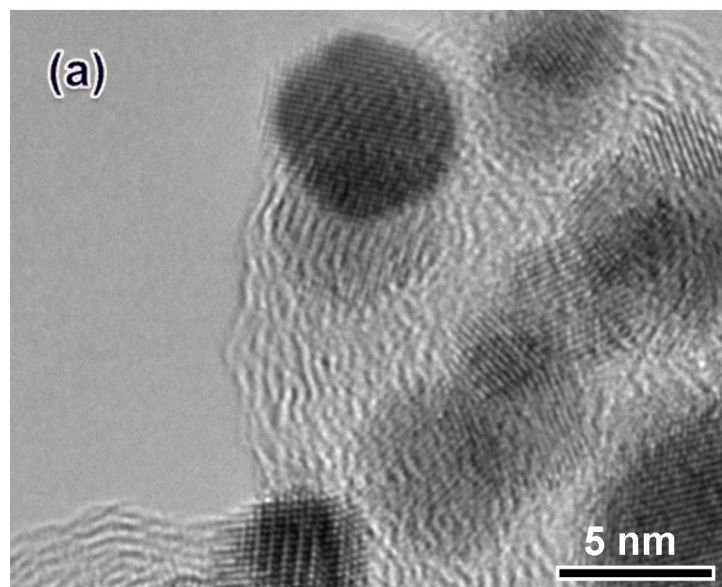
Figure 3.5: HRTEM of micrographs of (a) acid leached and (b) 900ºC thermally aged Pt/C catalysts
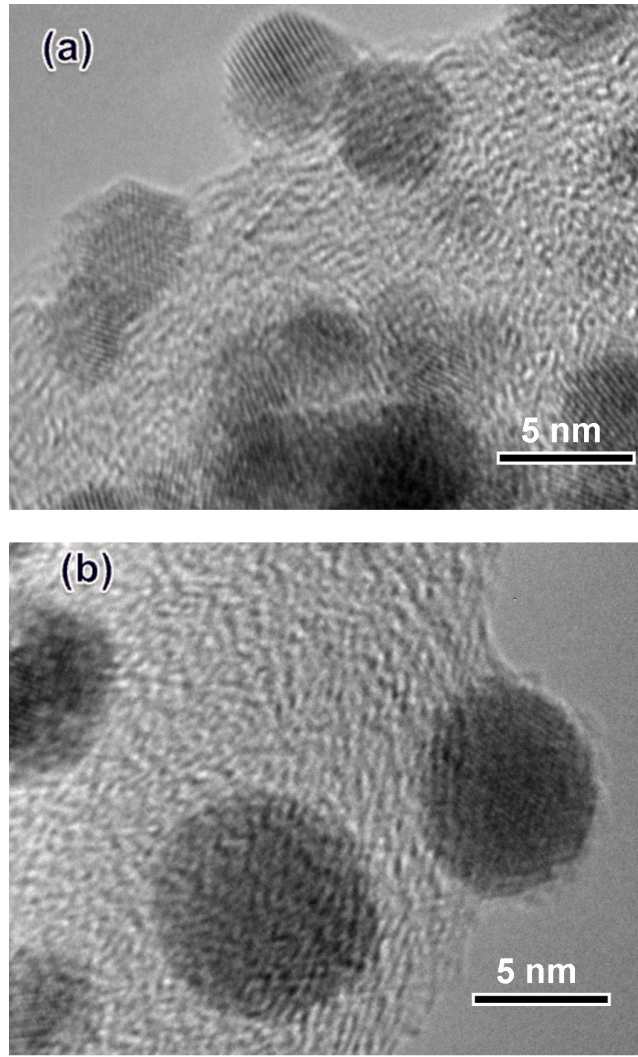
Figure 3.6: HRTEM of micrographs of (a) acid leached and (b)900ºC thermally aged
PtCo/C catalysts
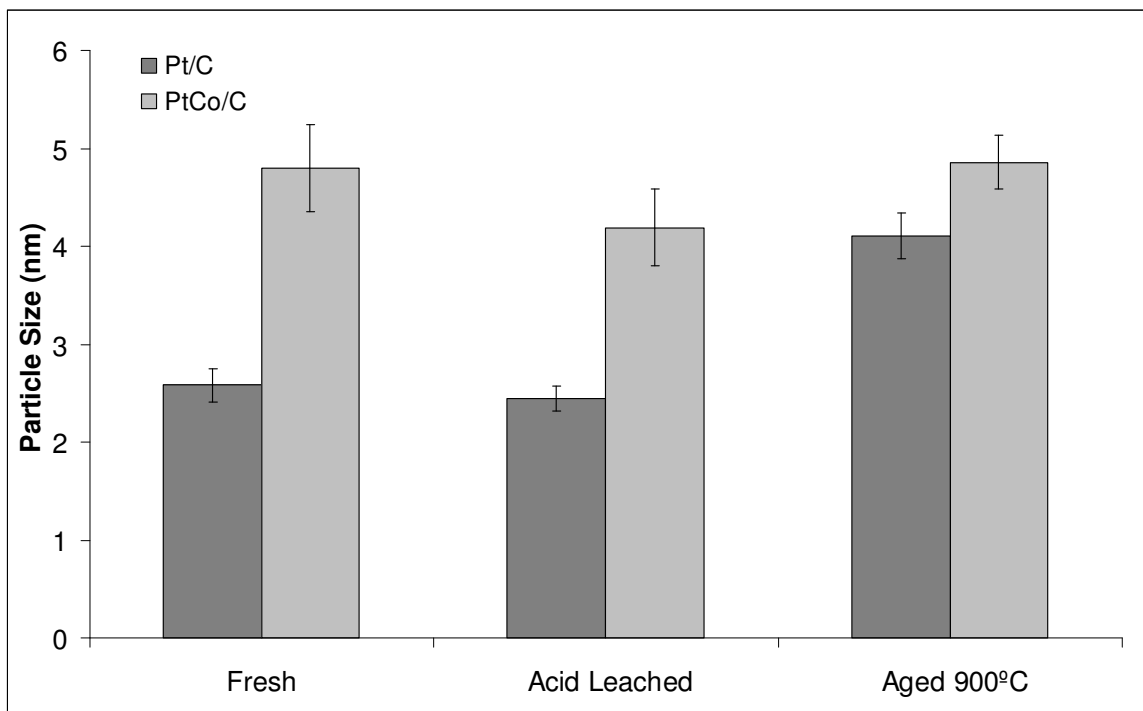
Figure 3.7: Mean particle size (in nm) for Pt/C and PtCo/C samples. Error bars represent the upper and lower bounds of the 95% confidence interval
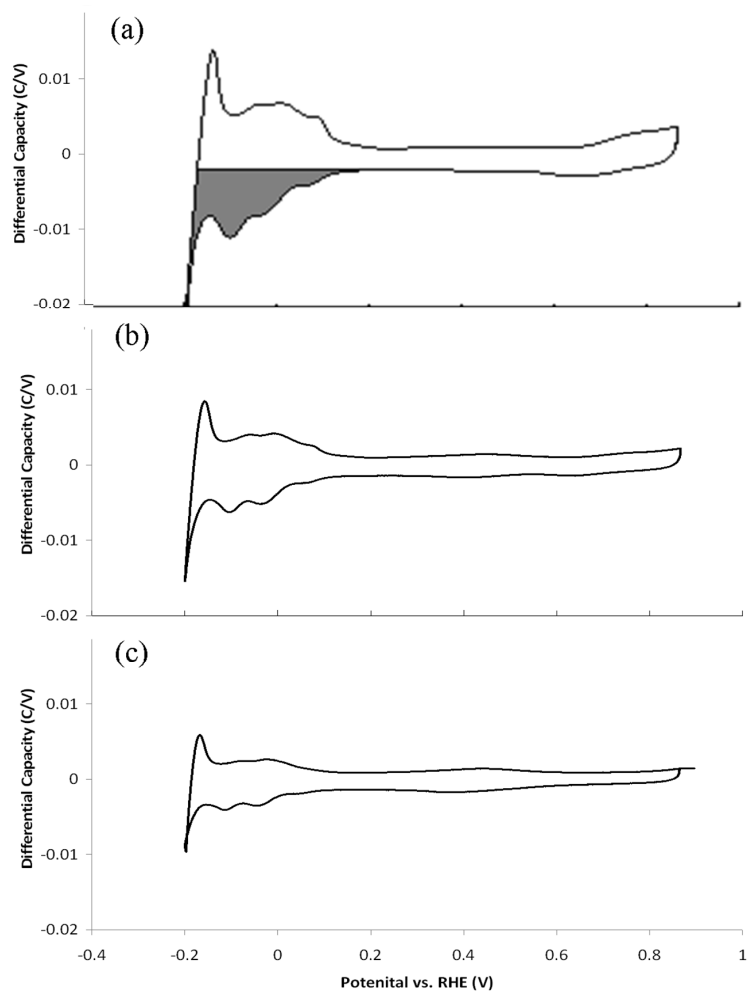
Figure 3.8: Plots showing typical cyclic voltamagrams of the Pt/C catalyst after (a) 0 min (b) 200 min (1800 cycles) and (c) 450 minutes (2280 cycles) of square of page potential cycling. The shaded region in (a) represents the integrated charge used to calculate the ECA.
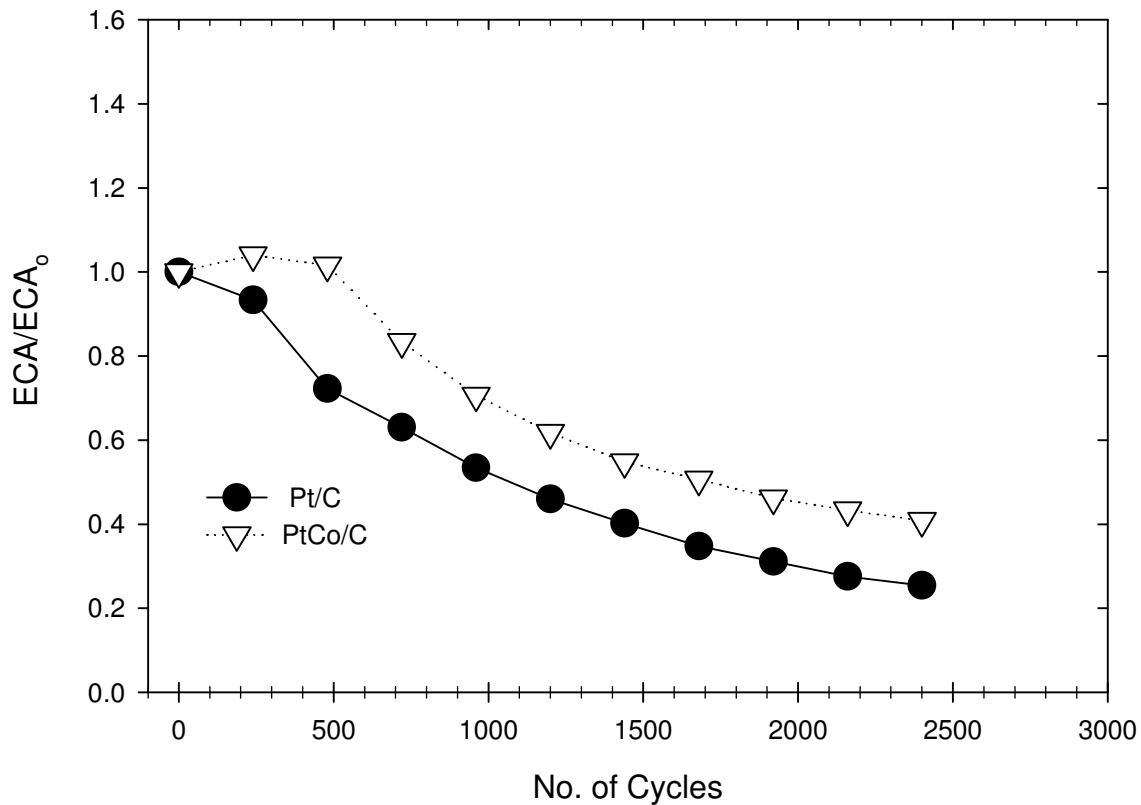
Figure 3.9: Decline in normalized electrochemical area (ECA) of PtCo/C and Pt/C, showing that the PtCo/C catalyst retains more electrochemical area than Pt/C.
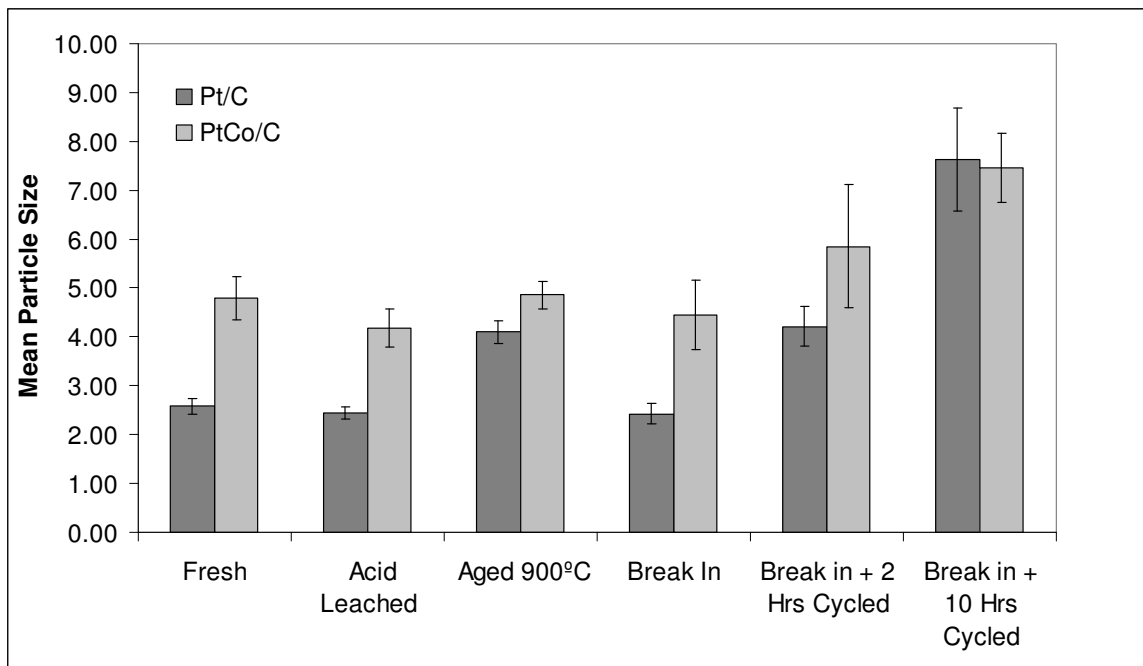
Figure 3.10: Mean particle size (in nm) for Pt/C and PtCo/C samples. Error bars represent the upper and lower bounds of the 95% confidence interval
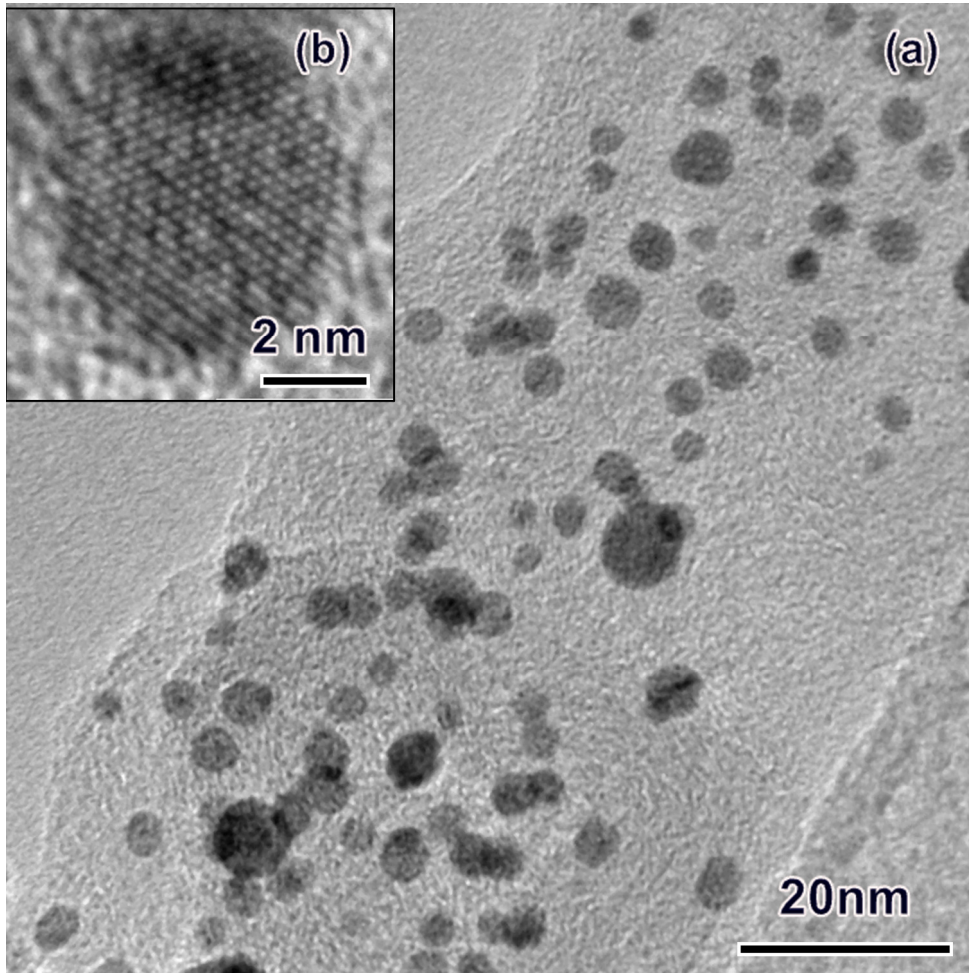
Figure 3.11: (a) TEM images for PtCo/C after 480 cycles. Inset (b), HRTEM of typical particle aligned to [111] FCC zone axis
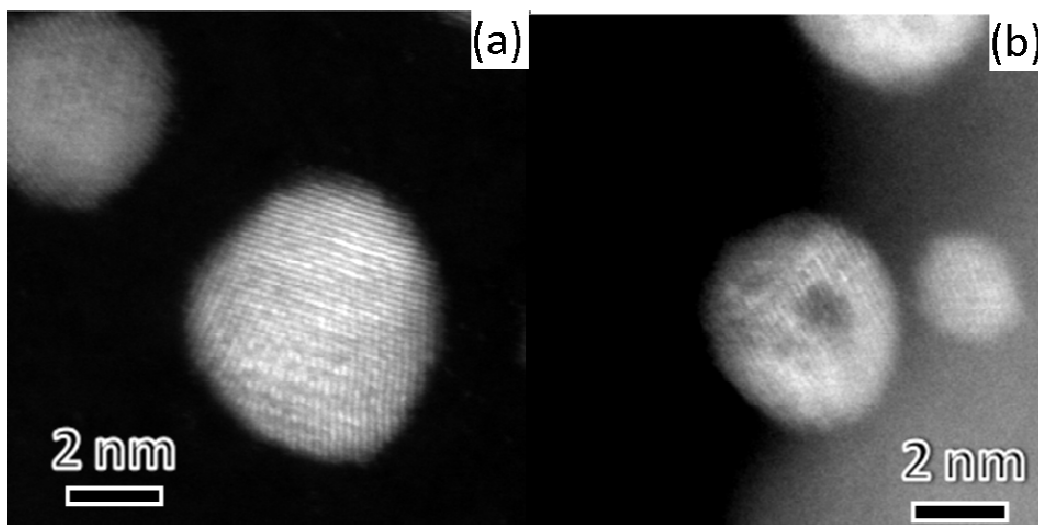
Figure 3.12: Typical high resolution aberration-corrected HAADF STEM images of (a) Pt/C after 480 cycles and (b) PtCo/C after 480 cycles. Note the significant intensity difference across the PtC catalyst particle.
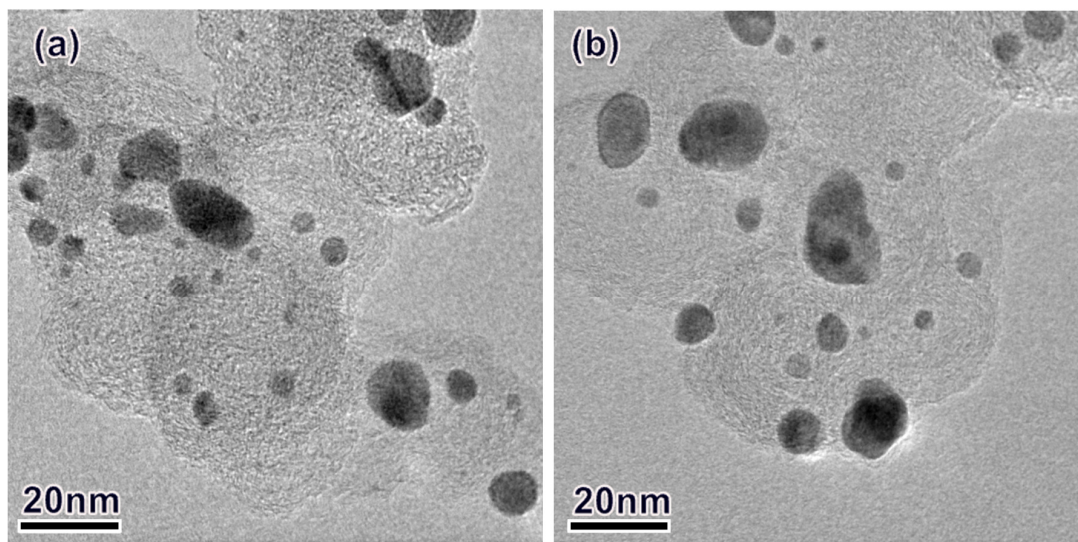
Figure 3.13: TEM images of (a) Pt/C and (b) PtCo/C catalysts samples after 2400 cycles
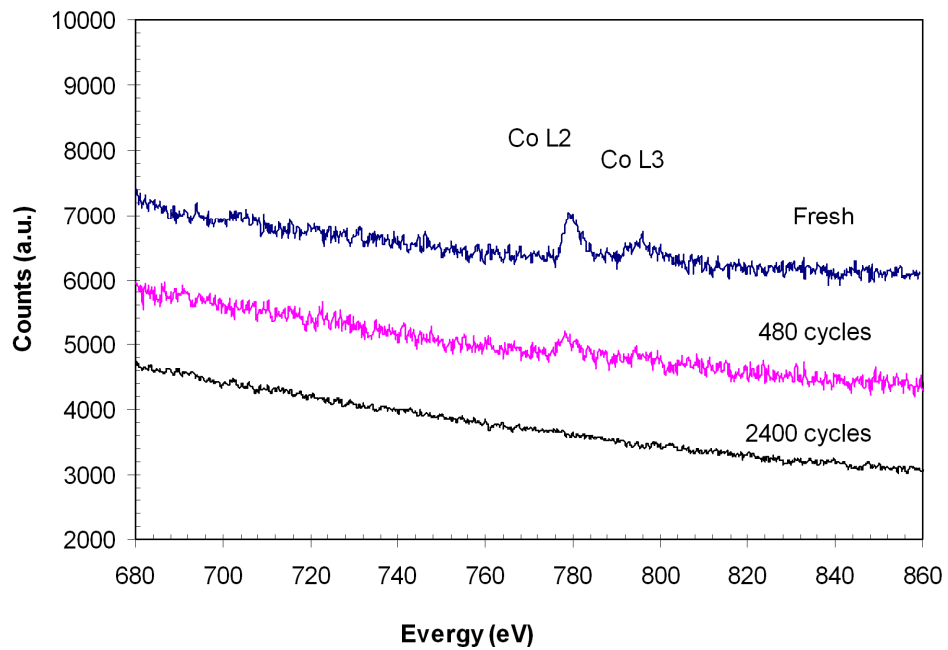
Figure 3.14: Normalized spectra showing the Co L$_{2,3}$ region of the electron energy loss spectra. These spectra indicate the loss of Co with electrochemical cycling.
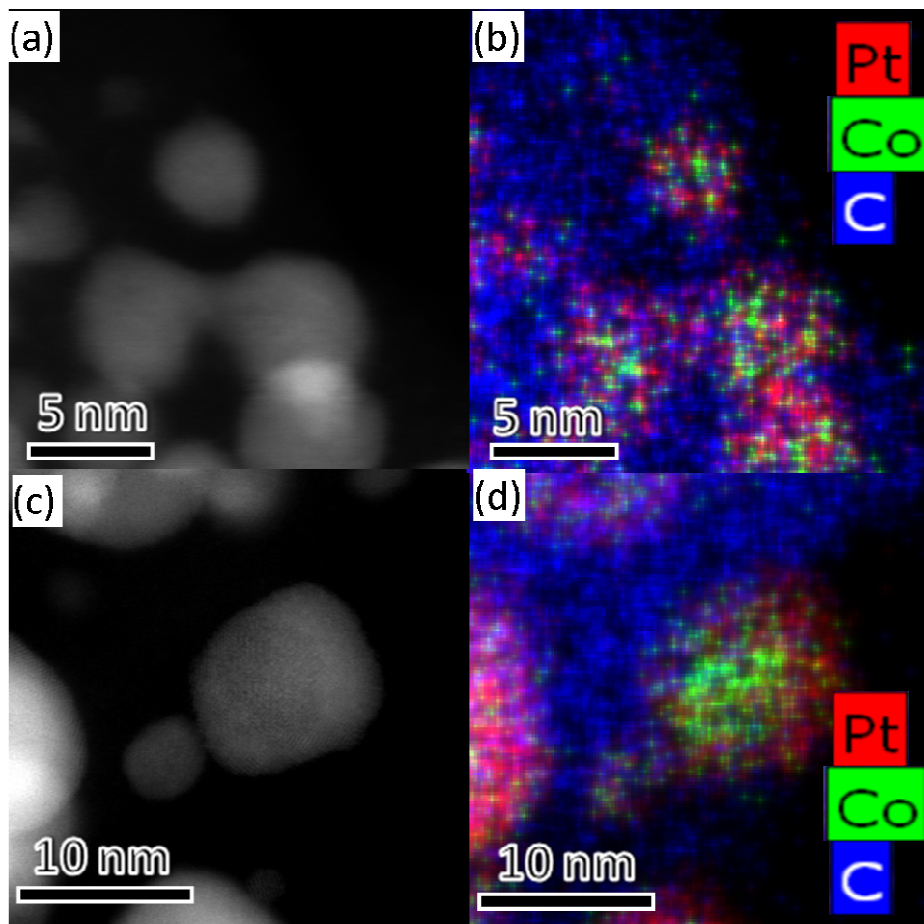
Figure 3.15: (a) DF image and (b) Pt and Co map of the fresh PtCo/C catalyst (c) DF image and (d) Pt and Co map of the PtCo/C catalyst after 480 cycles. The figure (d) clearly shows a Co rich 'core' surrounded by a Pt rich shell.
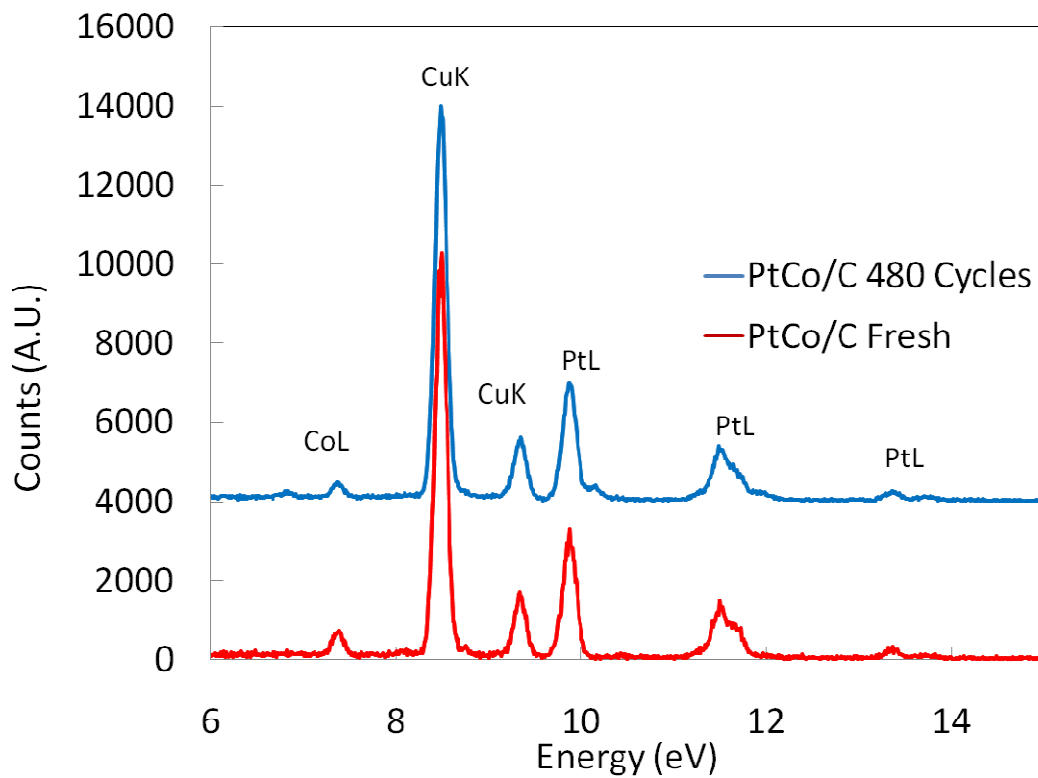
Figure 3.16: EDS sum spectra for fresh and cycled PtCo/C catalysts showing a significant loss of Co with electrochemical cycling.
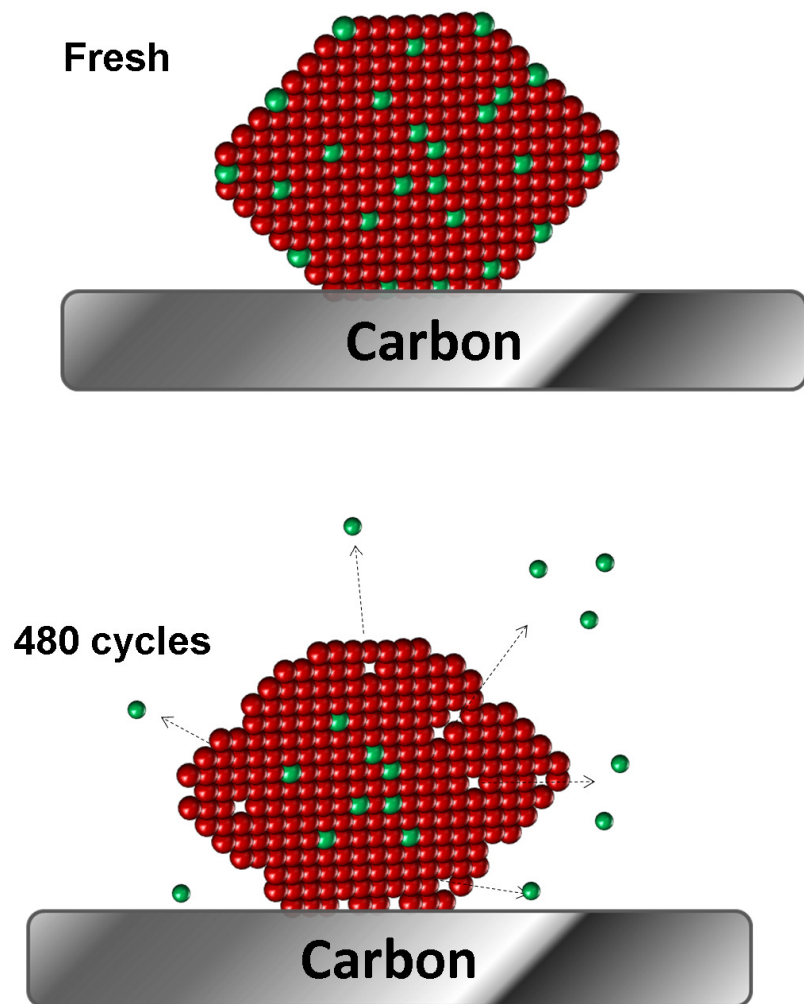
Figure 3.17: Model for selective dissolution showing the gradual loss of Co with voltage cycling.
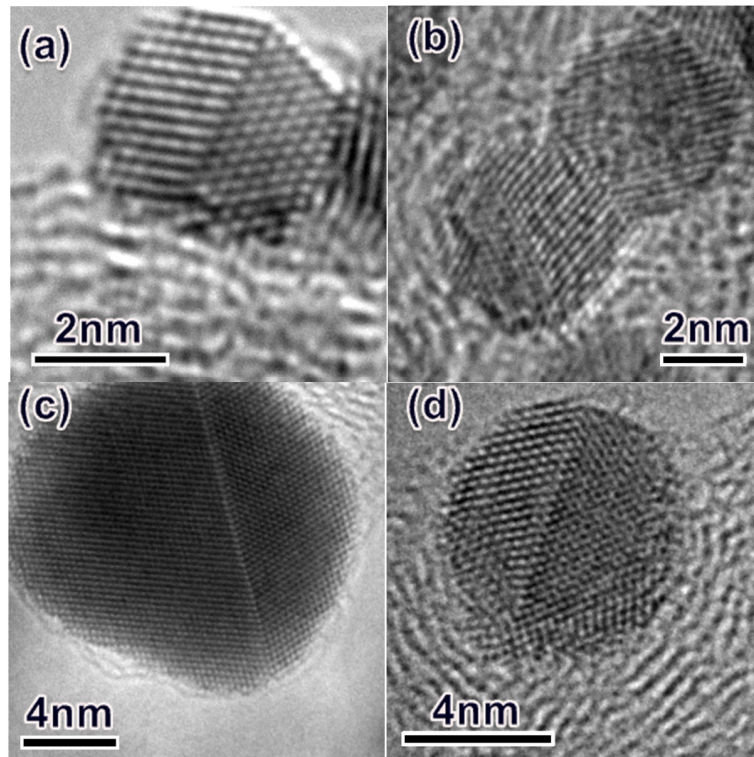
Figure 3.18: HRTEM images showing grain boundaries in (a) fresh Pt/C, (b) fresh PtCo/C, (c) Pt/C after 2400 cycles and (d) PtCo/ C after 2400 cycles.
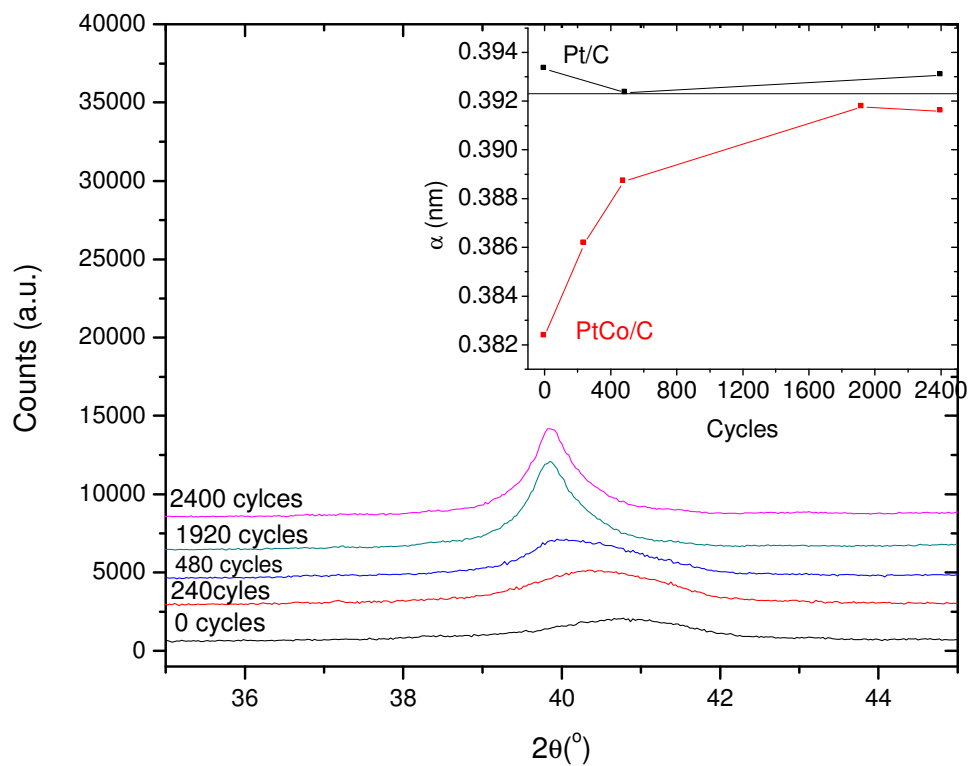
Figure 3.19: XRD results showing details of the fcc 111 peak for the PtCo/C catalyst sample. The inset shows that the PtCo lattice parameter approaches the value for bulk Pt (0.3923 nm) with cycling, while the Pt/C lattice constant does not change with cycling.
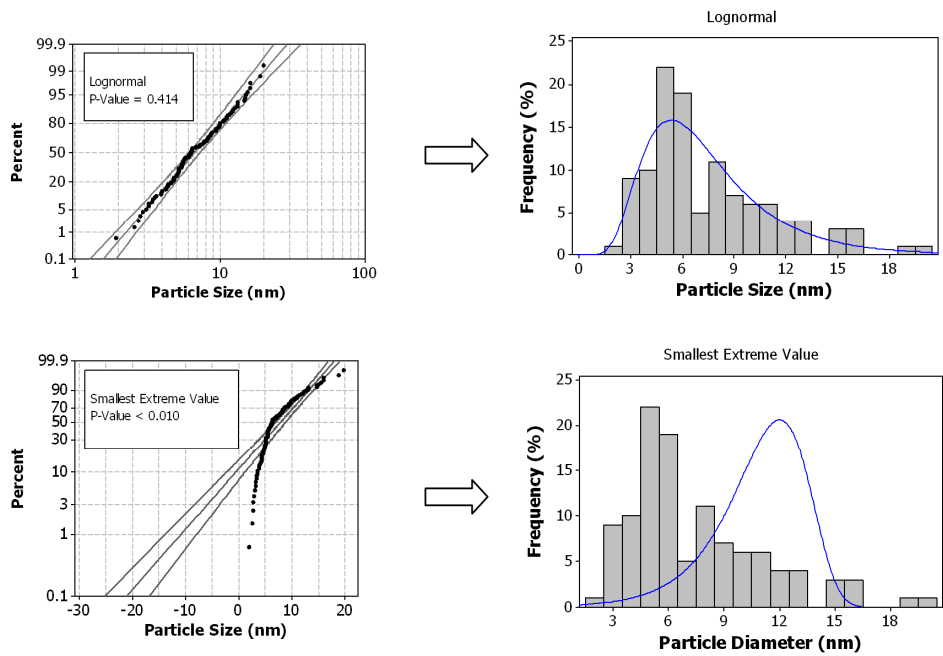
Figure 3.20: (top) Lognormal and (bottom) smallest extreme value probability plots for PtCo/C after 2400cycles. Because the lognormal plot has the highest p-value (p = 0.414 > 0.05), it was selected as the best fit distribution for the observed measurements.
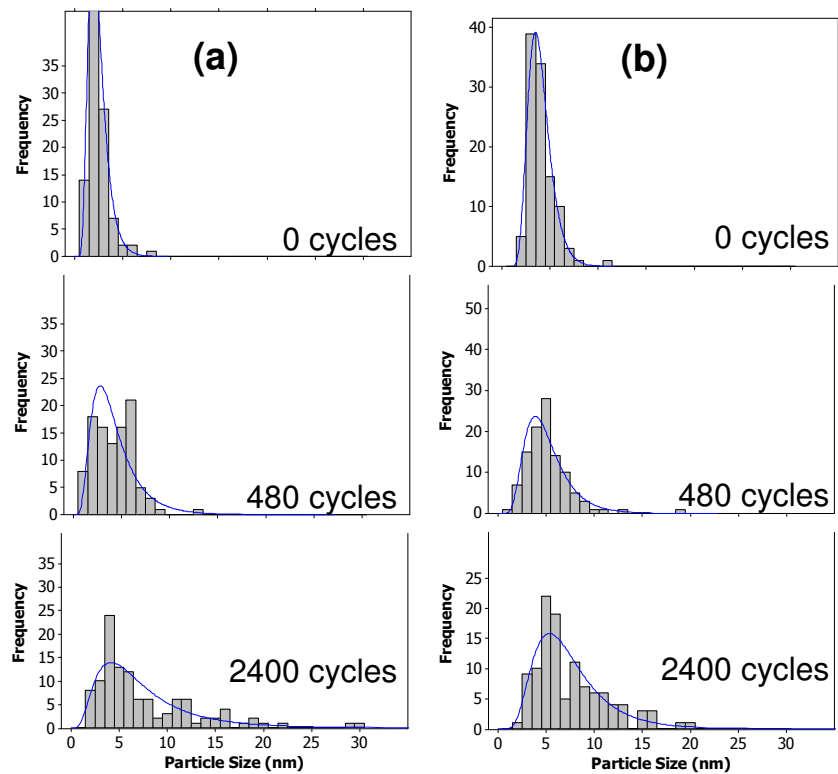
Figure 3.21: Measured particle size distributions for (a) Pt/C and (b) PtCo/C catalysts fitted to the lognormal distribution function.

3.8 References

1.   C. Jaffray and G. Hards, "Precious metal supply requirements." in *Handbook of Fuel Cells: Fundamentals, Technology, and Applications*, W. Vielstich, A. Lamm, and H.A. Gasteiger, Editors., Wiley. p. 509 (2003).

2.   R.J. Spiegel, "Platinum and fuel cells." *Transportation Research Part D-Transport and Environment*. **9**(5): p. 357-371 (2004).

3.   H.A. Gasteiger, S.S. Kocha, B. Sompalli, and F.T. Wagner, "Activity benchmarks and requirements for Pt, Pt-alloy, and non-Pt oxygen reduction catalysts for PEMFCs." *Appl. Catal., B*. **56**(1-2): p. 9-35 (2005).

4.   P. Yu, M. Pemberton, and P. Plasse, "PtCo/C cathode catalyst for improved durability in PEMFCs." *J. Power Sources*. **144**(1): p. 11-20 (2005).

5.   A. Bonakdarpour, J. Wenzel, D.A. Stevens, S. Sheng, T.L. Monchesky, R. Lobel, R.T. Atanasoski, A.K. Schmoeckel, G.D. Vernstrom, M.K. Debe, and J.R. Dahn, "Studies of transition metal dissolution from combinatorially sputtered, nanostructured $Pt_{1-x}M_x$ (M = Fe, Ni; $0 < x < 1$) electrocatalysts for PEM fuel cells." *J. Electrochem. Soc.* **152**(1): p. A61-A72 (2005).

6.   A. Seo, J. Lee, K. Han, and H. Kim, "Performance and stability of Pt-based ternary alloy catalysts for PEMFC." *Electrochim. Acta*. **52**(4): p. 1603-1611 (2006).

7.   D.A. Stevens, J.M. Rouleau, R.E. Mar, A. Bonakdarpour, R.T. Atanasoski, A.K. Schmoeckel, M.K. Debe, and J.R. Dahn, "Characterization and PEMFC testing of $Pt_{1-x}M_x$ (M=Ru,Mo,Co,Ta,Au,Sn) anode electrocatalyst composition spreads." *J. Electrochem. Soc.* **154**(6): p. B566-B576 (2007).

8.   N. Travitsky, T. Ripenbein, D. Golodnitsky, Y. Rosenberg, L. Burshtein, and E. Peled, "Pt-, PtNi- and PtCo-supported catalysts for oxygen reduction in PEM fuel cells." *J. Power Sources*. **161**(2): p. 782-789 (2006).

9.   J.S. Cooper, "Combinatorial Screening of Fuel Cell Catalysts". The University of Notre Dame,Ph.D. Thesis (2007).

10.   D. Thompsett, "Pt Alloys as oxygen reduction catalysts." in *Handbook of Fuel Cells- Fundamentals, Technology and Applications*, H.A. Gasteiger and A. Lamm, Editors., John Wiley and Sons. p. 467-480 (2003).

11. T. Tada, "High dispersion catalysts including novel carbon supports." in *Handbook of Fuel Cells- Fundamentals, Technology and Applications*, H.A. Gasteiger and A. Lamm, Editors., 481-488 (2003).

12. V.A. Grinberg, T.L. Kulova, N.A. Maiorova, Z.V. Dobrokhotova, A.A. Pasynskii, A.M. Skundin, and O.A. Khazova, "Nanostructured catalysts for cathodes of oxygen-hydrogen fuel cells." *Russ. J. Electrochem.* **43**(1): p. 75-84 (2007).

13. S.C. Ball, S.L. Hudson, D. Thompsett, and B. Theobald, "An investigation into factors affecting the stability of carbons and carbon supported platinum and platinum/cobalt alloy catalysts during 1.2 V potentiostatic hold regimes at a range of temperatures." *J. Power Sources*. **171**(1): p. 18-25 (2007).

14. T.J. Schmidt and H.A. Gasteiger, "Rotation thin-film method for supported catalysts." in *Handbook of Fuel Cells- Fundamentals, Technology and Applications*, H.A. Gasteiger and A. Lamm, Editors., John Wiley and Sons. p. 317-333 (2003).

15. S. Mukerjee and S. Srinivasan, "O2 reduction and structure-related parameters for supported catalysts." in *Handbook of Fuel Cells- Fundamentals, Technology and Applications*, H.A. Gasteiger and A. Lamm, Editors., John Wiley and Sons. p. 502-519 (2003).

16. T.R. Ralph and M.P. Hogarth, "Catalysis for Low Temperature Fuel Cells. Part II: The Anode Challenges." *Platinum Met. Rev.* **46**(3): p. 117-135 (2002).

17. A.J. Appleby and F.R. Foulkes, *Fuel Cell Handbook*. New York: Van Nostrand Reinhold. (1989).

18. C.H. Paik, G.S. Saloka, and G.W. Graham, "Influence of cyclic operation on PEM fuel cell catalyst stability." *Electrochemical and Solid State Letters*. **10**(2): p. B39-B42 (2007).

19. Y. Shao, G. Yin, and Y. Gao, "Understanding and approaches for the durability issues of Pt-based catalysts for PEM fuel cell." *J. Power Sources*. **171**(2): p. 558-566 (2007).

20. C.J. Maggiore, "The Nuclear Microprobe - Investigating Surfaces with Ions." *Los Alamos Science*. **2**(2): p. 26-46 (1982).

21. X. Wang, R. Kumar, and D.J. Myers, "Effect of Voltage on Platinum Dissolution Relevance to Polymer Electrolyte Fuel Cells." *Electrochem. Solid-State Lett.* **9**(5): p. A225-A227 (2006).

22. J.P. Meyers and R.M. Darling, "Model of carbon corrosion in PEM fuel cells." *J. Electrochem. Soc.* **153**(8): p. A1432-A1442 (2006).

23. K. Yasuda, A. Taniguchi, T. Akita, T. Ioroi, and Z. Siroma, "Characteristics of a platinum black catalysts layer with regard to platinum dissolution phenomena in a membrane electrode assembly." *J. Electrochem. Soc.* **153**(8): p. A1599-A1603 (2006).

24. R.L. Borup, J.R. Davey, F.H. Garzon, D.L. Wood, and M.A. Inbody, "PEM fuel cell electrocatalyst durability measurements." *J. Power Sources*. **163**(1): p. 76-81 (2006).

25. C.H. Bartholomew, "Mechanisms of catalyst deactivation." *Applied Catalysis A: General*. **212**: p. 17-60 (2001).

26. E. Antolini, J.R.C. Salgado, and E.R. Gonzalez, "The stability of Pt-M (M = first row transition metal) alloy catalysts and its effect on the activity in low temperature fuel cells: A literature review and tests on a Pt-Co catalyst." *J. Power Sources*. **160**(2): p. 957-968 (2006).

27. D.A. Stevens and J.R. Dahn, "Electrochemical characterization of the active surface in carbon-supported platinum electrocatalysts for PEM fuel cells." *J. Electrochem. Soc.* **150**(6): p. A770-A775 (2003).

28. D.A. Blom, S.A. Bradley, W. Sinkler, and L.F. Allard, "Observation of Pt Atoms, Clusters and Rafts on Oxide Supports, by Sub Ångström Z-Contrast Imaging in an Aberration-Corrected STEM/TEM." *Microsc. Microanal.* **12**((Supp 2)): p. 50-51 (2006).

29. L.F. Allard, D.A. Blom, M.A. O'Keefe, and S. Mishina, "Design and Performance Characteristics of the ORNL Advanced Microscopy Laboratory and JEOL 2200FS-AC Aberration-Corrected STEM/TEM." *Microsc. Microanal.* **11**(SupplementS02): p. 2136-2137 (2005).

30. D.A. Blom, L.F. Allard, S. Mishina, and M.A. O'Keefe, "Early results from an aberration-corrected JEOL 2200FS STEM/TEM at Oak Ridge National Laboratory." *Microsc. Microanal.* **12**(6): p. 483-491 (2006).

31. L. Allard and S. Rozeveld, "Performance of a Silicon-Drift Detector in 200kV TEM Environments." *Microsc. Microanal.* **15**(SupplementS2): p. 228-229 (2009).

32. J. Friel and C. Lyman, "Tutorial Review: X-ray Mapping in Electron-Beam Instruments." *Microsc. Microanal.* **12**(01): p. 2-25 (2006).

33. H.E. Swanson and E. Tatge, *Standard x-ray diffraction powder patterns* Washington, D. C. : U. S. Government Printing Office. (1953).

34. H. Berg and J. Cohen, "Long-range order and ordering kinetics in CoPt3." *Metallurgical and Materials Transactions B*. **3**(7): p. 1797-1805 (1972).

35.   D. Schebarchov and S.C. Hendy, "Thermal instability of decahedral structures in platinum nanoparticles." *The European Physical Journal D - Atomic, Molecular, Optical and Plasma Physics*. **43**(1): p. 11-14 (2007).

36.   C. Solliard and M. Flueli, "Surface stress and size effect on the lattice parameter in small particles of gold and platinum." *Surf. Sci.* **156**(PART 1): p. 487-494 (1985).

37.   J. Kazemi, *Personal Communication* (2006).

38.   S. Chen, W.C. Sheng, N. Yabuuchi, P.J. Ferreira, L.F. Allard, and Y. Shao-Horn, "Origin of Oxygen Reduction Reaction Activity on "Pt3Co" Nanoparticles: Atomically Resolved Chemical Compositions and Structures." *Journal of Physical Chemistry C*. **113**(3): p. 1109-1125 (2009).

39.   M. Watanabe, K. Tsurumi, T. Mizukami, T. Nakamura, and P. Stonehart, "Activity and Stability of Ordered and Disordered Co-Pt Alloys for Phosphoric-Acid Fuel-Cells." *J. Electrochem. Soc.* **141**(10): p. 2659-2668 (1994).

40.   T.P. Moffat, J.J. Mallett, and S.-M. Hwang, "Oxygen Reduction Kinetics on Electrodeposited Pt, Pt[sub 100 - x]Ni[sub x], and Pt[sub 100 - x]Co[sub x]." *J. Electrochem. Soc.* **156**(2): p. B238-B251 (2009).

41.   A.S. Darling, "Cobalt-Platinum Alloys." *Platinum Met. Rev.* **7**(3): p. 96-104 (1963).

42.   P. Scherrer, *Göttinger Nachrichten; Math. Phys.*: p. 98 (1918).

43.   A.L. Patterson, "The Scherrer formula for x-ray particle size determination." *Physical Review*. **56**(10): p. 978-982 (1939).

44.   J.A. Bett, K. Kinoshita, and P. Stonehart, "Crystallite growth of platinum dispersed on graphitized carbon black." *J. Catal.* **35**(2): p. 307-316 (1974).

45.   C.G. Granqvist and R.A. Buhrman, "Size distributions for supported metal catalysts : Coalescence growth versus ostwald ripening." *J. Catal.* **42**(3): p. 477-479 (1976).

46.   P. Ascarelli, V. Contini, and R. Giorgi, "Formation process of nanocrystalline materials from x-ray diffraction profile analysis: Application to platinum catalysts." *J. Appl. Phys.* **91**(7): p. 4556-4561 (2002).

47.   A.K. Datye, Q. Xu, K.C. Kharas, and J.M. McCarty, "Particle size distributions in heterogeneous catalysts: What do they tell us about the sintering mechanism?" *Catal. Today*. **111**(1-2): p. 59-67 (2006).

48.   C. He, S. Desai, G. Brown, and S. Bollepalli, "PEM fuel cell catalysts: Cost, performance, and durability." *Electrochem. Soc. Interface*. **14**(3): p. 41-44 (2005).

49.   J.T. Mcginn, V.A. Greenhut, and T. Thomas, "A mechanism for fault formation in fine particles and implications for theories of annealing twins in f.c.c. metals--II." *Acta Metall.* **30**(12): p. 2103-2110 (1982).

50.   P.J.F. Harris, "The sintering of platinum particles in an alumina-supported catalyst: Further transmission electron microscopy studies." *J. Catal.* **97**(2): p. 527-542 (1986).

51.   L.C. Gontard, R.E. Dunin-Borkowski, M.H. Gass, A.L. Bleloch, and D. Ozkaya, "Three-dimensional shapes and structures of lamellar-twinned fcc nanoparticles using ADF STEM." *J Electron Microsc (Tokyo).* **58**(3): p. 167-174 (2009).

52.   H.R. Colón-Mercado, H. Kim, and B.N. Popov, "Durability study of Pt_3Ni_1 catalysts as cathode in PEM fuel cells." *Electrochem. Commun.* **6**(8): p. 795-799 (2004).

Chapter 4

Investigation of Alumina Supported Pt and Pt-Pd Alloy NO Oxidation Catalysts with Advanced Electron Microscopy

4.1 Introduction

Lean-burn gasoline and diesel engines provide significant increase in fuel economy over conventional gasoline engines for transportation applications, but the catalytic after-treatment of exhaust, notably NO_x and soot, presents unique challenges. Accordingly, after-treatment technology has been extended beyond three-way catalysts to include NO_x storage and release (NSR) catalysts, diesel particulate filters and selective catalytic reduction catalysts. As is often the case, however, improved durability and lower precious metal loading remain important goals for further improvement.

Oxidation of NO plays a prominent role in the catalytic after-treatment of exhaust gas from lean-combustion vehicles. It is a critical step in the overall reaction that leads to NO storage in the NO_x-storage/reduction (NSR) catalyst.[1] Pt is one of the best NO oxidation catalysts, but previous studies have shown it quickly tends to lose surface area through particle coarsening at high temperatures.[2] This effect is especially apparent under excess-oxygen (lean burn) conditions.[3] Although the mechanisms are not understood, alloying Pt with other metals is known to inhibit such particle growth. Several years ago, for example, Chen and Schmidt found that alloying Pt with Pd suppressed particle growth (and/or volatile loss of Pt) on a planar SiO_2 support that was

110

heated in air.[4] However, multimetallic alloy catalysts, may have different catalytic properties than their constituents.[5] Additionally, few systematic studies of alloying on the dispersion stability of supported catalysts have been performed.[6] Further, the effect of Pd alloying on NO oxidation activity of alumina supported Pt has not been determined over a wide range of dispersions

4.2 Previous Work: Effect of alloy composition on dispersion stability and catalytic activity for NO oxidation over alumina-supported Pt–Pd catalysts

In an effort to address some of these issues, several compositions of Pt-Pd bimetallic nano-particulate alumina supported catalysts were investigated.[7] Four of the five samples spanned the Pt-rich half of the composition range, while the final sample consisted of pure Pd. All five compositions of Pt-Pd catalysts on Al_2O_3 were prepared from Pt- and Pd-(acetylacetonate)$_2$ precursors (Figure 4.1) according to the method documented by Wang.[8] The composition of the precious metal component of each Pd-Pt catalyst is summarized in Table 4.1. After drying at 70°C under vacuum, catalysts were calcined at 300°C in 5% O_2 in N_2 and reduced in 1% H_2 in N_2 at 300°C.

Catalyst samples were investigated in the following three conditions:

1.) the as calcined or 'fresh' condition (no additional thermal aging)

2.) after aging at 500°C,

3.) after aging at 900°C.

Aging took place in a quartz-tube furnace under a flowing (5 l/min) gas mixture of 5% O_2 and 10% H_2O in N_2 for 3 hours. Subsequently, the samples were also reduced for 1 h at 500°C under a flow of 1% H_2 in N_2.

Catalyst particles were prepared for TEM observation by dispersing a small amount of powder onto a 300 mesh carbon-coated copper TEM grid obtained from Structure Probe, Inc. To avoid excessive contamination during TEM or STEM imaging, no hydrocarbon solvent was used as a dispersing agent. Electron microscopy analysis was performed on a JEOL 3011 high resolution microscope located at The University of Michigan Electron Microbeam Analysis Laboratory (EMAL) and discussed in greater detail in section 3.3.

Typical HRTEM mages of particles from the Pt-100-Pd-0 (pure Platinum) samples (a) before aging, (b) aged at 500°C, and (c) aged at 900°C are presented in Figure 4.2. The particle size distributions for catalysts grown at 500ºC and 900ºC are shown in Figures 4.3 and 4.4 respectively. As shown by these particle size distributions in Figures 4.3 and 4.4, large particles (greater than 100nm) formed at 900°C in the pure Pt sample are absent in samples containing Pd. An image of one of these large Pt particles is shown in Figure 4.5. Statistics derived from the measurements (at least 100 particles per sample) that produced these distributions are summarized in Table 4.2. No particles exceeding 5nm in size were observed in samples of any composition in the fresh samples.

In this earlier study, alloying Pt with Pd in alumina-supported catalysts for NO oxidation was found to produce the expected effect of suppression of particle coarsening upon aging under lean conditions. Variations with Pd content clearly became more significant as aging temperature increased. These TEM measurements generally agreed with XRD conclusions (Table 4.3) that Pd alloying suppressed Pt particle growth with

aging.   Furthermore, the turn-over frequency for NO oxidation was found to be relatively insensitive to a Pd content approaching 50 mol % (as shown in Figure 4.7).

4.3 Objective

Although the previous study[7], summarized above, demonstrated that substitution of Pd for up to 50 mol% of the Pt reduced particle growth during lean aging with little or no impact on the NO oxidation turn-over frequency, it left two primary areas for further investigation. First, we were not able to clearly characterize these Pt and Pd catalysts from AcAc precursors in the as calcined or "fresh" state using HRTEM. Also, we were not able to directly confirm the composition of individual metal particles of either fresh or slightly aged bimetallic catalysts.   A second area of further investigation is contrasting these earlier results to those obtained from a new set of Pt and Pt-Pd bimetallic catalysts prepared from nitrate precursors (Figure 4.8) and produced via incipient wetness, a widely used, commercially advantageous method for large scale production of heterogeneous catalysts.[9]

Therefore, this study focuses on an extension of the previous study of alumina-supported Pt and Pt-Pd bimetallic catalysts, making use of advanced electron microscopy techniques that allow investigation of both particle size and composition in the fresh state as well as the changes induced by lean aging. This study will particularly highlight results obtained using emerging transmission electron microscopy (TEM) techniques such as aberration corrected electron microscopy (ACEM), along with more established techniques such as high angle annular dark field (HAADF) imaging, energy dispersive spectroscopy (EDS) and conventional TEM imaging.

4.4 Experimental Details

4.4.1 Catalysts Preparation and Aging

Two catalyst compositions, both having a nominal precious metal loading equivalent (in molar terms) of approximately 1 wt% Pt, were used for this study. The first contained only Pt (labeled Pt100-Pd0), and the second was a 50 mol% combination of Pt and Pd (labeled Pt50-Pd50). Catalysts of both compositions were synthesized using two different methods. The first set, (labeled Ac-Ac) was a subset of the catalyst in the previous study [13] (described in detail in section 4.2) prepared from adsorption from mixtures of solutions of platinum(II) and palladium(II) bis-acetylacetonates in toluene at at 70 °C onto a high–surface-area alumina (W. R. Grace, MI-307). After drying at 70 °C under vacuum, these catalysts were calcined at 300 °C in 5% O_2 in N_2 and reduced in 1% H_2 in N_2 at 300 °C.

The second set of catalysts (labeled Nitrate) was prepared by impregnating the same high-surface-area alumina with mixtures of aqueous Pt- and Pd-nitrate solutions to incipient wetness. After impregnation, the support/solution mixtures were homogenized, dried, and calcined at 300 °C in air for 1h. The actual metal loadings for both sets of catalysts used in this study are summarized in Table 4.4 .

Aliquots of each fresh catalyst were aged in a quartz-tube furnace under a flowing (5 l/min) gas mixture of 5% O_2 and 10% H_2O in N_2 at both 500°C and 900°C for 3 h (heating and cooling occurred under pure N_2). Additionally, the two nitrate specimens were aged at approximately 690°C (see Appendix 1). The scope of this study is shown

114

schematically in Figure 4.6. Before examination, all samples were reduced for 1 h at 500°C under flowing 1% H_2 in N_2

4.4.2 Microcopy Characterization

Particle size, morphology, and composition were characterized using TEM. Samples were prepared for TEM examination by ultrasonicating a small amount of powder in ethanol and dispersing it on a 300 mesh carbon-coated copper grid. Because of the reported difficulty in direct imaging of small (diameter < 2 nm) metal particles using conventional electron microscopy[7, 10], an aberration-corrected STEM/TEM instrument was used to obtain structural information for catalysts in the fresh state. This instrument, a JEOL 2200FS, fitted with a hexapole aberration corrector (CEOS GmbH) for the probe-forming optics, is capable of sub-100 pm spatial resolution in STEM mode. Further details of the instrument, which is located in the Advanced Microscopy Laboratory (AML) at Oak Ridge National Laboratory, and is available through the High Temperature Materials Laboratory's (HTML) National User program, can be found in earlier reports.[11-12]

HAADF imaging was also performed on a Hitachi HF3300, operated at 300 kV with STEM resolution 0.2 nm. The HF-3300, which is also located at the HTML, was equipped with an integrated Thermo-Noran EDX analyzer for compositional analysis. The Cliff-Lormier integration method (without absorbance –Equation 4.1) was used to quantify the compositional results.[13]

$$\frac{C_{Pt}}{C_{Pd}} = k_{Pt-Pd} \frac{I_{Pt}}{I_{Pd}} \quad \text{and} \quad C_{Pt} + C_{Pd} = 1 \qquad\qquad \text{Equation 4.1}$$

Where: C_{Pt} = weight percent Pt

C_{Pd} = weight percent Pd

I_{Pt} = intensity of Pt peak

I_{Pd} = intensity of Pd peak

k_{a+b} = Cliff-Lorimer sensitivity factor (dependant on particular TEM/EDS system and voltage [14])

Quantitative particle size analysis for aged catalysts was performed on the JEOL 3011 located in EMAL at The University of Michigan. Histograms were created for each catalyst sample from TEM observation of approximately 100 particles. A surface weighted mean diameter, d_s (Equation 4.2), was subsequently obtained from these distributions.

$$d_s = \frac{\sum nd^3}{\sum nd^2} \qquad\qquad \text{Equation 4.2}$$

Where: d = measured particle diameter

d_s = surface weighted mean diameter

Previously reported electron microscopy results and Monte-Carlo simulations indicate that such particles typically have a cubo-octohedral shape.[15-19] Assuming a spherical or cubo-octohedral particle shape, dispersion, D, can be calculated from the surface weighted mean diameter using the following expression (Equation 4.3):

$$D = 6 \frac{M}{N_A \rho a d_s}$$
<div align="right">Equation 4.3</div>

Where: d = measured diameter

M = atomic mass

N_A = Avogadro's number

ρ = mass density of the particle

a = surface area occupied by an atom on the particle surface

Following the procedure of Morfin and others, equal proportions of the (111), (100), and (110) planes on the particle surface were assumed[16], and thus the surface area occupied by an atom on the particle surface is 0.0807 nm^2 for Pt [15] and 0.079 nm^2 for Pd.[20] For bimetallic catalysts, this parameter was derived from the atomic proportions of the constituent metal atoms.

4.4.3 X-Ray Characterization

X-ray diffraction (XRD) data from the nitrate catalysts were collected in a Scintag X2 diffractometer equipped with a Si(Li) solid state detector using Cu Kα radiation and configured in Bragg-Bretano focusing geometry. Diffraction data were obtained over the range 10 – 90° (2θ) in steps of 0.03°. XRD samples were prepared by packing powder into a shallow cavity etched into a glass plate. Peaks in the background-subtracted scan were profile-fit using a Pearson 7 function[21] to characterize the breadth and position of the precious-metal peaks. Crystallite sizes were estimated from the corrected XRD peak

breadths using a Scherrer analysis of the (311) peak of the face-centered cubic (fcc) lattice (located near 81.2° for Pt), assuming spherical particles.

Because both platinum and palladium crystallize in a fcc lattice and are isostructural, the effect of alloying on the XRD peaks will be manifested only by changes in the observed lattice parameter and the relative peak intensities. For the aged catalyst samples, the lattice parameter for the fcc phase was estimated from the positions of the (111), (200) and (311) peaks. In the case of the Pt50-Pd50 catalyst, poor peak intensities only allowed fitting of the (311) peak.

4.4.4 NO Oxidation Activity Measurements

NO oxidation measurements were performed on the Nitrate catalysts using a 10-channel flow reactor manufactured by Altamira Instruments that has been described previously.[22] Experimental conditions were matched to those previously described for the Ac-Ac catalysts.[7, 22] Briefly, reactor tubes were loaded with 50 mg of catalyst sample, fixed between quartz wool plugs, and steady state measurements were performed at a series of temperatures from 75 to 325°C, following a 90 min equilibration at each temperature. The feed gas composition was a mixture of 500ppm NO and 8% O_2 in N_2 at a flow rate of 60 sccm in each channel (space velocity = 20,000 h^{-1}).

4.5 Results

4.5.1 Microscopy Results –AcAc Catalysts

4.5.1.1 ACEM Imaging of Fresh AcAc Catalysts

Aberration-corrected electron microscopy (ACEM) was used to determine the particle size and morphology of fresh Ac-Ac catalysts. Typical HAADF images of the Pt50-Pd50 sample are shown in Figure 4.9 In HAADF imaging, image contrast results primarily from differences in the atomic mass, and thus in these images, the brightest particles are the precious metals, the less bright regions are the γ-Al_2O_3 support, and the darkest areas are carbon coated copper grids or vacuum.

Typical HAADF and bright field (BF) STEM images for the Pt100-Pd0 and the Pt50-Pd50 samples are shown in Figure 4.10. In the Pt100-Pd0 HAADF image (Figure 4.10a), one large (d~4nm) particle and several smaller Pt clusters are visible. In the corresponding BF image (Figure 4.10b), only the large Pt particle is clearly evident. For the Pt50-Pd50 sample, small clusters of metal are visible in HAADF (Figure 4.10c) images but not in BF imaging (Figure 4.10d).

A notable feature of the Pt50-Pd50 samples is the appearance of regions where the precious metal is very highly dispersed, either as single atoms or clusters of atoms. The visibility of these sub-nanometer features, shown in (Figures 4.10a and 4.10c), demonstrates the importance of aberration corrected HAADF imaging, as these features cannot be resolved in conventional HRTEM. Previous studies of supported precious-metal catalysts using the JEOL 2200FS ACEM have identified single atoms [23], as well as atomic "rafts" - 2d clusters that do not display coherent crystallinity.[11, 24] That these

smaller clusters do not appear in BF imaging provides further evidence of their lack of crystalline nature. Intensity profile plots across bright features in these clusters signify the presence of single atoms. In the HAADF STEM image shown in Figure 4.11, the dimensions of the features, as defined by the FWHM's of the intensity profiles measured across them, are comparable to reference values of single atomic diameters.[25] This supports the conclusion that these features are single precious metal atoms on the Al_2O_3 support. It should be noted that atomically dispersed Pt atoms are not as prevalent in the Pt100-Pd0 sample, although 2d "rafts" were visible in HAADF STEM imaging (Figure 4.10a).

HAADF STEM imaging may also provide an indication of the chemical composition of these atomically dispersed species. For the feature indicated as "A" in Figure 4.11, the difference in intensity between the feature and the alumina support is approximately $50x10^4$, while for the brighter feature (indicated as "B"), this difference is approximately $30x10^4$. These numbers generally follow the expected trend, i.e., that contrast varies with $Z^{1.5-2}$ in HAADF imaging[26-27], assuming that this difference in contrast (relative to the Al_2O_3 support) is an indication that both Pt and Pd atoms are atomically dispersed in this catalyst.

ACEM imaging was used to produce particle size distributions, as shown in Figure 4.12. The shapes of the distributions are quite similar, but the Pt100-Pd0 extends to slightly larger particle sizes. The mean metal particle size for the Pt100-Pd0 and the Pt50-Pd50 catalysts are 1.27 nm and 1.03 nm, respectively. Although this difference is small, statistical analysis indicates that the observed difference in the means of the two samples is unlikely to arise from random variation (P value = 0.00856).

ACEM imaging was also used to measure the fresh pure Pd (Pt0-Pd100) catalysts. Because of the lower atomic mass of Pd relative to Pt (46 vs 78), HAADF imaging provided less contrast between the Pd and alumina.   Both HAADF and BF images of the Pt0-Pd100 catalyst is shown in Figure 4.13.

4.5.1.2 Imaging of Aged Ac-Ac Catalysts

Particle size distributions for the aged Ac-Ac catalysts were collected using a JEOL 3011 HRTEM. The histograms for the aged catalysts were originally presented in the previous study[7] and in Figure 4.3. The results for the Pt100-Pd0 and the Pt50-Pd50 after aging at 500ºC and 900ºC are summarized in Figure 4.14 (note the break in the vertical axis, particle size). For both compositions, particle growth clearly occurs with aging, but as suggested previously, on the basis of XRD results, alloying with Pd inhibits the growth of anomalously large particles (ALPs), which are most apparent in the 900ºC aged Pt100-Pd0 sample.   In the 900ºC aged Pt100-Pd0 sample the largest observed particle was 501 nm, however in the Pt50-Pd50 sample, the largest observed particle was only 63.8 nm.

4.5.1.3 Compositional Analysis of Ac-Ac Catalysts

STEM imaging with EDS analysis was performed on individual particles from Pt50-Pd50 samples in the fresh condition and after both aging treatments. For the fresh catalysts, instability under electron beam exposure prevented us from obtaining quantitative EDS. This beam instability is illustrated in Figure 4.15 (a-b). However,

quantitative EDS over a large area (shown in Figure 4.15c) gave a composition close to the nominal value (41 ± 19 at% Pd and 59 ±17 at% Pt).

The compositions of individual particles for the two aging conditions are compared in Figure 4.16. Catalyst particles tend to be Pt-rich after 500ºC aging (unfilled triangles in Figure 4.16c), but after aging at 900ºC (unfilled squares in Figure 4.16c), the composition of the catalyst particles converge to the nominal composition. It can be seen from this plot that both particle growth and alloying occur simultaneously during aging.

To assess the compositional homogeneity of particles after aging at 900°C, EDS line scans were obtained for many particles. A 50 point EDS line scan (Figure 4.17) across a typical particle shows relatively equal Pt L and Pd L signals, demonstrating a homogenous mixture of Pt and Pd across the particle. Previous experimental[6, 28] and theoretical[29-30] reports have suggested that a core-shell segregation of Pt and Pd can occur under certain conditions, but we see no convincing evidence of such structure in these catalysts.

4.5.2 Microscopy Results - Nitrate Catalysts

4.5.2.1 ACEM Imaging of Fresh Nitrate Catalysts

Typical ACEM BF and HAADF STEM images of fresh Pt100-Pd0 and Pt50-Pd50 catalysts made from nitrate precursors are shown in Figure 4.18. Several small Pt clusters are visible in the HAADF image of the Pt100-Pd0 catalyst (Figure 4.18a) which are not apparent in the corresponding BF image (Figure 4.18b). For the Pt50-Pd50 sample, one large (d ≈ 8.5 nm) metallic particle with clear lattice fringes is visible in both

HAADF (Figure 4.18c) and BF (Figure 4.18d) imaging. This particle is surrounded by smaller clusters that are visible in HAADF (Figure 4.18c) but not in BF imaging. The fast Fourier transform (FFT) of the BF image from the large particle (inset of the Figure 4.18d), indicates a plane spacing of 0.225nm, in agreement with the expected spacing of the Pd [111] planes.[31] The atomically dispersed metal particles seen in the Pt50-Pd50 Ac-Ac sample, described in section 4.5.1.1 are conspicuously absent in samples made from nitrate precursors.

As was the case for samples of Ac-Ac catalysts, aberration corrected microscopy was used to obtain the distribution of particle sizes. Histograms comparing the particle size distributions for both compositions are shown in Figure 4.19. The distributions obtained from Ac-Ac catalysts (Figure 4.3) are overlaid for comparison. The most significant difference among all the samples is that the Pt50-Pd50 Nitrate catalyst has a notably larger mean particle size, due to the presence of a significant number of much larger particles.

4.5.2.2 Imaging of Aged Nitrate Catalysts

Histograms of particle size measurements from TEM observation for Pt100-Pd0 and Pt50-Pd50 are given in Figure 4.20a and 4.20b respectively. These results, along with results from aged Ac-Ac catalysts (Figure 4.14) for comparison, are further summarized in Figure 4.21. Regardless of the aging temperature, the Pt100-Pd0 Ac-Ac catalysts have a larger mean particle size than the corresponding Nitrate catalysts (Table 4.5), possibly arising from small differences in particle size distributions of the fresh catalysts (Figure 4.19a and Table 4.5). In the case of the Pt50-Pd50 composition,

the presence of a significant number of very large particles in the fresh Nitrate catalyst is likely responsible for the larger (relative to the Ac-Ac catalyst) mean particle sizes after aging, especially at 500°C. After aging at 900°C, the Pt50-Pd50 catalysts had a smaller mean particle size than the Pt100-Pd0 catalysts for both precursors, primarily due to the absence of anomalously large particles (ALPs) of Pt (particles with d>100 nm, as indicated in Figure 4.21).

For Pt100-Pd0 catalysts from both precursors, 900°C aging resulted in large, highly-faceted particles, some of which were clearly not spherical. Regardless of precursor used, the addition of Pd appeared to suppress the growth of these particles, as illustrated by the images obtained from the 900°C aged Nitrate catalysts shown in Figure 4.22.

Surface-weighted mean-diameters and dispersions were calculated according to Equations 4.2 and above and are presented in Table 4.5 with other statistics obtained from the TEM measurements. As expected, the dispersion (Figure 4.23) generally follows an inverse relationship to mean particle size. For all samples, dispersion decreased with aging due to particle growth, though bimetallic catalyst particles grew less than pure Pt catalyst particles resulting in a somewhat less severe decrease in dispersion. The unexpected relative dispersions of the Pt100-Pd0 and Pt50-Pd50 Nitrate catalysts after 500°C aging are likely a consequence of the unusually wide particle size distribution measured for the fresh Pt50-Pd50 catalyst (Figure 4.19b), the nature of which is described in Section 4.5.2.3 below.

In the third set of aged catalysts (those aged at approximately 690°C), a unique core-shell structure (shown in Figure 4.24) was observed. Although this structure cannot

be considered typical, it was observed in both conventional HAADF and aberration corrected HAADF imaging.   Although high resolution EDS was not available at the time of these observations, differences in contrast indicate that a Pt rich shell surrounding a Pd rich core.

4.5.2.3 Compositional Analysis of Nitrate Catalysts

STEM imaging with EDS analysis was also performed on individual particles in catalysts made from the nitrate precursor. For the fresh Pt50-Pd50 sample, the average particle composition was 42% Pd. However, the Pd was distributed bi-modally (Figure 4.25), with small (d<3 nm) particles biased to Pt-rich and larger particles (in the 4-11 nm size range) biased to Pd-rich.

The compositions of individual particles in Pt50-Pd50 Nitrate catalysts after aging are compared in Figure 4.26. While aging at 500ºC (Figure 4.26, filled triangles) induced particle growth, the distribution retained most of the bimodal nature evident in the fresh state. After aging at 900°C (filled squares), the compositions of the particles were much more tightly distributed around the nominal alloy composition. The effect of the difference in initial state between the Pt50-Pd50 Nitrate and Ac-Ac catalysts on subsequent changes in particle size and composition induced by aging (Figure 4.27) is clearest in the 500°C sample. Thus, while particle growth and alloying again appear to occur simultaneously in the Pt50-Pd50 Nitrate catalyst, the apparent influence of Pd on particle growth at 500°C is lower than in the corresponding Ac-Ac catalyst.

To assess the compositional homogeneity of individual catalysts particles from nitrate precursors, a 20 point EDS line scan was performed across a 900ºC aged Pt50-

Pd50 (nitrate) sample. In this scan, the dwell time per point was 10 seconds, and is presented in Figure 4.28. Like similar analysis for AcAc catalysts (Figure 4.17), this particle shows Pd composition of approximately the nominal composition across the particle.

4.5.3 XRD Results

XRD data for the Nitrate catalysts was collected to further investigate crystallite size and lattice parameter. Examples of the XRD data are shown in Figure 4.29, comparing the untreated alumina substrate, the Pt100 nitrate catalyst after aging at 500°C and the Pt100 nitrate catalyst after aging at 900°C. A comparison of the crystallite sizes for each aged Nitrate catalyst is shown in Figure 4.30a. Clearly, the Pt100-Pd0 catalyst experiences much more metal particle growth at 900°C than the Pt50-Pd50 catalyst. Additionally, the Pt100-Pd0 crystallites appear to be significantly larger than the Pt50-Pd50 crystallites after aging at only 500°C, a result that is not consistent with the TEM finding (Table 2).

A comparison of the lattice parameters obtained by fitting the peak positions was also performed, and is shown in Figure 4.30b. As expected, the aged Pt100-Pd0 catalysts have lattice parameters that closely correspond to the value expected for bulk Pt (α_{Pt}=3.92 Å[31]) while the aged Pt50-Pd50 catalysts both yield lattice parameters very close to the average value for a 50:50 alloy of Pt and Pd. In the case of the catalyst aged at 900°C, this is in agreement with previous findings that Pt-Pd alloys deviate only slightly from Vegard's Law.[32] In the case of the catalyst aged at 500°C, however, it could reflect an averaging over particles of varying composition, ranging from Pt-rich to Pd-rich, as

revealed in the EDS compositional analysis (Figure 4.26c). The inconsistency in crystallite size noted above could thus be a consequence of inhomogeneous broadening.

4.5.4 CO Chemisorption and NO Oxidation Activity Measurements

NO oxidation activity data, measured under lean conditions, were collected for both Nitrate (this study) and Ac-Ac (previous study[7])catalysts in our multichannel flow reactor. The NO oxidation activity profiles (conversion as a function of temperature) for the Pt100-Pd0 and Pt50-Pd50 catalysts are shown in Figure 4.31. The general shape of these oxidation activity plots is dictated by the kinetic inhibition of the NO oxidation reaction at low temperatures and the thermodynamic equilibrium between NO and NO_2 at high temperatures. A more active NO oxidation catalyst will have a "light – off" up-slope of the activity curve shifted to lower temperatures [22]. For both precursors and metal compositions, we see that 500ºC aged catalysts are more active than those aged at 900ºC, which themselves are more active than the fresh catalysts.

NO Activity: 500ºC Aged > 900ºC Aged > Fresh

This ordering of activities is consistent with the known structure sensitivity of the NO oxidation reaction, where very small Pt particles have intrinsically low activities, and harshly aged catalysts suffer from low overall Pt surface area. For the purpose of comparing the activity of the catalysts, the conversion just above light-off (150 ºC) is plotted as a function of dispersion derived from the TEM particle-size (Table 4.5) in Figure 4.32.

4.6 Discussion

Application of advanced electron microscopy techniques, especially ACEM for imaging very small features and HAADF imaging coupled with EDS for compositional analysis of small particles, has provided new and useful information about the Pt and Pt-Pd catalysts prepared for our previous study of the effects of alloying on dispersion stability and performance of NO oxidation catalysts.[7] Our updated observations reveal subtle, but significant differences in the initial metal distributions that can reasonably be related to catalyst synthesis. Previous work has suggested a tendency for platinum(II) and palladium(II) bis-acetylacetonates dissolved in acetone to become associated into bimetallic complexes in solution [16, 33], leading to a high degree of Pt-Pd association in a freshly-prepared bimetallic catalyst. In our earlier study, we found a substantial difference in the efficiency of adsorption of the single-metal acetylacetonate precursors from solution onto the alumina support, Pt adsorption being much more limited than Pd. Assuming that the higher efficiency of Pd adsorption could be imparted, to some degree, to the bimetallic complex in solution, it is not surprising to find a somewhat higher dispersion in the case of the Pt50-Pd50 than the Pt100-Pd0 catalyst.

The presence of larger particles in the fresh Pt100-Pd0 Ac-Ac catalyst shown in Figure 4.12 is consistent with this expectation, but an even more significant piece of supporting evidence is the qualitative observation that more atomically-dispersed features (e.g., Figures 4.10c and 4.11) appear in the Pt50-Pd50 than the Pt100-Pd0 catalyst. ACEM observations made on fresh Pt0-Pd100 (i.e., pure Pd) Ac-Ac catalysts (Figure 4.13) also revealed the presence of more atomically-dispersed metal features than in the

corresponding Pt100-Pd0 catalyst, though poor contrast was a significant limitation in this case.

In this study, we were not able to confirm spectroscopically (via EDS) the presence of both Pt and Pd in individual metal particles in the fresh Pt50-Pd50 (Ac-Ac) catalyst. However, area-averaged results (Figure 4.15), suggest that much of the Pd in the fresh catalyst is more highly dispersed than Pt, and thus not in direct association with Pt. Indeed, the compositional measurement of metal particles after aging at 500ºC reveals that they are Pt-rich (Figure 4.16). The missing Pd is likely still in a highly dispersed and relatively immobile oxidized form.[7] Eventually, though, all of the Pd becomes incorporated into the initially Pt-rich particles after aging at 900ºC. As was demonstrated in the previous study, the degree to which addition of Pd inhibits particle growth increases with Pd concentration, but since the actual amount of Pd in the particles at intermediate stages of aging appears to be varying with exposure to lean conditions. Experiments aimed at probing the correlation between particle composition and size as a function of time at fixed aging temperatures are needed in order to sort out the precise dependence.

The mechanism (or mechanisms) by which particle growth inhibition occurs is (are) still unknown. Previous experimental[6, 28] and theoretical [29-30] reports have suggested that a core-shell segregation of Pt and Pd can occur under certain conditions. Our current EDS results, such as that shown in Figures 4.17 and 4.28, are not consistent with the suggestion that a thick surface layer of PdO (or Pd) simply protects Pt from direct exposure to O_2.

The newly-prepared set of Pt and Pt-Pd bimetallic catalysts, made with nitrate precursors, provide a number of interesting points of contrast with the Ac-Ac catalysts. Starting with the fresh catalysts, a large reversal in the relative dispersions of the two catalyst compositions was observed (Figure 4.23 and Table 4.5), due to the formation of fairly large (3-10 nm) Pd-rich particles (the compositions of which could readily be measured by EDS) in the Pt50-Pd50 catalyst. This circumstance, which may not be of fundamental significance, suggests that the change in both particle size and composition can be determined upon aging at 500ºC, as shown in Figure 4.26. As might be expected, both the Pd-rich and Pt-rich particles grow, and the composition range shrinks. A substantial number of large, Pd-rich particles, not found in the corresponding Ac-Ac catalyst, are present after aging at 500ºC, as shown in Figure 4.27. Nevertheless, after aging at 900ºC a fairly narrow range of particle compositions was observed, centered at the nominal value, just as in the case of the Pt50-Pd50 Ac-Ac catalyst.

Evolution of the Pt100-Pd0 nitrate catalyst was quite similar to that of the corresponding Ac-Ac catalyst, as expected in view of the similarity of their initial states. In neither case was there evidence for large particles in the fresh catalyst that could have seeded the growth of the ALPs. This suggests that the presence of ALPs in the aged catalysts is more a consequence of the growth mode than the initial particle size distribution. The presence of these particles is consistent with earlier studies that identified bi-pyramids, multiply-twinned particles, rods, and plate-like particles in alumina supported Pt catalysts after both laboratory and vehicle aging conditions[34-35].

Much effort has been devoted to using particle size distributions to identify particle growth mechanisms in the past[36]. In this study, particle size distributions after

aging at 900ºC closely fit the log normal distribution function, which suggests that the dominant sintering mechanism is particle migration and coalescence[36-37]. However, the presence of the highly faceted ALPs is not consistent with a migration and coalescence growth model. In an early report on the sintering of alumina-supported Pt, Harris *et al.*[35] found migration and coalescence was the dominant growth mode for short sintering times, while growth of ALPs at longer sintering times was mediated by inter-particle transport. Relative to the current study, the role of Pd in inhibiting Pt particle growth, primarily through the suppression of ALP formation, may thus be linked to its effect on inter-particle transport of Pt.

The NO oxidation performance of both sets of catalysts (Figure 4.31) are generally comparable and in reasonable agreement with expectation. It is worth noting that the fresh Pt100-Pd0 Nitrate catalyst, which has significantly higher activity than the corresponding Ac-Ac catalyst was calcined under a higher O_2 concentration, 20%, versus 5% in the case of the Ac-Ac catalyst. This may have stimulated the formation of somewhat larger Pt particles than appear to be present[3], according to the TEM measurements. In general, however, the dispersions calculated from TEM are within a factor of 2 of those measured by CO chemisorption in the case of the Ac-Ac catalysts[7], as shown in Table 4.5.

It is perhaps more significant that the activity of the Pt50-Pd50 Nitrate catalyst increased so dramatically between its fresh and 500ºC aged states, in spite of the fact that its dispersion was relatively low in the fresh state (14.3%) and did not change much (to 12.7%) upon aging, as shown in Figure 4.32. A likely explanation for the low initial activity is that the low dispersion in the fresh state is primarily due to the contribution of

large Pd-rich particles, for which the intrinsic NO oxidation activity is expected to be much lower than Pt-rich particles of comparable size[7, 38]. The dramatic increase in activity with aging would then simply be due to the increase in size of the Pt-rich particles. Considering the Pd concentration as a function of particle size (Figure 4.16), it is evident that there is a critical point (~ 2.5 nm) at which the particles transition from small and Pt-rich to large and Pd-rich. If one does not consider the Pd-rich particles, which are expected to have low intrinsic activity, the initial dispersion increases to 63.7%, and the trends in Figure 4.32 are more consistent.

There remains a question regarding the mechanism in which Pd alloying inhibits Pt particle growth without greatly effecting NO oxidation activity, especially given much lower rates of NO oxidation reported on supported Pd/Al_2O_3 catalysts vs Pt/Al_2O_3 catalysts over the optimal range of particle sizes observed in our study[38]. However, recently reported[39] first principles results of NO oxidation on metastable Pd surface oxide films (observed experimentally by Lundgren *et al.*[40]) have shown NO oxidation rates comparable to those reported for Pt, thus suggesting that surface PdO could have a similar characteristic in supported Pt-Pd particles typical of our study. As mentioned earlier, no strong evidence of a thick Pd or PdO shell protecting a Pt rich core was observed in this study. However, our characterization techniques would not have identified a monolayer type PdO surface film on the larger alloyed particles produced after 500ºC and 900ºC aging. Thus our present results do not contradict the possibility of an ultrathin metastable surface PdO film characterized by high NO oxidation activity.

The case of the 690ºC aged catalyst provides an interesting contrast to determine the particle growth mechanism. The Pd rich core surrounded by a Pt rich shell

(Figure 4.24) is consistent with the present observations on NO oxidation activity. As the shape of the measured particle size distributions largely fit the shape predicted by the particle migration and coalescence growth mechanism. We can propose that there are mechanisms in which more mobile Pt rich particles impinge on less mobile PdO particles upon heating. Before these particles fully coalesce, it is reasonable to posit that these particles result in a core shell structure (like the ones shown in Figure 4.24). In this mechanism (shown schematically in Figure 4.33), the lower mobility of the PdO on alumina subsequently slows further particle growth. This mechanism does not address the inhibition of growth of ALPs, but preliminary in-situ heating experiments (see section 6.2.2) indicate that the aging under 900ºC might have a different mechanism than aging at lower temperatures. Unfortunately, the details of this aging condition are not fully known and the aging temperature could only be estimated from fitting the XRD data to a previously presented exposure model (See Appendix A). Nevertheless, this model provides a reasonable explanation for the retardation of particle growth along with maintaining a high NO oxidation activity due to a Pt rich shell.

4.7 Conclusion

Application of advanced electron microscopy techniques to the characterization of alumina-supported Pt and Pt-Pd bimetallic catalysts has allowed us to refine our knowledge of the degree of alloying that exists at various stages of aging under lean conditions and thus better understand its relationship to particle coarsening. Although some direct association between Pt and Pd may be attained at the initial stage of bimetallic catalyst synthesis, there is clearly a strong tendency for alloying to proceed *in*

situ during the course of lean aging, and this certainly has a positive influence on limiting the growth of anomalously large particles typically found in pure Pt catalysts that have been harshly aged under lean conditions.

We have also again demonstrated that replacement of moderate amounts of Pt with Pd can be done with little or no loss of activity for NO oxidation. Further, standard catalyst precursors and synthesis methods have been shown to suffice. The use of Pd to both increase catalyst durability and decrease Pt loading in Pt-based catalysts for lean-burn engine exhaust-gas treatment thus appears even more favorable than before.

4.8 Tables and Figures

(a)   (b)
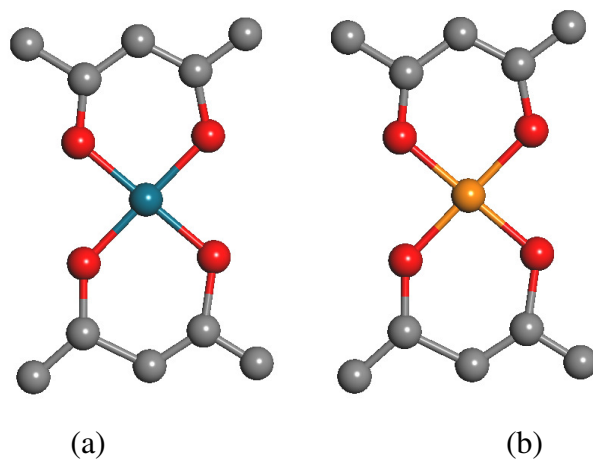
Figure 4.1: Molecular model of (a) Pd-(acetylacetonate)$_2$ and (b) Pt-(acetylacetonate)$_2$

Table 4.1: Catalysts composition for the catalysts from AcAc precursors.

Sample	Composition	% $\gamma - Al_2O_3$	Atomic Ratio
Pt-100-Pd-0	0.87wt%Pt	99.13	$Pt_{100}Pd_0$
Pt-90-Pd-10	0.75wt%Pt+0.063wt%Pd	99.19	$Pt_{87}Pd_{13}$
Pt-80-Pd-20	0.70wt%Pt+0.11wt%Pd	99.19	$Pt_{78}Pd_{22}$
Pt-50-Pd-50	0.58wt%Pt+0.28wt%Pd	99.14	$Pt_{53}Pd_{47}$
Pt-0-Pd-100	0.56wt%Pd	99.44	Pt_0Pd_{100}
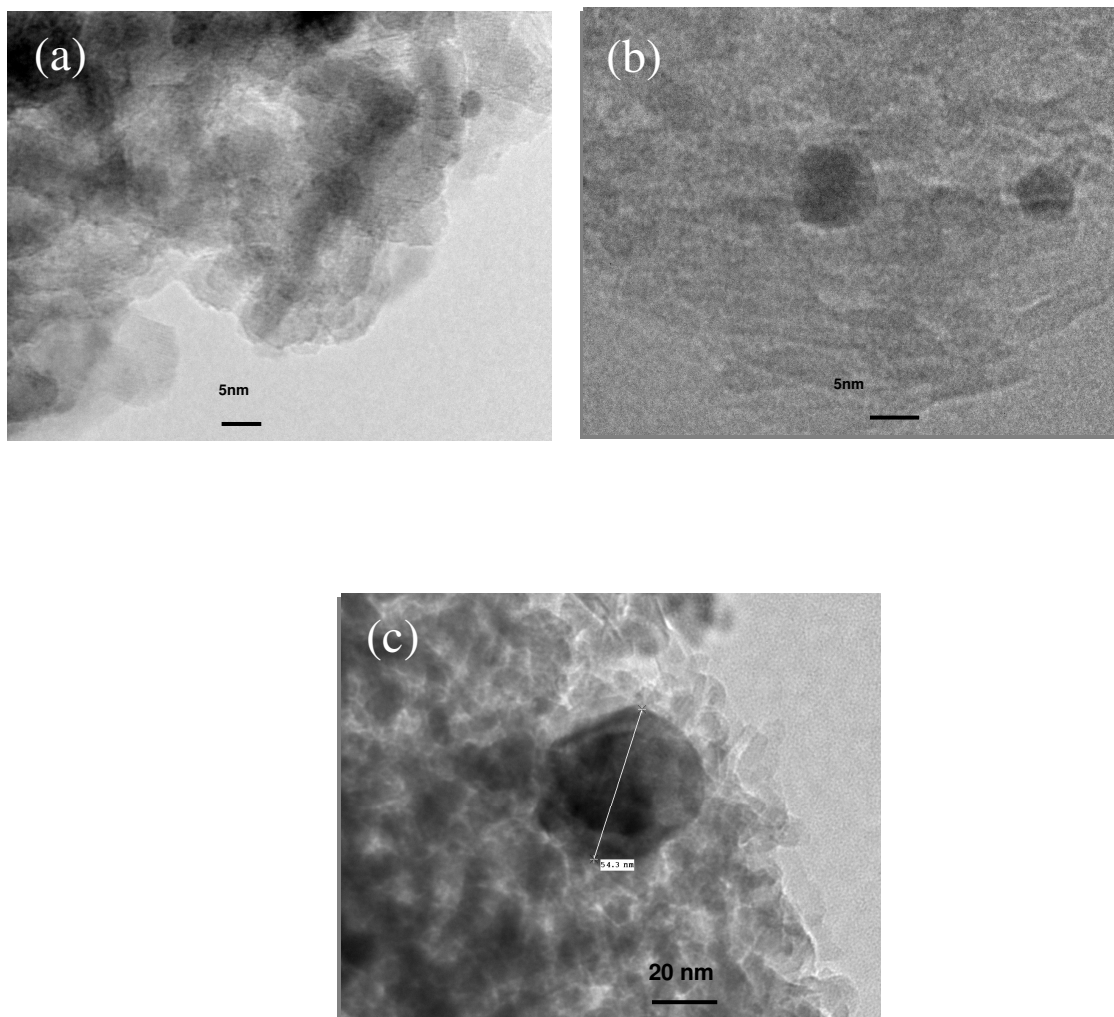
Figure 4.2: HRTEM images of particles from pure Pt90-Pd10 samples (a) before aging, (b) aged at 50 ℃, and (c) aged at 900℃.

Table 4.2: Particle-size-distribution statistics.

<u>500°C Aging</u>

Catalyst Name	N	Mean (nm)	Std. Dev.	Q1	Min	Med.	Max	Q3
Pt-100-Pd-0	109	9.04	3.01	6.95	2.80	8.96	19.40	10.90
Pt-90-Pd-10	104	7.69	1.98	6.25	3.44	7.70	12.40	8.86
Pt-80-Pd-20	112	4.71	1.43	3.76	1.31	4.79	8.75	5.60
Pt-50-Pd-50	101	4.90	1.26	3.98	2.61	4.74	8.57	5.52

<u>900°C Aging</u>

Catalyst Name	N	Mean (nm)	Std. Dev.	Q1	Min	Med.	Max	Q3
Pt-100-Pd-0	102	56.25	36.38	34.83	15.70	45.25	245.00	65.18
Pt-90-Pd-10	103	45.35	16.18	35.55	6.15	45.50	130.00	53.70
Pt-80-Pd-20	111	29.30	12.22	18.80	7.61	26.10	59.40	40.00
Pt-50-Pd-50	103	22.09	14.54	10.10	2.48	19.00	63.80	31.35
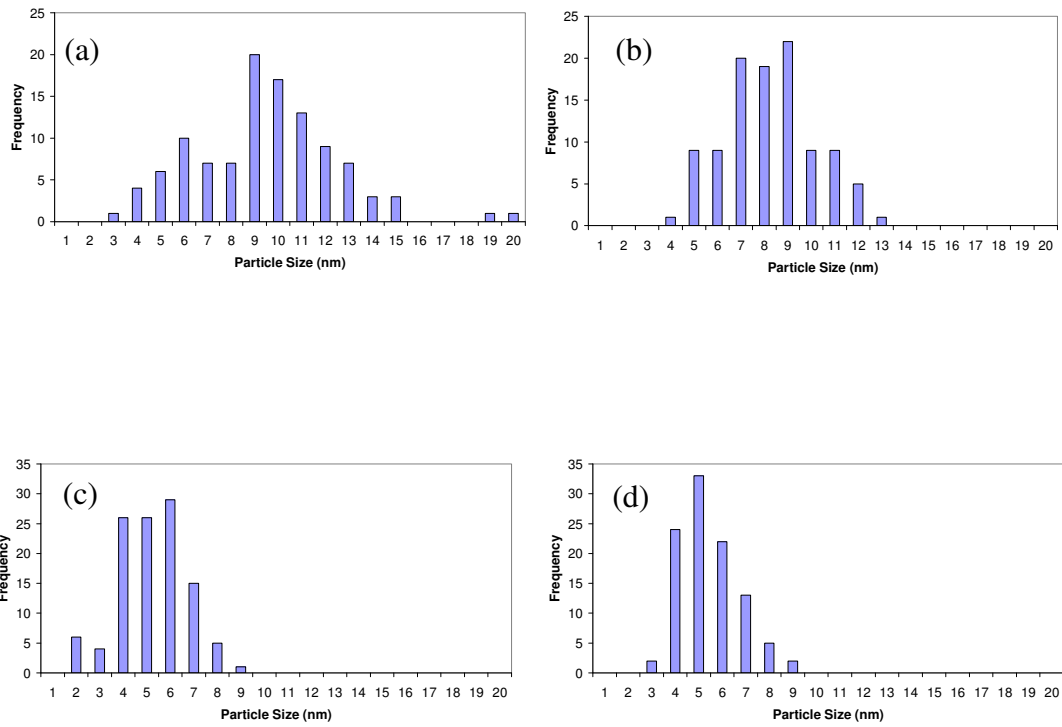
Figure 4.3: Particle size distributions of catalysts aged at 500°C, measured by TEM: (a) Pt-100-Pd-0, (b) Pt-90-Pd-10, (c) Pt-80-Pd-20, and (d) Pt-50-Pd-50.
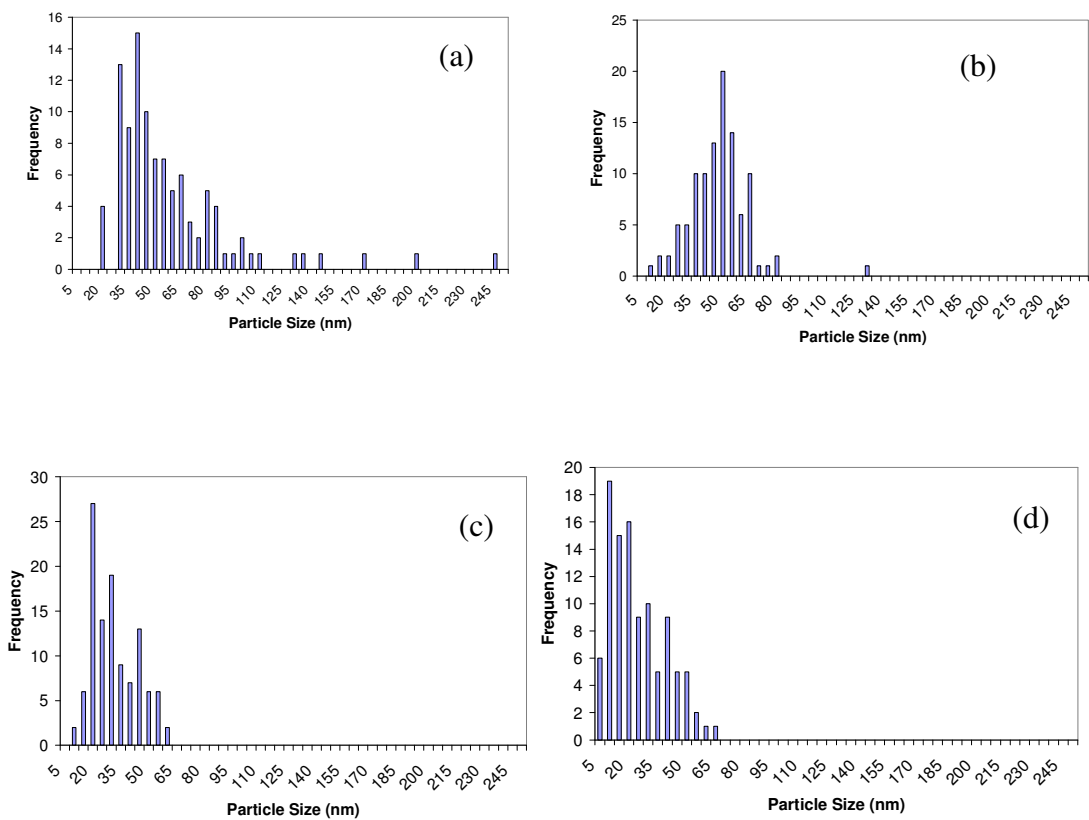
Figure 4.4: Particle size distributions of catalysts aged at 900°C, measured by TEM: (a) Pt-100-Pd-0, (b) Pt-90-Pd-10, (c) Pt-80-Pd-20, and (d) Pt-50-Pd-50.
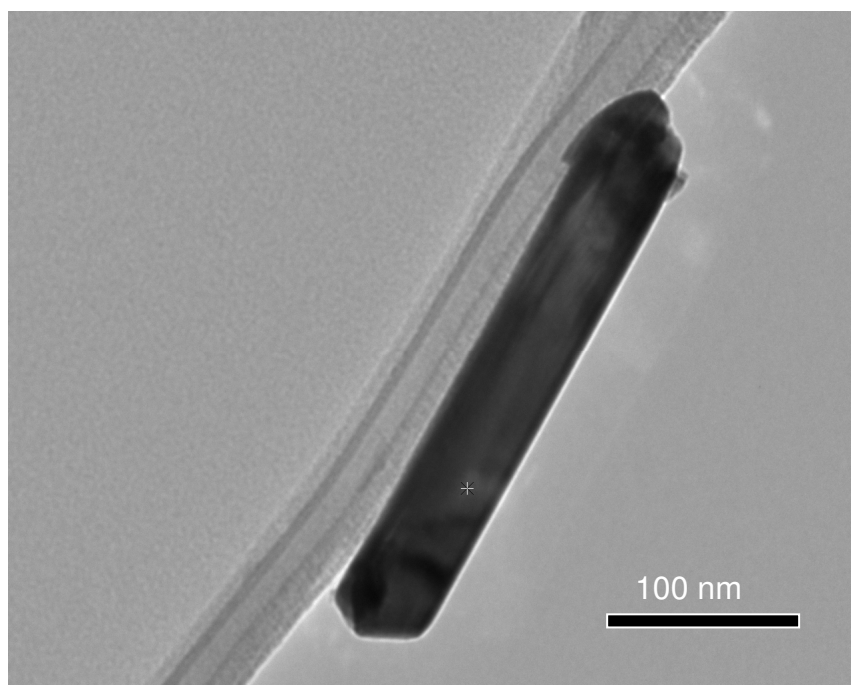
Figure 4.5: Large needle like particle seen in the Pt100-Pd0 (Ac-Ac) catalyst aged at 900ºC.
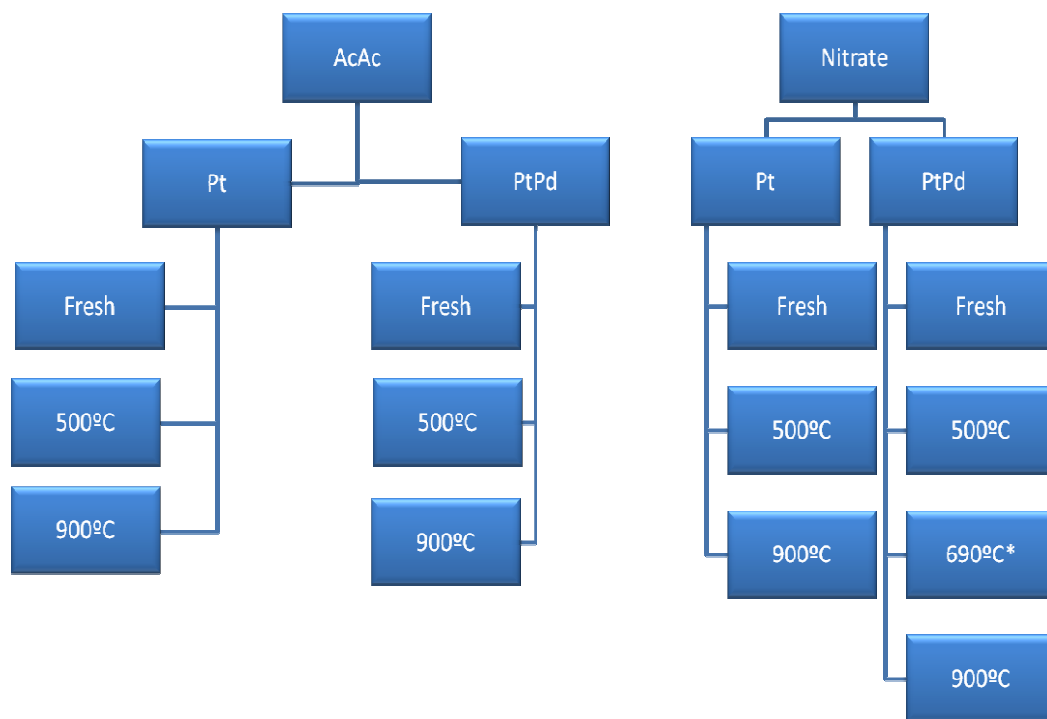
Figure 4.6: Schematic of the experimental matrix for this study

Table 4.3: Comparison of XRD parameters and TEM observation

Catalyst Name	Aging T (°C)	Position (°)	Intensity (cps)	$<d>_{XRD}$ (nm)	$<d>_{TEM}$ (nm)
Pt-100-Pd-0	900	81.18	108	43	56.25 ± 36.58
Pt-100-Pd-0	500	81.2	79	12	9.04 ± 3.01
Pt-90-Pd-10	900	81.32	99	28	45.35 ± 16.18
Pt-90-Pd-10	500	81.22	70	8	7.69 ± 1.98
Pt-80-Pd-20	900	81.42	100	28	29.3 ± 12.22
Pt-80-Pd-20	500	81.21	42	6	4.71 ± 1.43
Pt-50-Pd-50	900	81.66	88	28	22.09 ± 14.54
Pt-50-Pd-50	500	81.34	51	6	4.9 ± 1.26
50-50 mixture	900	81.63	79	27	n/a
50-50 mixture	500	81.22	44	11	n/a
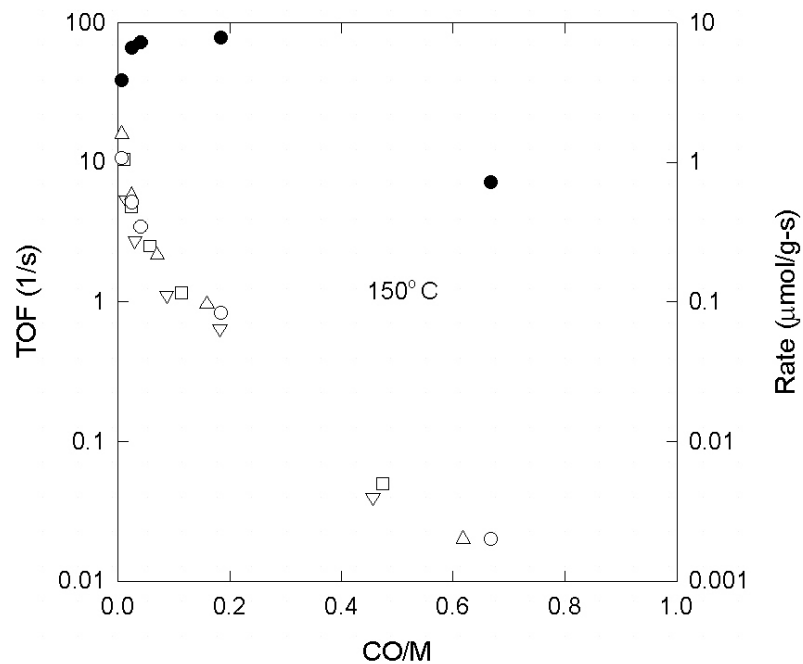
Figure 4.7: Rate of NO conversion (to NO_2) at 150ºC over Pt-100-Pd-0 as a function of CO/M (solid circles) and turn-over frequency (TOF) at 150ºC as a function of CO/M for Pt-100-Pd-0 (open circles), Pt-90-Pd-10 (open up triangles), Pt-80-Pd-20 (open squares), and Pt-50-Pd-50 (open down triangles), all derived using the kinetic expression described in [22]. [from Graham *et. al.*[7]].
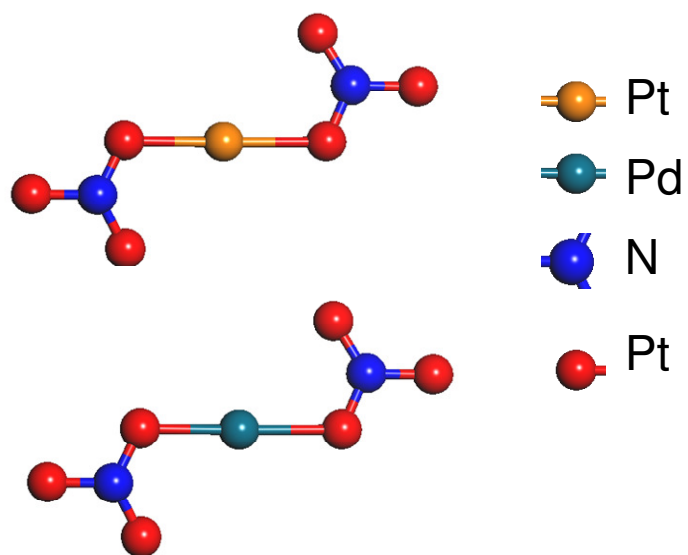
Figure 4.8: Model of nitrate precursors

Table 4.4: Catalyst designations and compositions

Catalyst Name	Composition (wt%)		Atom Fraction		Equivalent Pt (wt%)
	(Pt)	(Pd)	(Pt)	(Pd)	
Pt100-Pd0 Ac-Ac	0.87	0	100	0	0.87
Pt50-Pd50 Ac-Ac	0.58	0.28	53	47	1.09
Pt100-Pd0 Nitrate	0.87	0	100	0	0.87
Pt50-Pd50 Nitrate	0.58	0.28	53	47	1.09
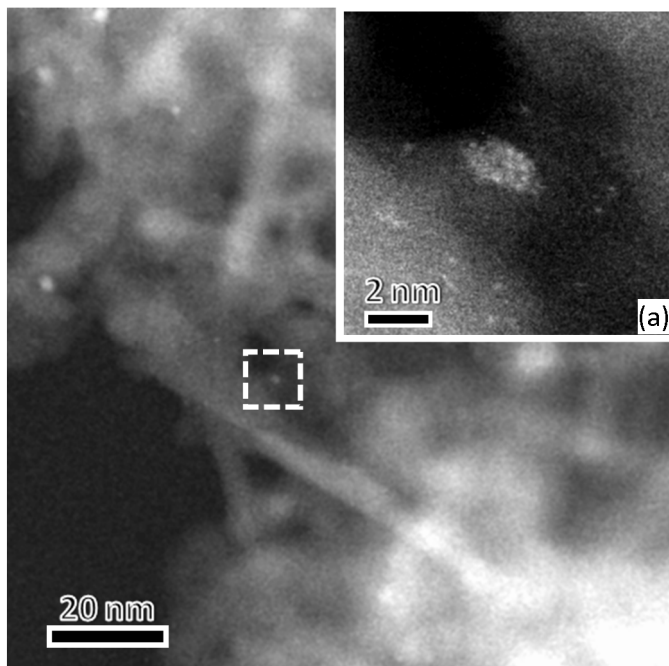
Figure 4.9: Representative ACEM HAADF image of the fresh Pt50-Pd50 Ac-Ac catalyst. Insert (a) is the highlighted region showing an approximately 2 nm metallic cluster surrounded by atomically dispersed metal.
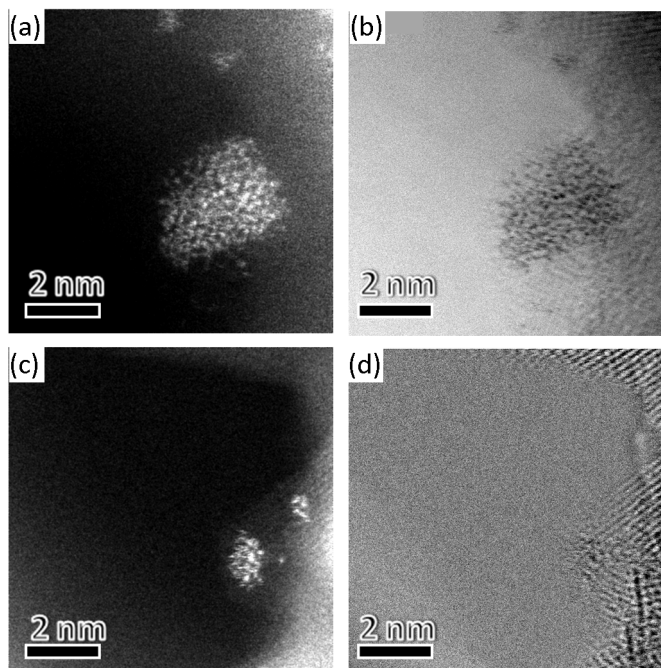
Figure 4.10: (a) HAADF and (b) BF STEM images of typical particles in the fresh Pt100- Pd0 Ac-Ac catalyst. (c) HAADF and (d) BF STEM images of typical particles in the fresh Pt50Pd50 Ac-Ac catalyst.
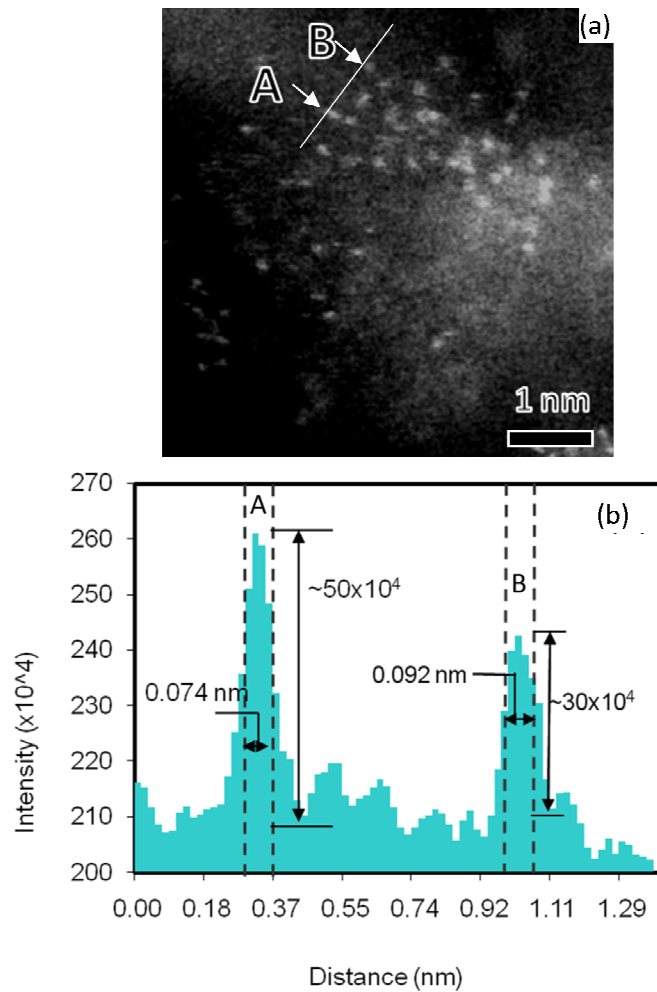
Figure 4.11: High resolution ACEM HAADF image of a cluster of atomically dispersed atoms in the fresh Pt50-Pd50 Ac-Ac catalyst. The breadths of the intensity line scans suggest that these particles are single atoms of **(A)** platinum and **(B)** palladium.
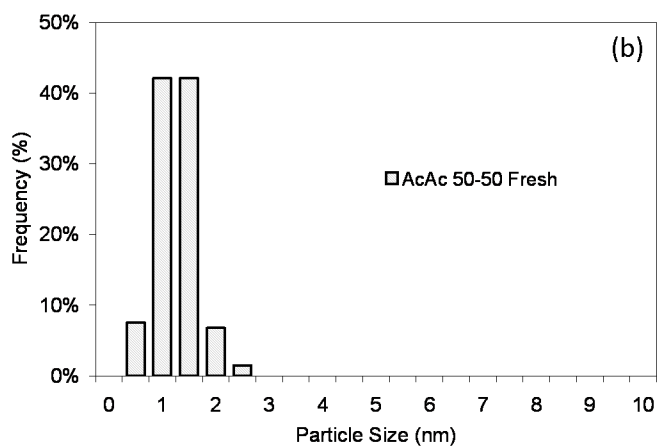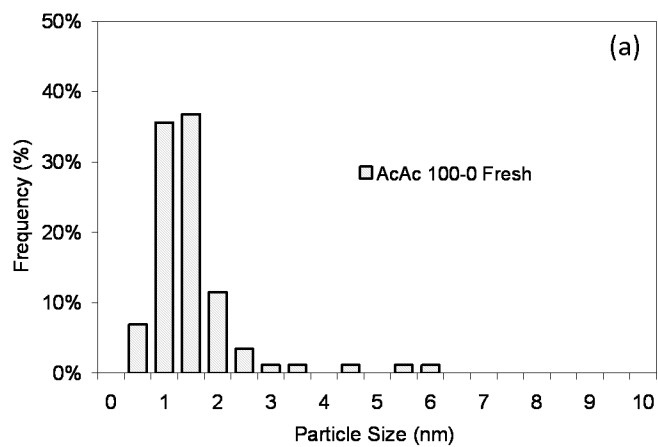
Figure 4.12: Particle size distributions of fresh (a)Pt100-Pd0 and (b) Pt50-Pd50 Ac-Ac catalysts collected from ACEM HAADF imaging
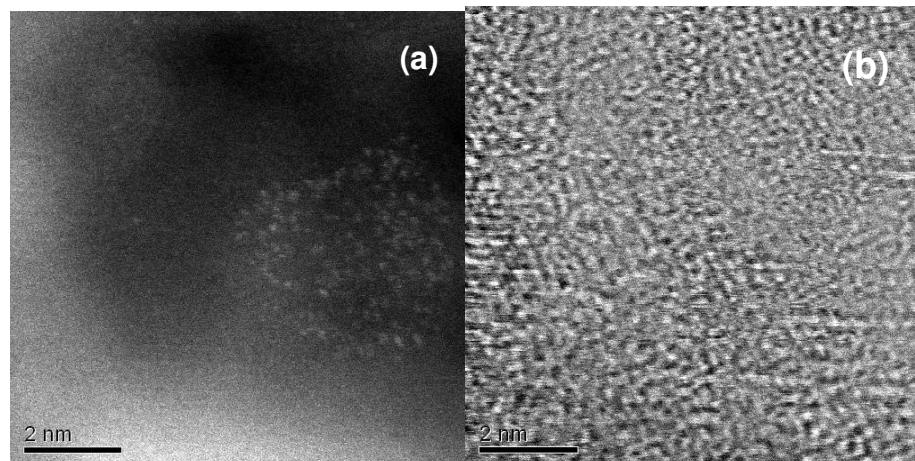
Figure 4.13: (a) HAADF and (b) BF STEM images of typical particles in the fresh Pt50Pd50 Ac-Ac catalyst.
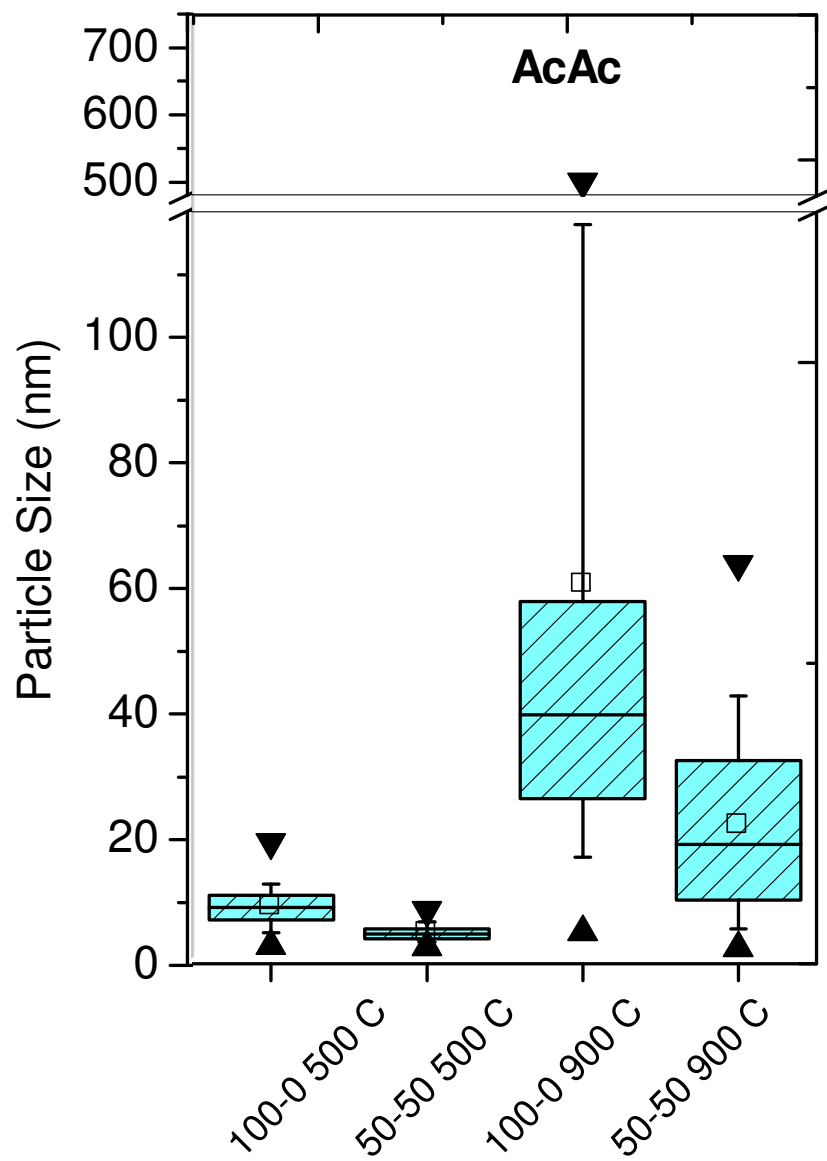
Figure 4.14: Box-plot summarizing descriptive statistics of aged Ac-Ac catalysts
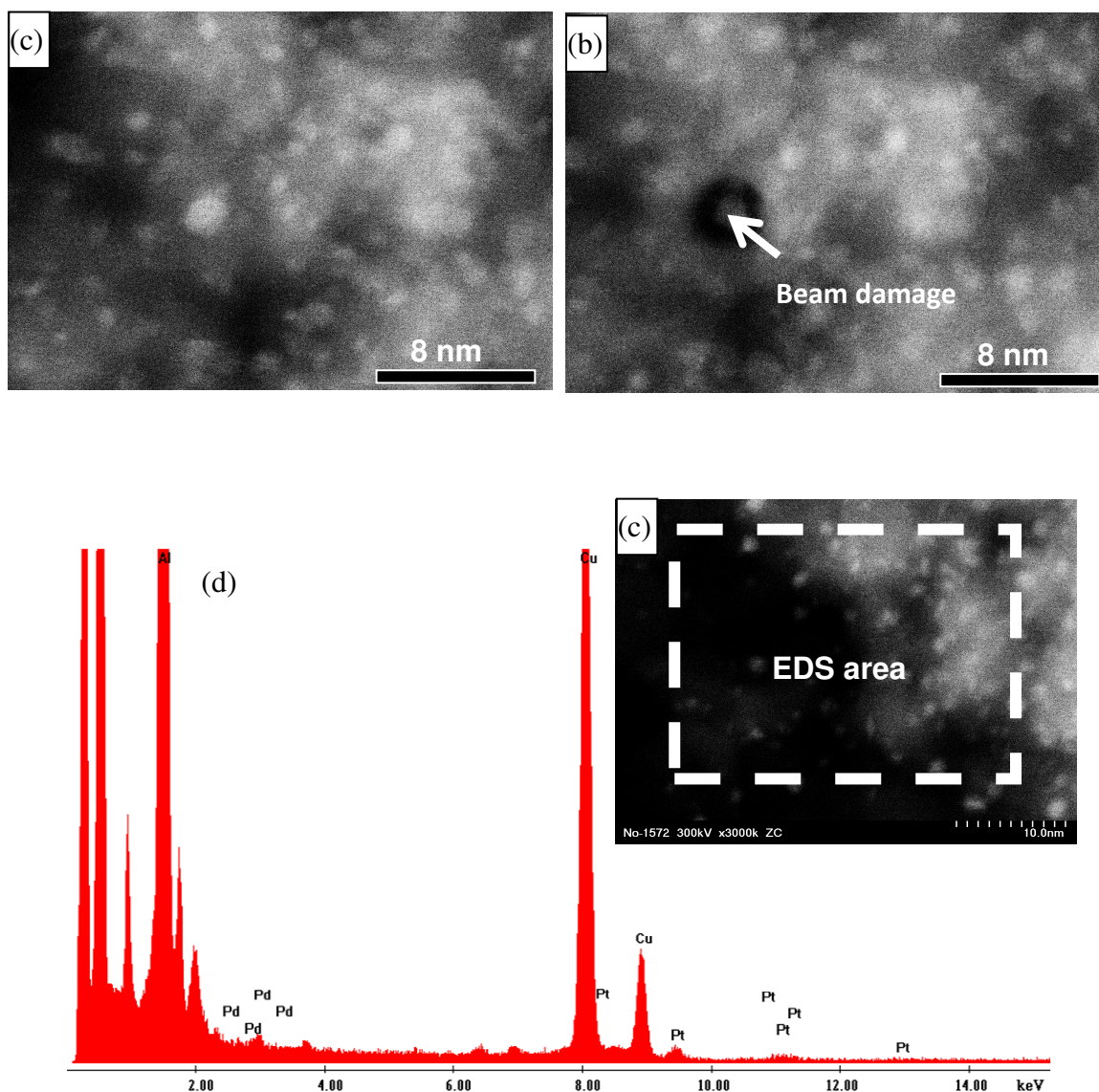
Figure 4.15: (a) Low magnification HAADF-STEM image of the fresh Pt50-Pd50 Ac-Ac catalyst, (b) HAADF-STEM image of the same region of the same sample after EDS analysis, (c) HAADF-STEM region of many particles, and (d) EDS spectra showing both Pt and Pd peaks with intensities corresponding to near nominal composition (41 ± 19 at% Pd and 59 ±17 at% Pt).
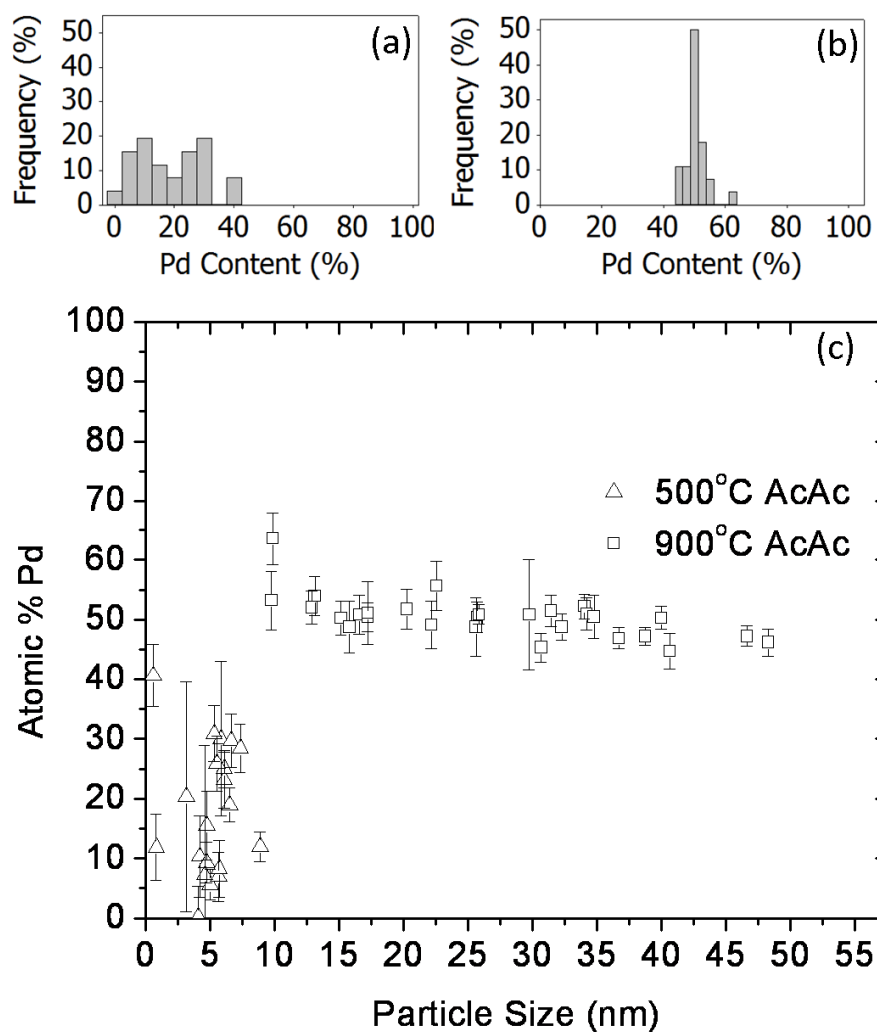
Figure 4.16: The compositional distributions of Pt50-Pd50 Ac-Ac catalysts aged 500ºC (a) and 900ºC (b), together with their particle compositions plotted as a function of particle size (c). The error bars represent the Pd compositional measurement uncertainty from the EDS integration.
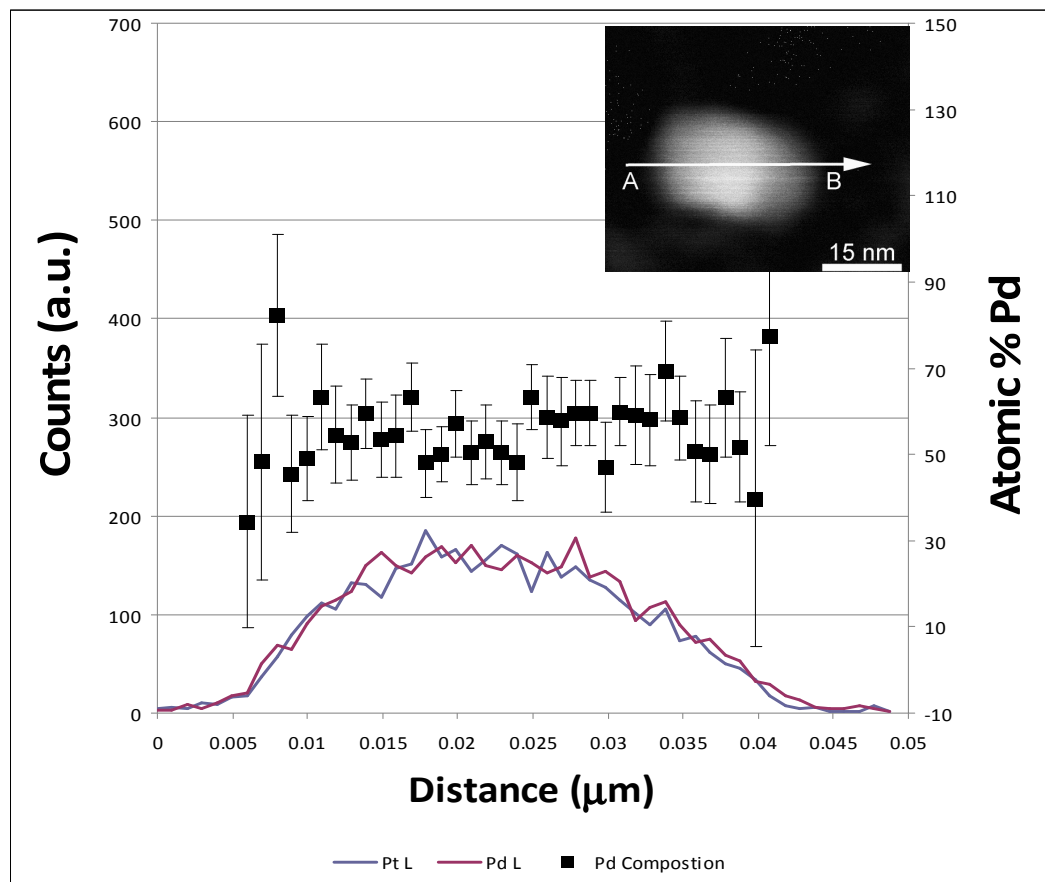
Figure 4.17: 50 point EDS line scan across a typical particle in the Pt50-Pd50 Ac-Ac catalyst aged at 900ºC showing relatively equal Pt L and Pd L signals across the particle. The Cliff-Lormier integration (right axis) shows that Pd composition is close to the nominal composition throughout the particle.
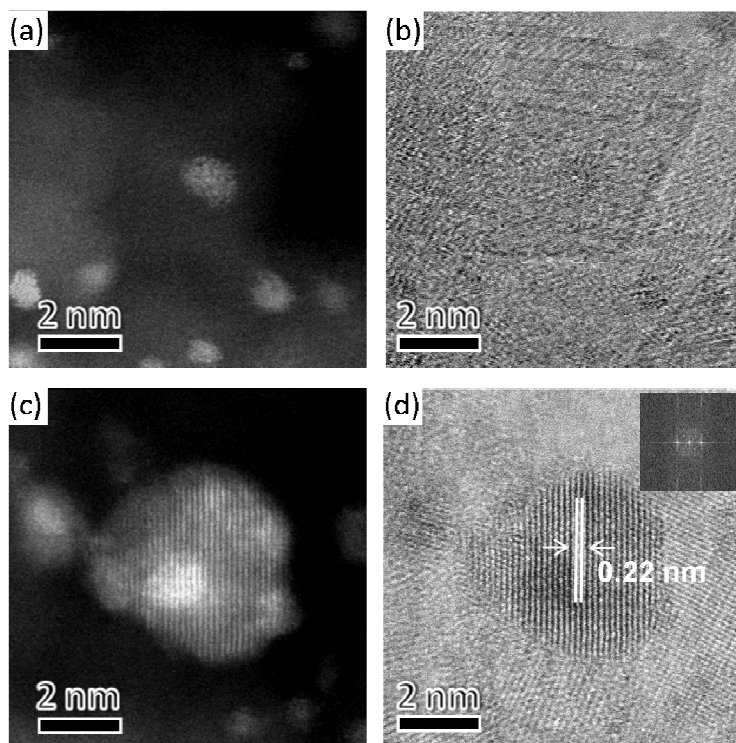
Figure 4.18: (a) HAADF and (b) BF STEM images from the fresh Pt100-Pd0 Nitrate catalyst. (c) HAADF and (d) BF STEM images from the fresh Pt50–Pd50 Nitrate catalyst.
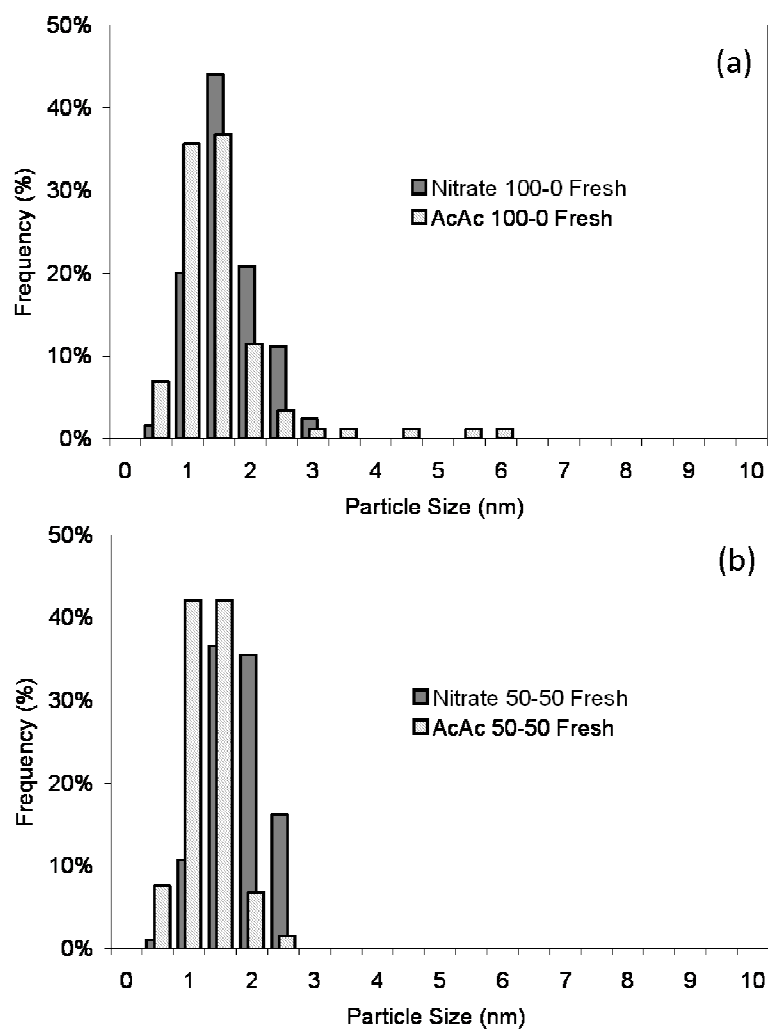
Figure 4.19: Particle size distributions collected from TEM imaging of fresh (a) Pt100-Pd0 and (b) Pt50-Pd50 catalysts. White bars represent Ac-Ac catalysts, grey bars represent Nitrate catalysts.
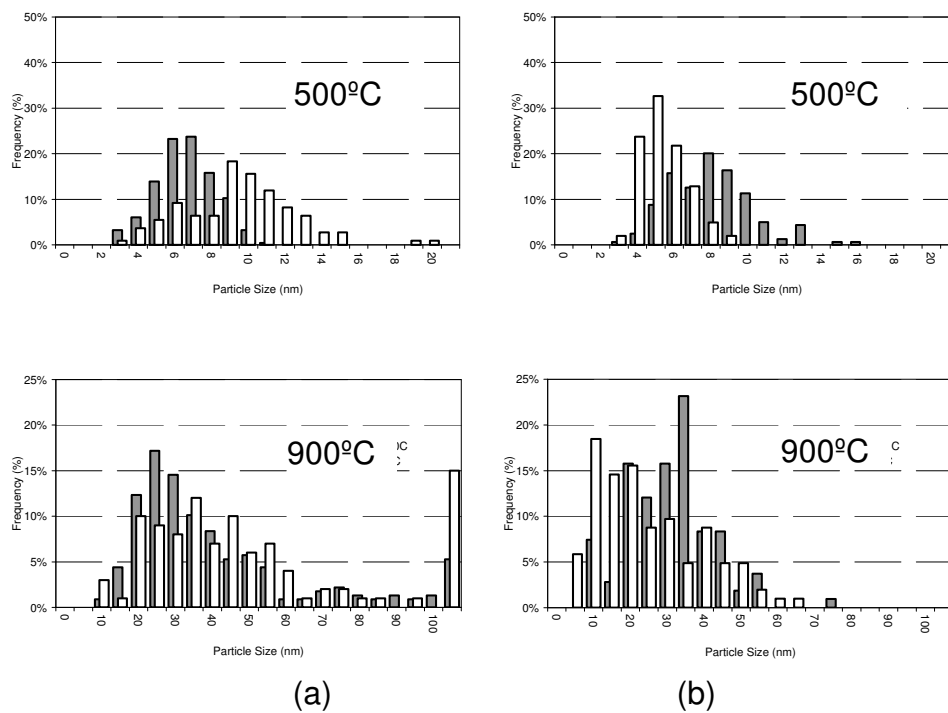
Figure 4.20: Particle size distributions were collected from TEM imaging for (a) Pt100-Pd0 and (b) Pt50-Pd50 catalysts (white bars represent AcAc catalysts, grey bars represent nitrate precursors)
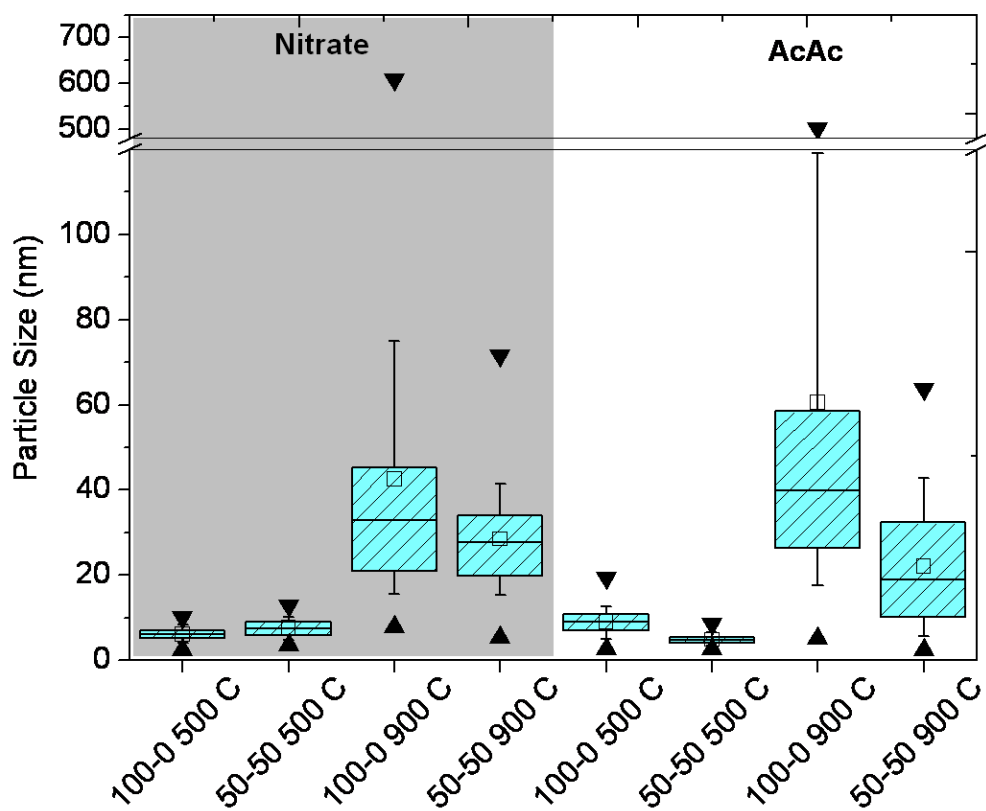
Figure 4.21: Box-plot summarizing descriptive statistics of the aged Nitrate and Ac-Ac catalysts.[boxes represent the inter-quartile range, whiskers represent 5th and 95th percentile, (▼) maximum value (▲) minimum value, (━) median, and (□) arithmetic mean]
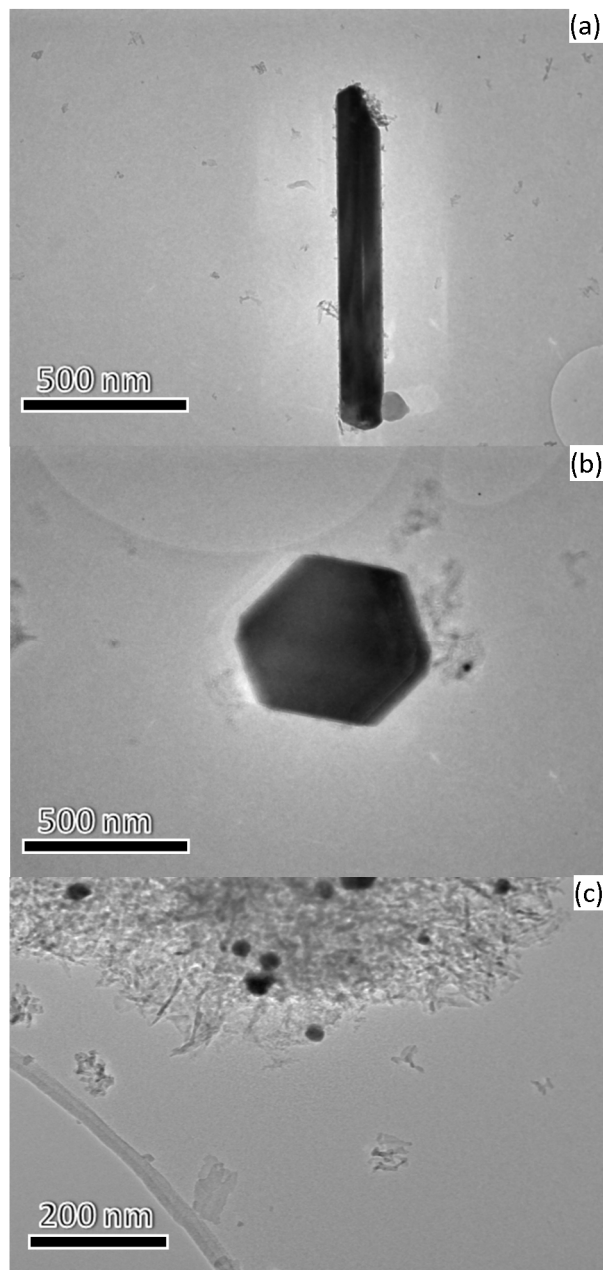
Figure 4.22: (a) TEM image of a Pt needle found in a Pt100-Pd0 Nitrate catalyst aged 900°C. (b) Highly faceted Pt particle from the same catalyst sample shown in (a). (Structures like this were noticeable features of the Pt100-Pd0 samples aged at 900°C from both catalyst precursors.) (c) TEM image of metallic particles in the Pt50-Pd50 Nitrate catalyst aged 900°C.

Table 4.5: Summary of TEM-derived particle size statistics. Fresh catalysts were measured using HAADF STEM imaging in the JEOL 2200FS while aged catalysts were measured using BF TEM imaging on the JEOL 3011 microscope.

Sample	Counts	Mean (nm)	Std Dev (nm)	Min (nm)	Max (nm)	d_s (nm)	Dispersion D (%)
Pt100-Pd0 Fresh (Nitrate)	125	1.38	0.50	0.12	2.78	1.74	64.6%
Pt50-Pd50 Fresh (Nitrate)	127	2.79	2.62	0.08	14.9	7.87	14.3%
Pt100-Pd0 500ºC (Nitrate)	215	6.15	1.58	2.39	10.1	7.52	14.9%
Pt50-Pd50 500ºC (Nitrate)	159	7.58	2.32	2.05	15.3	8.86	12.7%
Pt100-Pd0 900ºC (Nitrate)	227	43.4	48.6	7.84	527	146	0.77%
Pt50-Pd50 900ºC (Nitrate)	108	28.2	11.5	5.38	71.7	37.0	3.04%
Pt100-Pd0 Fresh (Ac-Ac)	87	1.27	0.89	0.18	5.68	2.95	38.0%
Pt50-Pd50 Fresh (Ac-Ac)	133	1.03	0.38	0.08	2.03	1.27	88.5%
Pt100-Pd0 500ºC (Ac-Ac)	109	9.04	3.01	2.80	19.4	10.9	10.3%
Pt50-Pd50 500ºC (Ac-Ac)	101	4.90	1.26	2.61	8.57	5.55	20.3%
Pt100-Pd0 900ºC (Ac-Ac)	100	60.5	70.4	5.06	501	277	0.41%
Pt50-Pd50 900ºC (Ac-Ac)	103	22.1	14.5	2.48	63.8	38.2	2.95%
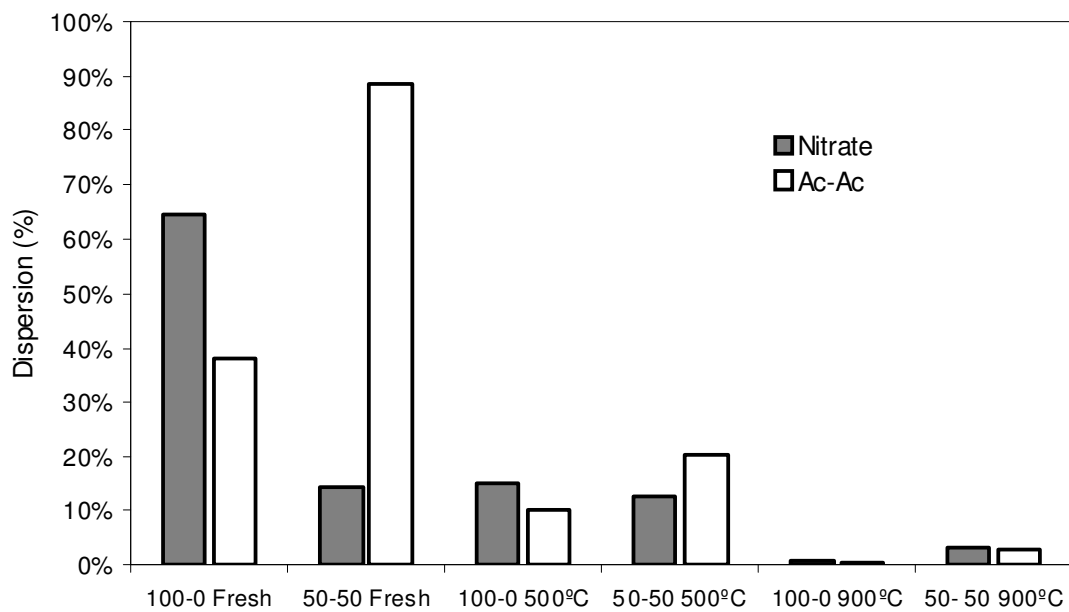
Figure 4.23: Dispersion calculated from TEM observations for all the catalysts used in this study
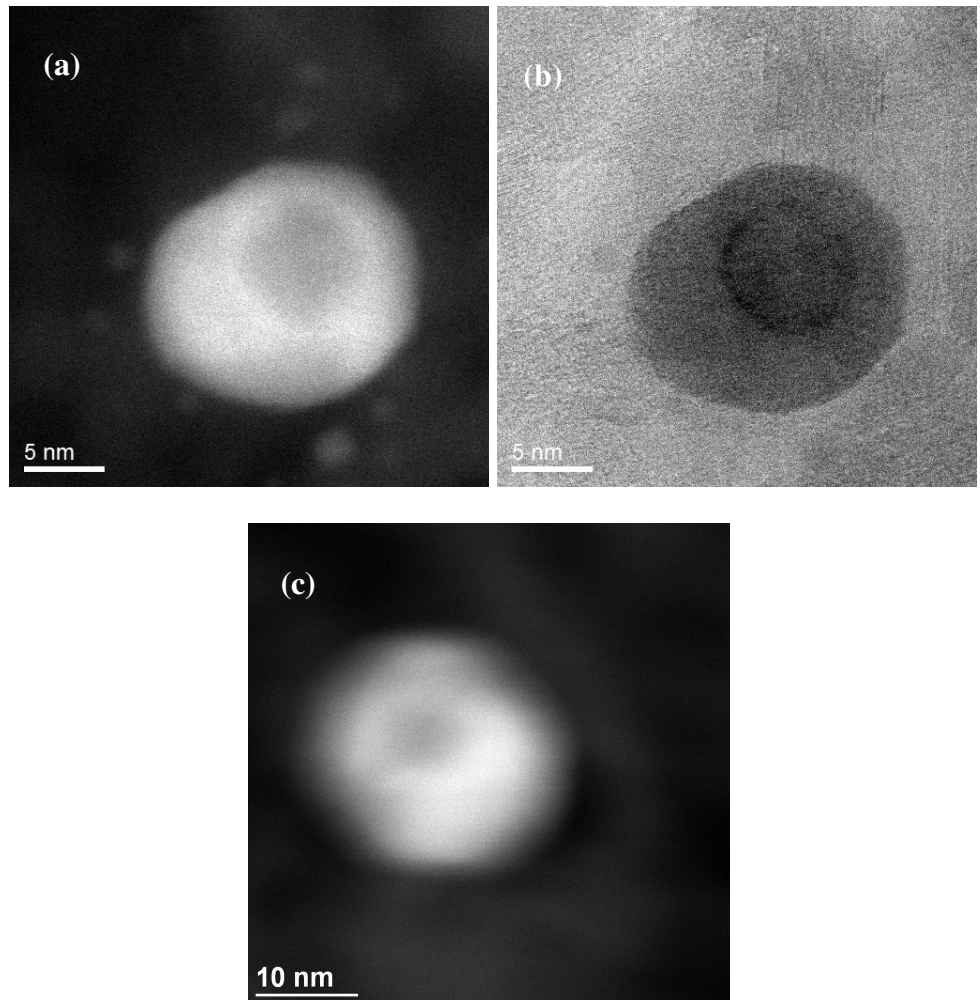
Figure 4.24: (a) Aberration corrected HAADF STEM, (b) aberration corrected BF STEM, and (d) conventional HAADF STEM images of a core shell nanoparticles that were observed in the 690ºC aged Pt50-Pd50 (nitrate)
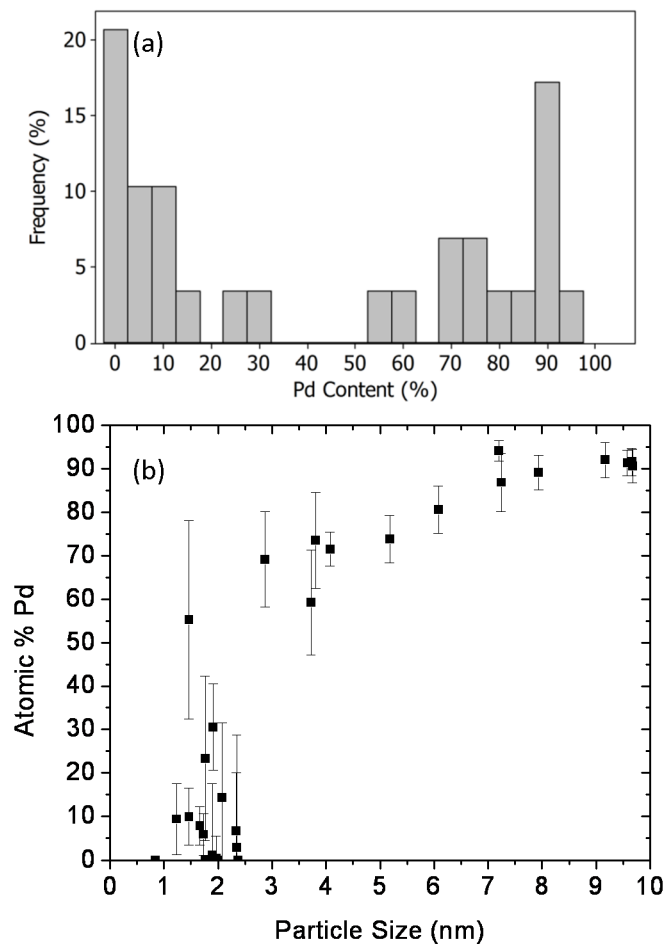
Figure 4.25: (a) Compositional distribution of fresh Pt50-Pd50 Nitrate catalyst, and (b) the particle composition plotted as a function of particle size. The error bars represent the Pd compositional measurement uncertainty from the EDS integration.

(
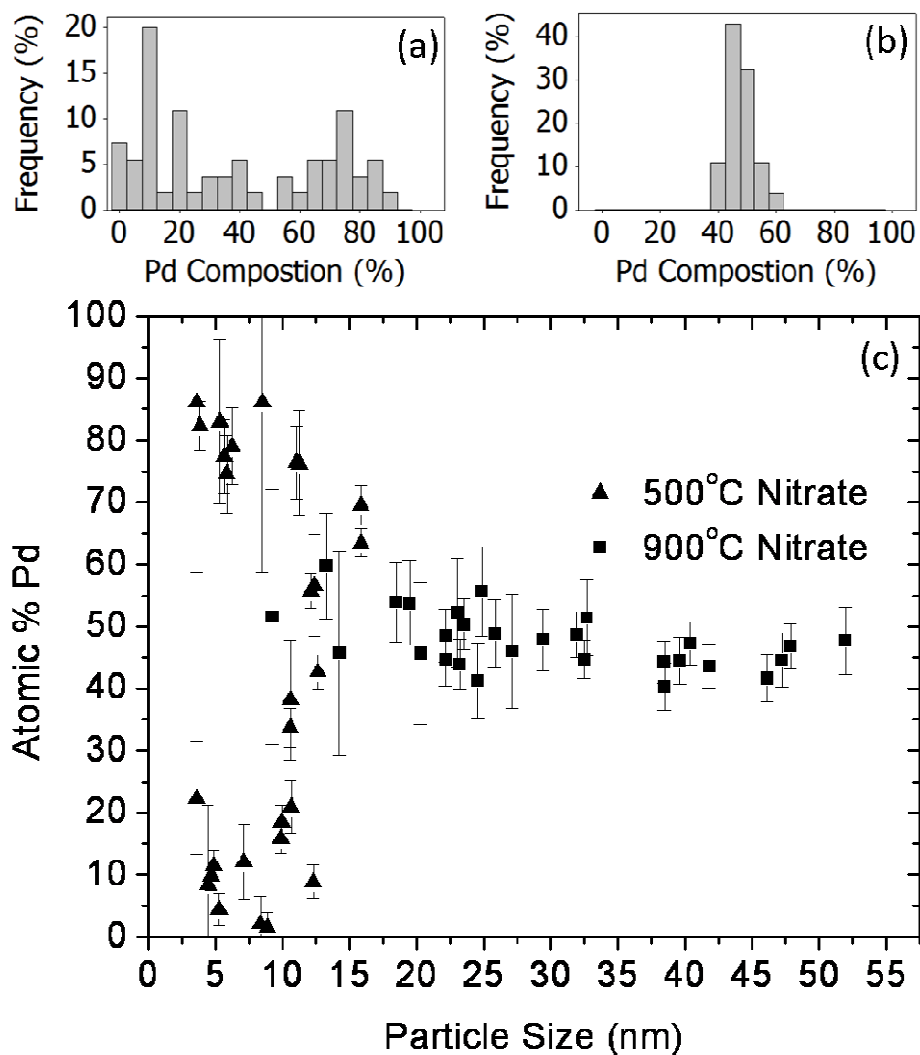
Figure 4.26: The compositional distributions of Pt50-Pd50 Nitrate catalysts (a) aged 500ºC , (b) 900ºC and (c) together with their particle compositions plotted as a function of particle size.
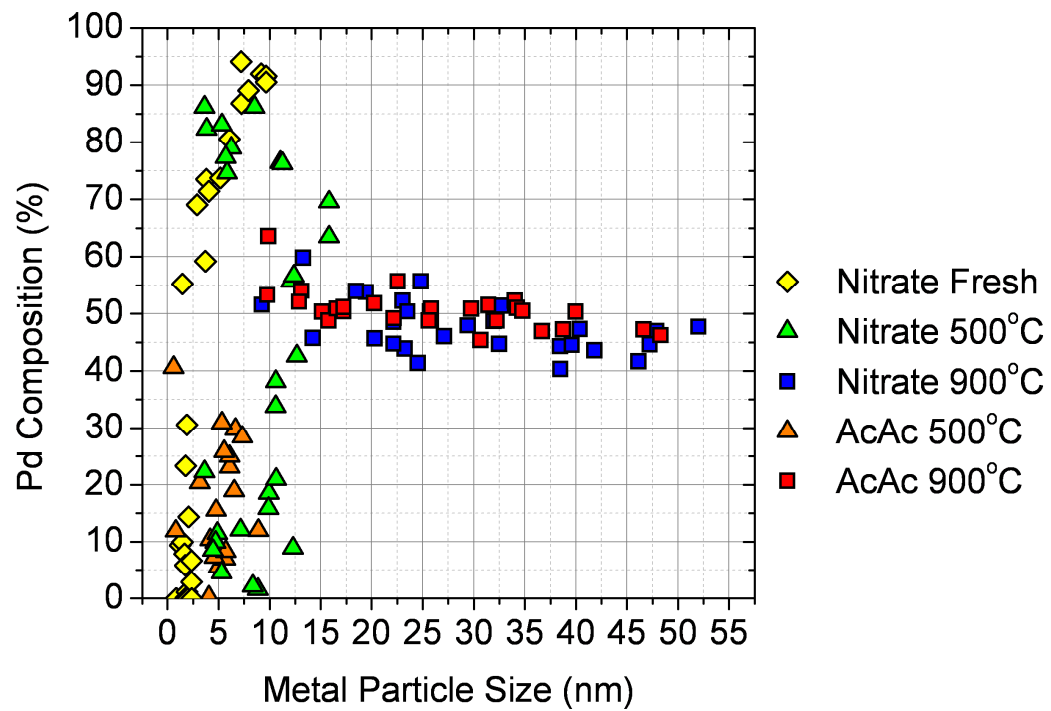
Figure 4.27: Particle compositions plotted as a function of particle size for Pt50-Pd50 catalysts
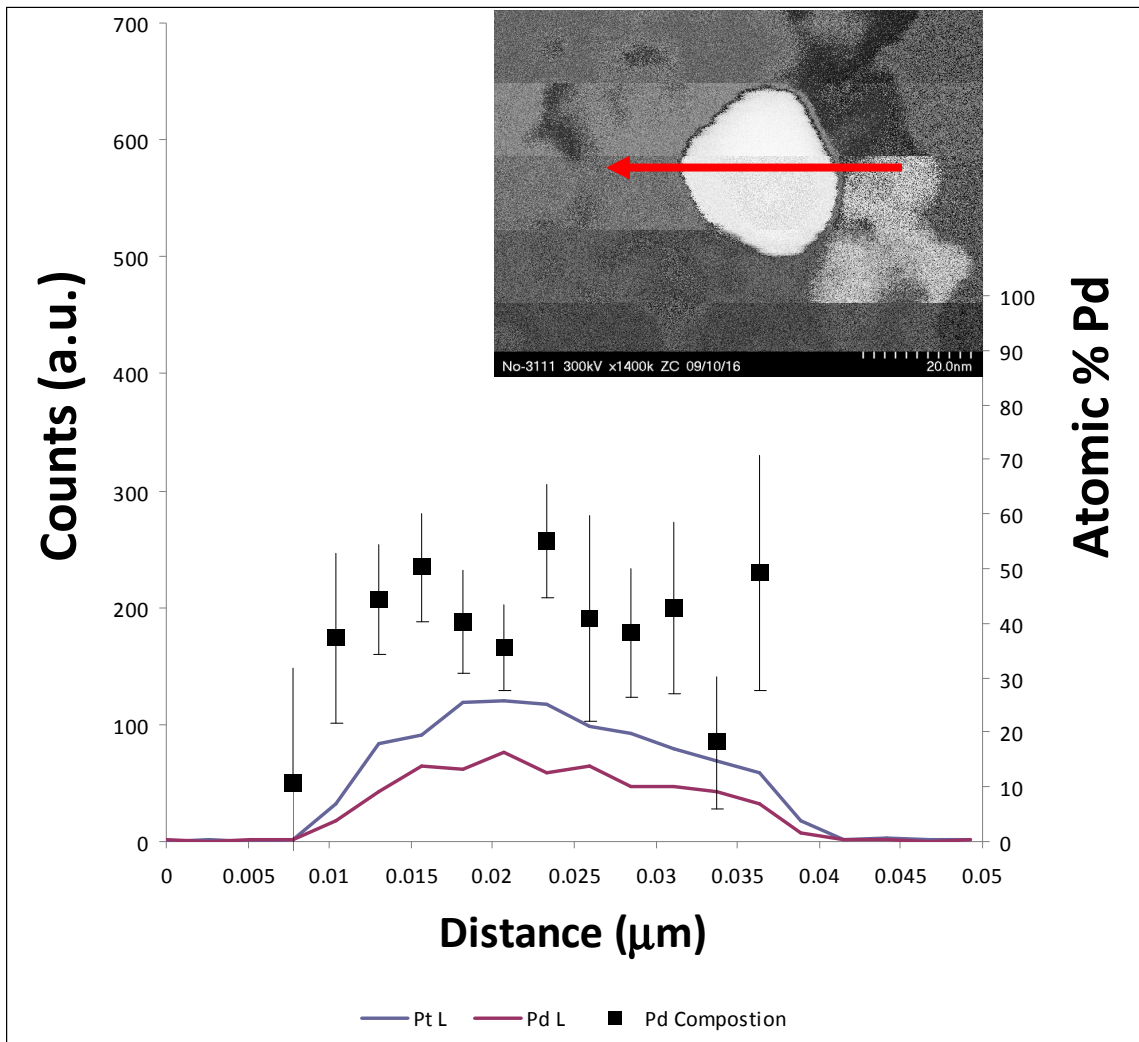
Figure 4.28: 20 point EDS line scan across a typical particle in the Pt50-Pd50 Nitrate catalyst aged at 900ºC . Although, there are differences in Pt L and Pd L signals across the particle, the Cliff Lormier integration (right axis) shows that Pd composition is close to the nominal composition throughout the particle. The overall measured composition of this particle 48.71 ± 3.75 Pd.
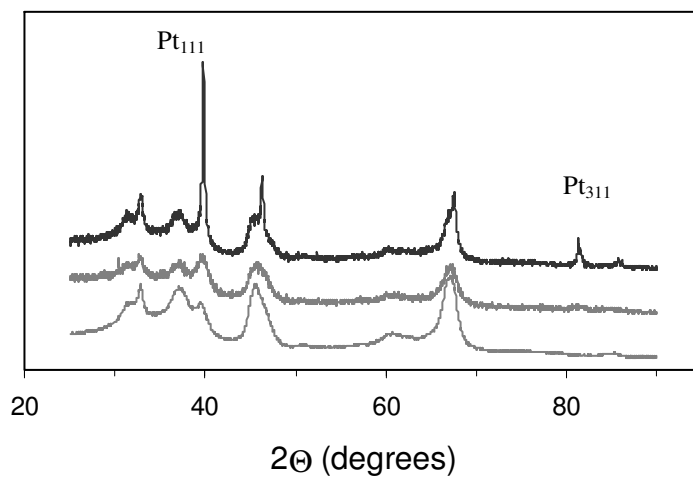
Figure 4.29: XRD scans for the untreated alumina support (bottom), the 500°C aged Pt 100 nitrate preparation (middle) and the 900°C aged Pt100 nitrate preparation (top).
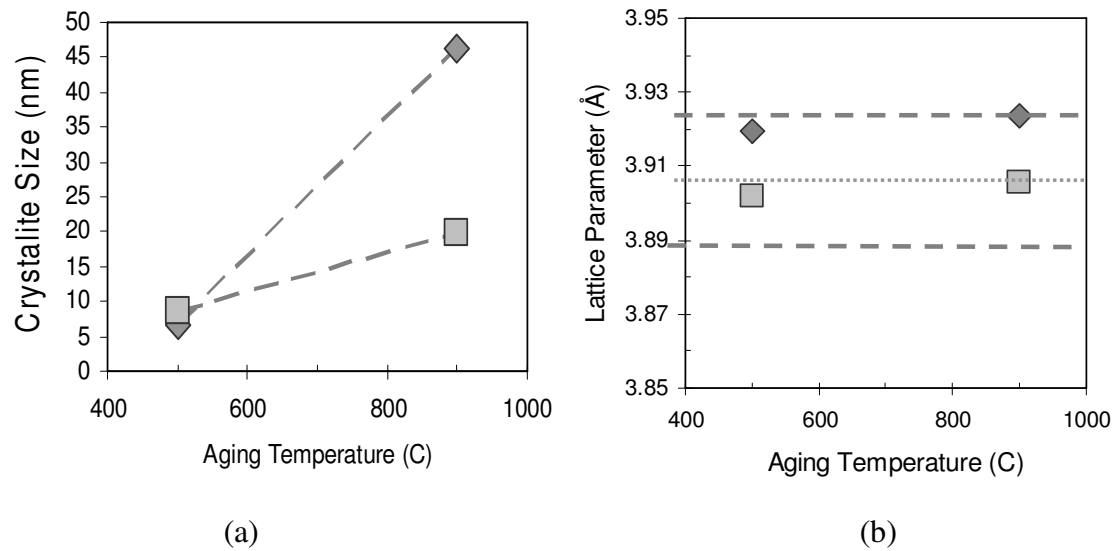
Figure 4.30: (a) Crystallite size and (b) lattice parameter for the Pt 100 nitrate
preparation (diamonds) and Pt50-Pd50 nitrate preparation (squares) as a function of aging
temperature. The dashed lines indicate the expected values of the lattice parameters for Pt
(upper), Pd (lower) and Pt50-Pd50 (middle).
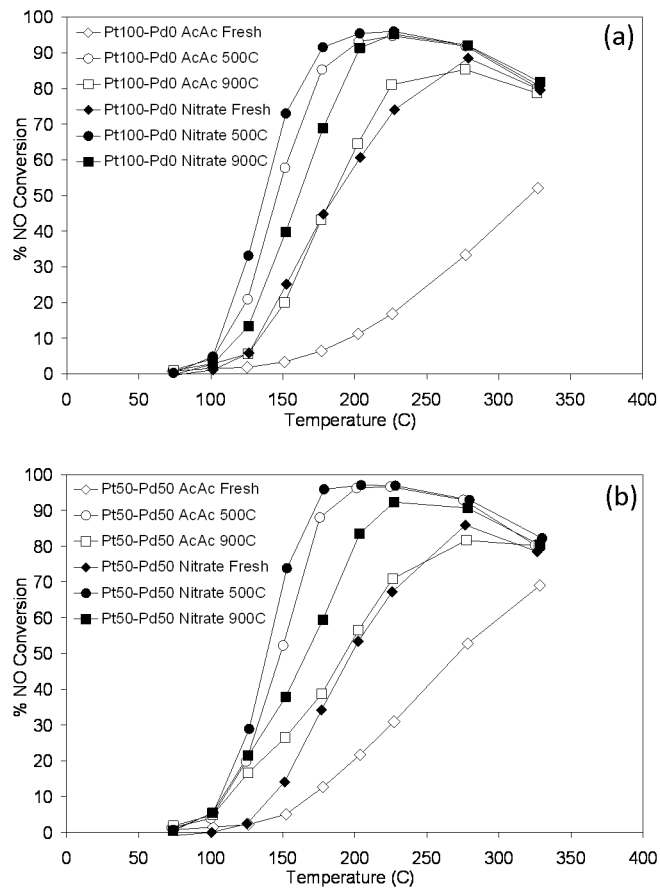
Figure 4.31: NO oxidation light-off curves for (a) Pt100-Pd0 catalysts and (b) Pt50-Pd50 catalysts
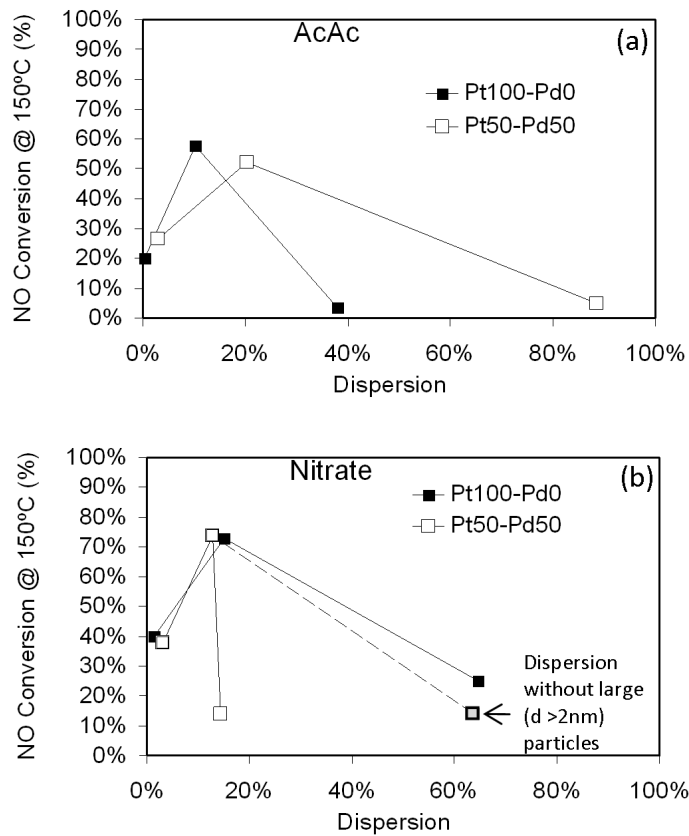
Figure 4.32 NO conversion at 150 ºC plotted as a function of particle size for catalysts from Ac-Ac precursors (a) and Nitrate precursors (b). Pure Pt catalysts are shown with solid squares, and bimetallic catalysts with open squares. The grey symbol in, (b) represents the dispersion calculated without including large Pd rich particles, which presumably do not contribute significantly in NO conversion.
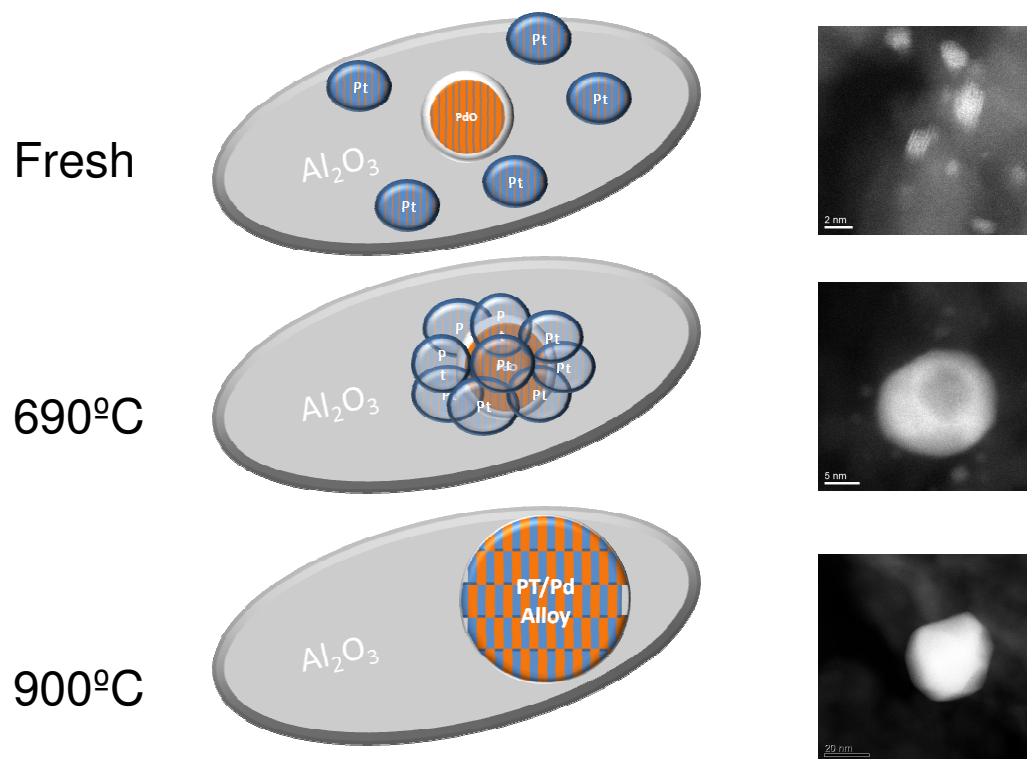
Figure 4.33: Schematic of aging mechanism resulting in core shell structure in the Pt50-Pd50 (Nitrate) catalyst.

4.9 References

1. N. Takahashi, H. Shinjoh, T. Iijima, T. Suzuki, K. Yamazaki, K. Yokota, H. Suzuki, N. Miyoshi, S. Matsumoto, T. Tanizawa, T. Tanaka, S. Tateishi, and K. Kasahara, "The new concept 3-way catalyst for automotive lean-burn engine: NOx storage and reduction catalyst." *Catal. Today*. **27**(1-2): p. 63-69 (1996).

2. R.J. Kudla, H.W. Jen, P.J. Schmitz, C.T. Goralski, and R.W. McCabe, "NO Oxidation over Alumina-Supported Pt-Pd and Pt-Rh". North American Catalysis Scoeitey 19th NAM (2005).

3. G.W. Graham, H.W. Jen, W. Chun, H.P. Sun, X.Q. Pan, and R.W. McCabe, "Coarsening of Pt particles in a model NOx trap." *Catal. Lett*. **93**(3-4): p. 129-134 (2004).

4. M. Chen and L.D. Schmidt, "Morphology and composition of Pt---Pd alloy crystallites on SiO2 in reactive atmospheres." *J. Catal*. **56**(2): p. 198-218 (1979).

5. G.W. Graham, H. Sun, H.W. Jen, X.Q. Pan, and R.W. McCabe, "Aging-Induced Metal Redistribution in Bimetallic Catalysts." *Catal. Lett*. **81**(1): p. 1-7 (2002).

6. A. Morlang, U. Neuhausen, K.V. Klementiev, F.-W. Schütze, G. Miehe, H. Fuess, and E.S. Lox, "Bimetallic Pt/Pd diesel oxidation catalysts: Structural characterisation and catalytic behaviour." *Appl. Catal., B*. **60**(3-4): p. 191-199 (2005).

7. G.W. Graham, H.W. Jen, O. Ezekoye, R.J. Kudla, W. Chun, X.Q. Pan, and R.W. McCabe, "Effect of alloy composition on dispersion stability and catalytic activity for NO oxidation over alumina-supported Pt-Pd catalysts." *Catal. Lett*. **116**(1-2): p. 1-8 (2007).

8. X. Wang, S.M. Sigmon, J.J. Spivey, and H.H. Lamb, "Support and particle size effects on direct NO decomposition over platinum." *Catal. Today*. **96**(1-2): p. 11-20 (2004).

9. J. Hagen, *Industrial catalysis: a practical approach*. 2 ed., Weinheim, Germany: Wiley-VCH. (2006).

10. J.A.A. van den Tillaart, J. Leyrer, S. Eckhoff, and E.S. Lox, "Effect of support oxide and noble metal precursor on the activity of automotive diesel catalysts." *Appl. Catal., B*. **10**(1-3): p. 53-68 (1996).

11. D.A. Blom, L.F. Allard, S. Mishina, and M.A. O'Keefe, "Early results from an aberration-corrected JEOL 2200FS STEM/TEM at Oak Ridge National Laboratory." *Microsc. Microanal.* **12**(6): p. 483-491 (2006).

12. L.F. Allard, D.A. Blom, M.A. O'Keefe, and S. Mishina, "Design and Performance Characteristics of the ORNL Advanced Microscopy Laboratory and JEOL 2200FS-AC Aberration-Corrected STEM/TEM." *Microsc. Microanal.* **11**(SupplementS02): p. 2136-2137 (2005).

13. G. Cliff and G.W. Lorimer, "Quantitative-Analysis of Thin Specimens." *J. Microsc.-Oxf.* **103**(MAR): p. 203-207 (1975).

14. P. Ascarelli, V. Contini, and R. Giorgi, "Formation process of nanocrystalline materials from x-ray diffraction profile analysis: Application to platinum catalysts." *J. Appl. Phys.* **91**(7): p. 4556-4561 (2002).

15. J.L. Rousset, B.C. Khanra, A.M. Cadrot, F.J.C.S. Aires, A.J. Renouprez, and M. Pellarin, "Investigations on supported bimetallic PdPt nanostructures." *Surf. Sci.* **352-354**: p. 583-587 (1996).

16. F. Morfin, J.-C. Sabroux, and A. Renouprez, "Catalytic combustion of hydrogen for mitigating hydrogen risk in case of a severe accident in a nuclear power plant: study of catalysts poisoning in a representative atmosphere." *Appl. Catal., B*. **47**(1): p. 47-58 (2004).

17. D. Bazin, D. Guillaume, C. Pichon, D. Uzio, and S. Lopez, "Structure and size of bimetallic palladium - Platinum clusters in an hydrotreatment catalyst." *Oil & Gas Science and Technology-Revue De L Institut Francais Du Petrole*. **60**(5): p. 801-813 (2005).

18. J.L. Rousset, A.J. Renouprez, and A.M. Cadrot, "Ion-scattering study and Monte Carlo simulations of surface segregation in Pd-Pt nanoclusters obtained by laser vaporization of bulk alloys." *Physical Review B*. **58**(4): p. 2150-2156 (1998).

19.   J.L. Rousset, J.C. Bertolini, and P. Miegge, "Theory of segregation using the equivalent-medium approximation and bond-strength modifications at surfaces: Application to fee Pd-X alloys." *Physical Review B*. **53**(8): p. 4947-4957 (1996).

20.   H.R. Aduriz, P. Bodnariuk, B. Coq, and F. Figueras, "Alumina-supported bimetallics of palladium alloyed with germanium, tin, lead, or antimony from organometallic precursors : I. Preparation and characterization." *J. Catal.* **119**(1): p. 97-107 (1989).

21.   M.M. Hall, Jnr, V.G. Veeraraghavan, H. Rubin, and P.G. Winchell, "The approximation of symmetric X-ray peaks by Pearson type VII distributions." *J. Appl. Crystallogr.* **10**(1): p. 66-68 (1977).

22.   P.J. Schmitz, R.J. Kudla, A.R. Drews, A.E. Chen, C.K. Lowe-Ma, R.W. McCabe, W.F. Schneider, and J. Goralski, C.T., "NO oxidation over supported Pt: Impact of precursor, support, loading, and processing conditions evaluated via high throughput experimentation." *Appl. Catal., B*. **67**(3-4): p. 246-256 (2006).

23.   J.H. Kwak, J.Z. Hu, D. Mei, C.W. Yi, D.H. Kim, C.H.F. Peden, L.F. Allard, and J. Szanyi, "Coordinatively Unsaturated Al3+ Centers as Binding Sites for Active Catalyst Phases of Platinum on gamma-Al2O3." *Science*. **325**(5948): p. 1670-1673 (2009).

24.   D.A. Blom, S.A. Bradley, W. Sinkler, and L.F. Allard, "Observation of Pt Atoms, Clusters and Rafts on Oxide Supports, by Sub Ångström Z-Contrast Imaging in an Aberration-Corrected STEM/TEM." *Microsc. Microanal.* **12**((Supp 2)): p. 50-51 (2006).

25.   L. Pauling, "Atomic Radii and Interatomic Distances in Metals." *J. Am. Chem. Soc.* **69**: p. 542-553 (1947).

26.   S.J. Pennycook, "Z-contrast stem for materials science." *Ultramicroscopy*. **30**(1-2): p. 58-69 (1989).

27.   B. Fultz and J.M. Howe, *Transmission electron microscopy and diffractometry of materials*. Physics and astronomy online library. Berlin: Springer. (2001).

28.   N. Toshima, M. Harada, T. Yonezawa, K. Kushihashi, and K. Asakura, "Structural-Analysis of Polymer-Protected Pd/Pt Bimetallic Clusters as Dispersed

Catalysts by Using Extended X-Ray Absorption Fine-Structure Spectroscopy." *J. Phys. Chem.* **95**(19): p. 7448-7453 (1991).

29.   A. De Sarkar, M. Menon, and B.C. Khanra, "Effect of metal-support interaction on surface segregation in Pd-Pt nanoparticles." *Appl. Surf. Sci.* **182**(3-4): p. 394-397 (2001).

30.   D. Cheng, S. Huang, and W. Wang, "Structures of small Pd-Pt bimetallic clusters by Monte Carlo simulation." *Chem. Phys.* **330**(3): p. 423-430 (2006).

31.   E. Kern, " Mineralogisch-Petrograph. Inst., University of Heildelberg, Germany, ICDD", (1993).

32.   I. Moysan, V. Paul-Boncour, S. Thiébaut, E. Sciora, J.M. Fournier, R. Cortes, S. Bourgeois, and A. Percheron-Guégan, "Pd-Pt alloys: correlation between electronic structure and hydrogenation properties." *J. Alloys Compd.* **322**(1-2): p. 14-20 (2001).

33.   A.J. Renouprez, A. Malhomme, J. Massardier, M. Cattenot, and G. Bergeret, "Sulphur resistant palladium-platinum catalysts prepared from mixed acetylacetonates." in *12th International Congress on Catalysis, Proceedings of the 12th ICC*, F.V.M. Avelino Corma, Segrario Mendioroz and José Luis G. Fierro, Editor., Elsevier. p. 2579-2584 (2000).

34.   J. Andersson, M. Antonsson, L. Eurenius, E. Olsson, and M. Skoglundh, "Deactivation of diesel oxidation catalysts: Vehicle- and synthetic aging correlations." *Applied catalysis. B, Environmental*. **72**(1-2): p. 71-81 (2007).

35.   P.J.F. Harris, E.D. Boyes, and J.A. Cairns, "The sintering of an alumina-supported platinum catalyst studied by transmission electron microscopy." *J. Catal.* **82**(1): p. 127-146 (1983).

36.   A.K. Datye, Q. Xu, K.C. Kharas, and J.M. McCarty, "Particle size distributions in heterogeneous catalysts: What do they tell us about the sintering mechanism?" *Catal. Today*. **111**(1-2): p. 59-67 (2006).

37.   C.G. Granqvist and R.A. Buhrman, "Size distributions for supported metal catalysts : Coalescence growth versus ostwald ripening." *J. Catal.* **42**(3): p. 477-479 (1976).

38.   B.M. Weiss and E. Iglesia, "Mechanism and site requirements for NO oxidation on Pd catalysts." *J. Catal.* **272**(1): p. 74-81 (2010).

39.   J. Jelic, K. Reuter, and R. Meyer, "The Role of Surface Oxides in NOx Storage Reduction Catalysts." *Chemcatchem.* **2**(6): p. 658-660 (2010).

40.   E. Lundgren, J. Gustafson, A. Mikkelsen, J.N. Andersen, A. Stierle, H. Dosch, M. Todorova, J. Rogal, K. Reuter, and M. Scheffler, "Kinetic Hindrance during the Initial Oxidation of Pd(100) at Ambient Pressures." *Phys. Rev. Lett.* **92**(4): p. 046101 (2004).

Chapter 5

Investigation of Model Catalysts of Pd and Rh on Ceria and Ceria-Zirconia Supports

5.1 Introduction

In this chapter, we present two studies that illuminate our investigations of two model catalysts consisting of Pd and Rh on single crystalline ceria and ceria-zirconia supports. These materials were chosen because together they make up the active components of modern automotive three way catalysts (TWCs). The automotive TWC is considered one of the major engineering achievements of the last century.[1] TWCs have been highly effective in mitigating harmful emissions from IC engines since their widespread introduction in the late 1970s.[2] The automotive TWC resides in the catalytic converter (Figure 5.1) and consists of a ceramic monolith, a washcoat containing both precious metal nanoparticles and a high surface area ceramic support (Figure 5.1d). As mentioned in section 1.5.3, Pd, Rh, and Pt are the primary precious metal components in TWCs.[3-4] The primary function of the washcoat is to provide a large surface area upon which to disperse the precious metal nanoparticles.[5] To this end, the first washcoats consisted primarily of alumina, as the ceramic support was not considered to have much of an impact on the catalytic reaction. However, the discovery of metal support interactions led to the idea that the support could be an effective *catalysis promoter*.[6] Today, modern commercial washcoats are still based on alumina, but all of them contain

a complex mixture of oxides of nickel, lanthanum, yttrium, barium and, most importantly, cerium.[5, 7]

Ceria (CeO$_2$) has been identified as an important additive in washcoat materials for automotive TWCs.   Ceria was chosen as a support material in automotive TWCs because it is an effective catalyst promoter, has a high oxygen storage capacity, and high thermal stability.[8] Because of these desirable properties, ceria and ceria-based oxides have been widely investigated as electronic promoters of activity, selectivity, and thermal stability in a variety of catalysts.[7] Pd on ceria-based supports is an important catalyst system for a variety of applications, including the catalytic combustion of methane[9], diesel oxidation[10], and water gas shift reactions[11-12].

Cerium oxide (Figure 5.2) has a fluorite structure with a bulk lattice parameter of 0.541nm.[13] Cerium-zirconium mixed oxides are isostructural with ceria with up to ~40% ZrO$_2$.[14-15] Also, it was found that ceria-zirconia (CZO) shows an improvement in thermal stability and oxygen storage capacity.[16] Despite the advantageous properties of cerium oxides, the operating environment, consisting of high temperatures and cyclic redox conditions, can, over long periods of time, cause damaging interactions between the precious metal particles and the oxide support.

While research and development efforts over many years have led to a number of advances, catalyst deactivation (due to metal particle growth, agglomeration, and encapsulation, for example) remains a major problem, with significant opportunity for mechanistic studies to yield new and useful insight in this area.[17] Moreover, metal-support interactions play a major role in TWCs and heterogeneous catalysts in general, sometimes affecting catalytic performance dramatically.[18-19]

As stated earlier, this chapter presents two studies of model catalysts of Pd and Rh on single crystalline ceria and ceria-zirconia supports. In the first study we investigated the mechanisms and thermodynamics of Rh and Pd cluster formation and growth on the CeO_2 (111) surface. The second study investigated the role of film stress in oxide wetting of metal particles in ceria-zirconia-supported Pd model catalysts. Both of these studies shed light on the atomic-scale interactions between these precious metals and ceria-based oxide supports.

5.2 Experimental Studies of Rh and Pd on a CeO_2 (111) Surface

5.2.1 Background and Objectives

Ceria supported Pd and Rh are important materials in automotive TWCs. TEM of materials collected directly from catalysts (Figure 5.1d) can yield valuable information about particle size, shape, and thermal stability. However, TEM of washcoat materials yields limited information pertaining to the fundamental interaction between the ceramic support and the metal nanoparticles. Detailed investigation of the interfacial microstructure of Pd and Rh particles on CeO_2 can be revealed by cross-sectional TEM of model planar catalyst samples. Furthermore, cross sectional TEM can provide a visual image of a supported metal particle cross section that can be used to investigate the thermodynamic properties of the interface.

The objective of this study is to fabricate and investigate ceria supported Pd and Rh model catalysts in order to probe the fundamental thermodynamic properties between the metal and the ceria (111) surface using electron microscopy. An additional objective

of this study is to investigate the aging, coursing, and agglomeration behavior of these

metals on CeO_2. In this work, HRTEM was used to evaluate the morphology and

contrast the coarsening behavior of Pd and Rh on the CeO_2 (111) surface. These

experimentally collected data were contrasted to collaboratively prepared first-principles

density functional theory (DFT) calculations and molecular dynamics simulations of the

behavior of Pd and Rh on (111) surface of CeO_2.

5.2.2 Experimental Methods

Thick (~150nm) CeO_2 films were grown on the (111) surface of yttria-stabilized

zirconia (YSZ) using pulsed laser deposition (PLD) in an on-axis geometry. The PLD

system was described earlier in Section 2.3.1 and shown schematically in Figure 2.12.

Two different commercial substrates were used for the growth of ceria films in this study.

The ceria film (Sample A) used for the Pd/CeO_2 part of the study was grown on

10x10mm YSZ substrates from MTI Corporation, while the film later used for Rh/CeO_2

(Sample B) was grown on 5 x 5mm YSZ substrates from Princeton Scientific Inc.

Deposition parameters were varied to optimize crystalline quality, measured by $\theta/2\theta$

measurements and ω-rocking curves in XRD (equipment described in Section 2.2.2.1).

Surface finish was also monitored ex-situ using AFM (as described in Section 2.2.3.1).

Growth conditions for both CeO_2 films were as follows: substrate temperature of 800°C,

laser energy of 100mJ, laser repetition rate of 5 Hz, and an oxygen partial pressure of 6

mTorr O2. Films and samples examined in this work are summarized in Table 5.1.

The CeO_2 films were first calcined (heated) in air for 1 hour at 600 ˚C (873K)

after their deposition onto the YSZ substrates, and the samples were then placed in an

ultra high vacuum (UHV) chamber (Physical Electronics Industries), described in detail previously (Section 2.3.3). A monolayer equivalent of Pd or Rh was deposited, using a thermal evaporation source, onto the CeO_2 film surface. The term "monolayer equivalent' is used because thermal evaporation of Pd and Rh onto the CeO_2 films at room temperature, was not expected to produce uniform one-atom-thick layers of either metal, even at sub-monolayer coverage.[20] Metal coverage was monitored using X-ray photoelectron spectroscopy (XPS), as described in Section 2.2.3.2.

Thermal treatments were performed in a four channel quartz tube furnace. Our basic experimental approach was to focus on the effect of a subsequent thermal treatment. This was chosen so as to be more directly comparable with the theoretical molecular dynamics simulations presented in Section 5.2.5 below. Due to the highly reducible nature of precious-metal-loaded CeO_2[21], treatments were performed in air, in order to more nearly maintain thermodynamic equilibrium conditions. To this end, after deposition, the samples were again calcined in air for 1 hour at 600ºC (873K).

A second portion of our experimental approach extended the thermal treatment to an investigation of the behavior of these model catalysts under reducing conditions along with extended high temperature exposure. Because the working environment for automotive TWCs often consists of high temperatures and cyclic redox conditions, we used a previously identified[22] thermal treatment protocol to observe any structural changes with reduction followed by high temperature annealing. Consequently, following metal deposition and calcination, some samples were subjected to two reduction/annealing cycles. Each cycle consisted of the following: 1.) 20 minutes of 1%

H_2 in N_2 at 200°C, 2.) 5 hours of pure N_2 at 700ºC, and 3.) cooling to room temperature under N_2. The reduction and annealing treatment is shown schematically in Figure 5.3.

Cross-section transmission electron microscopy (TEM) specimens were thinned to electron transparency using traditional methods of mechanical grinding and argon ion milling, (described generally in Section 2.2.1.6). TEM studies were carried out on a JEOL 3011 high resolution electron microscope described earlier in this thesis.

5.2.3 Results

5.2.3.1 Film Growth and Characterization

As described above, CeO_2 films were grown by PLD and $\theta/2\theta$ and ω-rocking curves are given in Figure 5.4. XRD analysis indicated that the sample B had a higher film quality than sample A, as indicated by the smaller FWHM of the respective ω-curves (Figure 5.4b). Further evidence of this difference was observed in AFM analysis (Figure 5.5), as the surface of sample A had large scratches which resulted in a rougher CeO_2 film.

5.2.3.2 Metal Deposition

A monolayer equivalent of Pd (on Film A) or Rh (on Film B) was deposited via room temperature thermal evaporation under UHV conditions. XPS survey spectra of the ceria films (for both Films A and B) before and after metal deposition are shown in Figure 5.6. The amount of metal deposited corresponds to a monolayer equivalent based

on previous experience with these specific evaporations sources[23-24].   The insets of

Figure 5.6 (a and b) show details of the Pd 3d and Rh 3d region, respectively.

5.2.3.3 Transmission Electron Microscopy - Calcined Samples

Figure 5.7 is a low-magnification cross sectional TEM image of a typical CeO_2

film on YSZ substrate. The TEM image indicates that the CeO_2 film is approximately

150nm thick. The image also shows a uniform film with no noticeable voids, indicating a

high quality film. Figure 5.8 (a) is a low magnification image of the surface of a CeO_2

film with Pd after the calcination treatment at 600˚C. This image, taken slightly off zone

axis, clearly reveals particles on the ceria surface. An HRTEM image of one of these

particles is shown in Figure 5.8 (b). Most particles observed were in contact with CeO_2

surface.   However, some particles were removed from the ceria surface during TEM

sample preparation and became fully encapsulated in M-Bond layer. This is presumably

an artifact of sample preparation and not of fundamental significance for this study. The

diameters of 100 particles (selected from both on the surface and from the glue layer)

were measured and the mean particle size was 2.99 nm.   A histogram of the particle size

distribution is shown in Figure 5.8(c). The composition of this particle was confirmed

using EDS (Figure 5.8(d)). In contrast, there was no evidence of Rh-derived particles on

the surface of the CeO_2 film (Figure 5.9) in the calcined samples.

5.2.3.4 Transmission Electron Microscopy - Calcined and Reduced Samples

In an extension of the above work (reported in Section 5.2.3.3), both Pd/CeO$_2$ and Rh/CeO$_2$ model catalysts were calcined and reduced as described in Section 5.2.2. TEM results for the Pd/CeO$_2$ model catalyst are presented in Figure 5.180. In both low magnification TEM (Figure 5.180a) and HRTEM imaging (Figure 5.18b), crystalline Pd particles are clearly evident. Like the calcined-only Pd/CeO$_2$ sample, particles were both on the ceria surface and in the M-Bond layer. A histogram of the Pd particle sizes, presented in Figure 5.18c, illustrates that calcined and reduced particles are significantly larger (mean diameter of 11.0 nm) than particles in the calcined only sample. EDS was used to confirm the composition of the particles (Figure 5.10d).

In the case of the Rh/CeO$_2$ model catalyst, TEM investigation (Figure 5.11) shows the presence of metal particles on the CeO$_2$ (111) surface. Although no particles were seen in the calcined only sample (Figure 5.9), small Rh particles were observable in HRTEM in the calcined and reduced sample. The mean particle size for these particles was 1.7 nm. In order to gain spectroscopic confirmation of these particles, EDS was performed in STEM mode on the JEOL 2010F (Figure 5.11(d)).

5.2.4 Discussion

As was presented above, there were significant differences in the film quality and surface finish of the two CeO$_2$ films. However, θ/2θ XRD analysis (Figure 5.4 a) and subsequent TEM showed that the film and the substrate have an epitaxial relationship. Furthermore, both thin films are single crystalline with no secondary

phases.   Therefore, it is proposed that the observed difference in surface finish and crystalline-quality do not significantly contribute to differences in the metal support interaction between the precious metal and the ceria support.

In the investigation of the calcined samples, particles are evident on the oxide surface in the case of Pd/CeO$_2$. It should be noted that after calcination in air at 600ºC (873K) particles are likely oxidized to PdO.[25] The particle (shown in Figure 5.8b) shows crystalline lattice planes corresponding to crystalline metallic Pd. The presence of these fcc lattice features can most likely be attributed to electron beam reduction of PdO to metallic Pd, which is known to occur during TEM observation [26]. With reduction and annealing, Figure 5.10, significant particle growth takes place (most likely occurring during the two high temperature annealing treatments).

In the case of the Rh/CeO$_2$ model catalyst, distinct Rh particles are not visible after the initial calcination treatment.   This indicates that Rh did not agglomerate and remained essentially a monolayer of rhodium oxide (RhO$_x$).   A single monolayer of RhO$_x$ is not easily resolvable in cross sectional HRTEM, and the relative atomic numbers (45 for Rh and 58 for Ce) are not favorable for HAADF imaging. This difference in behavior suggests that the adhesive energy between the metal adatoms and the CeO$_2$ (111) surface is greater for Rh than it is for Pd. This effect has been suggested in previous STM studies on the nature of the CeO$_2$ interaction and Rh or Pd[20].   After the reduction and annealing cycles, small Rh particles are visible on the ceria surface (Figure 5.9), but the mean particle size is much smaller than that of similarly treated Pd, indicating a lower mobility for Rh on the CeO$_2$ (111) surface.

Figure 5.12 is a schematic of the agglomeration and growth mechanisms for both

Pd and Rh on the CeO_2 (111) surface. In both samples, the precious metal monolayer is

presumably oxidized after calcination. Visible PdO particles formed in the Pd samples,

but in the corresponding Rh sample, RhO_x particles were not visible after calcination.

After reduction and annealing, metallic particles were observed in HRTEM in both

samples, but the Pd particles had a notably larger mean particle size (11.0 ± 3.0 nm for Pd

vs. 1.7 ± 0.5 nm for Rh).   This indicates that Pd has a higher mobility than Rh on the

CeO_2 (111) surface.

Surface energy (γ) denotes the total energy content of a solid surface and is

equivalent to the surface tension of a liquid. Surface energy exists because the species of

a condensed phase are attracted to each other.[27] The lower the surface energy of a

substrate free surface (γ_s), the more difficult it becomes for an adhesive or coating to

"wet" that surface. In general, nucleation behavior of a metal is highly influenced by the

surface energy of the metal relative to that of the substrate.[28] The shape of a supported

metal particle can be used to measure the interaction energy between hard particles and

oxide surfaces.   One of the most common methods is estimating the deviation from the

ideal equilibrium particle shape, as predicted by Wulff in 1901.[29]   If the crystal is on a

support, then the interaction between the particle and the support will affect its

equilibrium shape[30]. Kaichew[31] and later Witterbottom[32], independently formulated that

the adhesion energy can be calculated from the equilibrium shape using the following

equations following Equation 5.1 (hereafter referred to as the Wulff-Kaichew

construction):

$$W_{adh} = \frac{\Delta h}{h} \times \gamma_{Pd(111)} \hspace{3cm} \text{Equation 5.1}$$

Where: W_{adh} = the adhesion energy between the Pd particle and the CeO_2 surface

h = deal equilibrium distance from an edge facet to center of the metal particle

Δh = change or truncation in the from the ideal Wulff shape

$\gamma_{Pd(111)}$ = free surface energy for (111) facet of Pd (0.665eV/Atom from [33])

Figure 5.13 illustrates the use Wulff-Kaichew construction to estimate adhesion energy along with an example of its application in a zirconia supported Pd model catalyst.   In previous investigations of model catalysts[34], this technique has been used in cross sectional HRTEM to provide direct visual evidence of the fundamental thermodynamic properties of metal particles and oxide supports.

In this study, the Wulf-Kaichew method was applied to estimate the adhesion energy between the metal particles and the CeO_2 surface.   We chose to focus on the calcined and reduced Pd sample because the particles were large enough to clearly estimate their equilibrium shape and the particles were mostly single crystalline (free of twin boundaries). Furthermore, due to the high number of surface and edge atoms, the Wulf-Kaichew construction is of limited applicability in particles much smaller than 10nm.[35] An example of the Wulf-Kaichew construction applied to the calcined and reduced Pd/CeO_2 is shown in Figure 5.14. Applying this equation to our data, the adhesion energy between Pd and YSZ (0.29 eV/atom) is roughly comparable with that between Pd and CeO_2 (0.33eV/atom).

5.2.5 Comparison to Theory

In an effort to further understand the experimentally observed trends, complimentary first principles calculations and molecular dynamics (MD) simulations were performed. These studies, performed by Bai Hai Li under the supervision of Liang Chen of the Chinese Academy of Sciences, were performed using the Vienna Ab Initio simulation package (VASP). Briefly, VASP is a plane wave, all-electron code that utilizes the projector-augmented wave (PAW) method for the treatment of the core electrons. VASP has been used for total energy calculations, as well as *ab-initio* MD simulations for a variety of topics in condensed matter physics, quantum chemistry, and material science.[36-37] Our first principles calculations utilized the Kohn–Sham density-functional theory (DFT) calculations. Climbing NEB methods were used to determine the minimum energy pathway. GGA_PBE was used to treat the electron exchange and correlation, and the cut-off energy for all calculations was 300 eV. Details of these complimentary theoretical calculations are presented in detail elsewhere.[38]

Briefly, we present some selected theoretical results that support our experimental observations. The first experimental observation was that the PdO particles formed on the CeO_2 surface after calcination, while RhOx particles were not observable. The first DFT calculation was a determination of the absorption geometry and binding orientation of single metal atoms (M_1), tetrahedra (M_4=four atom clusters), and icosahedra (M_{13}=13 atom clusters) on the CeO_2 (111) surface. A representation of these binding energies is provided in Figure 5.15. The corresponding adhesion energies and cohesive energies are provided in Table 5.2. Since the adhesion energy is less than the cohesive energy for both metals, cluster formation is energetically favorable for both metals. However, in our

experimental studies, cluster formation was not observed in the calcined Rh/CeO$_2$ model catalyst. This could be due to differences in the adhesive energies of these metals to the CeO$_2$ surface, which is supported by the DFT calculations showing that the adhesion energies for Rh are higher than those for Pd. Additionally, as the cluster gets larger, the adhesion decreases. The E$_{adh}$(Pd$_{13}$) is comparable to what was estimated from the Wulf-Kaichew construction (0.27 eV/atom vs. 0.33 eV/atom respectively).

In an attempt to identify the specific surface diffusion mechanism that occurs during clustering, potential energy plots were constructed and shown in Figure 5.16. Although both metals seem to favor the same scheme of surface diffusion for clustering, the energy barriers for diffusion of Rh are significantly higher than the barriers for Pd. The highest energy barriers in this proposed clustering scheme are 0.50 eV for Pd and 0.33 eV for Rh. Elementary diffusion theory reminds us that the energy barrier for diffusion and the mobility of a given species are inversely related.[39-40] This result supports our experimentally observed results for both the calcined and the reduced and annealed catalysts. After reduction, both metals favored clustering as was predicted by DFT calculations. However, particle growth in the Pd catalysts was much greater than Rh due to their higher mobility.

Differences in the experimental data, notably the kinetics of island formation, were further explored using *ab-initio* MD simulations. MD simulations showed that Pd atoms formed clusters (within 2500 fs) by 627ºC. On the other hand, Rh atoms formed a RhOx layer but did not form distinct clusters (up to 5000 fs) at 927ºC. Snapshots of the MD simulations are provided in Figure 5.17. Again, the presence of this oxide overlayer provides further clarification of the experimentally observed differences in these two

metals. Providing further agreement with experimental results, additional MD

simulations of the behavior of this RhO_x overlayer after reduction (removing the

outermost oxygen atoms), showed that clustering can occur under these conditions.

These theoretical calculations along with MD simulations tend to support the

experimentally determined observation on the nature of agglomeration and coarsening in

Pd and Rh on the CeO_2 (111) surface. However, it is important to point out some

differences that prevented us from making more conclusive parallels.   The first is that

calcined-only samples were calcined in air under a constant oxygen partial pressure,

while the theoretical calculations were performed in vacuum. Additionally, constrained

by the cost of computing resources, the cluster sizes considered in the energetics

calculations were quite small (a maximum of 13 atoms). For the same reason, the *ab-

intio* simulations were performed on relatively short time scales, where longer time scales

might have yielded a more realistic picture of the agglomeration and coarsening behavior.

For these reasons, the most we can say is that the experimental results are consistent with

present theoretical calculations of the relative stabilities and motilities of Pd and Rh

atoms and clusters on $CeO_2(111)$.

5.3 Role of Stress in Oxide Wetting of Metal Particles in Ceria-Zirconia-Supported Pd Catalysts

5.3.1 Background and Objectives

Pd encapsulation from ceria-zirconia is a potentially major problem in

automotive TWCs which leads to an irreversible decrease in activity and a corresponding

increase in precious metal cost to suppliers.[41-42] Cross-sectional HRTEM studies of

Pd/CZO model catalysts has previously provided visual evidence for this phenomenon with the observation of partial Pd particle encapsulation due to the migration of the CZO support material resulting in particle wetting.[43-44] Although the previous research emphasized the role of ceria in driving this phenomenon, the more recent results (presented in Section 5.2) indicate that pure CeO_2 is not as likely to undergo migration and wetting as CZO. In fact, the Pd/CeO_2 system appears more like Pd/YSZ than Pd/CZO (shown schematically in Figure 5.18). It is possible that this difference may be explained in part by the fact that ceria-zirconia mixed oxides (containing between 20-50% mole fraction zirconia) are known to have a high oxygen storage capacity, and are therefore much more reducible than pure CeO_2.[22]

While the difference between CeO_2 and CZO in their wetting behavior of Pd may be due to real chemical differences, another possible driver could be the difference in internal stress; i.e. reduction generates a compressive stress in the film (due to the creation of Ce^{+3} ions, which are about 10% larger than the original Ce^{+4} cations), but the stress is much greater in CZO than in CeO_2 due to the greater reducibility of CZO.[22] Another possible source of stress is the effect, if any, of native misfit compressive stress in the film arising from the misfit between the lattice parameters of the substrate YSZ (α = 5.139Å)[43] and $Ce_{0.7}Zr_{0.3}O_2$ (α = 5.381Å)[44]. Therefore, the objective of this investigation on the role of stress in oxide wetting is to expand on previous work [34, 45] and reveal additional subtleties involved in ceria-based catalyst support migration and particle wetting.

5.3.2 Experimental Methods

In this investigation of Pd supported on ceria based oxides, CZO thin films with a target composition of ($Ce_{0.7}Zr_{0.3}O_2$) were grown on commercial YSZ(111) by oxygen plasma-assisted molecular beam epitaxy (OPA-MBE) in a dedicated dual chamber ultrahigh vacuum (UHV) system, configured specifically for oxide epitaxy and described in Section 2.3.2. The YSZ (111) (10x10x1 mm) substrates were ultrasonically cleaned in acetone for ~10 min prior to loading into the UHV system. The substrate in the chamber was then cleaned at 650°C for ~10 min by exposure to oxygen plasma operating at 200 W under ~2×10^{-5} Torr of O_2; the same condition was maintained till the end of deposition. High-purity cerium and zirconium metals (99.9%) were used as the source materials in an electron beam evaporator. The thin films were grown by directing the predetermined quantity of Ce and Zr metal fluxes onto the substrate, which was kept at 650°C in activated oxygen plasma. The thin film growth was monitored using *in-situ* RHEED with 15 kV e$^-$ beam at an incidence angle of ~3-5°. The target thickness of these films ranged from 10nm to 100nm. In addition, one film was a bi-layer consisting of a 10nm $Ce_{0.7}Zr_{0.3}O_2$ layer on a 100nm CeO_2 layer on top of the YSZ substrate. The films examined in this study are shown in Table 5.3. Following MBE growth, CZO films were studied *ex situ* using XRD, AFM, and XPS.

Rutherford backscattering spectrometry (RBS) experiments along both random and channeling directions using a 2.0 MeV He$^+$ ion beam were also carried out in the Environmental Molecular Sciences Laboratory (EMSL) accelerator facility at the Pacific Northwest National Laboratory (PNNL). The backscattering spectra were collected using

a silicon surface barrier detector at a scattering angle of 150°. The details of the accelerator facility and the end stations are described elsewhere.[46-47]

Metal deposition and thermal treatments generally parallel conditions identified in previous investigations[16] and described in Section 5.2.2. One notable exception is that in this study (Pd/CZO), we chose to focus on the effect of calcination and subsequent reduction and annealing, while the investigation of Pd/CeO_2 focused on both calcined-only and the calcined/reduced/annealed samples. Briefly, thermal treatments were performed in a four channel quartz tube furnace. To ensure that the CZO films were fully oxidized, all films were calcined (600ºC in air) before a monolayer of Pd was deposited using the UHV system described in Sections 5.2.2 and 2.3.3. In order to best observe the partial encapsulation phenomena, we selected the treatment protocol that provided the highest degree of partial wetting in previous investigations.[45] This previously identified protocol (shown in Figure 5.3) consisted of calcination in air, followed by two cycles of low temperature reduction (200ºC 1% H_2 in N_2) and an extended high temperature annealing (700ºC flowing N_2).

Three microscopes were used for analysis of the model catalysts: a JEOL 3011 for HRTEM, a JEOL 2010F for HAADF, and a JEOL 2100F for aberration corrected HADDF imaging and EELS spectrum imaging. All of these microscopes are located at The University of Michigan and have been described in greater detail earlier in this thesis.

5.3.3 Results

Film growth was monitored *in-situ* using RHEED, and film quality was further

explored using a variety of *ex-situ* characterization techniques such as AFM and RBS.

Selected MBE grown CZO films were further characterized using a variety of XRD

techniques. Film thickness was measured by Keissig fringe analysis in XRR (as

described in Section 2.2.2.2 and demonstrated in Figure 2.10).   Examples of $\theta/2\theta$

measurements and ω-rocking curve measurements for selected CZO films are presented

in Figure 5.19. The $\theta/2\theta$ measurements confirm that CZO films are single crystalline and

are in an epitaxial relationship with the YSZ (111) substrates, but they can be further

utilized to provide some insights into film strain. As was mentioned in section 2.2.2,

shifts combining the Bragg equation with the plane spacing equation for cubic crystals

can be used to measure lattice constant. Therefore, shifts in the peak location of the CZO

(111) peak relative to YSZ reflect true differences in strain state with changes in film

thickness, as shown in Figure 5.19a. The ω-scan (rocking curve) of sample CZ3 is

provided in Figure 5.19b. The full width at half maximum of the $Ce_{0.7}Zr_{0.3}O_2$ (111)

reflection is 0.925°. This indicates a high crystal quality considering the film thickness

(47.6 nm) and the fact that rocking curve breadth increases with increasing Zr doping due

to large lattice distortions.[46] All of these characterization techniques demonstrated that

the MBE grown films were relatively smooth (<1 nm RMS) and of acceptable crystalline

quality.

Film quality was further analyzed using Rutherford backscattering spectroscopy

(RBS). As mentioned in Chapter 2, RBS spectroscopy is a versatile materials

characterization technique that can be used to determine strain, crystalline quality, and

composition.   Figure 5.20 shows results of RBS channeling data for sample CZ3

(47.3nm CZO film). Two Ce peaks are observed in the channeling spectrum,

representing the surface peak and the interface lattice disorder, respectively. The window

defined by the dashed lines (Figure 5.20) was used for estimation of the minimum yield.

The minimum yield (χ_{min}) was calculated from this data to be ~13% for the interior of the

CZO film, indicating a high film quality. However, the severe peak overlap makes a

more accurate interpretation of crystalline quality difficult.

CZO film composition was characterized at PNNL using XPS as described in

Section 2.2.3.2, and the results are summarized in Table 5.4. The target film composition

for the CZO films was $Ce_{(1-x)}Zr_xO_2$ with x=0.3. XPS results indicate that the actual

composition ranged from 28 – 39% Zr with a mean composition of 34.0 ± 5.4% Zr.

Similar to Section 5.3.2 , a monolayer equivalent of Pd was deposited under UHV

conditions at room temperature. As was presented in Section 5.2, the amount of actual Pd

deposited was estimated from previous experience with this UHV system and monitored

using XPS.

TEM and AFM reveal some details about the strain state of the MBE grown CZO

films on YSZ. Results from the 10nm Pd/CZO sample are presented in Figure 5.21. In

this figure, results are shown for both the film "as deposited" (with no thermal treatment

after metal UHV metal deposition, Figure 5.21 a-b) and after the calcination and

extended reduction cycle, Figure 5.21 c-d. Both HAADF and HRTEM examination of

the "as deposited" sample indicated that the film is smooth, with no cracks or voids.

Also, small (~2nm) distinct Pd particles are visible in the "as-deposited" Pd/CZ1 film

(Figure 5.21 b), giving further evidence that significant agglomeration occurs with room temperature deposition of Pd under UHV.[20]

HRTEM (Figure 5.21 c) of calcined and extended reduced sample showed a much rougher film surface characterized by film fracture to the YSZ substrate and the formation of 10-20nm islands of CZO along with ~10nm Pd particles. AFM analysis of the corresponding film (Figure 5.21 d) supports these HRTEM results, as RMS roughness has increased to 7.244nm. Furthermore, it should be noted that similar surface roughing took place in both Pd/CZ2 as well as the CZ1 samples without Pd.

Cross section TEM analysis of the CZO-YSZ interface supports XRD and RBS inferences about the strain state in thicker films. Figure 5.22a shows a HAADF STEM image of the interfacial region of a calcined and reduced CZ3(47nm) CZO film. In this image, misfit dislocations are clearly evident in the Fourier filtered image (Figure 5.22b) and are indicated by arrows. The nature of these dislocations is further illuminated in a high resolution aberration-corrected HAADF STEM image of a dislocation core in this film (Figure 5.22c). A Burger circuit around the dislocation core shows the burgers vector to be $\mathbf{b}=\alpha_{CZO}[¼-½¼]$. The average measured dislocation spacing was 6.9±0.9nm.

TEM was also performed on calcined and reduced Pd supported CZO films of varying thickness. TEM images of model catalysts supported on CZ3, CZ5, and CZ6 (bi-layer) films are shown in Figure 5.23 a-c, respectively. The particle size distribution was measured for Pd/CZ3 sample, and Pd particles were found to be normally distributed with a mean particle size of 14.5 ± 4.04 nm.

Examining the Pd/CZO model catalysts on in the JEOL 2100F provides us the opportunity for not only aberration-corrected imaging, but also the capability of

performing electron energy loss spectroscopy (EELS) with high spatial resolution. As

mentioned in section 2.2.15, EELS can be used to determine the oxidation state of

transition metals. Figure 5.24 shows a survey HAADF image (Figure 5.24a) along with

point-and-shoot EELS spectra from various points in the film. It should be mentioned

that the camera length for this image was 2cm to optimize for high EELS counts;

therefore, the image resolution is not as high as it could be for aberration corrected

HAADF imaging. From this analysis we can observe that the Ce M4-to-M5 ratio varies

from 1.2 close to the surface (marked "D" in figure 5.24) to over 1.5 approximately

10nm into the CZO layer (marked "A").

Combining this observation with EELS spectrum imaging along with STEM can

provide useful information on the spatial effect of metal on the reduction of CZO support.

Figure 5.25 presents a HHADF survey image along with an image obtained from

spectrum imaging on the JEOL 2100F. The Figure 5.25b provides an image of the cerium

M4-to-M5 ratio over a 10.8nm x 41.8nm area near the surface of the CZO film near a

partially encapsulated Pd particle (the film in question in this sample was CZ6).   The

pixel size for this measurement was (1.8nmx1.8nm) and the dwell time per pixel was 5

seconds. In contrast, the background normalized EELS spectra in a region of the CZO

film far away (>500nm) from a partially encapsulated Pd particle does not show

significant variation with depth into the film (Figure 5.26).

5.3.4 Discussion

As stated earlier, MBE growth conditions were optimized by characterizing the

films using RBS, RHEED, AFM, and X-ray characterization to produce smooth, single-

crystalline, high quality films. Severe film roughening was observed in several cross

sections of calcined and reduced CZ1 and CZ2. The fact that this phenomenon was

observed in several cross-sections of these thinner CZO films and not observed in the

thicker ones (above ~47.5 nm) provides some insights into the strain state in these thinner

films. As the thickness of these films is less than the critical thickness for stress

relaxation (given that t_{cr} = ~50nm in CeO_2/YSZ [48], where the lattice mismatch is less), we

propose that the catastrophic film fracture is the result of a combination of high

temperatures and the additional stress brought on by reduction. Diffusive mass transport

to relax strain energy is a common mechanism for rapid roughening in heteroepitaxial

films[49], and similar island morphologies have been formed from controlled annealing

experiments of epitaxially grown semiconductors.[50] In our current set of films, the

thicker films had better structural integrity and were significantly thicker than t_{cr}; thus

they experienced a smaller contribution from intrinsic misfit strain. Therefore, although

the thinner films (CZ1 and CZ2) might be highly strained, their tendency to quickly

roughen renders them not useful under our treatment protocol. However, the tendency to

roughen provides us with the evidence that there are, in fact, real differences in the strain

state of the thinner films.

Our calcination and reduction treatment of Pd on CZO supports that were thicker

than 47nm did not induce catastrophic film fracture, and HRTEM revealed that all

samples showed some degree of partial encapsulation after calcination and extended

reduction, confirming previously reported results[45]. Caution should be used when making

conclusive statements relating the degree of encapsulation to film thickness because there

was larger variability in morphology within samples than between samples. On a second

related note, only a small fraction of the metal particles were imaged. The most common artifact of sample preparation was the tendency of Pd particles to dislodge from the sample surface during observation in the microscope (similar to the particle separation observed in Section 5.3.3) leaving behind a "crater" from the particle encapsulation. Given this, we will present qualitative comments on the occurrence of Pd encapsulation.

The mean particle size of the CZO (111) supported Pd particles was 14.80 ± 4.04 nm, larger than the mean particle size for Pd/CeO_2(111) (11 ± 2.99 nm presented in Figure 5.10). Statistical analysis comparing the particle size distributions of Pd/CeO_2 and Pd/CZO indicates that the observed difference in the mean particle sizes is significant (e.g. that these differences did not arise from random variation). Whether this apparent difference in mobility is truly an effect of the strong metal support interactions (SMSI) has been the topic of debate for some time in many other TiO_2-based catalyst systems.[51-52] This result is somewhat surprising because Pd/CeO_2 does not show particle wetting. Additionally, DFT calculations, in a study that did not account for any ensemble effects in a mixed oxide, show nearly identical energetics between Pd/CeO_2 and $Pd/c-ZrO_2$.[53] Moreover, it is important to consider that slight differences in metal loading may be responsible for the observed differences in particle size.[54] Therefore, although the mean particle sizes differ statistically, they are comparable, and these differences might not be due to differences in attractive forces.

The objective of investigating the CZ6 (a bi-layer) film was to generate a surface in which the (CZO) film would actually be under tensile stress initially. This would occur because a thick (100nm) CeO_2 buffer layer (with lattice constant larger than CZO) should be almost fully relaxed[48]. Since the $CZO-CeO_2$ interface is presumed to be

coherent (due the very small thickness of the CZO film), the lattice mismatch between

CeO_2 and $Ce_{0.7}Zr_{0.3}O_2$ should leave the 10nm film in tension initially. The reference

lattice parameters of the materials used in this study are provided in Table 5.5.

Upon reduction, some of the Ce^{4+} will be reduced C^{3+} ions, which are about 10%

larger than the original Ce^{4+} cations.[55] This change in ionic radius could result in the

introduction of additional compressive stress in CZO film. In order to estimate the strain

induced by reduction, the percentage of Ce in the $Ce_{0.7}Zr_{0.3}O_2$ film that was reduced was

estimated from previous XPS investigations[16, 56] of aged model powder catalysts.

Assuming comparable levels of reduction took place for our current reducing treatments,

we concluded that 39% of Ce cations were reduced from Ce^{4+} to Ce^{3+}.

First principles calculations[57-58] and experiments[59] have identified cubic phases of cubic

$CeO_{1.5}$ with a fluorite structure (space from Fm-3m). A Vegard's type relationship was

used to calculate the lattice parameter of $0.7((CeO_{1.5})_{0.39}+(CeO_2)_{0.61})+0.3(ZrO_2)$ to be

5.371Å . This value corresponds to lattice parameter expansion of approximately 1%

upon reduction.

Table 5.6 lists the misfit strain between films and substrates at various points in

this study. Because the top CZO layer of the bi-layer film is initially in tension, this

compression induced by reduction does not overcome the native misfit between CZO and

CeO_2. Therefore, because some degree of wetting is observed in both thick single layers

and this bi-layer configuration, we can make a qualitative argument that induced

compressive film strain is not a major contributor to the partial encapsulation phenomena.

Our study has provided further evidence to support the many chemical explanations (such

as: SMSI, shadow diffusion, oxygen vacancy migration) that have been previously postulated by other researchers.

Several researchers have used the so called "white line" ratio to determine the oxidation state of Ce.[60-62]   In previous studies[63], an EELS spectrum taken near the free surface of a reduced film found that a significant proportion of the Ce in the $Ce_{0.7}Zr_{0.3}O_2$ was reduced to Ce^{3+} (characterized by ratio, Ce_{M4} /C_{M5}, being less than 1) while the oxidation state of Ce at the CZO/YSZ interface remained tetravalent (4+). This result was reproduced in this present work using EELS in conjunction with conventional transmission electron microscopy. TPR experiments[16] have shown that the presence of Pd lowers the reduction temperature of $Ce_{0.7}Zr_{0.3}O_2$, and we suspect that there is a significant variation in Ce^{+3} concentration in regions near Pd particles. Exploration of this hypothesis requires high resolution EELS spectrum imaging which was not possible in the previous studies.[45]

In order to determine the extent to which regions containing Ce^{3+} are localized around the Pd particles in this study, STEM EELS was performed on calcined and reduced Pd/CZ6 model catalysts. The relatively large pixel size for this measurement (1.8nmx1.8nm) resulted in lower beam intensity on a given area of specimen thereby decreasing the likelihood of adverse beam interaction, which has been reported in previous investigations. [60, 64] The plot of the Ce M4-to-M5 ratio in a region near a partially encapsulated particle (Figure 5.25b), does not conclusively show a variation in Ce^{3+} concentration within the surface. These results do, however, increase the granularity of previous results and indicate that the most reduced region of the CZO film (indicated as dark blue in Figure 5.25b) is confined in a very thin region near the film

surface. Within a few nanometers from the surface, the CZO film appears to be fully

oxidized, although this could due to the influence of the nearby ceria substrate. It should

be noted, however, that a significant variation between the surface and the interior of the

film was not found in thin regions that were far (>500nm) away from Pd particles (Figure

5.26). Although these initial results aimed at determining the spatial extent of the effect

of Pd on the reducibility of CZO are promising, more experiments should be performed

to obtain a more complete picture.

5.4 Conclusions

In the first section of this chapter (Section 5.2), we presented fundamental

studies of the behavior of Pd and Rh on single crystalline, PLD-grown CeO_2 films

epitaxially grown on the (111) surface of yttria stabilized zirconia (YSZ). In the calcined

samples, HRTEM revealed the presence of PdO particles (particle size 2.99 ± 1.42 nm).

However, RhO_x particles were not visible on the surface in HRTEM after calcination in

air, indicating thermodynamic differences in the behavior of Pd and Rh on (111) CeO_2.

Extending the above thermal treatment to calcined, reduced, and annealed

samples, HRTEM revealed that Rh does cluster after reduction, yet the lower mobility of

Rh on (111) CeO_2 limits the resultant particle size. After the same treatment, significant

Pd particle growth occurs most likely during the annealing cycles. In either case for both

metals, wetting of the Pd particles by ceria was not observed. Our results are consistent

with theoretical calculations which show that kinetically, Pd exhibits greater tendency to

agglomerate into 3D particles than Rh. The MD simulations show that under oxidative

conditions, the strong Rh-O interactions inhibit Rh agglomeration. However,

agglomeration of metallic Rh is possible under reducing conditions. Generally, experimental TEM observations are consistent with theoretical calculations of the relative stabilities of Pd and Rh atoms and clusters on $CeO_2(111)$.

The second section of this chapter (5.3) focused on the effect, if any, of native misfit compressive stress in the film arising from the misfit between the lattice parameters of the substrate YSZ ($\alpha = 5.139$ Å) and $Ce_{0.7}Zr_{0.3}O_2$ ($\alpha = 5.381$Å). In this study, single crystalline, $Ce_{0.7}Zr_{0.3}O_2$ films were grown via MBE onto (111)YSZ. RHEED, XRD and AFM confirmed a high crystalline quality with a good surface finish for most samples. Very thin CZO film underwent severe roughening after calcination and reduction, a phenomena not observed in thicker (t>47nm) films.

In the thicker films, the previously observed partial encapsulation phenomenon was observed. However, the particle size distribution of the Pd particles on the CZO surface was larger, yet comparable, to the one observed from Pd/CeO_2. This difference may be attributable to a true chemical difference in the relative mobilities and attractive forces between Pd and CeO_2 or CZO. The fact the wetting phenomena was observed in all films above the critical thickness suggests that film stress in not a major contributor the particle wetting. To further test the importance of film stress, the bi-layer film was constructed so as to ensure that the film was actually in tension upon reduction. Wetting was also observed in this film, in tension, lending credence to the likelihood that this phenomenon is due to real chemical differences or more subtle effects of stress, such as stress gradients around Pd particles. Although the previous work [45] emphasized the role of Ce in driving this interaction, these results indicate the driver for partial encapsulation reside in the nature of the mixed cerium-zirconium oxides.

5.5 Tables

Table 5.1: Model catalysts and treatments presented in Section 5.2

Film ID	Substrate	CeO$_2$ Thickness	Metal	Treatments
A	MTI	147 nm	Pd	Calcined
A	MTI	147 nm	Pd	Calcined +2 x Reduced
B	Princeton Scientific	153 nm	Rh	Calcined
B	Princeton Scientific	153 nm	Rh	Calcined +2 x Reduced

Table 5.2: Adhesion and cohesive energies of M_1, M_4, M_{13} (M= Pd, Rh) clusters on the CeO_2 (111) surface)

	M_1/CeO$_2$(111)	**M_4/CeO$_2$(111)**	**M_{13}/CeO$_2$(111)**
$E_{adh}(Pd)$	1.87 eV/atom	0.78 eV/atom	0.27 eV/atom
$E_{coh}(Pd)$	-	1.69 eV/atom	2.32 eV/atom
$E_{adh}(Rh)$	2.86 eV/atom	1.10 eV/atom	0.31 eV/atom
$E_{coh}(Rh)$	-	2.62 eV/atom	3.63 eV/atom

Table 5.3:   MBE grown films used in Section 5.3

	Sample ID	Sample #	Thickness (nm)	
			Target	XRR
	CZ1	081209-b	10	11
	CZ2	050109	50	39
CZO	CZ3	022710	50	47.3
	CZ4	061809	50	48
	CZ5	081209-a	100	90
CZO/CeO$_2$/YSZ	CZ6	081309	10 CZO 100 CeO$_2$	115

Table 5.4: Film composition of MBE grown CZO films measured by XPS

Sample ID	Thickness (nm)	Cation %	
		Ce	Zr
CZ1	11	66.8	33.2
CZ2	39	64.94	35.06
CZ5	90	60.8	39.2
CZ6	115	71.69	28.31

Table 5.5: Bulk lattice-parameters of materials used in this study

Material	Bulk lattice Parameter (nm)	Reference
CeO_2	0.5411	NIST
$Y:ZrO_2$	0.5141	Bokhimi[65]
$Ce_{0.7}Zr_{0.3}O_2$	0.5330	Yashima[66]
$CeO_{1.5}$	0.5565	Kawabuchi[59]
Reduced CZO	0.5372	Calculated*

*see text

Table 5.6: Lattice mismatch between films and substrates

Lattice Mismatch	YSZ	CeO$_2$
CeO$_2$	5.01%	-
CZO	3.38%	-1.71%
Reduced CZO	4.32%	-0.73%

*calculated (see text)
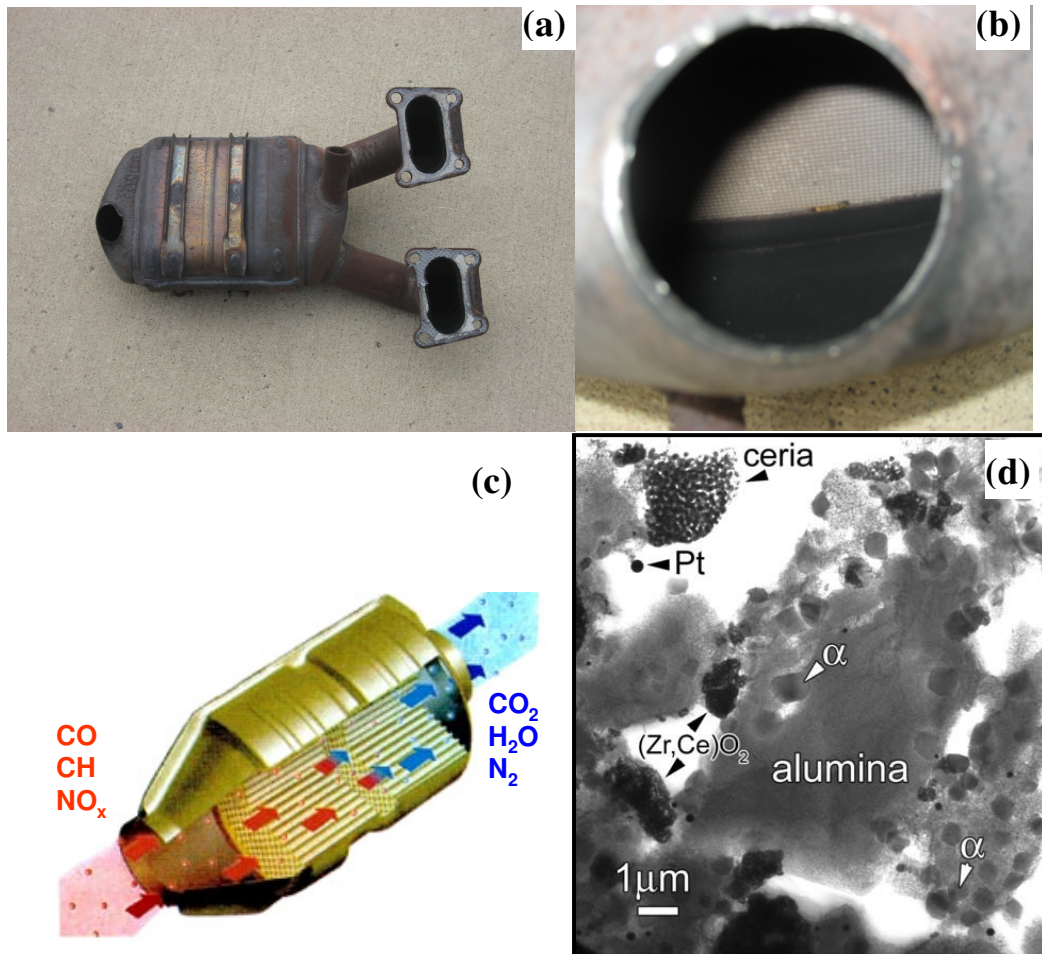
Figure 5.1: (a) photograph of modern catalytic converter from 1999 Nissain Senta GXE, (b) close-up photograph of the ceramic monolith showing channels in the ceramic monolith. (c) diagram of an automotive TWC showing common reactants and products (from McCabe[67]), and (d) TEM image of general microstructure of aged commercial TWC washcoat (reproduced from Hangas[68])
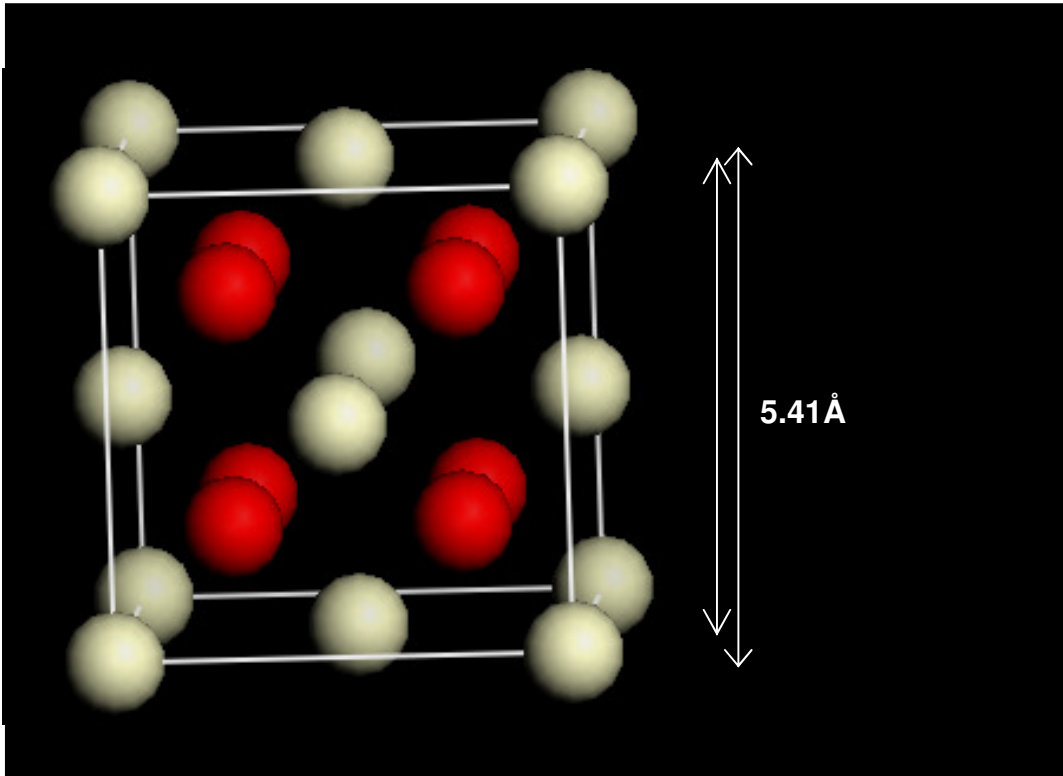
Figure 5.2: Fluorite structure of CeO$_2$ showing Ce atoms in red and oxygen atoms in white.
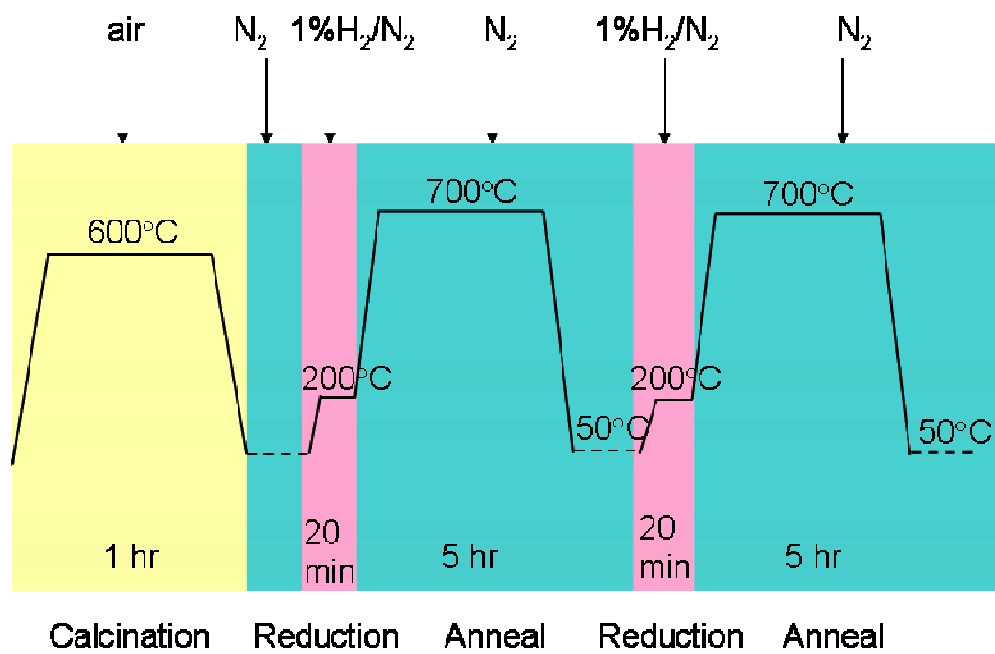
Figure 5.3: Aging protocol used for calcination and reduction treatment with extended high temperature N_2 annealing
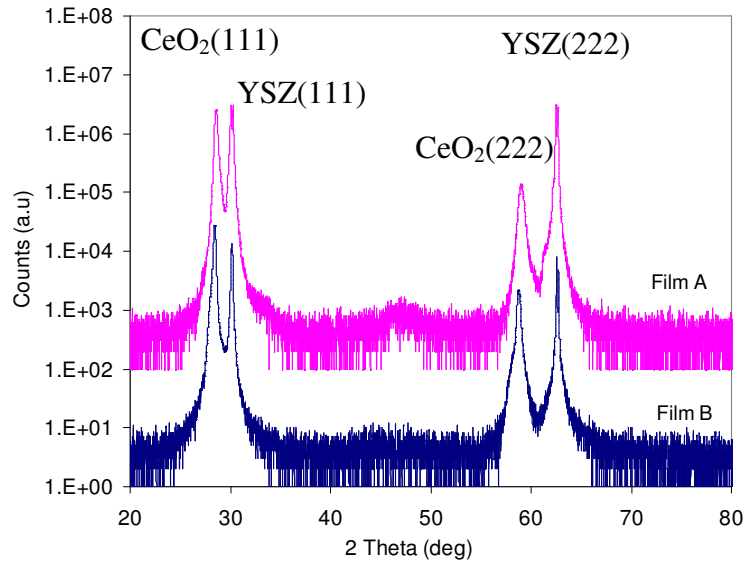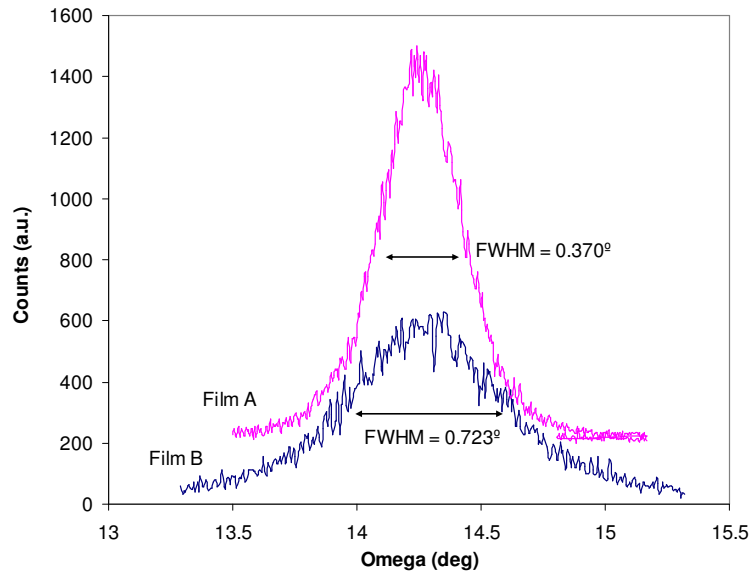
Figure 5.4: (a) θ/2θ XRD scans and (b) ω-rocking curve (around the CeO$_2$ (111) peak) of single crystalline CeO$_2$ films grown by PLD
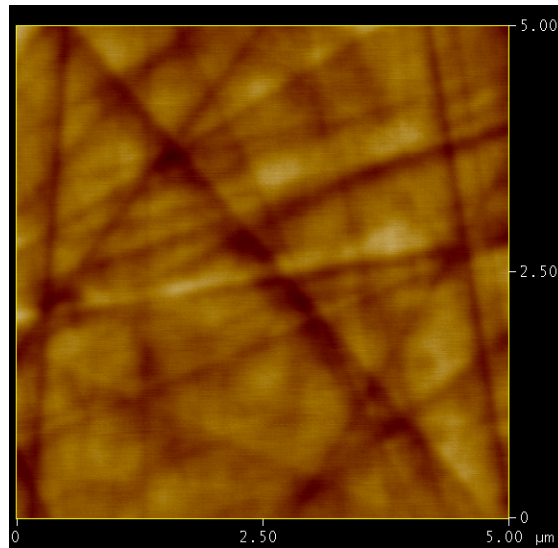
(a)
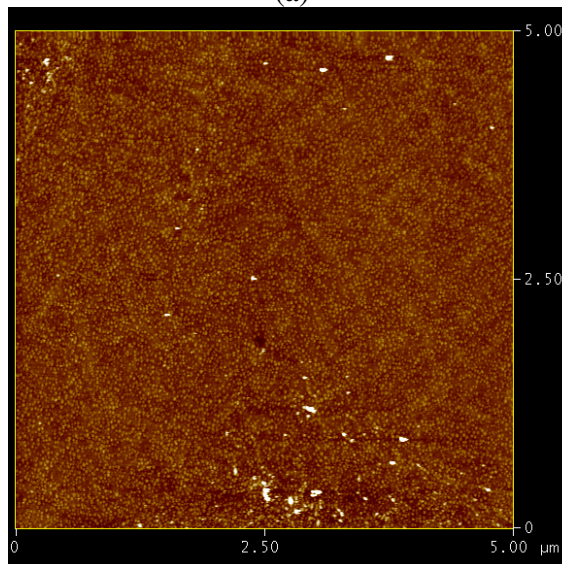
(b)

Figure 5.5: AFM surface plots for (a) Film A and (B) Film B.   The measured root mean squared (rms) roughness is 0.711nm and 0.415nm respectively.
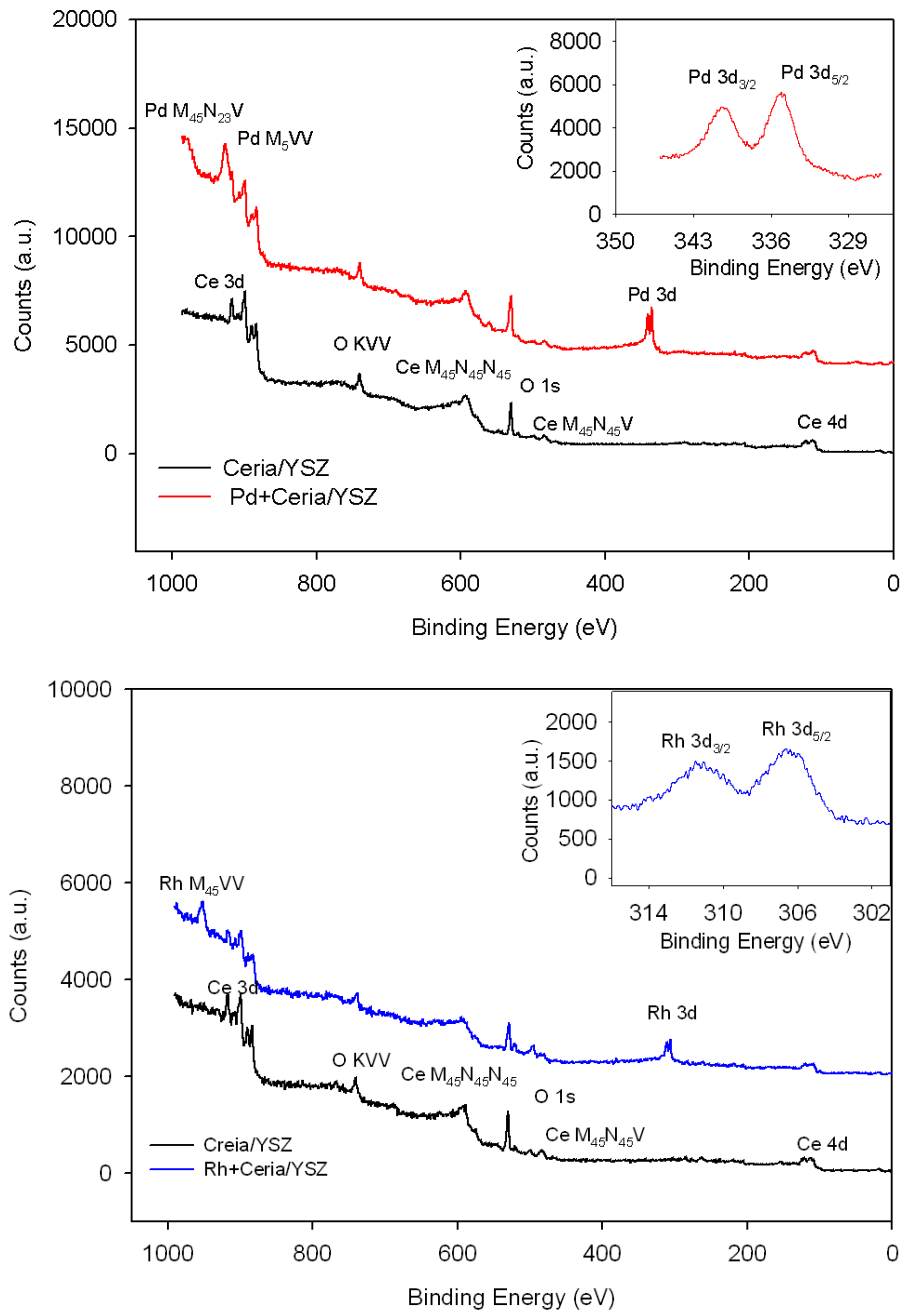
Figure 5.6: XPS spectra of CeO$_2$/YSZ films before and after (top) Pd deposition and (bottom) Rh deposition. Inserts show detail of the Pd-3d and Rh-3d spectra, respectively.
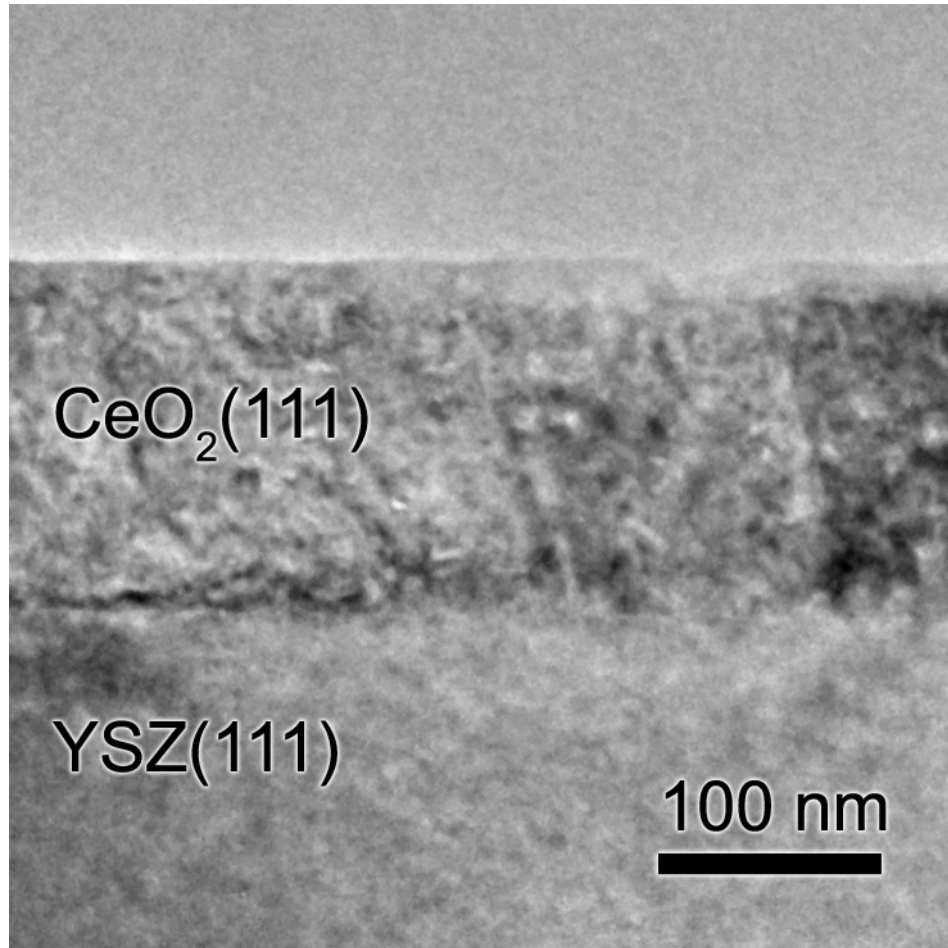
Figure 5.7: Low magnification cross-sectional TEM image of a PLD grown CeO$_2$ film (Film A) on a YSZ substrate
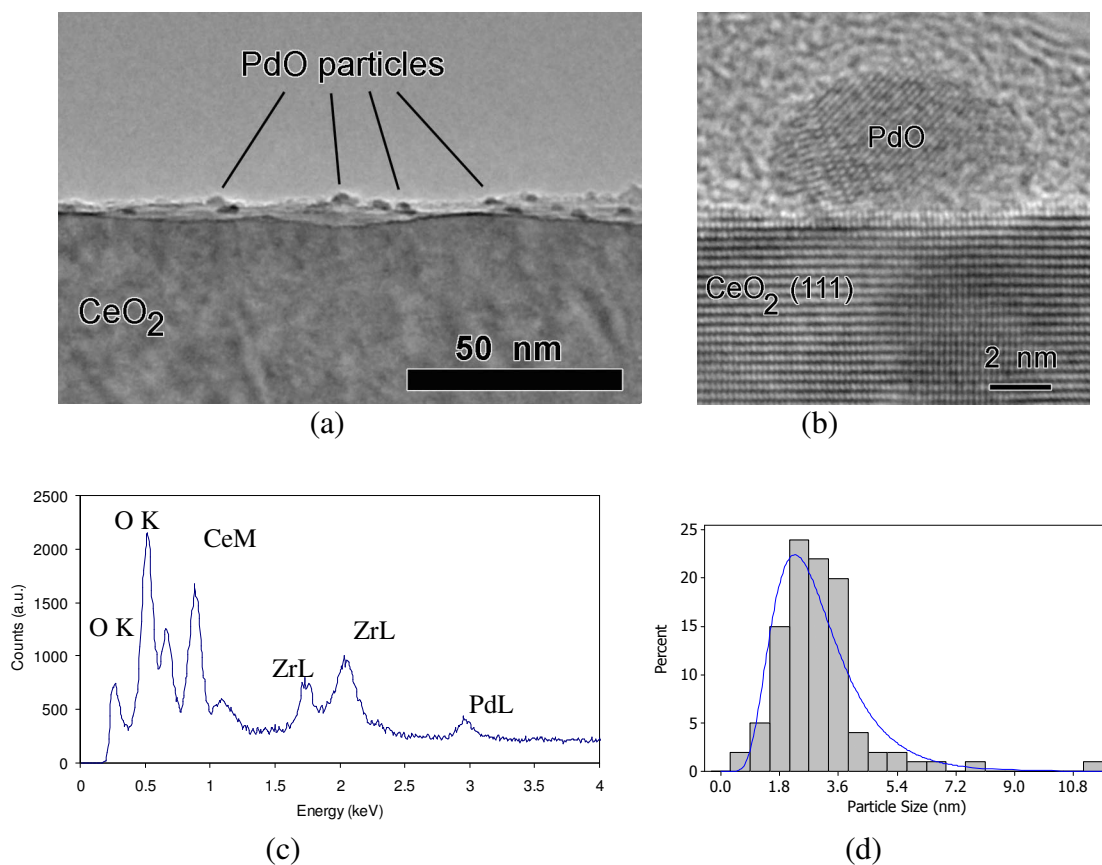
Figure 5.8: (a) Low magnification TEM micrograph and (b) HRTEM of calcined Pd/CeO₂ sample. (c)EDS spectra of the surface region, (d) histogram illustrating the particle size distribution on the film surface.

{RhOx}

CeO2 (111)

50 nm

(a)

{RhOx}

CeO2 (111)

2 nm
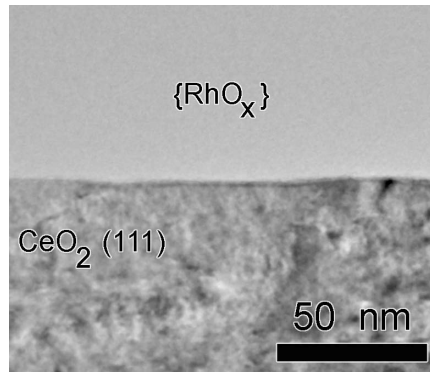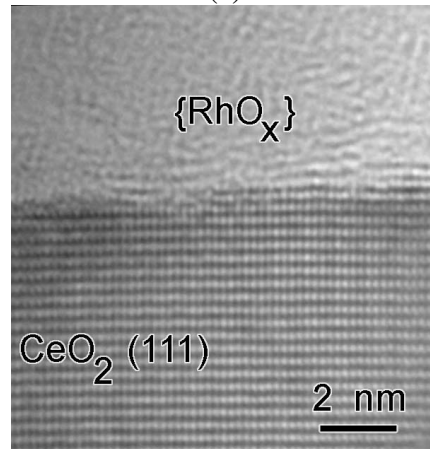
(b)

Figure 5.9: (a) Cross section TEM image of Rh/CeO$_2$ film after calcinations (b) HRTEM of CeO$_2$ surface. Neither image shows Rh particles

(a)

(b)

(c)

(d)
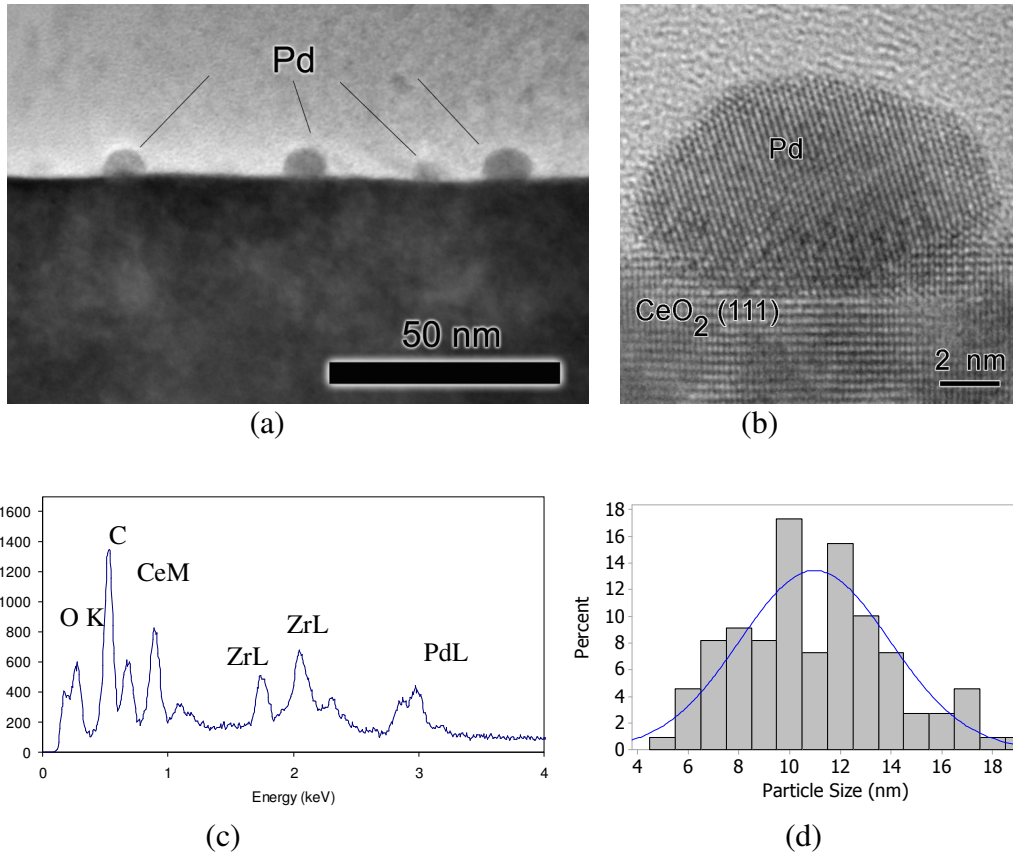
Figure 5.10: (a) Low magnification TEM micrograph and (b) HRTEM of calcined and reduced Pd/CeO$_2$ sample. (c)EDS spectra of the surface region, (d) histogram illustrating the particle size distribution on the film surface
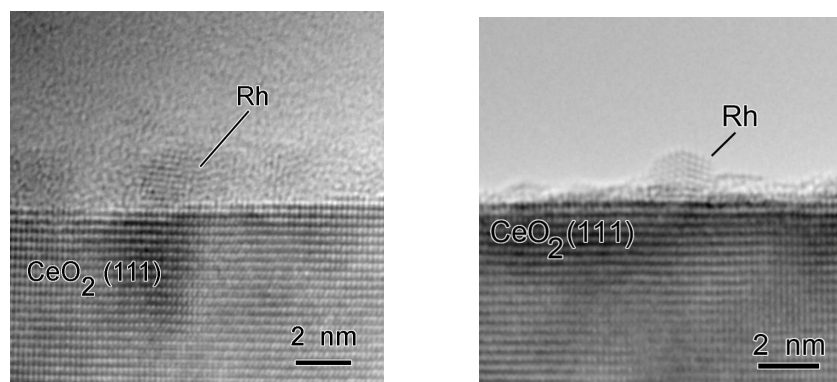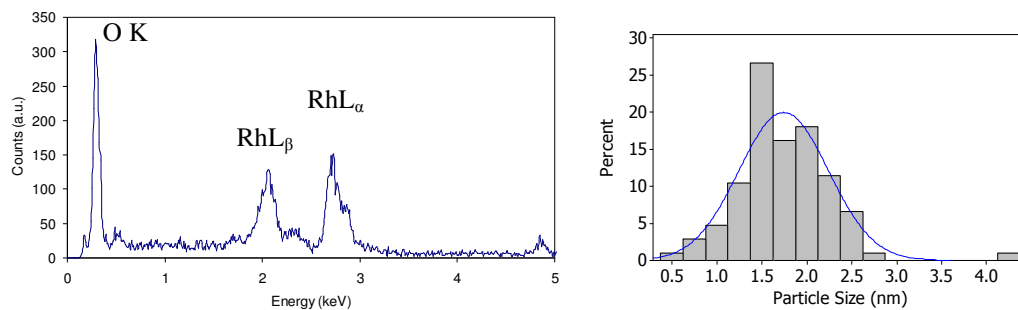
Figure 5.11: (a and b) HRTEM of surface of calcined and reduced Rh/CeO$_2$ sample. (c) EDS spectra of the metallic particles confirming the composition of the particles in Rh, (d) histogram illustrating the particle size distribution metal particles taken from particles on the surface as well as encapsulated in the glue layer. (Note that probe size used for EDS of Rh is smaller than that used for EDS of Pd in Figs. 5.8 and 5.10, allowing clear separation of CeO$_2$ and YSZ peaks).

'as deposited"   calcined   reduced and annealed

1 -6 nm   6 -16 nm

1-2 nm

● Metallic Pd,Rh
◉ Metal oxide (MO_x =Pd,Rh)
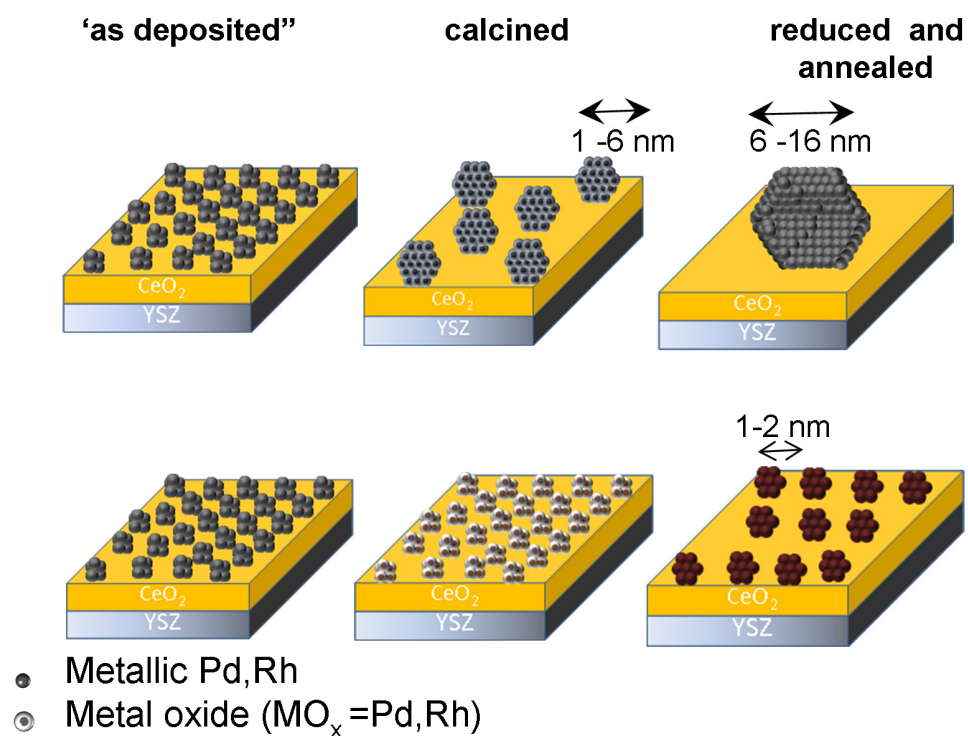
Figure 5.12: Schematic of agglomeration and particle growth mechanisms for (top) Pd and (bottom) Rh.   In the Pd sample PdO oxide particles are visible after calcination. After reduction and annealing, large (6-10 nm) Pd particles are visible on the CeO_2.   In the corresponding Rh sample, RhO_x samples are not visible after calcination, however small metallic particles are visible after calcination and reduction.
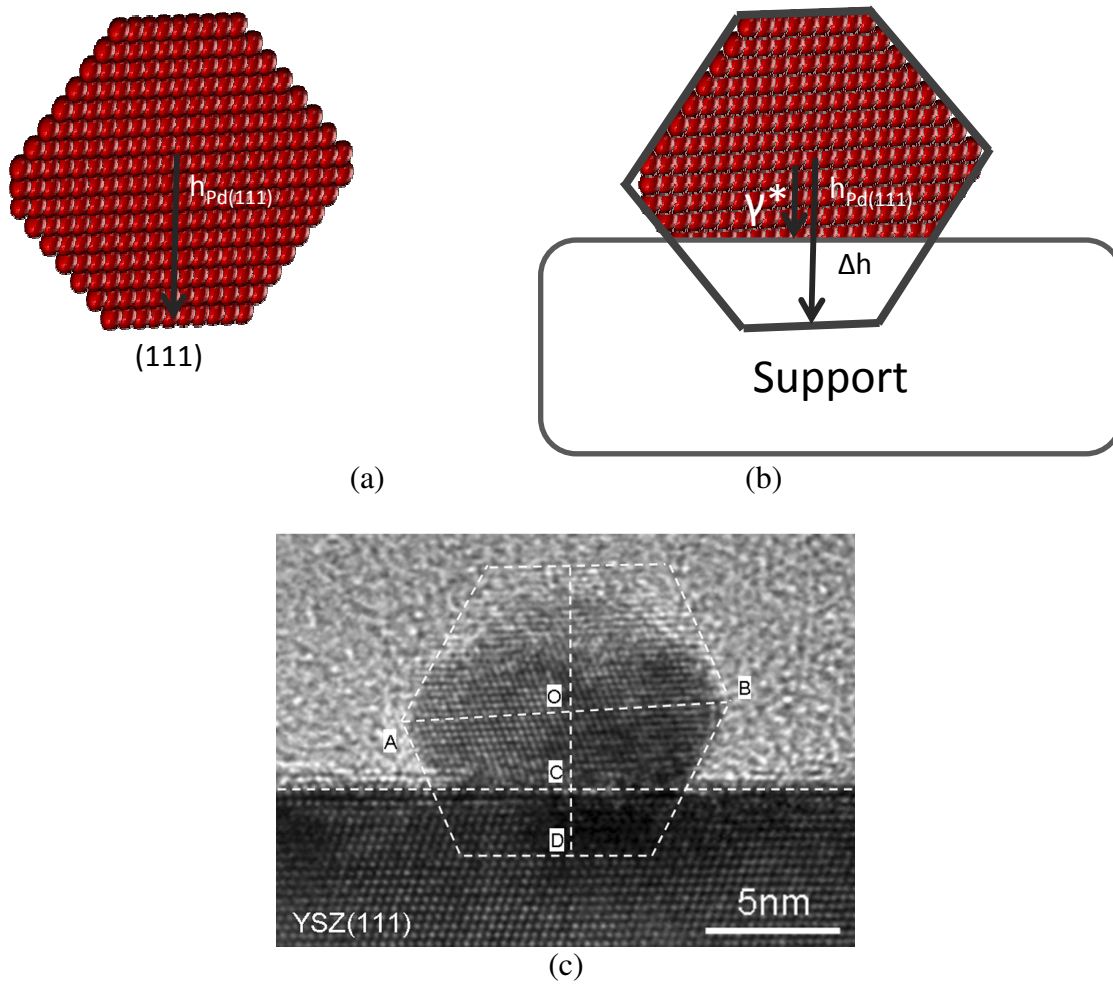
Figure 5.13: (a) Schematic illustration of the use an unconstrained particle showing it's ideal or Wulff shape (b) Wulff-Kaichew construction to estimate adhesion energy, and (c) an example of its application in a zirconia supported Pd model catalyst. The adhesion energy is calculated from the ratio of OD/CD, and the energy in this case was calculated to be 0.29eV/atom (adapted from Sun[63]).
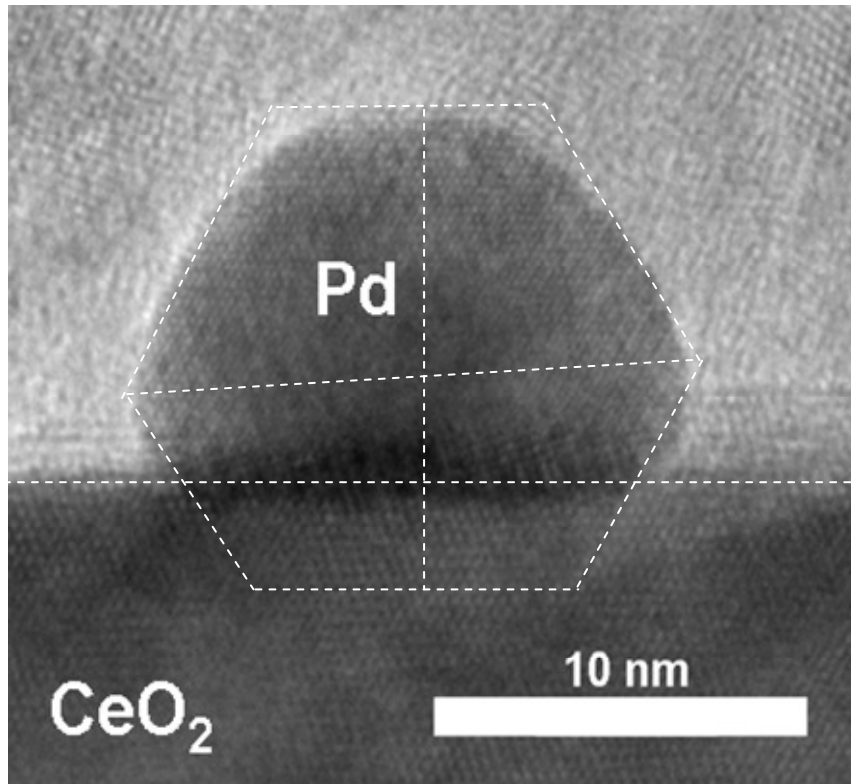
Figure 5.14: Application of the Wullf-Kaichew method to the calcined and reduced Pd/CeO$_2$ The adhesion energy in for this particle was calculated to be 0.33eV/atom
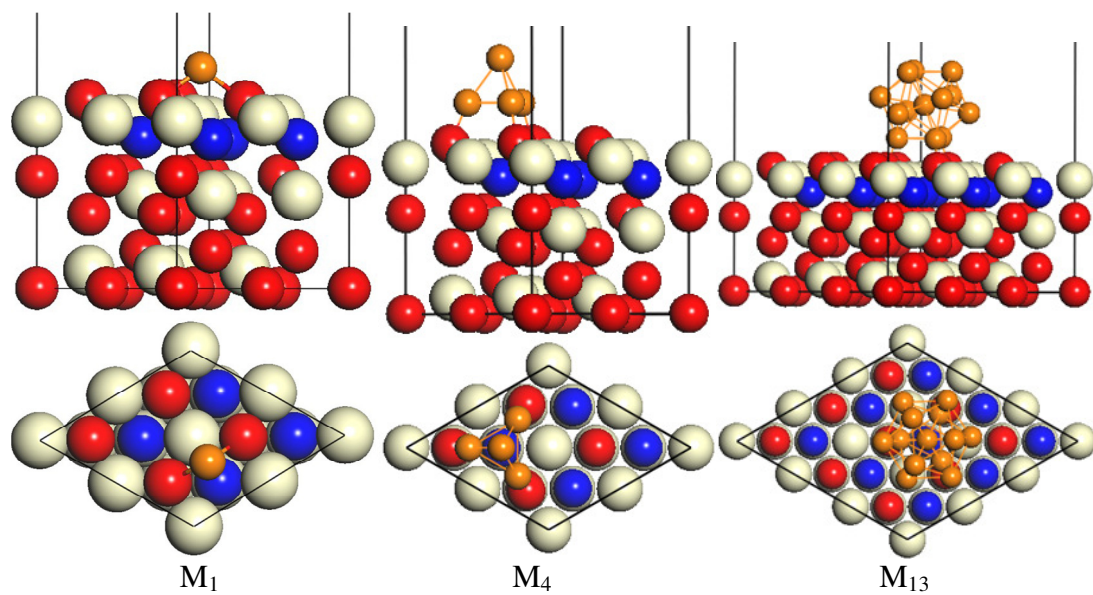
Figure 5.15: Absorption geometry of M_1, M_4, M_{13} cluster formation on $CeO_2(111)$ (M=Pd or, Rh)
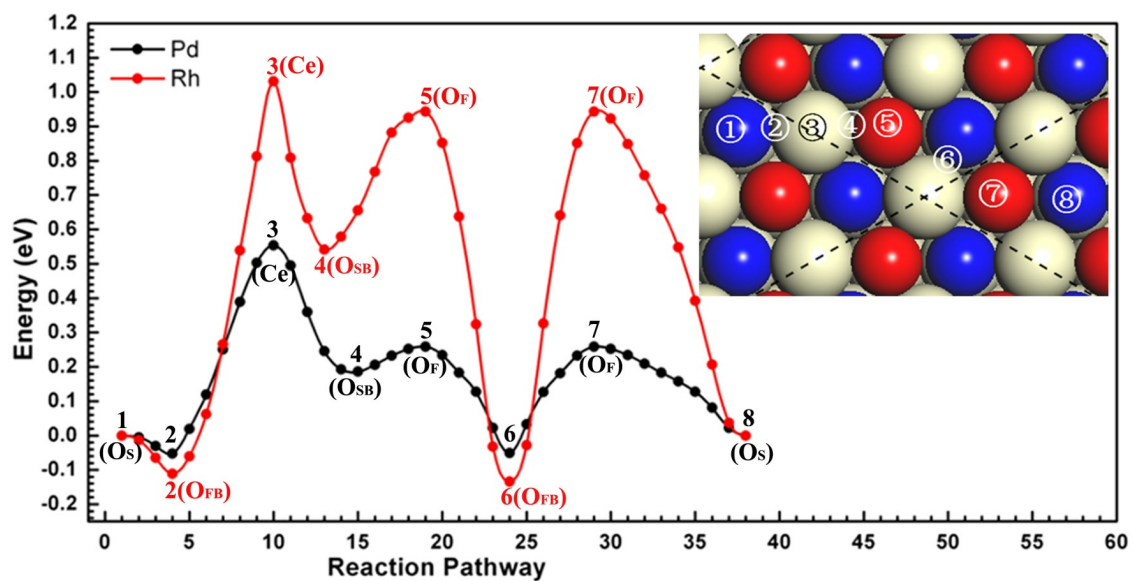
Figure 5.16: The energy landscape of the single atom migration for both Pd and Rh on CeO$_2$(111). The activation energy barriers for Rh are much higher than those of Pd resulting in a lower mobility
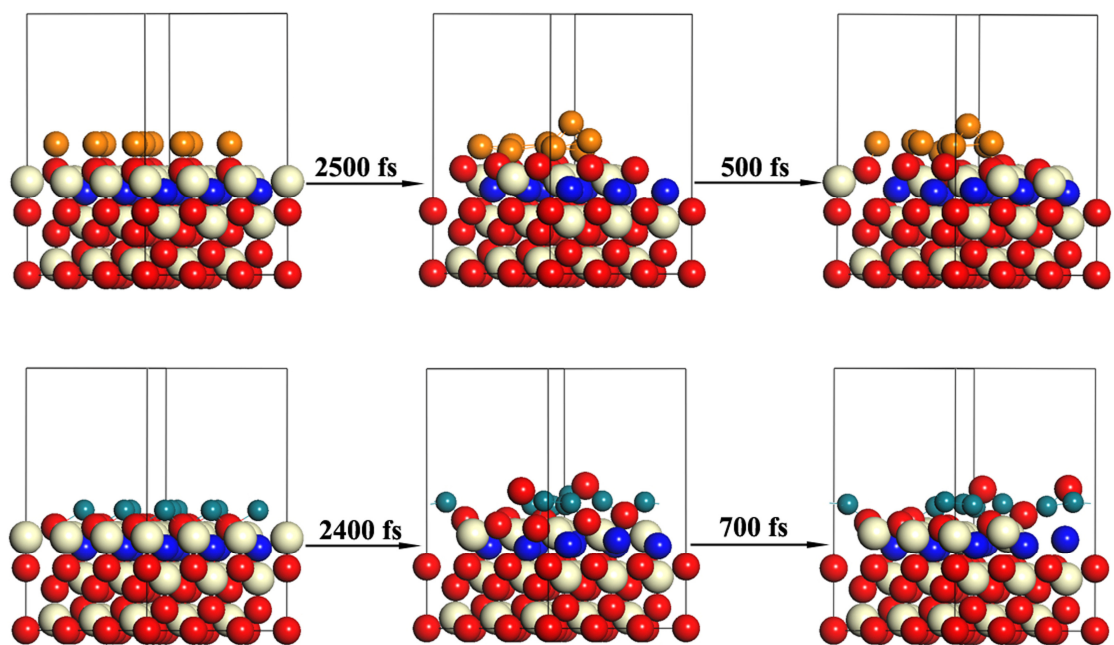
Figure 5.17: Snapshots of molecular dynamics simulations for (top) Pd agglomeration on the CeO$_2$(111) surface at 627ºC, and (bottom) Rh behavior on the CeO$_2$(111) surface at 927ºC
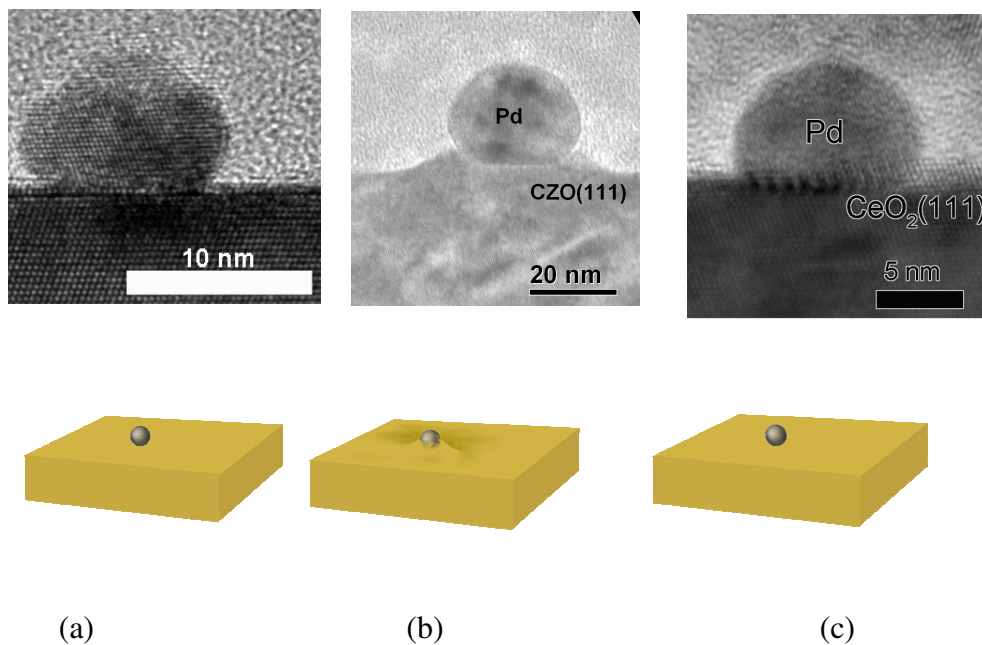
Figure 5.18: HRETM of calcined and reduced model catalysts from previous research[63] showing Pd/YSZ and Pd/CZO. (c) Comparison to present results of Pd/CeO$_2$ along with a representation of the partial encapsulation behavior.

(a)

(b)
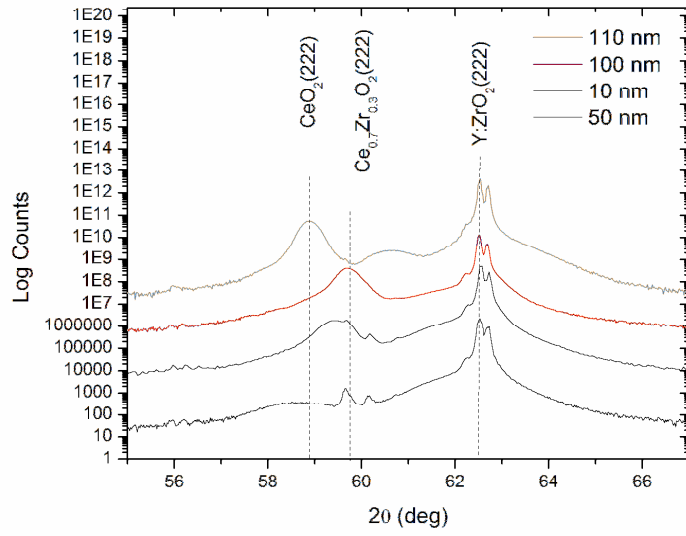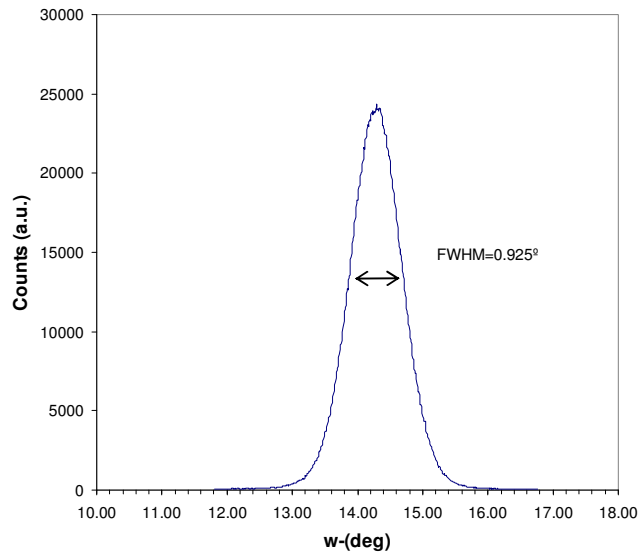
Figure 5.19: (a) θ/2θ patterns for the (222) peak region of MBE grown ceria and CZO films, and (b) ω-scan of the (111) peak of the CZ3 (47.3nm CZO sample.)
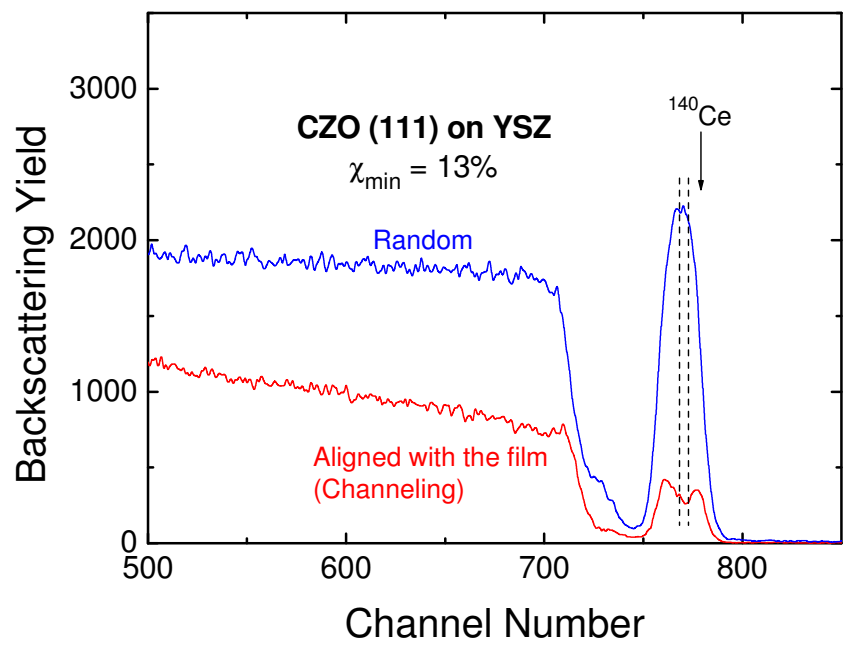
Figure 5.20: RBS channeling data for sample MBE grown CZ3
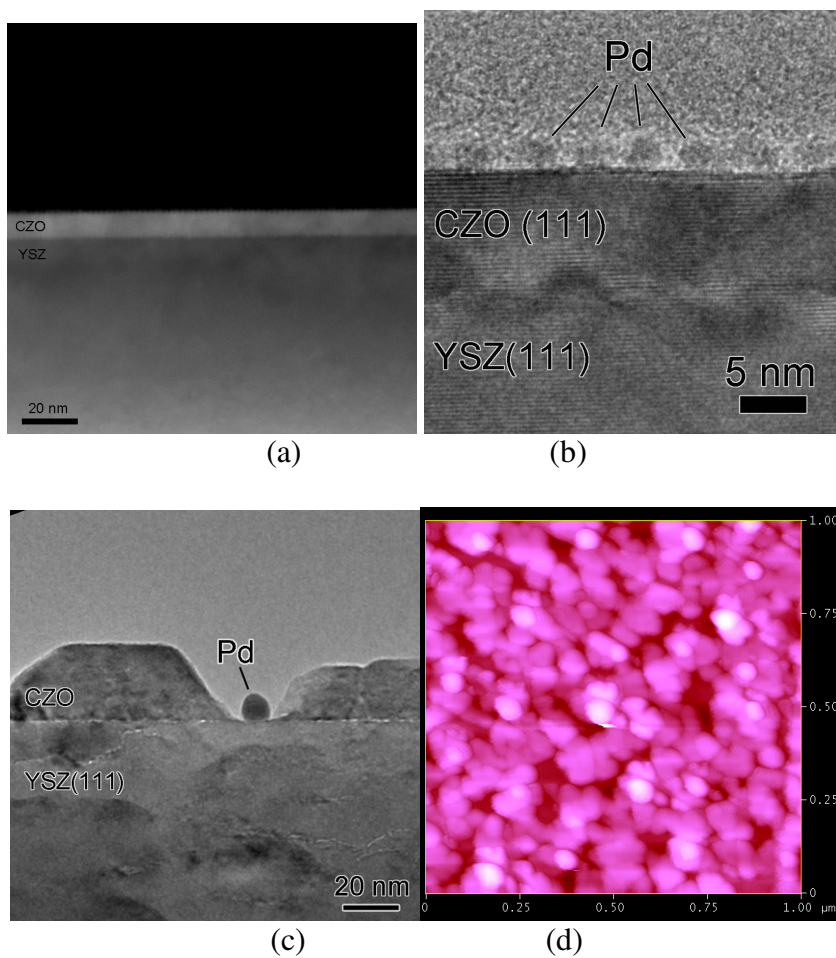
Figure 5.21: (a) Low magnification HAADF STEM image of 'as-deposited' Pd/CZ1, (b) HRTEM image of same sample, (c) TEM image of Pd/CZ1 (after calcination and 2X extended reduction), indicating fracture of the CZO film, and (d) 1μm x 1μm AFM surface plot showing RMS roughness of 7.244nm.
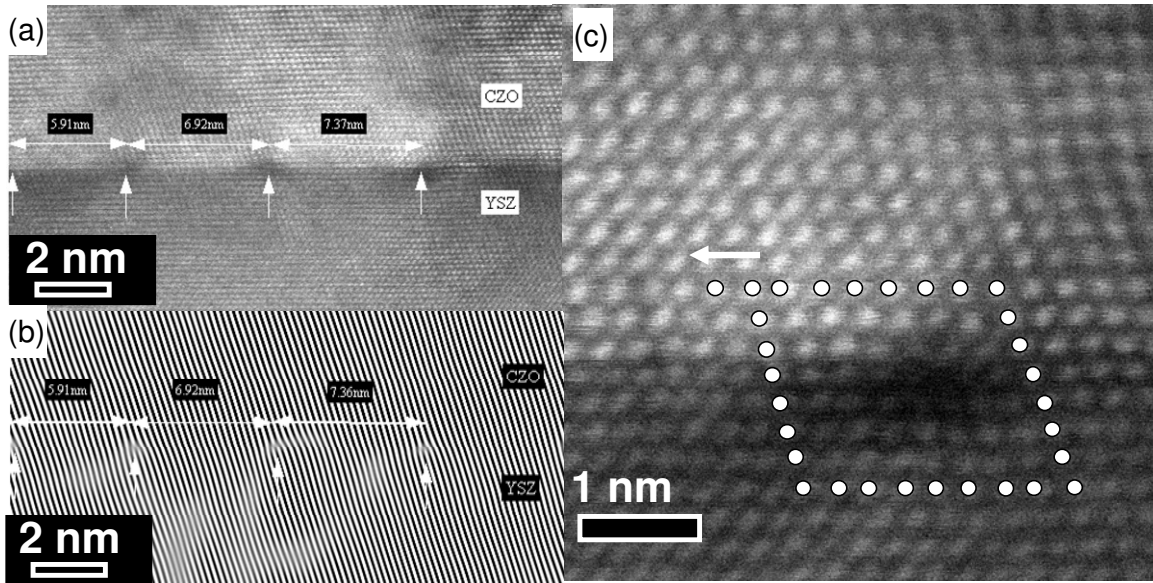
Figure 5.22: (a) HAADF STEM image of the CZO-YSZ interface for the calcined and reduced CZ3 sample. (b) Fourier filtered image of (a) indicating misfit dislocations at the interface. (c) High resolution HAADF image of a Burgers circuit around a dislocation core.
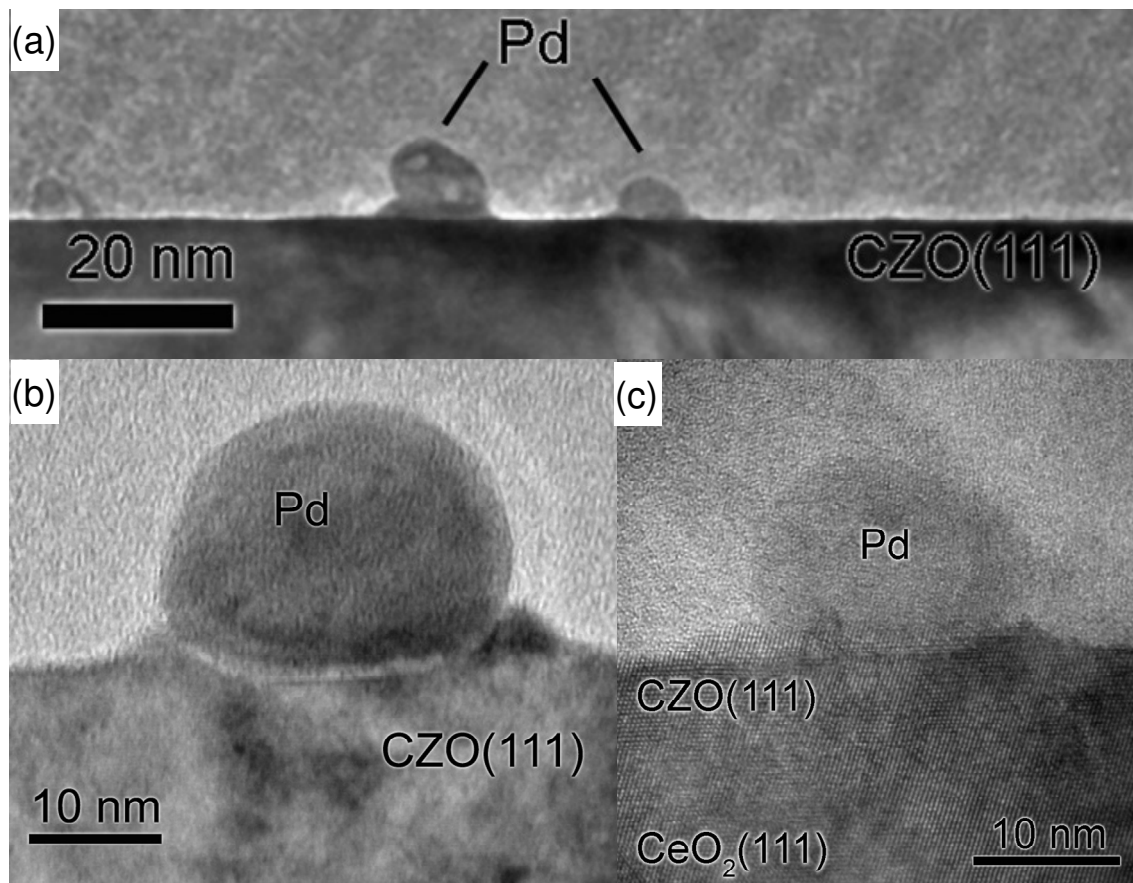
Figure 5.23: TEM images showing partial encapsulation of Pd supported on (a) CZ3 (47 nm) (b) CZ5 (100nm) and (c) CZ6 (bi-layer) films
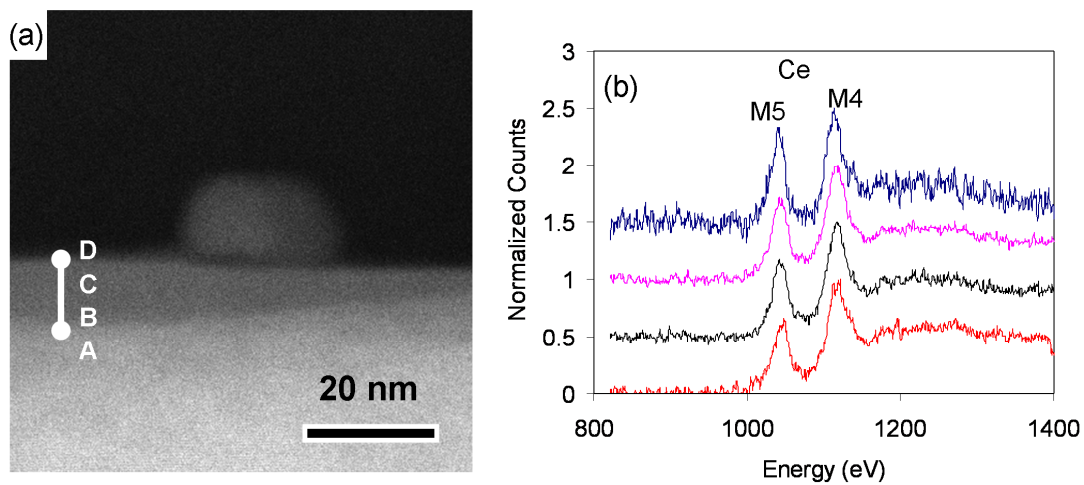
Figure: 5.24: (a) HAADF STEM image of a Pd particle on the CZ6 film surface indicating the approximate locations of EELS point analyses shown in (b). (b) Normalized EELS spectra showing changes in the Ce M4-to-M5 ratio with position.
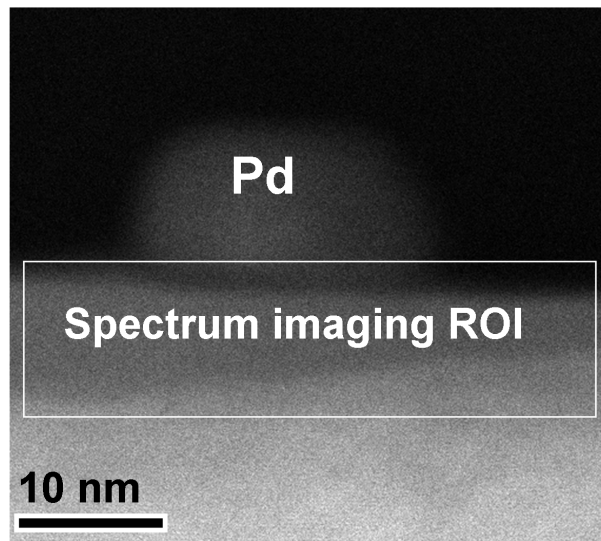
(a)
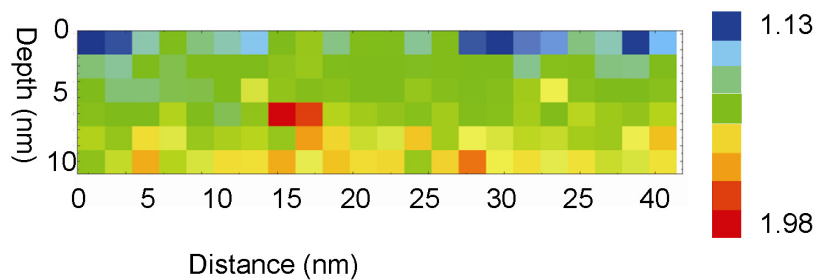
(b)

Figure 5.25: (a) HAADF STEM survey image indicating the region of interest (ROI) for EELS spectrum imaging. (b) Plot showing the Ce M4-to-M5 ratio as a function of position. The deeper blues near the surface of the film indicate that a higher concentration of Ce^{3+} exists near the surface of the film than in its bulk.
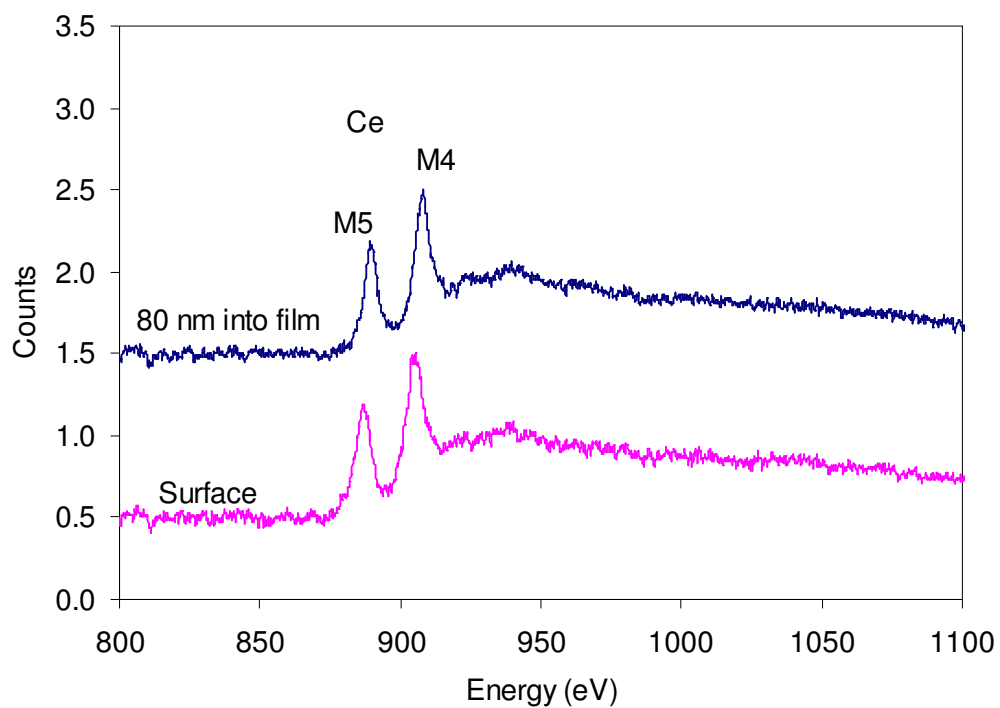
Figure 5.26: Background normalized EELS spectra of calcined and reduced Pd/CZ6 in a thin region far away (>500nm) from a partially encapsulated Pd particle. In this region, the Ce M4-to-M5 ratio does not change significantly between the surface and deeper into the film.

5.7 References

1. J.H. Seinfeld, "Air pollution: A half century of progress." *AlChE J.* **50**(6): p. 1096-1108 (2004).

2. J. Heywood and G. Lecture, "Motor vehicle emissions control: Past achievements, future prospects." *Institution of Mechanical Engineers*,(1997).

3. H.S. Gandhi, G.W. Graham, and R.W. McCabe, "Automotive exhaust catalysis." *J. Catal.* **216**(1-2): p. 433-442.

4. M. Shelef and R.W. McCabe, "Twenty-five years after introduction of automotive catalysts: what next?" *Catal. Today*. **62**(1): p. 35-50 (2000).

5. P. Eastwood, *Critical topics in exhaust gas aftertreatment*. Engineering design series. Baldock, Hertfordshire: Research Studies Press ; Research Studies Press. (2000).

6. Kim, "Ceria-promoted three-way catalysts for auto exhaust emission control." *Industrial & engineering chemistry product research and development*. **21**(2): p. 267-274 (1982).

7. A. Trovarelli, *Catalysis by Ceria and Related Materials*. London: Imperial College Press. (2002).

8. Y.C. Hu, "Hydrothermal synthesis of nano Ce-Zr-Y oxide solid solution for automotive three-way catalyst." *J. Am. Ceram. Soc.* **89**(9): p. 2949-2951 (2006).

9. L.H. Xiao, K.P. Sun, X.L. Xu, and X.N. Li, "Low-temperature catalytic combustion of methane over Pd/CeO2 prepared by deposition-precipitation method." *Catal. Commun.* **6**(12): p. 796-801 (2005).

10. T. Kolli, M. Huuhtanen, A. Hallikainen, K. Kallinen, and R. Keiski, "The Effect of Sulphur on the Activity of Pd/Al2O3, Pd/CeO2 and Pd/ZrO2 Diesel Exhaust Gas Catalysts." *Catal. Lett.* **127**(1-2): p. 49-54 (2009).

11. S. Bali, F.E. Huggins, R.D. Ernst, R.J. Pugmire, G.P. Huffman, and E.M. Eyring, "Iron−Ceria Aerogels Doped with Palladium as Water−Gas Shift Catalysts for the Production of Hydrogen." *Industrial & Engineering Chemistry Research*. **49**(4): p. 1652-1657 (2010).

12. X. Wang and R.J. Gorte, "A study of steam reforming of hydrocarbon fuels on Pd/ceria." *Applied Catalysis A: General*. **224**(1-2): p. 209-218 (2002).

13. V. Morris, R. Farrell, A. Sexton, and M. Morris. "Lattice Constant Dependence on Particle Size for Ceria prepared from a Citrate Sol-Gel." IOP Publishing. (2006).

14. Y.J. Kim, S. Thevuthasan, V. Shutthananadan, C.L. Perkins, D.E. McCready, G.S. Herman, Y. Gao, T.T. Tran, S.A. Chambers, and C.H.F. Peden, "Growth and structure of epitaxial $Ce_{1-x}Zr_xO_2$ thin films on yttria-stabilized zirconia (111)." *J. Electron. Spectrosc. Relat. Phenom.* **126**(1-3): p. 177-190 (2002).

15. M. Yashima, S. Sasaki, Y. Yamaguchi, M. Kakihana, M. Yoshimura, and T. Mori, "Internal distortion in ZrO2-CeO2 solid solutions: Neutron and high-resolution synchrotron x-ray diffraction study." *Appl. Phys. Lett.* **72**(2): p. 182-184 (1998).

16. H.W. Jen, G.W. Graham, W. Chun, R.W. McCabe, J.P. Cuif, S.E. Deutsch, and O. Touret, "Characterization of model automotive exhaust catalysts: Pd on ceria and ceria-zirconia supports." *Catal. Today*. **50**(2): p. 309-328 (1999).

17. J. Kaspar, P. Fornasiero, and N. Hickey, "Automotive catalytic converters: current status and some perspectives." *Catal. Today*. **77**(4): p. 419-449 (2003).

18. S.J. Tauster, S.C. Fung, and R.L. Garten, "Strong Metal-Support Interactions - Group-8 Noble-Metals Supported on TiO_2." *J. Am. Chem. Soc.* **100**(1): p. 170-175 (1978).

19. S.J. Tauster, "Strong Metal-Support Interactions." *Acc. Chem. Res.* **20**(11): p. 389-394 (1987).

20. J. Zhou, A.P. Baddorf, D.R. Mullins, and S.H. Overbury, "Growth and Characterization of Rh and Pd Nanoparticles on Oxidized and Reduced

CeOx(111) Thin Films by Scanning Tunneling Microscopy." *The Journal of Physical Chemistry C*. **112**(25): p. 9336-9345 (2008).

21.   E.S. Putna, T. Bunluesin, X.L. Fan, R.J. Gorte, J.M. Vohs, R.E. Lakis, and T. Egami, "Ceria films on zirconia substrates: models for understanding oxygen-storage properties." *Catal. Today*. **50**(2): p. 343-352 (1999).

22.   H. Vidal, J. Kaspar, M. Pijolat, G. Colon, S. Bernal, A. Cordón, V. Perrichon, and F. Fally, "Redox behavior of CeO_2-ZrO_2 mixed oxides: I. Influence of redox treatments on high surface area catalysts." *Appl. Catal., B*. **27**(1): p. 49-63 (2000).

23.   G.W. Graham, "NO chemisorption on supported Pd." *Surf. Sci.* **268**(1-3): p. 25-35 (1992).

24.   M. Smirnov and G. Graham, "Pd oxidation under UHV in a model Pd/ceria–zirconia catalyst." *Catal. Lett.* **72**(1): p. 39-44 (2001).

25.   H. Zhang, J. Gromek, G.W. Fernando, S. Boorse, and H.L. Marcus, "PdO/Pd system equilibrium phase diagram under a gas mixture of oxygen and nitrogen." *Journal of Phase Equilibria*. **23**(3): p. 246-248 (2002).

26.   R.F. Klie, K. Sun, M.M. Disko, J. Liu, and N.D. Browning, "Atomic Scale Studies of Heterogeneous Catalysts." *Dekker Encyclopedia of Nanoscience and Nanotechnology*: p. 179 - 193 (2004).

27.   D.L. Smith, *Thin Film Deposition: Principles and Practices*. 1 ed., Boston, MA: McGraw-Hill, Inc. (1995).

28.   A.W. Adamson, *Physical chemistry of surfaces*. New York: Wiley. (1990).

29.   G. Wulff and Z. Kristallogr, "On the question of the rate of growth and dissolution of crystal surfaces". Mineral (1901).

30.   C. Henry, "Catalysis by Nanoparticles." in *Nanocatalysis*, U. Heiz and U. Landman, Editors., Springer Berlin Heidelberg. p. 245-268 (2007).

31.   R. Kaischew, *Communications of the Bulgarian Academy of Science*. **1**: p. 100 (1950).

32.   W.L. Winterbottom, "Equilibrium shape of a small particle in contact with a foreign substrate." *Acta Metall.* **15**(2): p. 303-310 (1967).

33.   F. Raouafi, C. Barreteau, M.C. Desjonquères, and D. Spanjaard, "Energetics of stepped and kinked surfaces of Rh, Pd and Cu from electronic structure calculations." *Surf. Sci.* **505**: p. 183-199 (2002).

34.   H.P. Sun, X.Q. Pan, G.W. Graham, H.-W. Jen, R.W. McCabe, S. Thevuthasan, and C.H.F. Peden. "Evaluation of the Adhesion Energy of Pd Particles on Reduced Ceria-Zirconia Surface by Cross-sectional TEM Imaging." in *16th International Microscopy Congress*. Sapporo, Japan. (2006).

35.   H. Graoui, S. Giorgio, and C. Henry, "Effect of the interface structure on the high-temperature morphology of supported metal clusters." *Philosophical magazine. B, Physics of condensed matter, electronic, optical, and magnetic properties*. **81**(11): p. 1649-1658 (2001).

36.   J. Hafner, "*Ab-initio* simulations of materials using VASP: Density-functional theory and beyond." *J. Comput. Chem.* **29**(13): p. 2044-2078 (2008).

37.   J. Tse, "Ab initio molecular dynamics with density functional theory." *Annu. Rev. Phys. Chem.* **53**: p. 249-290 (2002).

38.   B.H. Li, O.K. Ezekoye, Q.J. Zhang, L.A. Chen, P. Cui, G. Graham, and X.Q. Pan, "Origin of Rh and Pd agglomeration on the CeO2(111) surface." *Physical Review B*. **82**(12)(2010).

39.   P.C. Flynn and S.E. Wanke, "A model of supported metal catalyst sintering : I. Development of model." *J. Catal.* **34**(3): p. 390-399 (1974).

40.   P.C. Flynn and S.E. Wanke, "A model of supported metal catalyst sintering : II. Application of model." *J. Catal.* **34**(3): p. 400-410 (1974).

41.   G. Graham, A. O'Neill, and A. Chen, "Pd encapsulation in automotive exhaust-gas catalysts." *Applied catalysis. A, General*. **252**(2): p. 437-445 (2003).

42. G.W. Graham and A.N. Shigapov, "Revised Model of Strain in Ceria–Zirconia-Encapsulated Precious-Metal Particles." *Catal. Lett.* **81**(3): p. 253-257 (2002).

43. H.M. Kandil, J.D. Greiner, and J.F. Smith, "Single-Crystal Elastic Constants of Yttria-Stabilized Zirconia in the Range 20° to 700°C." *J. Am. Ceram. Soc.* **67**(5): p. 341-346 (1984).

44. G. Balducci, M.S. Islam, J. Kaspar, P. Fornasiero, and M. Graziani, "Bulk Reduction and Oxygen Migration in the Ceria-Based Oxides." *Chem. Mater.* **12**(3): p. 677-681 (2000).

45. H.P. Sun, X.P. Pan, G.W. Graham, H.W. Jen, R.W. McCabe, S. Thevuthasan, and C.H.F. Peden, "Partial encapsulation of Pd particles by reduced ceria-zirconia." *Appl. Phys. Lett.* **87**(20)(2005).

46. Y. Gao, G.S. Herman, S. Thevuthasan, C.H.F. Peden, and S.A. Chambers, "Epitaxial growth and characterization of $Ce_{1-x}Zr_xO_2$ thin films." *Journal of Vacuum Science & Technology A: Vacuum, Surfaces, and Films*. **17**(3): p. 961-969 (1999).

47. S. Thevuthasan, C.H.F. Peden, M.H. Engelhard, D.R. Baer, G.S. Herman, W. Jiang, Y. Liang, and W.J. Weber, "The ion beam materials analysis laboratory at the environmental molecular sciences laboratory." *Nuclear Instruments & Methods in Physics Research Section a-Accelerators Spectrometers Detectors and Associated Equipment*. **420**(1-2): p. 81-89 (1999).

48. C.M. Wang, S. Thevuthasan, and C.H.F. Peden, "Interface structure of an epitaxial cubic ceria film on cubic zirconia." *J. Am. Ceram. Soc.* **86**(2): p. 363-365 (2003).

49. H. Gao and W.D. Nix, "Surface roughening of heteroepitaxial films." *Annu. Rev. Mater. Sci.* **29**(1): p. 173-209 (1999).

50. C. Ozkan, W. Nix, and H. Gao, "Strain relaxation and defect formation in heteroepitaxial SiGe films via surface roughening induced by controlled annealing experiments." *Appl. Phys. Lett.* **70**: p. 2247 (1997).

51.   M.S. Spencer, "Models of strong metal-support interaction (SMSI) in Pt on TiO2 catalysts." *J. Catal.* **93**(2): p. 216-223 (1985).

52.   R.T.K. Baker, E.B. Prestridge, and L.L. Murrell, "Electron microscopy of supported metal particles : III. The role of the metal in an SMSI interaction." *J. Catal.* **79**(2): p. 348-358 (1983).

53.   M. Alfredsson and C.R.A. Catlow, "A comparison between metal supported c-ZrO2 and CeO2." *PCCP*. **4**(24): p. 6100-6108 (2002).

54.   M. Che and C. Bennett, "The influence of particle size on the catalytic properties of supported metals." *Advances in Catalysis*. **36**(1989): p. 55-172 (1989).

55.   G. Rao and B. Mishra, "Structural, redox and catalytic chemistry of ceria based materials."

56.   G.W. Graham, H.W. Jen, R.W. McCabe, A.M. Straccia, and L.P. Haack, "Characterization of model automotive exhaust catalysts: Pd on Zr-rich ceria-zirconia supports." *Catal. Lett.* **67**(2-4): p. 99-105 (2000).

57.   J.L.F. Da Silva, "Stability of the Ce2O3 phases: A DFT+U investigation." *Physical Review B*. **76**(19)(2007).

58.   C. Loschen, J. Carrasco, K.M. Neyman, and F. Illas, "First-principles LDA plus U and GGA plus U study of cerium oxides: Dependence on the effective U parameter." *Physical Review B*. **75**(3)(2007).

59.   K. Kawabuchi and S. Magari, "Deposition of crystals from the plasmas of ZrO_2, HfO_2, ThO_2, and CeO_2." *J. Appl. Phys.* **50**(10): p. 6222-6229 (1979).

60.   D.R. Baer, J.E. Amonette, M.H. Engelhard, D.J. Gaspar, A.S. Karakoti, S. Kuchibhatla, P. Nachimuthu, J.T. Nurmi, Y. Qiang, V. Sarathy, S. Seal, A. Sharma, P.G. Tratnyek, and C.M. Wang, "Characterization challenges for nanomaterials." *Surf. Interface Anal.* **40**(3-4): p. 529-537 (2008).

61.   S. Gilliss, J. Bentley, and C. Carter, "Electron energy-loss spectroscopic study of the surface of ceria abrasives." *Appl. Surf. Sci.* **241**(1-2): p. 61-67 (2005).

62.   P.A. Crozier, R. Wang, and R. Sharma, "In situ environmental TEM studies of dynamic changes in cerium-based oxides nanoparticles during redox processes." *Ultramicroscopy*. **108**(11): p. 1432-1440 (2008).

63.   H. Sun, "Transmission electron microscopy investigation of auto catalyst and cobalt germanide". The University of Michigan,Ph.D. Thesis (2005).

64.   C.M. Wang, D.R. Baer, J.E. Amonette, M.H. Engelhard, J.J. Antony, and Y. Qiang, "Electron beam-induced thickening of the protective oxide layer around Fe nanoparticles." *Ultramicroscopy*. **108**(1): p. 43-51 (2007).

65.   X. Bokhimi, A. Morales, A. Garcia-Ruiz, T.D. Xiao, H. Chen, and P.R. Strutt, "Transformation of yttrium-doped hydrated zirconium into tetragonal and cubic nanocrystalline zirconia." *J. Solid State Chem.* **142**(2): p. 409-418 (1999).

66.   M. Yashima, K. Morimoto, N. Ishizawa, and M. Yoshimura, "Zirconia ceria solid-solution synthesis and the temperature time transformation diagram from the 1/1 composition." *J. Am. Ceram. Soc.* **76**(7): p. 1745-1750 (1993).

67.   R. McCabe and J. Kisenyi, "Advances in automotive catalyst technology." *Chem. Ind. (London)*,(15): p. 605-608 (1995).

68.   J. Hangas and A.E. Chen, "Comparative analytical study of two Pt-Rh three-way catalysts." *Catal. Lett.* **108**(1-2): p. 103-111 (2006).

Chapter 6

Summary, Future Work, and Conclusions

6.1 Summary

6.1.1 Comparative Study of Pt and PtCo Fuel Cell Catalysts Aged Under Aggressive Potentiodynamic Cycling

In this study, direct TEM observation of commercial Pt and PtCo alloy catalysts enabled both atomic-scale structural characterization and quantitative insights on dispersion and deactivation. One area investigated is size distribution. Statistical analysis of TEM results indicates that PtCo particles had a larger initial particle size than Pt/C catalysts, due to their synthesis. Moreover, in the PtCo/C sample, significant differences in the mean particle size could be attributed to acid leaching. While the Pt/C appeared to be sensitive to thermal aging, however acid leaching did not have a statistically significant effect on the Pt/C particle size. This indicates that the catalysts alloyed with a non-noble metal were more susceptible to acid leaching than pure platinum. However, Co alloying improved thermal stability of these catalysts.

With our electrochemical aging cycling protocol, particle growth under aggressive electrochemical aging was initially delayed. HRTEM alone did not provide evidence of selective Co leaching in the PtCo/C sample, but HAADF STEM provided more direct evidence of atomic-scale changes. Both EELS and XRD diffraction demonstrated that a

gradual removal of Co metal occurs with electrochemical cycling. EDS spectrum imaging indicates that this loss initially results in catalyst particles consisting of a Pt rich shell surrounding a Pt_3Co core. The maintenance of ECA under cyclic aging occurs during this period of selective Co corrosion.

Additionally, statistical analysis of TEM results indicates that significant differences exist between the PtCo/C and the Pt/C dispersions with cyclic aging. In both catalysts, significant differences in the mean particle size could be attributed to cyclic aging; however, the PtCo catalyst retained twice as much of its original electrochemical area as the pure-Pt catalysts. The shape of the resultant distribution supports the idea that migration and coalescence is the dominant particle growth mechanism in these catalysts. Differences in the particle growth behavior may be attributed to the anchoring effect of Co, which diminishes as Co is lost during electrochemical cycling.

6.1.2 Investigation of Alumina Supported Pt and Pt-Pd Alloy NO Oxidation Catalysts

This study investigated the coarsening behavior of alumina supported Pt and Pt-Pd catalysts from both AcAc and nitrate precursors. In the case of the pure Pt, fresh clusters from both precursors had comparable mean particles sizes. The measured particle size distributions were very similar with AcAc precursors having a slightly broader distribution and lower dispersion

Extending the discussion to bimetallic samples, particle growth and alloying are a consequence of aging under lean conditions, regardless of initial conditions. Nitrate samples did exhibit a wider distribution in composition after aging, possibly reflective of

greater inhomogeneity in starting composition. For both aging conditions, AcAc

precursors always produce smaller particles on average. Additionally, alloying Pt with Pd

in alumina-supported catalysts for NO oxidation was found to suppress the particle

coarsening upon aging under these aging conditions. Combining aberration corrected

HAADF and EDS revealed that the major difference between the precursors is the

presence of large Pd rich particles in the fresh bimetallic nitrate catalyst.

For the more severe aging condition at 900 ° C, the catalysts made from the

nitrate precursor behaved in a similar fashion as the more costly AcAc precursor. The

suppression of the formation of anomalously large Pt particles by alloying with Pd may

have implications for the relative importance of different coarsening mechanisms.

Addition of Pd inhibits the growth of the largest Pt particles for both precursors

Data collected from TEM observation was further related to catalytic conversion

of NO to NO_2. NO oxidation was found to be relatively insensitive to a Pd content

approaching 50 mol%.

6.1.3 Fundamental studies of the interactions between Pd and Rh on Ceria and ceria-based supports.

In the study of Pd and Rh on CeO_2 (111) surface, high quality CeO_2 films were

grown by PLD on yttria stabilized zirconia substrates. A monolayer of Pd was deposited

on the ceria films and metal growth was monitored in situ via XPS. After calcination in

air, the samples were prepared for cross sectional TEM observation. In the case of the

Pd/CeO_2, particles (presumably PdO) were visable on the ceria surface. The mean particle

size for these particles was approximately 3nm. Rhodium particles, either in metallic

form or as RhO_x, were not observable in HRTEM imaging, thus indicating a strong adhesive energy between Rh adatoms and the cerium oxidize surface. These experimental results support recent theoretical calculations of the relative stabilities of Pd and Rh atoms and clusters on CeO_2 (111).

For the Pd/CeO_2 and Rh/CeO_2 samples exposed to the more extensive treatment of two cycles of reduction followed by extended thermal annealing, further distinctions could be made from HRTEM characterization. In the Pd/CeO_2 sample, significant Pd particle growth occurs during the 2x reduction treatment, most likely during the annealing cycles. In contrast to the calcined only sample, it was found that Rh did cluster after reduction. However, the lower mobility of Rh (relative to Pd) on CeO_2 limited the resultant particle size. In neither case, was the partial encapsulation phenomena as described in earlier reports of $Pd/Ce_{0.7}Zr_{0.3}O_2$, observed.

In an effort to determine the origin of the partial encapsulation phenomena (oxide wetting), a series of CZO supports were grown on YSZ by MBE. As was the case for the for Pd and Rh on CeO_2 study, cross sectional HRTEM was preformed subsequent to Pd deposition and calcination and reduction treatments. The objective of this work was to determine the role of native stress, relative to chemical bonding between ceria-zirconia and Pd, in driving the oxide-wetting process.

To investigate the stress in the film, Pd/CZO films of varying thicknesses were further studied to determine if the wetting phenomena could be observed. In our studies, it was found that $Ce_{0.7}Zr_{0.3}O_2$ films ranging in thickness from 50nm to 100nm all exhibit some degree of wetting. This indicates that the wetting process is related more strongly to an intrinsic chemical effect than a uniform film strain due to lattice mismatch. This

wetting effect could be due to stress induced by reduction, which generates a highly local compressive stress in the film (arising from to the creation of Ce^{+3} ions, which are about 10% larger than the original Ce^{+4} cations).

In an effort to separate these two sources of compressive stress from each other, a thin $Ce_{0.7}Zr_{0.3}O_2$ film on a thick (fully relaxed) CeO_2 film (α_{CeO2} = 5.411Å) was used as a support for a model catalyst. In the case of this bi-layer, the surface (CZO) film was assumed to be initially under tensile stress. In this "bi-layer" film wetting was also observed around the Pd particle which provided further evidence that wetting is a chemically driven phenomena

6.2 Future work

6.2.1 Comparative Study of Pt and PtCo Fuel Cell Catalysts Aged Under Aggressive Potentiodynamic Cycling

The characterization of PtCo alloy fuel cell catalysts is a relatively mature field with several hundred reports and almost 900 patent applications for PtCo fuel cell catalysts written in the past several years. However, this research offers a few areas for future work and further contributions. Perhaps the most promising area of future work is in the area of *in situ* microscopy. This technique utilizes the recent the development and introduction of environmental TEM capable of performing electrochemical testing. These holders (shown schematically in Figure 6.1), allow for *in situ* TEM observation of a variety of chemical and electrochemical phenomena [1-2]. This technique presents further opportunity for direct observation of fuel cell catalysts under more realistic conditions.

Furthermore, investigating these catalysts *in situ* could potentially eliminate a step between catalysts testing and TEM sample preparation, reducing the chance for sampling biases. In addition, *in-situ* observation allows researchers to directly verify deactivation mechanisms (e.g., migration and coalescence vs. interparticle transport).

Secondly, because this study investigated commercially obtained catalysts, the Pt/C and PtCo/C catalysts had different initial particle sizes. Our investigation noted that it is difficult to separate particle size from particle composition in determining the origin of the differences in the observed aging behavior. It would be interesting to see if the same effects could be observed in systems in which the initial particle size and distribution were uniform. As was mentioned in Section 3.3, thermal aging induced particle growth in the fresh Pt/C catalysts but did not significantly affect the PtCo/C catalysts. Therefore, one possible future study could be one in which the Pt/C catalyst was thermally aged in such a fashion that their particle size and dispersion closely resembled that of an untreated PtCo/C catalyst. In such a proposed investigation, repeating a similar electrochemical aging experiment with TEM characterization, as was performed in Chapter 3, would be very interesting.

Finally, two additional studies are proposed as possible means to investigate the mobility and interfacial attractive forces between platinum particles and the carbon support. It was noted in chapter 4 that as Co was selectively removed from the metal catalyst particles, the attractive forces between the PtCo particles and the carbon support decreased. This "anchoring effect" delayed the onset of particle migration and coalesces in the PtCo catalysts with cycling. Preliminary real –time observation of PtCo alloy particles in the electron microscope Figure 6.2 shows that the metal nanoparticles are

mobile on the carbon support under irradiation in the electron beam. Earlier studies have reported substantial morphological changes such as crystallization, migration, and coalescence under electron beam radiation[3]. Therefore, one proposed study could address the use of controlled exposure to the electron beam to measure the mobility of a catalyst particle on the surface.

Lastly, contact angle measurements using a modified Wulff construction have been shown as a quick and effective method to determine the fundamental thermodynamic properties between precious metal catalyst particles and support materials[4]. This previous report demonstrated that cross sectional TEM can provide a visual image required for thermodynamic predictions. Applying this concept to the current fuel cell projects could be a useful way to test the anchoring effect hypothesis by measuring any differences in adhesion energy between PtCo/C and Pt/C. A model catalyst system can be prepared by depositing Pt or PtCo onto a thin layer of glassy or graphitic carbon. This method was recently used to directly investigate the interfacial properties of Pt supported on glassy carbon[5].

6.2.2 Characterization of Pt-Pd bimetallic catalysts samples for NO Oxidation

The work offers several opportunities for future investigation. In this study, the samples were investigated at 500 º and 900 º C for a fixed time (3 hours in this study). This was an effective protocol for investigating thermal stability, however a more complete understanding of the kinetics of particle coarsening would require aging for varying times at a fixed temperature.   In TEM investigations of alumina supported Pt,

Harris varied the heat treatment times between 10 min and 8 hours, and found that a change in sintering order occurred after 6 hours of aging[6]. It would be interesting to determine if this effect was also observed in bimetallic catalysts, as it might elucidate effects of alloying on the particle growth mechanism.

Presently, long collection times and low resolution limits inhibited high resolution EDS mapping of the fresh Pt-Pd catalyst samples. The difficulties of producing reliable spectroscopy data from atomically dispersed precious metal elements on a crystalline supports should be acknowledged, as this information could be used to determine the specific role of Pd in inhibiting the growth in Pt. This would be especially important in the investigation of Pt-Pd catalysts from AcAc precursors where the composition of the fresh particles is not as clear cut as was the case for nitrate catalysts (as discussed in Section 4.3). In the near future, as newer microscopes with more sensitive EDS detectors become more commonly available, these experiments may become more feasible.

Another area of future work would be to study the catalytic performance of these catalysts under simulated diesel drive-cycle conditions. In the study referred to in Chapter 5, the catalysts were aged in 5% O_2 and 10% H_2O in N_2, while recent studies[7] have found that road testing and laboratory aging (in an atmosphere containing a mixture of C_3H_6, C_3H_8, CO, NO, O_2, CO_2, and SO_2) produced comparable amounts of thermal sintering with some differences in chemical deactivation.

Another area of investigation can be found in the emerging field of in-situ TEM. In a preliminary study, fresh Pt50-Pd50 (ac-ac) was dispersed on to MEMs based heating stage. The stage, produced by Protochips and shown in Figure 6.3, is capable of heating a TEM specimen from room temperature to 1000ºC in 1 ms[8]. Although discussed in

detail in previous reports [8-9], these MEMs-based heating stages work by resistively heating a ceramic membrane upon which the sample is supported. The fresh Pt50-Pd50 (ac-ac) were heated in vacuum for 500 ° C for 3 ten minute intervals followed by two ten minute intervals at 900ºC. Between these intervals, representative TEM images were collected at a variety of magnifications. The results of this preliminary *in-situ* heating experiment are shown in Figure 6.4.

For the fresh catalyst in the *in situ* experiment, a 2nm particle surrounded by smaller atomically dispersed material clusters, is visible on the alumina support (Figure 6.4a). After the first heat treatment (Figure 6.4 b), the majority of the atomically dispersed metal is no longer visible. At this point it is difficult to distinguish between these smaller particles coalescing into the larger particle or volatilizing and undergoing vapor phase transport.   Further treatments at 500ºC (Figures 6.4c and d) did not substantially affect morphology. However, after aging at 900ºC, the size of the central particle initially decreases and eventually disappears (Figure 6.4f). This process is possibly the result of vapor phase growth. 900ºC aging is also associated with changes to the underlying alumina support. Distinct differences in the aging behavior were found between aging at 500ºC and aging at 900ºC, however more systematic studies varying time and temperature are needed to make definitive conclusions.

One limitation of this preliminary heater experiment was that it was performed in vacuum. It is well known that the sintering mechanism and particle morphology are strongly related to the sintering environment.[10] Therefore, *in situ* aging in a variety of atmospheric conditions would be very useful. It would be interesting to investigate the sintering behavior of these particles after aging in air, in the hydrothermal conditions

used in Chapter 5, and in the simulated exhaust atmosphere presented above.   This line of research is becoming promising with the development of *in situ* environmental holders that can be used in conventional transmission microscopes.

Another opportunity for future study in this subject area is investigating the role of Pd alloying in the coarsening behavior of alumina supported Pt using X-ray absorption fine structure (*XAFS*) spectroscopy.   XAFS is an absorption spectroscopy technique that investigates the modulation of the x-ray absorption coefficient at energies near and above an x-ray absorption edge[11]. XAFS is a powerful tool in the characterization of heterogeneous catalysts, notably in determining the coordination numbers of specific atomic species in a sample[12]. Such information could theoretically yield more definitive information on the relationship between Pt and Pd in both the fresh state and at various points during hydrothermal aging.

Thus far, this study only focused on the Pt rich side of the Pt-Pd composition range.   As was observed in Chapter 4, the major difference between the bimetallic samples from both AcAc and nitrate precursors was the presence in of large Pd rich particles in the fresh nitrate samples. Recent research[13] supports the position that pure Pd has an intrinsically lower NO oxidation activity, however there has been less microscopy research on Pd-rich Pt-Pd alloys.   Characterizing the structure and activity for the Pd rich side of the composition range could lead to a more definitive relationship between microscopy and observed structure and NO oxidation properties for these catalysts.

6.2.3 Rh and Pd on CeO$_2$ and Ceria Based Supports

The treatment conditions chosen in Chapter 5 (calcination and metal deposition, followed by reduction and annealing cycles) were selected from previous studies[14] on the behavior of Pd on ceria and ceria-zirconia supports. These conditions were able to produce the unique wetting behavior in a model planar catalysts system described in our earlier study[15]. However, systematically modeling this system in a planar model system leads to many variables that could be explored further.

The first variable that can be considered is the size and frequency of metal particles after calcination (but before reduction). As Pd has been shown to promote the reduction of CZO, it is reasonable to suggest that this may be localized to the regions around the Pd particles. If the degree of reduction is not uniform (both the in-plane directions and the film growth direction) then knowing the particle size and frequency at the onset of reduction is important. These parameters are functions of the deposition conditions, metal loading, calcination temperature, and calcination time. A systematic study of these variables may possibly lead to a kinetic model for the coarsening of Pd and Rh on CZO that can be developed to further augment ongoing computational research. To determine the agglomeration behavior of Pd and Rh on (111) CZO as a function of time, atmosphere, and temperature, a design-of-experiments approach could be used. Preliminary experiments (Figure 6.5) have shown that AFM is a useful tool for quickly determining particle size and area density, but plan-view TEM may give a more accurate measurement.   As discussed earlier, grazing incidence X-ray diffraction is a useful tool for determining the mean size of particles of a surface, however X-ray line broadening

can be further analyzed to provide useful data for dispersion measurements. Comparing these three techniques (grazing incidence XRD, plane view TEM, and , atomic force microscopy) for determining the size and area density of supported precious metal particles would be an interesting study for the community.

Another factor that could be considered is the thermal treatment protocol in the reduction and annealing treatment cycles. The reducing temperature was chosen from previous TPR studies of Pd/CZO [14] and the current protocol was chosen because it provided the most extensive wetting in the previous studies[4, 15]. However, the effect of a more aggressive reducing annealing treatment has not been investigated. If the reduced regions in the $Ce_{0.7}Zr_{0.3}O_2$ are localized around the Pd particles, then one can hypothesize that a longer or higher temperature reduction step might produce a larger reduced area. Successful EELS spectrum imaging or valance state mapping in two samples, one reduced according to previous conditions and one "aggressively" reduced, is one way to investigate this idea.

There are some other factors that might be considered in the future studies, including replacing Pt with Rh or Pd. Early results comparing Pd and Rh on CeO_2 [16] indicate that Rh may behave in an entirely different manner. This would be especially important in determining the size and frequency of metal particles at the onset of reduction. Additionally, earlier catalytic studies have shown that Rh affects the reducibility of $Ce_{0.7}Zr_{0.3}O_2$ in a different fashion than Pd [14, 17-18]. Thus reductions and thermal treatment conditions would need to be tailored to Rh to be analogous to a similar study with Pd.

Studying other orientations of CZO is another good area for future investigations. Previous studies have shown that the (100) CeO_2 surface is unstable, compared to the (111) orientation[19], showing a mixture of O_2 and Ce terminated regions. In contrast, (110) and other higher index surfaces of CeO_2 have shown faceting toward (111) under a variety of growth conditions[19]. These, surfaces could be investigated as part of a more exhaustive study, but issues with growth conditions (faceting and instability) may complicate detailed study of the metal-support interactions.

A more exhaustive treatment of this topic might also investigate support composition. The composition used in this work was selected for study because $Ce_{0.7}Zr_{0.3}O_2$ has the highest oxygen storage capacity of the mixed ceria and zirconia oxides[14]. However our more recent results have shown that wetting is not observed for Pd on YSZ [4] and Pd on CeO_2 [16]. If wetting is primarily a chemical rather than a stress related phenomena, as results in section 6.2 suggest, then exploring other compositions while keeping the same treatment conditions would be of interest.

6.3 Conclusions

Heterogeneous catalysts are expected to play increasingly important roles as the global automotive industry strives to meet future energy, environmental, and regulatory requirements. In order for emerging catalyst technologies to fill the anticipated roles in facing these challenges, characterization of catalyst materials is essential. As most catalysis processes and reactions occur on nanometer scale active sites, atomic scale characterization is a necessary step to achieve these potential applications[20]. Therefore,

this thesis has presented the use of atomic scale characterization techniques to further the understanding of three catalysts systems, namely Pt-alloy fuel cell catalysts studied, Pt-Pd NO oxidation catalysts, and precious metals supported on ceria based supports.

Although it is important to understand catalysts structure and catalytic activity, it is equally important to identify methods of reducing precious metal loading and improving catalyst durability. This is due to the fact that the above mentioned catalyst systems are dependent on expensive and strategically important materials. As demand for PGMs is likely to increase in the future, limiting catalysts deactivation of these materials will become a primary engineering challenge to ensure maximum utilization of PGMs. The goal of this study has been to provide critical information on deactivation mechanisms as the industry develops novel, more active, and more durable catalyst technologies for vehicle technologies. In this thesis, we have been able to use atomic scale structural characterization to better understand mechanisms of heterogeneous catalysts deactivation. Catalyst characterization is an evolving and growing field of research, and our findings, combined with extensive catalytic testing are part of collaborative efforts to add to the existing knowledge of the fundamental science and engineering of these materials.
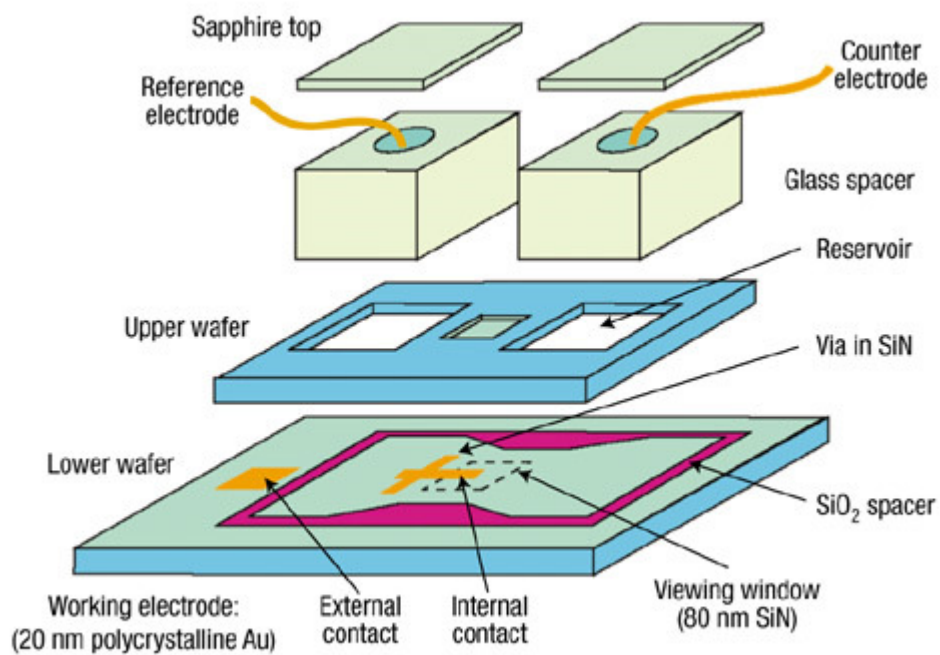
6.4 Figures

Figure 6.1: Schematic of in-situ electrochemical electron microscopy holder. It is suggested that such a configuration could directly confirm fuel cell catalyst aging mechanisms in situ (from Williamson[2])
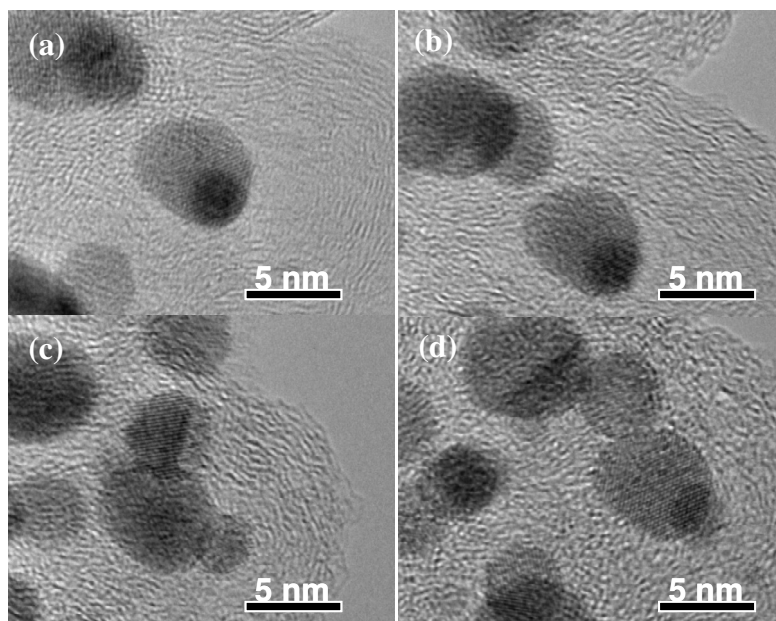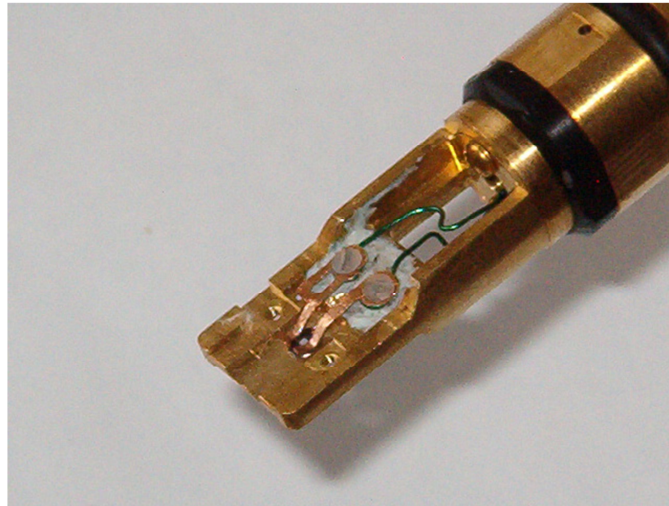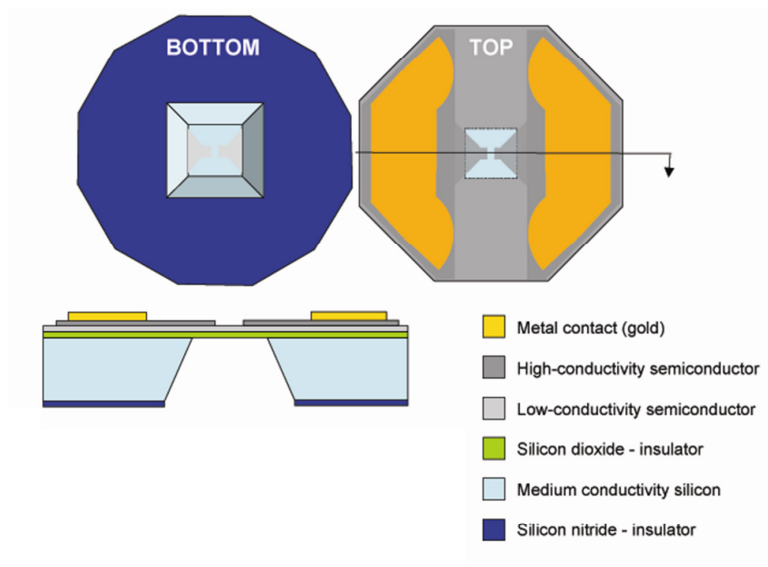
Figure 6.2: HRTEM images of fresh Pt/C nanoparticles after (a) 0 (b) 10 (c) 16, and (d) 22 minutes of electron beam exposure.

(a)

(b)

Figure 6.3: (a) Protochips holder (b) diagram of heating mechanism (image courtesy of L. Allard with permission)

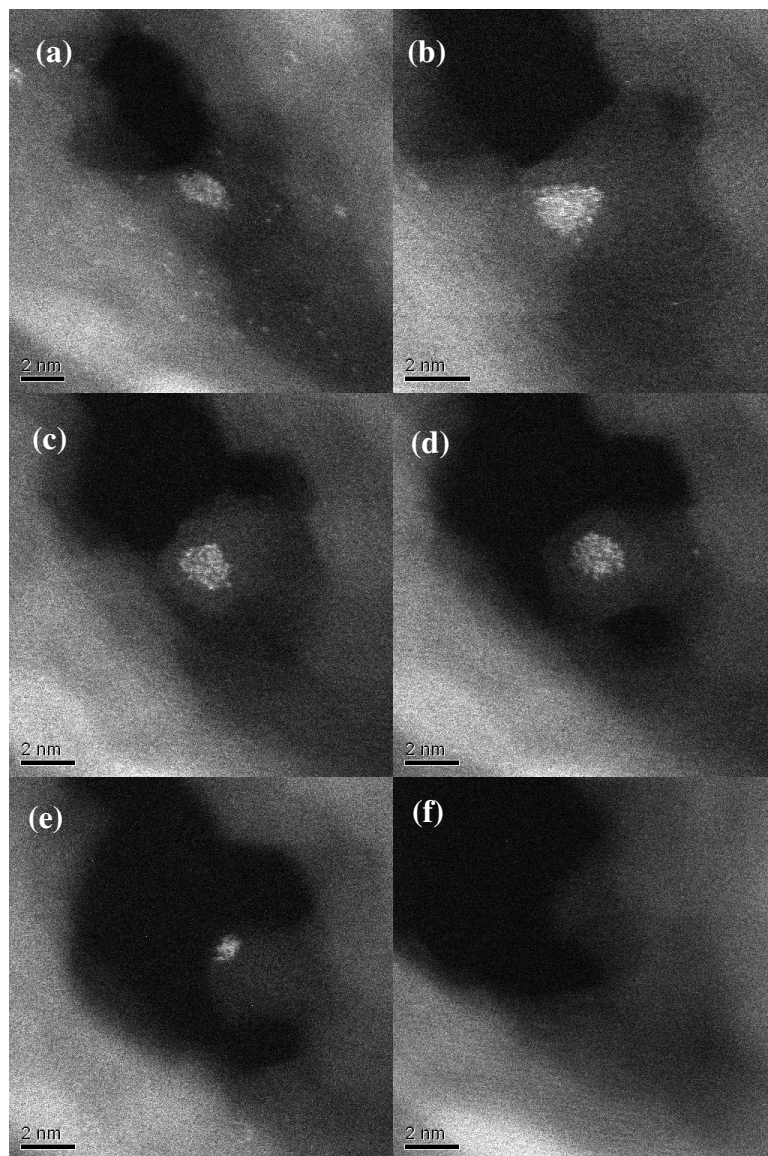Figure 6.4: Aberration corrected HAADF micrographs of Pt50-Pd50 (ac-ac) heated in situ on a Protochyps Aduro ® heater. Figure (a) shows the fresh catalyst. Figure (b) after one 10min heating interval at 500º C, (c) after a second 10min heating interval at 500ºC, (d) after a third 10min heating interval at 500ºC, (e) after a subsequent 10min heating interval at 900ºC, and (f) after a second 10min heating interval at 900ºC.
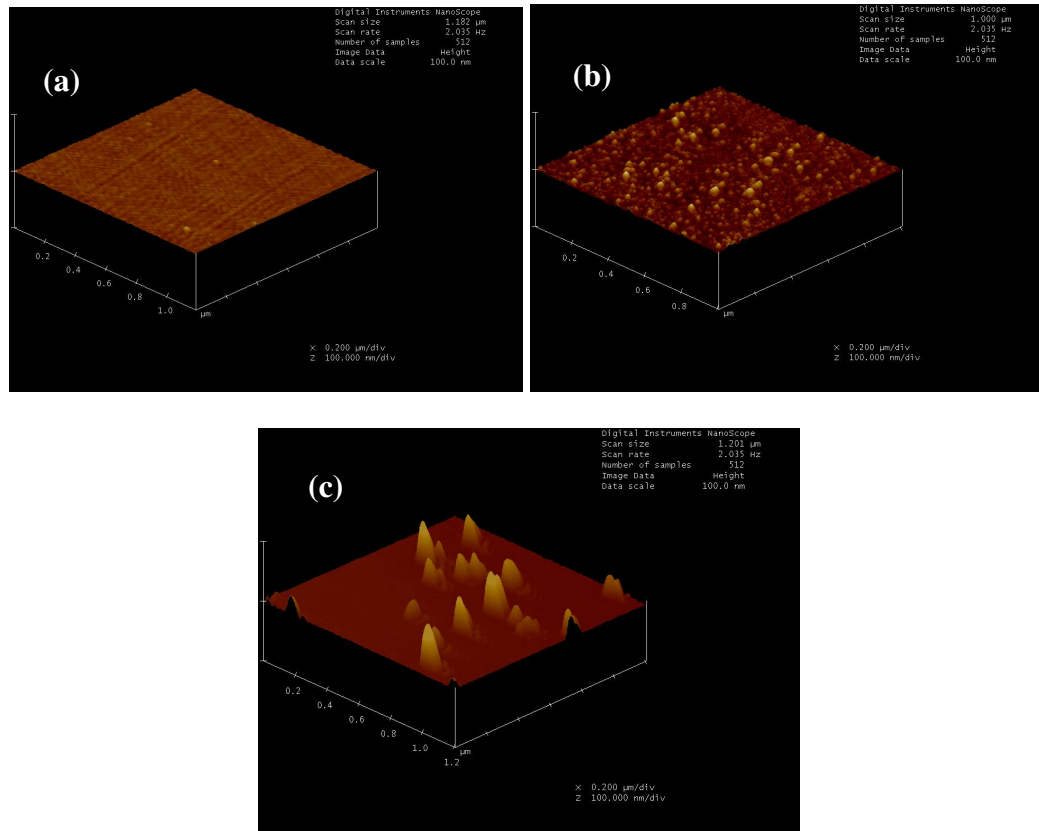
Figure 6.5: 1μm x 1μm AFM scans of Pd on CZO after (a) no treatment, (b) calcination in 600ºC in air for 1 h and (b) calcination and annealing in 700ºC in N$_2$ for 5 h. Particles are not observable in the fresh state, but after calcining, the mean particle size is 4.1 nm, and after further annealing, the mean particle size is 25 nm. These measurements of size and density are comparable results obtained from cross-sectional TEM observations in Chapter 5.

6.5 References

1. P. Gai, R. Sharma, and F. Ross, "Environmental (S)TEM studies of gas-liquid-solid interactions under reaction conditions." *MRS Bull.* **33**(2): p. 107-114 (2008).

2. M.J. Williamson, R.M. Tromp, P.M. Vereecken, R. Hull, and F.M. Ross, "Dynamic microscopy of nanoscale cluster growth at the solid-liquid interface." *Nat Mater*. **2**(8): p. 532-536 (2003).

3. Y. Tamou and S.-i. Tanaka, "Formation and coalescence of tungsten nanoparticles under electron beam irradiation." *Nanostruct. Mater.* **12**(1-4): p. 123-126 (1999).

4. H.P. Sun, X.Q. Pan, G.W. Graham, H.-W. Jen, R.W. McCabe, S. Thevuthasan, and C.H.F. Peden. "Evaluation of the Adhesion Energy of Pd Particles on Reduced Ceria-Zirconia Surface by Cross-sectional TEM Imaging." in *16th International Microscopy Congress*. Sapporo, Japan. (2006).

5. Y.E. Seidel, R.W. Lindstrom, Z. Jusys, M. Gustavsson, P. Hanarp, B. Kasemo, A. Minkow, H.J. Fecht, and R.J. Behm, "Stability of Nanostructured Pt/Glassy Carbon Electrodes Prepared by Colloidal Lithography." *J. Electrochem. Soc.* **155**(3): p. K50-K58 (2008).

6. P.J.F. Harris, "The sintering of platinum particles in an alumina-supported catalyst: Further transmission electron microscopy studies." *J. Catal.* **97**(2): p. 527-542 (1986).

7. J. Andersson, M. Antonsson, L. Eurenius, E. Olsson, and M. Skoglundh, "Deactivation of diesel oxidation catalysts: Vehicle- and synthetic aging correlations." *Applied catalysis. B, Environmental*. **72**(1-2): p. 71-81 (2007).

8. L.F. Allard, W.C. Bigelow, M. Jose-Yacaman, D.P. Nackashi, J. Damiano, and S.E. Mick, "A new MEMS-based system for ultra-high-resolution imaging at elevated temperatures." *Microsc. Res. Tech.* **72**(3): p. 208-215 (2009).

9.   L.F. Allard, W.C. Bigelow, S.A. Bradley, and J. Liu, "A Novel Heating Technology for Ultra-High Resolution Imaging in Electron Microscopes." *Microscopy Today*. **17**(04): p. 50-55 (2009).

10.   P.J.F. Harris, "The Morphology of Platinum Catalyst Particles Studied by Transmission Electron-Microscopy." *Surf. Sci.* **185**(1-2): p. L459-L466 (1987).

11.   M. Newville, "X-ray Absorption Fine-Structure Spectroscopy", (2008).

12.   J.A. Anderson and M. Fernández Garcia, "Characterization of Supported Meals Catalysts by Spectroscopic Techninques ", in *Supported metals in catalysis*, J.A. Anderson and M. Fernández Garcia, Editors., World Scientific: New Jersey (2005).

13.   B.M. Weiss and E. Iglesia, "Mechanism and site requirements for NO oxidation on Pd catalysts." *J. Catal.* **272**(1): p. 74-81 (2010).

14.   H.W. Jen, G.W. Graham, W. Chun, R.W. McCabe, J.P. Cuif, S.E. Deutsch, and O. Touret, "Characterization of model automotive exhaust catalysts: Pd on ceria and ceria-zirconia supports." *Catal. Today*. **50**(2): p. 309-328 (1999).

15.   H.P. Sun, X.P. Pan, G.W. Graham, H.W. Jen, R.W. McCabe, S. Thevuthasan, and C.H.F. Peden, "Partial encapsulation of Pd particles by reduced ceria-zirconia." *Appl. Phys. Lett.* **87**(20)(2005).

16.   B. Li, O.K. Ezekoye, Q. Zhang, L. Chen, G. Graham, and X. Pan, "On the Origin of Rh and Pd Agglomeration on the CeO2(111) Surface", in *Angew. Chem. Int. Ed.* (2010).

17.   P. Fornasiero, R. Dimonte, G.R. Rao, J. Kaspar, S. Meriani, A. Trovarelli, and M. Graziani, "Rh-Loaded CeO2-ZrO2 Solid-Solutions as Highly Efficient Oxygen Exchangers: Dependence of the Reduction Behavior and the Oxygen Storage Capacity on the Structural-Properties." *J. Catal.* **151**(1): p. 168-177 (1995).

18.   J.A. Wang, T. López, X. Bokhimi, and O. Novaro, "Phase composition, reducibility and catalytic activity of Rh/zirconia and Rh/zirconia-ceria catalysts." *J. Mol. Catal. A: Chem.* **239**(1-2): p. 249-256 (2005).

19.   A. Trovarelli, *Catalysis by Ceria and Related Materials*. London: Imperial College Press. (2002).

20.   P.L. Gai and E.D. Boyes, *Electron microscopy in heterogeneous catalysis*. Series in microscopy in materials science. Bristol: Institute of Physics Pub. (2003).

Appendix 1

Exposure Model for Estimating Aging Conditions in Alumina Supported Pt and PtPd Catalysts

Two sets of Pt100-Pd0 and Pt50-Pd50 nominally aged at 500ºC catalysts were made from Nitrate precursors. Both of these samples were fabricated and aged at the Research and Innovation Center at the Ford Motor Company, in Dearborn, MI. The first set of catalysts (labeled "sample A") was aged *in-situ* in a multichannel flow reactor in which NO oxidation measurements were preformed (described in 3.2).[1] Upon investigation sample A, the NO oxidation measurements were not consistent with previous observation and the well-known structure sensitivity of alumina supported Pt catalysts (as shown in Figure A.1).[2-3] This discrepancy in NO conversion in activity led to the conclusion that aging preceded very differently in theses two samples.

The actual aging temperature was estimated by comparing XRD data from Sample A to a previously-performed high-throughput study of the aging kinetics of alumina supported Pt and Pt-Pd NO oxidation catalysts.[4] Using a newly prepared and aged Pt/Al$_2$O$_3$ sample (labeled "Sample B") as a reference, the XRD data from "Sample A" was used in a previously proposed exposure model (given in the Equation A.1):

$$D = A * t^{\frac{1}{3}} * e^{\frac{-E}{kT}}$$

<div align="right">Equation A.1</div>

Where D = avg. particle diameter from Debye Scherer equation

t = time in minutes

A = prefactor

E = activation barrier

Solving for A and E, yields A=751.7min^{-1} and E=0.403eV.   Following this model, we can estimate the actual aging temperature of approximately 963K. This treatment assumes that both sets of catalysts follow the previously identified Arrhenius-type temperature dependence and is proportional to the cube-root of time (data for pure Pt Figure A.2). Therefore, we can estimate the actually aging temperate as 690°C as was presented in Chapter 4.
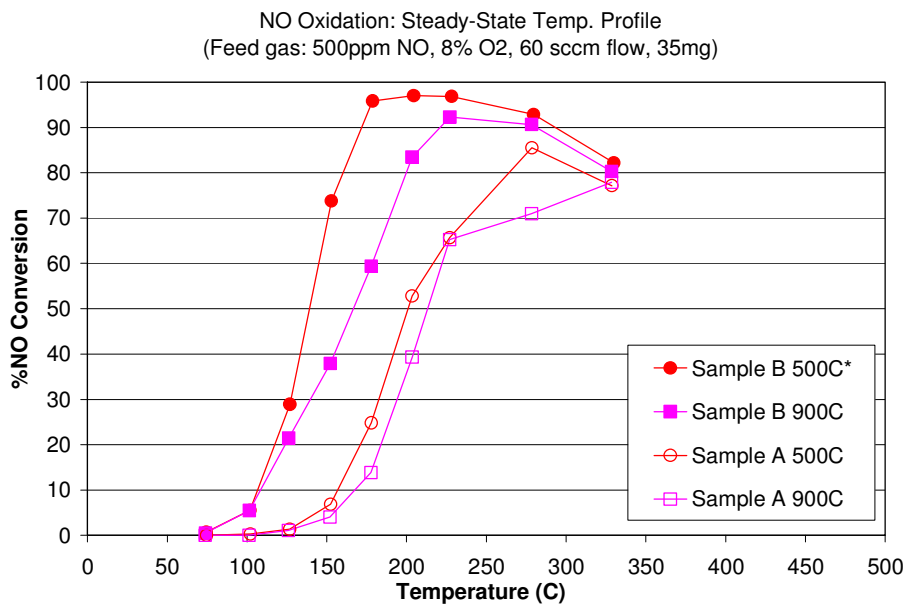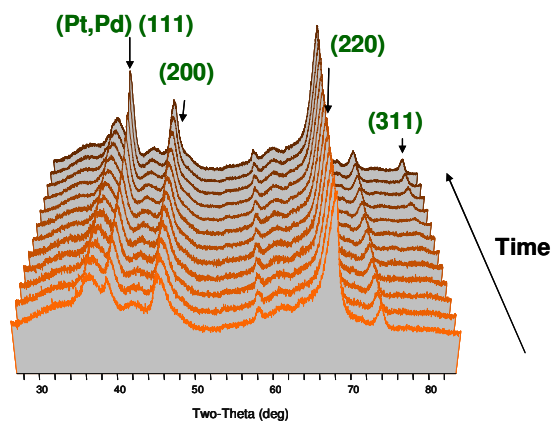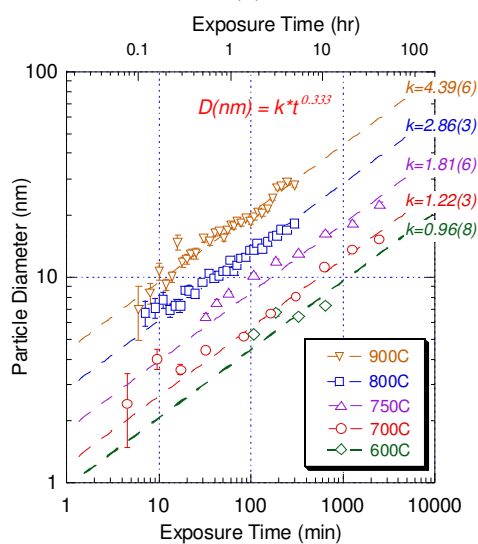
Figure A.1: NO oxidation steady state temperature profile for NO Oxidation measurements for bimetallic Pt-Pd catalysts aged under different conditions.

Figure A.2: (a) XRD time series showing in-situ aging of Pt/Al$_2$O$_3$ in an atmosphere of 10%O$_2$, 5%CO$_2$, 2%H$_2$O. (b) Arrhenius plot of particle sizes calculated from the corrected XRD peak widths. Fits to the data are constrained to a simple power-law with an exponent fixed at 1/3. (both figures adapted form Drews [3]).

1.   P.J. Schmitz, R.J. Kudla, A.R. Drews, A.E. Chen, C.K. Lowe-Ma, R.W. McCabe, W.F. Schneider, and J. Goralski, C.T., "NO oxidation over supported Pt: Impact of precursor, support, loading, and processing conditions evaluated via high throughput experimentation." *Appl. Catal., B*. **67**(3-4): p. 246-256 (2006).

2.   G.W. Graham, H.W. Jen, O. Ezekoye, R.J. Kudla, W. Chun, X.Q. Pan, and R.W. McCabe, "Effect of alloy composition on dispersion stability and catalytic activity for NO oxidation over alumina-supported Pt-Pd catalysts." *Catal. Lett.* **116**(1-2): p. 1-8 (2007).

3.   E. Xue, K. Seshan, and J.R.H. Ross, "Roles of supports, Pt loading and Pt dispersion in the oxidation of NO to NO2 and of SO2 to SO3." *Appl. Catal., B*. **11**(1): p. 65-79 (1996).

4.   A.R. Drews and R.J. Kudla, "Optimizing and Characterizing Pt:Pd Alloy Catalysts for DOC Applications Using a High-Throughput Approach ", in *Ford Motor Coompany Department Seminar*: Dearborn MI (2008).